

Supported ruthenium nanoparticles for supercritical water gasification - synthesis, activity and stability

Présentée le 15 octobre 2021

Faculté des sciences de base
Groupe Kröcher
Programme doctoral en chimie et génie chimique

pour l'obtention du grade de Docteur ès Sciences

par

Christopher Marc HUNSTON

Acceptée sur proposition du jury

Prof. R. Beck, président du jury
Prof. O. Kröcher, Prof. F. Vogel, directeurs de thèse
Prof. K. de Jong, rapporteur
Dr G. Peng, rapporteur
Prof. A. Züttel, rapporteur

Acknowledgements

I would like to thank Prof. Oliver Kröcher and Prof. Frédéric Vogel for giving me the opportunity to do my doctoral studies on a subject that is dear to me, renewable energies and more specifically biomass conversion. I thank them for all the interesting project discussions and feedback.

I would like to thank Dr. David Baudouin too, who supervised me during my thesis and always came up with interesting ideas for the project. I also want to thank him for the many hours spent doing TEM.

I want to express my gratitude to Prof. Krijn de Jong, Prof. Andreas Züttel and Dr. Gaël Peng for accepting being co-examiners of my thesis, and to Prof. Rainer Beck for being the jury president.

I sincerely thank all group members and colleagues who helped me during my research at PSI. In particular, Erich de Boni for knowing where to find any spare part for my setup, for knowing who to contact when requiring specific competences, for the SEM-EDX sessions and also for the great times outside of PSI. Also Leo Koning, who partly worked on my project during his internship and did a great job at synthesising and helping me characterise catalysts. I am very grateful to Pascal Unverricht, who did a tremendous job at upgrading and fixing Konti-I, keeping this great setup running smoothly through the years. I also want to thank Timon Käser for teaching me how to use our analytical instruments, Davide Ferri (DRIFTS), Ivo Alxneit (TEM), Andrea Testino (TGA), Łukasz Kondracki (Raman), Mohamed Tarik and Ayush Agarwal (ICP-MS) for helping me with their analytical devices.

I also want to thank Dominik Gschwend for his support with LaTeX-related issues, Martin Elsener for teaching me how to use the different reduction setups and showing me the best running routes in the hills around PSI. To everyone joining the lunch runs, swimming and after-work sessions in Baden, we had a good time, thanks !

I also want to use this opportunity to thank my family for supporting me during my studies and for always backing my decisions.

Last but not least, I want to thank Laetitia and our beautiful daughter Ella who were patient and supported me during my doctoral studies, especially in the latter stages when I was less available to help or play.

Zürich, 10th July 2021

Abstract

Supercritical water gasification (SCWG) is a promising and versatile technology for the conversion of a variety of wet biomass streams into renewable natural gas. In this work, the focus is set on methane production with the help of an active and stable methanation catalyst. The supercritical water (SCW) environment can unfortunately lead to rapid catalyst deactivation through different mechanisms, namely poisoning, coking, sintering or leaching. Although recent works focussed on these mechanisms to synthesise more robust Ru/C gasification catalysts, it remains challenging to discriminate between the different mechanisms because of the process conditions. The goal of this doctoral thesis is to get a better understanding of the aforementioned deactivation pathways by trying to study them individually, in order to tailor an active and robust SCWG catalyst.

The gasification activity of carbon supports exhibiting different properties was assessed by feeding glycerol at 400 °C and 30 MPa. The undesired effect of micropores was evidenced by significant coke deposition and surface area losses around 90 %, compared to mesoporous activated carbons (ACs) that only lost 20 %. Carbon nanofibers (CNF) proved to be an interesting support showing very good stability and remarkable inertness. The synthesis of 5 %Ru catalysts on selected supports confirmed these trends. Highly microporous Ru/AC catalysts were less stable than the ones supported on carbon frameworks of more open pore structure. Ru/CNF seemed to be a promising SCWG catalyst, with an enhanced resistance towards coke formation. The completely open pore structure of CNF was found to be a crucial parameter.

Ruthenium loss was investigated by measuring its content in the process waters with time-resolved ICP-MS. Ru was successfully quantified at levels close to thermodynamic equilibrium models for Ru/AC and Ru/CNF of different loadings. Furthermore, neither the temperature, the feed rate, nor the feed concentration had an effect on the quantified Ru, showing that the steady-state concentrations represent a thermodynamically-driven leaching. Fluctuations in feed rate and pressure damaged the catalyst through friction and led to higher Ru losses, mainly through the release of carbon domains containing Ru nanoparticles (NPs). A key learning for future pilot plants is the importance of operating at stable process conditions. Metal oxides were compared to AC by synthesising 2 %Ru catalysts on α -Al₂O₃, ZrO₂ and TiO₂.

They yielded 20–40 times higher Ru loss rates than for 2 %Ru/AC and a significantly lower activity, confirming once again the superiority of Ru/AC as SCWG catalyst.

With Ru/CNF proving to be an interesting SCWG catalyst, more in-depth studies were performed on this model system. Catalysts of different loadings (1–30 %Ru) were successfully synthesised from $\text{RuNO}(\text{NO}_3)_3$ and RuCl_3 yielding very small Ru NPs (0.9–2.2 nm) with an easy synthesis method. Ru/CNF catalysts exhibited high gasification activities and improved stability compared to Ru/AC. The initial activity correlated with the Ru dispersion, highlighting a particle size effect. However, 1 %Ru/CNF catalysts underwent rapid deactivation compared to 5 %Ru/CNF, showing the importance of the Ru NP density to avoid rapid deactivation. The effect of surface Ru atom density was shown with high turnover frequencies in the range $0.4\text{--}0.7 \text{ atom}_{\text{Ru,sfc}} \text{ nm}^{-2}$. For the first time, a particle size effect and more importantly a surface-atom density effect was shown during SCWG of glycerol.

Eventually, coke deposition was also investigated and observed at very high space velocities only, showing the advantage of using an inert, meso/macroporous support. The coke deposits could partially be removed by extraction in a mix of solvents, opening a potential new route for the regeneration of Ru/C catalysts.

With Ru/CNF, we found an alternative catalyst to the well-known Ru/AC, showing a similar activity and enhanced stability. The feasibility of using Ru/CNF on larger scales must however still be evaluated.

Keywords

Catalytic supercritical water gasification · Ruthenium · Activated carbon · Carbon nanofibers · Glycerol · Coking · Leaching · Sintering · Particle size effect

Résumé

La gazéification en eau supercritique (SCWG) est une technologie prometteuse et versatile pour la conversion de biomasse humide en gaz naturel renouvelable. Ce travail se concentre sur la production de méthane à l'aide d'un catalyseur de méthanation et gazéification stable et actif. En effet, les hautes pression et température de l'eau supercritique (SCW) peuvent malheureusement provoquer une désactivation rapide du catalyseur à travers différents mécanismes, comme l'empoisonnement, le cokage, le frittage ou la dissolution. Malgré de récentes études menées pour synthétiser des catalyseurs Ru/C plus robustes, il reste cependant difficile de dénouer ces différents mécanismes à cause des conditions extrêmes du procédé. Le but de cette thèse est d'obtenir une meilleure compréhension des processus de désactivation mentionnés antérieurement en les étudiant individuellement, pour finalement être capable de produire un catalyseur actif et plus résistant pour la gazéification en eau supercritique.

L'activité intrinsèque de différents supports à base de carbone a été évaluée avec du glycérol à 400 °C et 30 MPa. L'effet négatif des micropores a été mis en évidence par le dépôt significatif de coke et des pertes de surface spécifique atteignant les 90 %. En comparaison, les charbons actifs (AC) mesoporeux ne perdaient que 20 %. Les nanofibres de carbone (CNF) se sont révélées comme étant un support intéressant en gardant une très bonne stabilité et en étant inertes en conditions de gazéification. La synthèse de catalyseurs 5 %Ru sur différents supports évalués montrent la même tendance durant la gazéification. Les catalyseurs Ru/AC hautement microporeux étaient moins stables que ses analogues ayant une structure plus ouverte. Ru/CNF semble être un catalyseur prometteur pour la SCWG grâce à une résistance accrue envers le cokage. La structure ouverte des CNF s'est révélée être un paramètre crucial.

La perte de ruthénium du lit catalytique a été investiguée en mesurant la concentration de Ru dans les eaux de procédé grâce à l'ICP-MS. De très basses concentrations ont pu être quantifiées, proches de l'équilibre thermodynamique, pour des catalyseurs contenant différentes charges de Ru. Des variations de pression ont mené à des pertes plus importantes de ruthénium à cause de la friction générée dans le lit catalytique. Cet apprentissage est crucial pour la future mise en service de prototypes ou d'usines pilotes. En comparant des catalyseurs 2 %Ru sur AC aux oxydes métalliques, la dissolution de ruthénium s'est avérée 20 à 40 fois plus

élevée pour les catalyseurs à base de α -Al₂O₃, ZrO₂ ou TiO₂. De plus, leur activité était moins bonne, montrant à nouveau la supériorité de Ru/AC.

En démontrant que Ru/CNF est un catalyseur prometteur pour la SCWG, des études plus approfondies ont été menées sur ce système modèle. Des catalyseurs contenant des fractions de Ru différentes (1–30 %Ru) ont été synthétisés à partir de RuNO(NO₃)₃ et de RuCl₃, résultant en de très petites nanoparticules de Ru (0.9–2.2 nm). Les catalyseurs Ru/CNF étaient très actifs et ont également démontré une meilleure stabilité comparé aux Ru/AC. L'activité initiale était bien liée à la dispersion du Ru, démontrant l'effet de la taille des particules sur l'activité. Néanmoins, les catalyseurs 1 %Ru/CNF ont subi une rapide désactivation comparé aux 5 %Ru/CNF, montrant l'importance de la densité de sites actifs. Cet effet a été prouvé avec une concentration optimale se situant entre 0.4 et 0.7 atom_{Ru,sfc} nm⁻² menant à la meilleure activité catalytique. C'est la première fois que ces effets sont démontrés dans ce domaine.

Finalement, le cokage a aussi été étudié et n'était visible qu'après avoir traité le catalyseur dans des conditions extrêmes menant à une rapide désactivation. Ces dépôts ont pu être partiellement enlevés grâce à une extraction dans un mélange de solvants, montrant une nouvelle voie potentielle pour la régénération de catalyseurs Ru/C. Avec ce nouveau système Ru/CNF, nous avons démontré qu'il existe une alternative aux charbons actifs, bien qu'il faut encore valider son utilisation pour la gazéification en eau supercritique à plus grande échelle.

Mots-clés

Gazéification en eau supercritique · Ruthénium · Charbon actif · Nanofibres de carbone · Glycérine · Cokage · Dissolution · Frittage · Nanoparticules

Contents

Acknowledgements	i
Abstract (English/Français)	iii
List of Acronyms	xi
List of Symbols	xiv
List of Figures	xvii
List of Tables	xxiii
1 Introduction	1
1.1 Mitigating global warming	1
1.2 Biomass conversion technologies	2
1.2.1 Combustion	3
1.2.2 Gasification	3
1.2.3 Pyrolysis	4
1.2.4 Hydrothermal carbonisation	4
1.2.5 Hydrothermal liquefaction	4
1.2.6 Hydrothermal gasification	5
1.2.7 Fermentation	5
1.2.8 Anaerobic digestion	6
1.3 Supercritical water	6
1.4 Supercritical water gasification	11
1.5 Catalytic supercritical water gasification	12
1.5.1 State-of-the art catalysts for SCWG	13
1.5.2 Active Ru species	16
1.5.3 Continuous SCWG of biomass	17
1.6 Deactivation mechanisms in SCWG	18
1.6.1 Ru loss	19
1.6.2 Sintering	20
	vii

Contents

1.6.3	Coking	21
1.6.4	Poisoning	22
1.7	Size sensitivity of supported metal catalysts	23
1.8	Problem statement	25
1.9	Scope of the thesis	26
2	Methods and materials	29
2.1	Catalyst support preparation	29
2.1.1	Sieving	29
2.1.2	CNF purification	29
2.2	Catalyst synthesis	30
2.2.1	Wet impregnation	30
2.2.2	Incipient wetness impregnation	30
2.2.3	Calcination	31
2.2.4	Reduction	31
2.3	Catalyst characterisation methods	31
2.3.1	N ₂ physisorption	31
2.3.2	CO pulse chemisorption	32
2.3.3	X-ray diffraction	32
2.3.4	Thermogravimetric analysis	32
2.3.5	Diffuse reflectance infrared Fourier transform spectroscopy	32
2.3.6	Raman spectroscopy	33
2.3.7	Scanning electron microscopy - energy dispersive X-Ray spectroscopy	33
2.3.8	Transmission electron microscopy	33
2.3.9	High-resolution transmission electron microscopy	33
2.3.10	Particle size distributions	34
2.4	Analytical methods	36
2.4.1	Organic carbon determination	36
2.4.2	Gas chromatography	36
2.4.3	Elemental analysis	36
2.4.4	ICP-MS	37
2.4.5	Ash content determination	37
2.4.6	Error estimation and propagation	38
2.5	Continuous SCWG test rigs	38
2.5.1	Konti-I	38
2.5.2	Intermediate & Konti-C setups	44
2.6	Materials	45
3	Optimal carbon supports for Ru-based SCWG catalysts	47

3.1	Carbon support selection	47
3.2	Influence of carbon support on catalyst activity	53
3.3	Summary	59
4	Ru loss during SCWG	61
4.1	Commercial Ru/C catalysts	61
4.2	Effect of process parameters	66
4.3	Intentional pressure and feed variations	68
4.4	Impact of feed type and setup size	71
4.4.1	Sewage sludge gasification on the <i>intermediate</i> setup	73
4.5	Ru loss from metal oxide-supported catalysts	75
4.6	Summary	77
5	Ru/CNF as SCWG catalyst	81
5.1	Synthesis and characterisation of Ru/CNF catalysts	81
5.2	Catalytic testing of Ru/CNF	85
5.3	Coking on Ru/CNF catalysts during SCWG	97
5.4	Ru loss from CNF-supported catalysts	106
5.5	Comparison Ru/CNF vs. Ru/AC	108
5.6	Summary	110
6	Concluding remarks and outlook	111
6.1	Achieved results	111
6.2	Conclusions	113
6.3	Recommendations for further research	115
A	Konti-I setup	117
A.1	Setup control	117
A.2	List of experiments	121
B	Carbon supports for SCWG catalysts	125
C	Ru loss from SCWG catalysts	127
D	Ru/CNF catalysts	137
	Bibliography	149
	List of publications	165
	Curriculum Vitae	167

Acronyms

AC	activated carbon
AD	anaerobic digestion
BET	Brunauer-Emmett-Teller
bio-SNG	renewable natural gas
BJH	Barrett-Joyner-Halenda
BPR	back pressure regulator
CNF	carbon nanofibers
CNT	carbon nanotubes
DFT	density functional theory
DI	deionised
DRIFTS	diffuse reflectance infrared Fourier transform spectroscopy
DTG	differential thermogravimetric analysis
EDX	energy dispersive X-ray spectroscopy
EXAFS	extended X-ray absorption fine structure
FT	Fischer-Tropsch
GC	gas chromatography
hcp	hexagonal close-packed
HR-TEM	high-resolution transmission electron microscopy
HTC	hydrothermal carbonisation
HTG	hydrothermal gasification
HTL	hydrothermal liquefaction
ICP-MS	inductively coupled plasma - mass spectrometry

Acronyms

ICP-OES	inductively coupled plasma - optical emission spectroscopy
IEA	International Energy Agency
IR	infrared
IWI	incipient wetness impregnation
LC-MS	liquid chromatography - mass spectrometry
LHV	lower heating value
LoD	limit of detection
LoQ	limit of quantification
MS	mass spectrometer
MWCNT	multi-walled carbon nanotubes
n.a.	not applicable
NP	nanoparticle
P&ID	piping and instrumentation diagram
PAH	polycyclic aromatic hydrocarbon
PFR	plug-flow reactor
PSD	particle size distribution
PSI	Paul Scherrer Institute
PW	process water
RSD	residual standard deviation
RT	room temperature
SCF	supercritical fluid
SCW	supercritical water
SCWG	supercritical water gasification
SEM	scanning electron microscopy
SLW	synthetic liquefied wood
subCW	subcritical water
subCWG	subcritical water gasification
TC	total carbon
TCD	thermal conductivity detector

TEES	thermochemical environmental energy system
TEM	transmission electron microscopy
TGA	thermogravimetric analysis
TIC	total inorganic carbon
TOC	total organic carbon
TOS	time on stream
TPO	temperature-programmed oxidation
TPR	temperature-programmed reduction
WGS	water-gas shift
WI	wet impregnation
XANES	X-ray absorption near edge structure
XAS	X-ray absorption spectroscopy
XPS	X-ray photoelectron spectroscopy
XRD	X-ray diffraction
XRF	X-ray fluorescence

Symbols and terms

A_{CS}	reactor cross section	(m ²)
$a(i)$	activity of compound i	(-)
D	diffusivity	(m ² s ⁻¹)
D_{CO}	metal dispersion by CO chemisorption	(%)
D_{TEM}	metal dispersion by TEM	(%)
d_{cat}	catalyst grain diameter	(mm)
$d_{p,CO}$	mean particle size by CO chemisorption	(nm)
$d_{p,TEM}$	mean particle size by TEM	(nm)
d_R	reactor diameter	(mm)
F	feed rate	(g min ⁻¹)
GE_C	carbon gasification efficiency	(%)
H_{cat}	catalyst bed height	(mm)
K_W	dissociation constant of water	(-)
L	reactor length	(mm)
m_{cat}	catalyst mass	(g)
p	pressure	(MPa)
p_c	critical pressure	(MPa)
Ru_{sfc}	surface Ru atoms	(atoms)
Ru_{tot}	total (bulk) Ru atoms	(atoms)
SSA	specific surface area	(m ² g ⁻¹)
SSA_{ext}	external surface area	(m ² g ⁻¹)
SSA_{MP}	micropore surface area	(m ² g ⁻¹)
T	temperature	(°C)
T_c	critical temperature	(°C)

Acronyms

TOF	turnover frequency	(min^{-1})
u_s	superficial velocity	(m s^{-1})
V	volume	($\text{cm}^3, \text{mL}, \text{L}$)
V_m	molar volume	($\text{cm}^3 \text{mol}^{-1}$)
V_p	total pore volume	($\text{cm}^3 \text{g}^{-1}$)
V_{ext}	external pore volume	($\text{cm}^3 \text{g}^{-1}$)
V_{MP}	micropore volume	($\text{cm}^3 \text{g}^{-1}$)
$WHSV$	weight hourly space velocity	($\text{g}_{\text{org}} \text{g}_{\text{cat}}^{-1} \text{h}^{-1}$)
$WHSV_{\text{gRu}}$	weight hourly space velocity, per gram Ru	($\text{g}_{\text{org}} \text{g}_{\text{Ru}}^{-1} \text{h}^{-1}$)
X_C	carbon conversion	(%)
x_i	mass fraction of compound i	(%)
y_i	volume fraction of compound i	(%)
ΔH_{vap}	enthalpy of vaporisation	(kJ mol^{-1})
ϵ	dielectric constant	(-)
η	dynamic viscosity	(Pa s)
ν	kinematic viscosity	($\text{m}^2 \text{s}^{-1}$)
ρ	density	(kg m^{-3})
τ	residence time	(s)

List of Figures

1.1	World primary energy production in thousand tonnes of oil equivalent (ktoe) from 1971 to 2018. NGL stands for natural gas liquids. Data from the IEA [7]. . .	2
1.2	Thermochemical biomass conversion technologies and their main energy products. Adapted from [10], [11].	3
1.3	Isobaric water density as a function of temperature. Data from [38].	7
1.4	Isobaric water enthalpy as a function of temperature. Data from [38].	8
1.5	Evolution of the dielectric constant of water for different pressures as a function of temperature. Data computed from [38], [39].	9
1.6	Evolution of the ionisation constant of water K_W as a function of temperature. Adapted from [40].	10
1.7	Potential Ru loss mechanisms from activated carbon during SCWG, leaching (a) and attrition, self-gasification (b).	19
1.8	Size sensitivity of catalytic reactions. Re-used from [116].	23
2.1	Apparatus used to purify the CNF in KOH (1 M) at reflux.	30
2.2	Relationship between total (Ru_{tot}), surface (Ru_{sf}) Ru atoms and dispersion (D_{TEM}) as a function of Ru NP diameter, assuming a truncated bipyramid shape [118]. The lines represent the fitted 5 th -degree polynomial.	35
2.3	PID of the <i>Konti-I</i> setup (drawn by Pascal Unverricht).	40
2.4	Picture of the lab-scale continuous SCWG rig <i>Konti-I</i>	42
2.5	Scheme of the PFR with the different elements (left), and mounted on <i>Konti-I</i> (right).	43
2.6	Simplified scheme of the <i>Konti-C</i> test rig. Taken from [137].	44
3.1	Carbon conversion (left) and gas flow (right) during SCWG over carbon materials.	48
3.2	Carbon conversion rate of the different supports at the start and after 4 h of gasification.	50
3.3	Rate of carbon conversion normalised by the total surface area of the supports loaded in the reactor (TOS = 0.5 h).	51

List of Figures

3.4	Pore size distributions (differential volume dV as a function of pore radius r) of the fresh and spent (after exposure to 10 wt% glycerol) carbon supports.	52
3.5	Catalytic testing of 5 %Ru/AC-CGRAN with 10 % glycerol. $WHSV_{gRu}$ ($g_{Org}g_{Ru}^{-1}h^{-1}$) is indicated in the boxes (Exp. C3).	54
3.6	Catalytic testing of 5 %Ru/AC-H2S with 10 % glycerol. $WHSV_{gRu}$ ($g_{Org}g_{Ru}^{-1}h^{-1}$) is indicated in the boxes (Exp. C4).	55
3.7	Catalytic testing of 5 %Ru/AC-Spher with 10 % glycerol. $WHSV_{gRu}$ ($g_{Org}g_{Ru}^{-1}h^{-1}$) is indicated in the boxes (Exp. C2).	56
3.8	Catalytic testing of 22 %Ru/CNF with 10 and 20 % glycerol (changed at TOS =17 h). $WHSV_{gRu}$ ($g_{Org}g_{Ru}^{-1}h^{-1}$) is indicated in the boxes (Exp. C5).	57
3.9	Catalytic testing of 5 %Ru/AC-BM with 10 % glycerol. $WHSV_{gRu}$ ($g_{Org}g_{Ru}^{-1}h^{-1}$) is indicated in the boxes (Exp. C1).	58
4.1	Catalyst testing overview for Ru/AC-BM. The produced gas (top part of the graphs) and both the carbon conversion and Ru concentration (bottom part of the graphs) are shown as a function of the time on stream (Exp. C1).	63
4.2	Catalyst testing overview for Ru/AC-A. The produced gas (top part of the graphs) and both the carbon conversion and Ru concentration (bottom part of the graphs) are shown as a function of the time on stream (Exp. C7).	64
4.3	Catalyst testing overview for Ru/AC-B. The produced gas (top part of the graphs) and both the carbon conversion and Ru concentration (bottom part of the graphs) are shown as a function of the time on stream (Exp. C8).	65
4.4	Effect of process parameters on Ru loss from Ru/AC-A catalyst. 1 st catalyst load (left, Exp. C9), 2 nd catalyst load (right, Exp. C10-C12). Horizontal dashed lines represent the thermodynamic equilibrium solubility of Al and Ru (400 °C, 30 MPa), respectively [100]. A change in the varied parameter is indicated by a vertical dashed line, whereas a full vertical line indicates a complete setup restart.	67
4.5	Mean Ru concentration in the process waters for different reaction temperatures (left, Exp. C9,C10,C12) and glycerol concentrations (right, Exp. C11). Hatched area: below Ru LoQ (=0.007 $\mu g L^{-1}$).	68
4.6	Pressure (left) and mass flow rate (right) variations during the intentional fluctuations test (Exp. C13).	69
4.7	Ru loss comparison between the different process parameters assessed.	69
4.8	SEM images of the fresh Ru/AC-A catalyst (a: 100x, b: 500x) and spent having experienced fluctuations (c: 100x, d: 500x).	70
4.9	SEM images of the Ru/AC-A catalyst having experienced pressure and flow rate fluctuations (a: 375x, b: 3130x).	70

4.10	Normalised Ru loss rate for the commercial Ru/AC catalysts on the different SCWG setups. Empty symbols: 10 wt% glycerol (Exp. C1,C7,C8,C14), full symbols: sewage sludge (Exp. C15).	72
4.11	XRD spectra of fresh and spent samples of Ru/AC-A (top) and Ru/AC-BM (bottom). Spent-gly (Exp. C1,C7) and Spent-pFluct (Exp. C13) refer to catalysts treated with glycerol on <i>Konti-I</i> in normal operation and during the deliberate fluctuations test, respectively. Spent-SS refers to the experiment on the <i>intermediate</i> setup with sewage sludge (Exp. C15).	73
4.12	Ru loss rate as a function of catalyst bed aspect ratio $H_{cat}d_R^{-1}$. Empty symbols: 10 wt% glycerol, full symbols: sewage sludge.	74
4.13	Ru concentration in the effluent stream during SCWG of glycerol over 2 wt% Ru catalysts (left). Conversion and concentration profiles of Al and Ru for 2 %Ru/AC.	76
4.14	CH ₄ yield (left) and carbon conversion (right) for the 2 %Ru catalysts during SCWG of 10 wt% glycerol.	77
5.1	Evolution of the uncorrected (blue spheres) and loading-corrected (black squares) Ru/CNF pore volume (top) and surface area (bottom) as a function of Ru loading.	83
5.2	High-resolution micrographs of the fresh 1%Ru/CNF_2 (left) and 5%Ru/CNF_1 (right) catalysts. The small Ru NPs are seen as darker spots. Magnification: 250kX left, 600kX right.	84
5.3	Mean Ru NP diameter ($d_{p,TEM}$) as a function of Ru loading for the synthesised catalysts.	84
5.4	SCWG of glycerol (20 %) over 10 %Ru/CNF. The gas composition is shown in the top graph, the carbon gasification efficiency (GE_C , stars) and conversion (X_C , triangles) are shown in the bottom graph together with the produced gas flow (blue circles). $p = 28.5$ MPa, $T = 404$ °C, $WHSV_{gRu} = 4047$ g _{org} g _{Ru} ⁻¹ h ⁻¹ (Exp. C24).	85
5.5	Carbon flow during SCWG of glycerol over 10 %Ru/CNF. The carbon fed into the system (black dashed line) and the total carbon exiting the system (blue line) are shown, the latter being the sum of the carbon in the PW (grey area) and gas (blue area) phases.	86
5.6	Exponential decay fits for the conversion (left, red line) and the TOF (right) calculated from the fresh (black line) and spent (grey line) dispersions of the 10%Ru/CNF catalyst.	87
5.7	TOF overview after SCWG of glycerol (6–20 wt%) over Ru/CNF catalysts of different loadings. The left-hand side graph shows Ru/CNF (5–30 %) catalysts treated at $WHSV_{gRu} \approx 4000$ g _{org} g _{Ru} ⁻¹ h ⁻¹ (Exp. C22-C27). The right-hand side graph shows the 1 %Ru/CNF catalysts treated at $WHSV_{gRu}$ of 3000 and 9000 g _{org} g _{Ru} ⁻¹ h ⁻¹ (Exp. C20,C21). The shown TOFs were calculated with the fresh catalyst dispersion. $F = 9.4$ – 11.6 g min ⁻¹ , $p = 28.5$ MPa, $T = 400$ – 408 °C.	89

List of Figures

5.8	Final fitted turnover frequency (TOF_{end}) calculated from the spent dispersion for the different Ru/CNF catalysts.	89
5.9	TOF loss as a function of D_{TEM} loss for Ru/CNF catalysts tested for SCWG of glycerol.	92
5.10	PSD of a fresh 5 %Ru/CNF catalyst (red) and after treatment in SCW (blue). The main mode for $d_{p,TEM}$ as well as D_{TEM} are reported next to the histograms. . .	92
5.11	Final TOF after SCWG of glycerol over Ru/CNF catalysts as a function of Ru_{sfc} density. The reported TOF and Ru_{sfc} density relate to the spent catalysts. . . .	93
5.12	Thermogravimetric (TG, top), differential weight loss (DTG, middle) and heat flow (bottom) analyses for the fresh and spent 1 %Ru/CNF catalysts (Exp. C20,C21). .	94
5.13	HR-TEM images of the spent 1 %Ru/CNF_2 catalyst ($=9000 \text{ g}_{org} \text{ g}_{Ru}^{-1} \text{ h}^{-1}$, Exp. C21). Magnification: 800kX left, 600kX right.	95
5.14	HR-TEM images of the fresh 5 %Ru/CNF_1 catalyst. Magnification: 500kX left, 600kX right.	95
5.15	HR-TEM images of the spent 5 %Ru/CNF_1 catalyst ($=4000 \text{ g}_{org} \text{ g}_{Ru}^{-1} \text{ h}^{-1}$, Exp. C22). Magnification: 500kX.	96
5.16	SCWG activity of 5 %Ru/CNF_C at thermodynamic conditions <i>i.e.</i> $X_C = 100 \%$ (Exp. C30).	98
5.17	Carbon flow during glycerol SCWG over 5 %Ru/CNF_C at $X_C = 100 \%$ (Exp. C30). .	99
5.18	SCWG activity of 5 %Ru/CNF_C at kinetic conditions <i>i.e.</i> $X_C < 50 \%$ (Exp. C31). .	100
5.19	Carbon flow during glycerol SCWG over 5 %Ru/CNF_C at $X_C < 50 \%$ (Exp. C31). .	101
5.20	Evolution of $d_{p,TEM}$ for the different experiments with 5 %Ru/CNF_C and for the extracted catalyst sample.	102
5.21	TEM images of the fresh 5 %Ru/CNF_C catalyst (a), treated in SCW (b), spent at $1500 \text{ g}_{org} \text{ g}_{Ru}^{-1} \text{ h}^{-1}$ (c), spent at $11000 \text{ g}_{org} \text{ g}_{Ru}^{-1} \text{ h}^{-1}$ (d, e). 100kX magnification for a and b, 50kX for c, d and e.	103
5.22	Thermogravimetric (TG, top), differential weight loss (DTG, middle) and heat flow (bottom) analyses for the fresh and spent (Exp. C31) 5 %Ru/CNF catalysts. Conditions: 10 mg sample, air (10 mL min^{-1}), $5^\circ \text{C min}^{-1}$ ramp.	104
5.23	TEM images of the 5 %Ru/CNF_C catalyst treated at $11000 \text{ g}_{org} \text{ g}_{Ru}^{-1} \text{ h}^{-1}$ and extracted in a mix of solvents (MagicMix). 50kX magnification for a and c, 20kX for b.	105
5.24	Ru loss as a function of time on stream for selected Ru/CNF catalysts (Exp. C20,C23,C24,C26,C27).	106
5.25	X_C and Ru loss as a function of time on stream for 1 %Ru/CNF_1 (Exp. C20). . .	107
5.26	SCWG activity of 5 %Ru/AC-A. Conditions: 20 % glycerol, $F = 10.6 \text{ g min}^{-1}$, $p = 28.5 \text{ MPa}$, $T = 405^\circ \text{C}$ (Exp. C28).	108
5.27	Carbon flow during SCWG of glycerol over 5 %Ru/AC-A in kinetic regime (Exp. C28).	109

A.1	Screenshot of the main LabVIEW™ interface controlling <i>Konti-I</i>	117
A.2	Pressure and temperature monitoring in LabVIEW™.	118
A.3	LabVIEW™ settings for the automated sampling and data export.	119
A.4	Side installations of <i>Konti-I</i> : μ GC (a), gas counter (b), fumehood controls (c), emergency stop (d).	120
B.1	Gas composition after glycerol gasification over carbon supports. The total does not close to 100 % because of the low gas flows - the balance is N_2 (Exp. S1-S5).	125
C.1	ICP-MS time-resolved analysis for selected Ru/AC-BM SCWG samples. BM-xx.x refers to the sample TOS (h) (Exp. C1).	129
C.2	ICP-MS time-resolved analysis for selected Ru/AC-A SCWG samples. A-xx.x refers to the sample TOS (h) (Exp. C7).	129
C.3	ICP-MS time-resolved analysis for selected Ru/AC-B SCWG samples. B-xx.x refers to the sample TOS (h) (Exp. C8).	130
C.4	RSD of the time-resolved ICP-MS signals as a function of concentration for the three commercial Ru/AC catalysts. A main outlier is seen with Ru/AC-B-1.6 (Figure C.3) and smaller outlier with Ru/AC-BM-4.7 (Figure C.1).	130
C.5	ICP-MS time-resolved signal of the ionic Ru standards used for the calibration. RSD = 4.7, 3.9 and 3.5 % for the 0.5, 5 and 50 $ng\,mL^{-1}$ standards, respectively. The line of the blank sample (0 $ng\,mL^{-1}$) is discontinued because the measured signal is often zero.	131
C.6	Ru concentration as a function of superficial velocity u_s (left) and residence time τ (right) in the catalyst bed for the three SCWG setups.	131
C.7	SCWG of glycerol and sewage sludge over Ru/AC-A on the <i>intermediate</i> setup. The grey areas indicate gasification sections, either with glycerol (gly, Exp. C14) or sewage sludge (SS, Exp. C15). Another pump failure occurred at TOS = 16.8 h leading to $T_{min} = 196\,^{\circ}C$ and $p_{min} = 9\,MPa$	132
C.8	Elemental composition of the fresh and spent (sewage sludge) Ru/AC-A catalyst (Exp. C15). The catalyst was recovered in different fractions (1: reactor exit – 5: first catalyst fraction after sulfur absorber bed).	133
C.9	SSA of the fresh and spent (sewage sludge) Ru/AC-A catalyst (Exp. C15). The catalyst was recovered in different fractions (1: reactor exit – 5: first catalyst fraction after sulfur absorber bed).	133
C.10	Carbon conversion and Al, Ru, Ti concentrations in the process water as a function of TOS for 2%Ru/TiO ₂ (Exp. C18). Horizontal dashed lines: metal dissolution equilibrium (Table C.1) for the given species (not shown for Ti because its concentration is too low ($2 \times 10^{-5}\, \mu g\,L^{-1}$)).	134

List of Figures

C.11 Carbon conversion and Al, Ru concentrations in the process water as a function of TOS for 2%Ru/ α -Al ₂ O ₃ (Exp. C17). Horizontal dashed lines: metal dissolution equilibrium (Table C.1) for the given species.	134
C.12 Carbon conversion and Al, Ru, Zr concentrations in the process water as a function of TOS for 2%Ru/ZrO ₂ (Exp. C19). Horizontal dashed lines: metal dissolution equilibrium (Table C.1) for the given species.	135
D.1 High-resolution micrographs of 1%Ru/CNF_2.	137
D.2 High-resolution micrographs of 5%Ru/CNF_1.	138
D.3 Micrographs of 5%Ru/CNF_Cl.	138
D.4 Micrographs of 10%Ru/CNF.	139
D.5 Micrographs of 15%Ru/CNF.	140
D.6 Micrographs of 20%Ru/CNF.	141
D.7 Micrographs of 30%Ru/CNF.	142
D.8 Gas composition (top), X_C , GE_C and gas flow (bottom) for 1 %Ru/CNF_1. Feed: 6 wt% glycerol, m_{cat} = 0.89 g, F = 10.2 g min ⁻¹ , T = 403 °C, p = 28.5 MPa (Exp. C20).	142
D.9 Gas composition (top), X_C , GE_C and gas flow (bottom) for 1 %Ru/CNF_2. Feed: 8 wt% glycerol, m_{cat} = 0.50 g, F = 10.2 g min ⁻¹ , T = 404 °C, p = 28.5 MPa (Exp. C21).	143
D.10 Gas composition (top), X_C , GE_C and gas flow (bottom) for 5 %Ru/CNF_1. Feed: 20 wt% glycerol, m_{cat} = 0.60 g, F = 10.6 g min ⁻¹ , T = 403 °C, p = 28.5 MPa (Exp. C22).	143
D.11 Gas composition (top), X_C , GE_C and gas flow (bottom) for 5 %Ru/CNF_Cl. Feed: 10 wt% glycerol, m_{cat} = 0.27 g, F = 9.4 g min ⁻¹ , T = 408 °C, p = 28.5 MPa (Exp. C23).	144
D.12 Gas composition (top), X_C , GE_C and gas flow (bottom) for 15 %Ru/CNF. Feed: 20 wt% glycerol, m_{cat} = 0.20 g, F = 10.5 g min ⁻¹ , T = 403 °C, p = 28.5 MPa (Exp. C25).	144
D.13 Gas composition (top), X_C , GE_C and gas flow (bottom) for 20 %Ru/CNF. Feed: 20 wt% glycerol, m_{cat} = 0.14 g, F = 10.6 g min ⁻¹ , T = 400 °C, p = 28.5 MPa (Exp. C26).	145
D.14 Gas composition (top), X_C , GE_C and gas flow (bottom) for 30 %Ru/CNF. Feed: 20 wt% glycerol, m_{cat} = 0.11 g, F = 11.6 g min ⁻¹ , T = 403 °C, p = 28.5 MPa (Exp. C27).	145
D.15 DRIFTS spectra of CNF, the fresh and spent (Exp. C29-C31) 5%Ru/CNF_C catalysts.	146
D.16 Raman spectra of the fresh and spent (Exp. C31) 1%Ru/CNF_2 catalysts, deconvoluted into the different vibration modes.	146
D.17 Area ratios of the deconvoluted peaks for the fresh and spent (Exp. C31) 1%Ru/CNF_2 catalysts.	147

List of Tables

1.1	Main physical properties of fluids in the gas, liquid and supercritical (supercritical fluid (SCF)) state (adapted from [35])	7
2.1	Polynomial coefficients relating the total and surface Ru atoms to the particle diameter	35
2.2	Materials and chemicals used throughout this work	45
3.1	Characteristics of selected carbon materials	48
3.2	Surface area and pore volume of the fresh and spent carbon materials used for SCWG of glycerol	51
3.3	Characteristics of the catalysts synthesised on the supports of interest and the benchmark catalyst used as reference	53
3.4	Surface area and pore volume of the fresh and spent Ru/C catalysts	58
4.1	Main characteristics of the fresh 5 wt% Ru/AC catalysts	62
4.2	SSA comparison between the fresh and spent catalysts after SCWG of glycerol .	66
4.3	Characteristics of the different SCWG setups and main experimental conditions used	71
4.4	Characteristics of the in-house 2 %Ru catalysts and experimental conditions . .	75
4.5	SSA comparison between the fresh and spent catalysts after SCWG of glycerol .	77
5.1	Support and catalyst characteristics	82
5.2	Catalyst characteristics before and after glycerol conversion	90
5.3	Characteristics of the 5 %Ru/CNF_C catalyst	97
5.4	Experimental conditions for the 5 %Ru/CNF_C catalyst	97
5.5	Comparison between Ru/CNF and Ru/AC catalysts	109
A.1	Experiments discussed in Chapters 3 and 4	121
A.2	Experiments discussed in Chapters 3 and 4	122
A.3	Experiments discussed in Chapter 5	123
C.1	Modelled thermodynamic equilibrium solubilities of different materials in SCW	128

1 Introduction

1.1 Mitigating global warming

With CO₂ concentrations continuously increasing in our atmosphere, global changes are perceived around the world with rising sea levels and more frequent extreme weather conditions among many consequences. Climate change is clearly believed to be man-made, with a strong increase in CO₂ emissions between the start of the 19th century (280 ppm), mid-20th century (310 ppm) and today (420 ppm) [1]–[4]. Recently, there was a worldwide push to limit global warming to 2 °C, but preferably 1.5 °C compared to pre-industrial temperatures (COP21, Paris). However, this 1.5 °C barrier may be crossed as soon as 2030 with the continued consumption of fossil-based fuels [5]. To mitigate this rise, new technologies are being developed to implement the use of renewable energy with the aim of gently replacing the share of fossil fuels. Unfortunately, the target of replacing fossil-based energy by renewables is far from being achieved, as the global increase in energy consumption from 2016 to 2017 (5.6 EJ, i.e. 1.5 %) was still covered by oil, coal and natural gas [6]. Also, the recent annual increases in global primary energy production (Figure 1.1) were not made up from renewables sources alone, but mainly by coal and natural gas.

Among the different sources for renewable energy, bioenergy will become an increasingly important actor in the energy transition, as biomass contains all necessary building blocks to replace oil-based products. Biomass-derived products will not directly solve the increasing CO₂ emissions, but they will at least replace fossil-based emissions by CO₂-neutral ones. According to the International Energy Agency (IEA), the traditional use of biomass should be phased out by 2030 and replaced by modern bioenergy technologies, which will increase the biomass-based energy supply from 63 EJ in 2020 to 102 EJ in 2050¹ [8]. The share of modern gaseous bioenergy is expected to rise from 0.3 % (2020) to 13.4 % (2050). Although phasing out

¹ only for IEA member countries

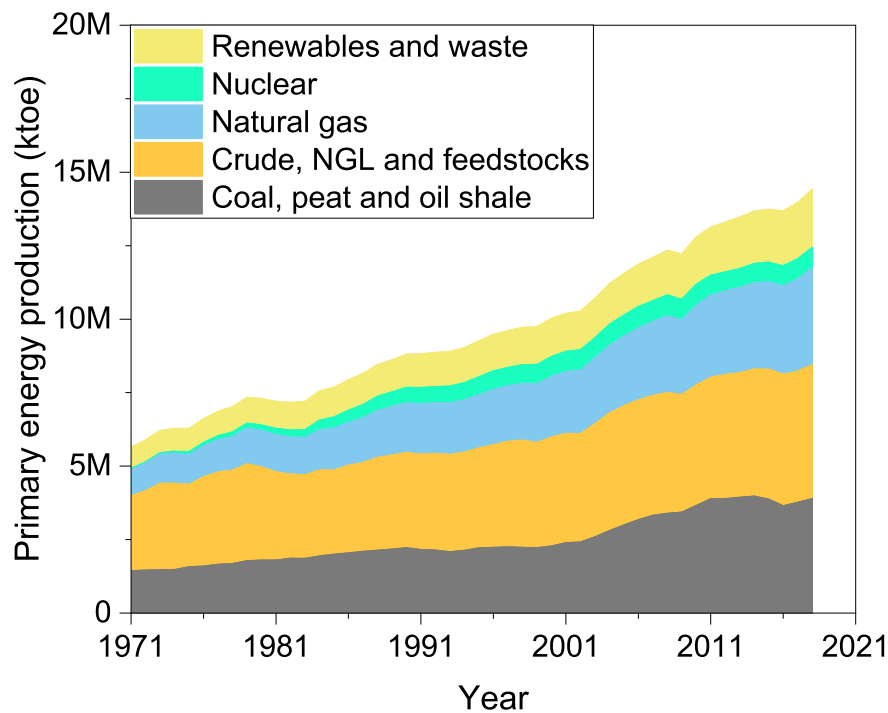


Figure 1.1 – World primary energy production in thousand tonnes of oil equivalent (ktoe) from 1971 to 2018. NGL stands for natural gas liquids. Data from the IEA [7].

the use of traditional biomass by 2030 seems unrealistic, there is great potential for increasing the share of biomass-based energy and hence bringing new conversion technologies to the market.

1.2 Biomass conversion technologies

To target CO₂ emission reduction with biomass as renewable energy source, it is important to have the optimal conversion technology for each biomass type. The term "biomass" includes a large variety of feedstocks *e.g.* wood, crops, algae, municipal wastes, etc. and each source has its advantages and disadvantages when converted to bioenergy with a given technology. In general, biomass can be divided into four types (woody, herbaceous, aquatic, manure), which possess different characteristics like mineral or moisture contents [9]. The first two types can be classified as dry biomass, which can efficiently be converted by conventional thermochemical processes such as combustion, gasification or pyrolysis [10]. Aquatic biomass, manures or municipal wastes are wet biomass types and are thus not well suited to the former conversion processes since the feed needs to be dried beforehand. Wet biomass feedstocks are thus better suited to hydrothermal or biochemical processes. An overview of the different

thermochemical biomass conversion routes is shown in Figure 1.2.

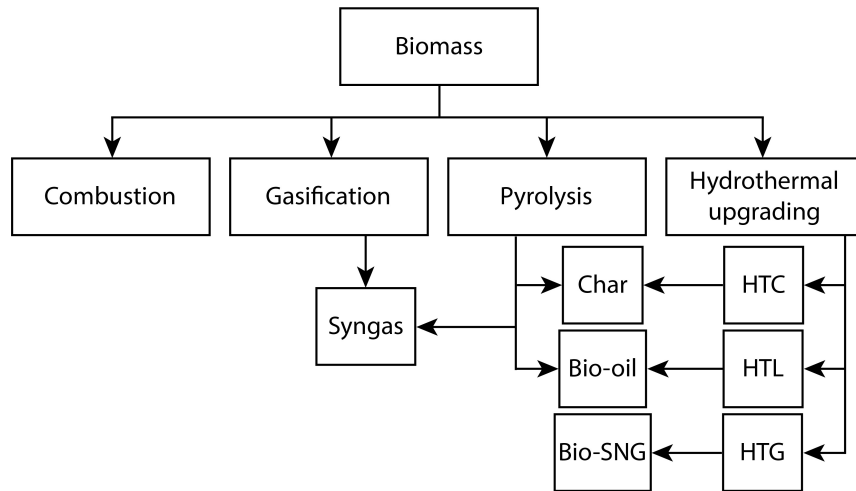


Figure 1.2 – Thermochemical biomass conversion technologies and their main energy products. Adapted from [10], [11].

1.2.1 Combustion

Biomass combustion is the oldest conversion technology available and is still heavily used (35 EJ *i.e.* 66 % of the biomass use in 2014 [12]), mainly for heating and cooking in less-developed countries. During this process, biomass is oxidised to hot gases (800–1000 °C), which in turn can be used to generate mechanical power or electricity [10]. The moisture content should generally be kept lower than 50 % for combustion. If not, conversion technologies for wet biomass are better suited. Globally, the energy conversion efficiency is relatively low, in the range 20–40 %.

1.2.2 Gasification

During gasification, biomass is partially oxidised into a mixture of combustible gases (H_2 , CO, CO_2 , H_2O and traces of hydrocarbons) at high temperatures (800–1100 °C). The gas composition can be tuned by modifying the process conditions, or by using a catalyst to favour H_2 production [13]. Nickel catalysts are widely used in gasification process due to their good water-gas shift (WGS) and tar-cracking activity [14]. The produced H_2 and CO *i.e.* syngas is then purified and can directly be used as fuel, or can be upgraded to hydrocarbons through Fischer-Tropsch (FT) synthesis. For gasification, it is important to have a relatively low moisture content, because the chemical efficiency rapidly drops above 50 wt% moisture. At a moisture content of 66 wt% (theoretical extrapolation), all the produced gas would be required just to evaporate the water, leading to a chemical efficiency of zero [15]. Hence showing the

importance of selecting the appropriate conversion technology.

1.2.3 Pyrolysis

In pyrolysis, the biomass is converted in an oxygen-free environment at temperatures around 300–700 °C. The main product is bio-oil, but syngas and bio-chars are also produced. The main advantage of this technology is the possibility to produce bio-oils (or bio-crude), which is a potential replacement for fossil oil. The drawback however, is that bio-oil consists of thousands of different molecules containing many oxygenated species, which lead to a decreased lower heating value (LHV) of the product as well as a lower thermal stability [16]. Bio-oils thus have to be upgraded in order to be used as engine fuel. Similarly to fossil oil, bio-oil can undergo deoxygenation and hydrotreating steps before being refined into more stable fractions (naphta, diesel, gasoline, etc.) [10].

1.2.4 Hydrothermal carbonisation

Hydrothermal carbonisation (HTC) enables the conversion of wet biomass at low temperatures (180–250 °C) and pressures (2 MPa) to bio-char (50–80 wt%), a bio-oil–water mixture (5–20 wt%) and gas (2–5 wt%) [17]. HTC is thus mainly used to produce high-density, coal-like products, which can be used for energy generation, transformed into advanced materials such as activated carbon (AC) or used as soil fertiliser [18], [19]. This conversion route also allows the treatment of trickier feedstocks such as manures, sewage sludges, human wastes or algae and is a promising alternative to biochemical treatments, which require longer times and can be deactivated by toxic compounds in the feedstock [17].

1.2.5 Hydrothermal liquefaction

Hydrothermal liquefaction (HTL) takes advantage of the higher temperatures (200–380 °C) and pressures (7–30 MPa) to convert wet biomass into bio-oils [20], [21]. The main goal of the process is to remove the oxygen functional groups to generate more stable and energy-dense bio-oils. The end product is similar to pyrolysis, however HTL bio-oil contains less oxygen than from fast pyrolysis (10–20 % vs. 30–40 %, respectively) and hence leads to higher energy-density products [20]. The disadvantages compared to pyrolysis are the larger residence times and the higher capital costs. HTL can be performed in the presence of homogeneous (acidic or basic) or heterogeneous catalysts. Na_2CO_3 is reported to decrease the solid residue and hence increase the bio-oil yield, whereas acidic catalysts increase the oxygen content of the oil [20], [22]. Heterogeneous catalysts can be used to increase the bio-oil yields *e.g.* from 35 wt% to 57 wt% over a Pd/C catalyst [23].

1.2.6 Hydrothermal gasification

Hydrothermal gasification (HTG) can be used to convert wet biomass streams to renewable natural gas (bio-SNG) or H_2 depending on the process conditions and whether a catalyst is used or not. HTG can be performed from near-critical temperatures (350 °C) to 700 °C approximately, at pressures above the critical pressure ($p_c = 22.1$ MPa). When the temperature is also higher than the critical temperature ($T_c = 374$ °C), the reaction environment is in the supercritical water (SCW) state and the process is thus referred to as supercritical water gasification (SCWG). HTG takes advantage of water's properties in the SCW state, *i.e.* low density, low dielectric constant, low dynamic viscosity and no phase change to overcome. These property changes lead to high a solubility for small organic molecules and light gases [20], [24], [25]. HTG can further be divided into three distinct sub-ranges depending on the process conditions [26]:

- (I) High-temperature SCWG (500–700 °C) – biomass decomposes by pyrolysis (free-radical mechanism) without the help of a catalyst. Homogeneous alkaline catalysts promote the WGS reaction and AC helps reducing char formation. H_2 formation is favoured at high temperatures.
- (II) Low-temperature SCWG (374–500 °C) – biomass decomposition occurs by hydrolysis (ionic mechanism), but requires an active gasification catalyst to achieve high gasification efficiencies. CH_4 formation is favoured at low HTG temperatures.
- (III) Subcritical water gasification (subCWG) (350–374 °C) – slower decomposition than in region II, a catalyst is required to gasify biomass.

For SCWG, two different approaches exist depending on the desired gas product. The high-temperature range favours H_2 production (with or without catalyst), whereas CH_4 is preferentially formed in the low-temperature range. The latter is thermodynamically favoured up to 400–450 °C, thus setting the optimal operating range for bio-SNG production [26], [27]. SCWG is a promising and versatile technology to fully convert a variety of biomass feedstocks of high water contents into bio-SNG with reasonable residence times (≈ 30 min) and interesting efficiencies (≈ 70 %) [28]–[30]. Region II *i.e.* low-temperature SCWG is the conversion technology used within this thesis and will thus be discussed more thoroughly in the following sections.

1.2.7 Fermentation

Fermentation is a widely-used technology to convert sugars to ethanol. The biomass feedstock first undergoes a grinding step before the starch is converted to sugars by enzymes, and eventually yeasts transform the sugars into ethanol and CO_2 [31]. The produced ethanol

is then purified by distillation, which is a drawback of the process due to its high energy consumption. Other limitations are that cellulose cannot directly be converted by yeasts, thus requiring an additional process step, and the difficulty to convert lignocellulosic biomass due to high recalcitrance of lignin [32]. However, biomass fermentation to bioethanol is already an established technology, with the USA and Brazil being the largest producers (9×10^{10} L *i.e.* 85 % of the world's production in 2017) due to the high availability of corn and sugar cane, respectively [33]. After pushing the development of yeast fermentation due to the oil crisis in the 1970s, Brazil now covers more than 30 % of its energy needs through bioethanol [32].

1.2.8 Anaerobic digestion

Anaerobic digestion (AD) uses bacteria to convert biomass into biogas, being a mixture of CH_4 and CO_2 and H_2S to a lesser extent, in the absence of oxygen. As for fermentation, AD is already an established technology to convert feedstocks of high water content into biogas, which can directly be used for energy generation or can be further purified to be injected in the natural gas grid [10]. Feedstocks such as plant residues, municipal, industrial and agricultural wastes can be converted to biogas by AD. Methane yields range from $0.2 \text{ m}^3 \text{ kg}^{-1}$ (lignin-rich or municipal waste) to $0.4\text{--}0.5 \text{ m}^3 \text{ kg}^{-1}$ (municipal or fruit and vegetable waste) [34]. The main disadvantages of AD are the long residence times (20–30 days) and the low thermal efficiencies 25–35 % (for < 8 wt% dry matter manure) [28].

1.3 Supercritical water

With the ongoing search for green (*i.e.* sustainable) solvents, SCW has attracted considerable attention due to its similar properties to organic solvents. Indeed, when water is compressed and heated towards the critical point ($T_c = 374^\circ\text{C}$ and $p_c = 22.1 \text{ MPa}$), its physico-chemical properties drastically change as the liquid and gas phases converge to a unique supercritical phase. The physical properties of SCW lie between those of the liquid or gas, as shown in Table 1.1. The density (ρ) is more water-like at ambient conditions, whereas the dynamic viscosity (η) and diffusivity (D) are closer to gases at ambient conditions. SCW hence allows higher rates for reactions that would be limited by diffusion in liquids or would have to overcome phase barriers [35].

When water is heated up, its density slightly decreases until vaporisation occurs (100°C at 1 bar), after which the density drastically drops. However, by compressing the water, this density drop is shifted to higher temperatures as shown in Figure 1.3. Evaporation takes place at 180°C at 1 MPa and 310°C at 10 MPa. By further increasing the pressure, the vaporisation step is suppressed as evidenced by the continuous density drop at 30 MPa compared to drop still present at 20 MPa. This steep density drop allows working in a relatively wide range

Table 1.1 – Main physical properties of fluids in the gas, liquid and supercritical (SCF) state (adapted from [35])

	Density ρ (kg m ⁻³)	Dyn. viscosity η (mPa s)	Kin. viscosity μ (10 ⁶ m ² s ⁻¹)	Diff. coefficient D (10 ⁶ m ² s ⁻¹)
Gas	0.6 - 2	0.01 - 0.3	5 - 500	10 - 40
SCF	200 - 500	0.01 - 0.03	0.02 - 0.1	0.07
Liquid	600 - 1600	0.2 - 3	0.1 - 5	0.0002 - 0.002

of SCW conditions (e.g. liquid-like vs. gas-like density) without facing phase transitions [36]. A recent study by Maxim *et al.* revealed the liquid-like to gas-like transition by neutron imaging, highlighting that both phases can clearly be distinguished at the millimetre level [37]. The suppression of the vaporisation step makes it energetically more interesting to work in supercritical conditions (Figure 1.4), as no "energy penalty" needs to be paid to evaporate water ($\Delta H_{vap} \approx 40 \text{ kJ mol}^{-1}$).

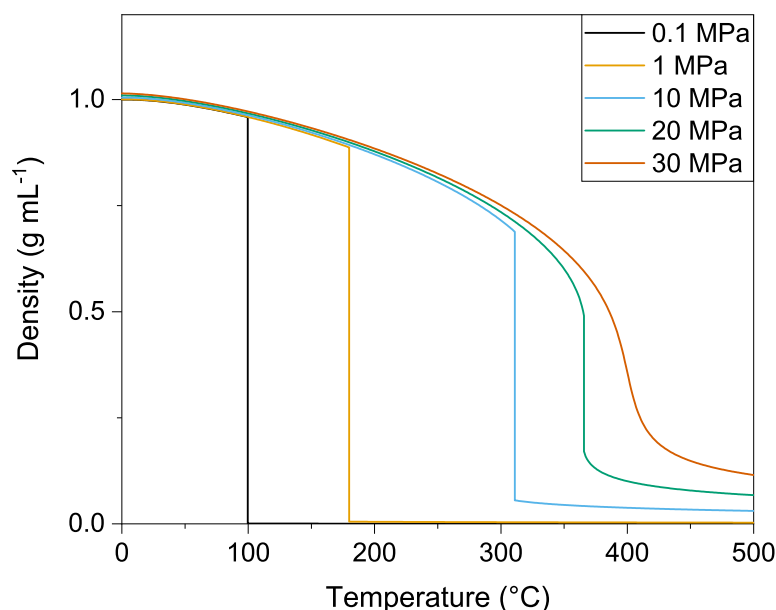


Figure 1.3 – Isobaric water density as a function of temperature. Data from [38].

Similar trends are observed for the dielectric constant (ϵ) when increasing the temperature at constant pressure because of vaporisation (Figure 1.5). In supercritical conditions however, the dielectric constant decreases to 11, 6 and 2 at 374, 400 and 450 °C, respectively (at 30 MPa). This decrease is due to the loss of over 60 % of the hydrogen bond network because of the expansion of water and leads to similar solvation properties as common organic solvents [35]. Typically, the dielectric constant of acetone and hexane are around 20 and 2, respectively. The low values of the dielectric constant makes organic molecules and light gases completely

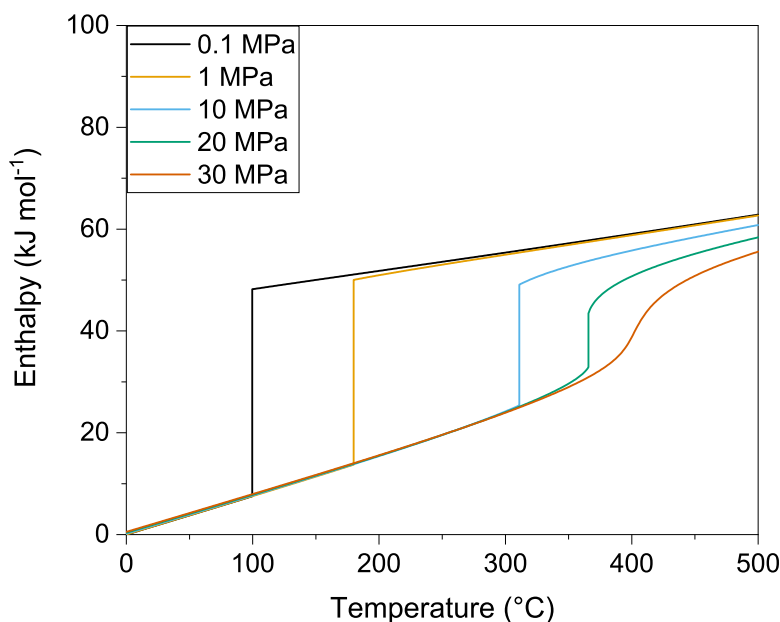


Figure 1.4 – Isobaric water enthalpy as a function of temperature. Data from [38].

miscible in SCW and thus particularly suited for reactions between organics and gases [41]–[43].

The ion product of water also varies with temperature, with an increase from 10^{-14} at 25 °C to $\approx 10^{-11}$ around 300 °C. The initial increase is due to the dissociation reaction of water being endothermic, whereas the decrease at higher temperatures is a direct consequence of low density and dielectric constant leading to a low solvation power for ions [36]. K_W is the product of the ion activity from water's autoprotolysis reaction ($\text{H}_2\text{O} \rightleftharpoons \text{H}^+ + \text{OH}^-$) and is calculated with Equation 1.1

$$K_w (\text{mol}^2 \text{kg}^{-2}) = a(\text{H}^+) \cdot a(\text{OH}^-) \quad (1.1)$$

where a is the activity of the ionic species. Figure 1.6 shows that K_W increases with pressure, but undergoes a rapid decrease around T_c , especially at lower SCW pressures. Hence, water acts as an acid or base catalyst precursor and catalyses ionic reactions in subcritical conditions as well as at higher pressures. At 400 °C the ion product is an order of magnitude lower than at ambient conditions ($K_W = 10^{-15} \text{ mol}^2 \text{kg}^{-2}$ [44]), meaning that ionic reaction mechanisms are not catalysed by the solvent and hence less favoured.

These different reaction pathways were evidenced by Antal *et al.* by analysing the gas and product yields after ethanol conversion in SCW, with or without acids as homogeneous catalysts [45]. They managed to distinguish the heterolytic (ionic) from the homolytic (free radical) mechanism in conditions where $K_W > 10^{-14}$ (400 °C, 34.5 MPa) and $K_W \ll 10^{-14}$ (500 °C,

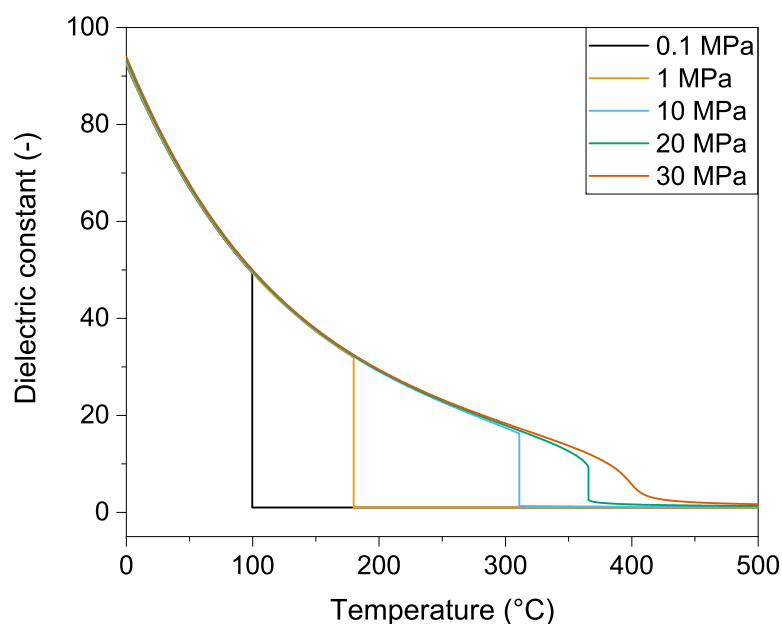


Figure 1.5 – Evolution of the dielectric constant of water for different pressures as a function of temperature. Data computed from [38], [39].

34.5 MPa), respectively. In the latter conditions, H_2SO_4 did not help in ethanol dehydration, whereas it efficiently and selectively catalysed its dehydration to ethylene at 400 °C ($K_W > 10^{-14}$). Further works confirmed heterolytic (ionic) mechanisms being favoured in hot compressed water (250 °C, 34.5 MPa), with the dehydration of *tert*-Butyl alcohol to isobutylene being catalysed by hydronium ions (H_3O^+) formed by water dissociation [46], [47]. The free-radical mechanism is initiated and propagated by $\text{H}\cdot$ and $\text{OH}\cdot$ from water. The propagation step can occur through addition, substitution, rearrangement, disproportionation or dehydration reactions. Coupling or disproportionation steps terminate the free radical mechanism [48].

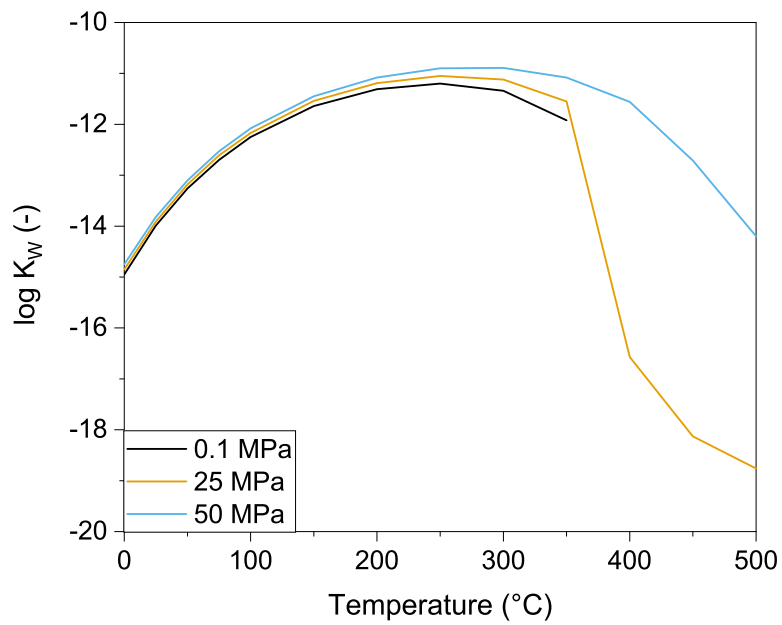


Figure 1.6 – Evolution of the ionisation constant of water K_W as a function of temperature. Adapted from [40].

1.4 Supercritical water gasification

Due to the nature of SCW, many organic molecules readily decompose. This was shown for formic acid, which undergoes rapid decomposition through decarboxylation and dehydration in the range 320–500 °C and 18–30 MPa [49]. From Savage's review, one can see that a considerable range of chemicals are prone to decomposition in SCW [50]. Long-chain alkanes (C_{16}) were shown to decompose much faster than aromatics during SCWG of algae at 500 °C [51]. Cellulose decomposes into oligo- and monomers through hydrolysis, the main product being glucose [48]. At high temperatures (600 °C, 25 MPa) as well as low temperatures (380 °C, 22.5 MPa), glucose is dehydrated to form furfural, hydroxymethylfurfural (HMF) and a variety of phenolic molecules [52], [53]. The decomposition of aromatic molecules was also extensively studied in order to better understand lignin decomposition mechanisms and char formation in SCW. Phenol decomposition was investigated in high-temperature SCW (500–700 °C) where it mainly decomposed to benzene through dehydroxylation or dibenzofuran through dimerisation, whereas dibenzofuran decomposed to a biphenyl as well as benzene, a variety of polycyclic aromatic hydrocarbons (PAHs) and char [54]. Benzene was also shown to mainly undergo dimerisation reactions. At lower temperatures (370–450 °C, 25 MPa), phenol was converted to benzene through a heterolytic mechanism, whereas the reversible reaction was governed by the homolytic mechanism [55]. The activation energy of benzene decomposition was almost double that of phenol (91 vs. 54 kJ mol⁻¹) because of the presence of the hydroxyl group which rapidly undergoes H-abstraction to form the phenoxy free radical. Char was directly formed from phenol because of the high reactivity of the radical intermediates, whereas it formed by ring combination from benzene. PAHs – being char precursors – were stable and required higher temperatures to decompose [54], [55].

Gasification of alcohols and acids was also extensively studied in the field. Chakinala *et al.* compared the gasification activity (600 °C, 26 MPa, 15 min) of acids and alcohols of different chain lengths (C_1 to C_8) and postulated decomposition mechanisms [56]. In general, alcohols gasified more easily compared to acids. For alcohols, methanol had the lowest carbon gasification efficiency (GE_C) and ethanol the highest while the GE_C decreased with increasing carbon number. For acids the trend was opposite, with formic acid exhibiting the highest GE_C (complete conversion), before decreasing with increasing chain length as for the alcohols. They also showed an interesting oscillating trend with acids containing an even number of carbon atoms showing a higher GE_C than their neighbouring molecules of odd carbon atoms, which was explained through the initial scission of the O–H group followed by β -scission reactions. For alcohols, the GE_C improved with increased OH groups, because of their stabilising effect for radical intermediates through electron-donating properties [56]. The reported mechanism for methanol decomposition (at 600 °C) occurs preferentially through O–H or C–H bond scis-

sion leading to formaldehyde via radical intermediates ($\text{H}_2\text{C}\cdot - \text{OH}$ or $\text{H}_3\text{C} - \text{O}\cdot$). C–O bond cleavage is the least favoured initiation pathway. Aldehyde formation is a key intermediate especially for higher alcohols ($> \text{C}_3$). As the reaction network increases in complexity, there is a higher probability of favouring aromatisation reactions [56].

Glycerol degradation was also widely studied with early publications already reporting the different degradation pathways (heterolytic vs. homolytic) depending on the process conditions. Antal *et al.* showed that glycerol underwent an acid-catalysed, carbonium-ion mechanism resulting in the formation of acrolein by elimination of water at lower temperature (360°C), whereas at higher temperature (500°C) the free-radical pathway prevailed through C–C cleavage forming preferentially acetaldehyde [57]. Acrolein formation was also shown to be favoured at 400°C , 34.5 MPa with higher glycerol and H_2SO_4 concentrations leading to high acrolein selectivity [58]. Glycerol was also shown to be stable in SCW with very low conversions (6–10 %) reported by different studies [59], [60]. Coke formation occurred in subcritical water (subCW) but was not observed in SCW [60]. Bühler *et al.* extensively studied glycerol degradation mechanisms by systematically varying the temperature ($350\text{--}475^\circ\text{C}$), pressure (25, 35 and 45 MPa) and residence time (32–165 s) [61]. They reported the formation a series of compounds as the main products (*i.e.* methanol, acetaldehyde, propionaldehyde, acrolein, allyl alcohol, ethanol, formaldehyde, CO, CO_2 and H_2) through competing ionic and radical mechanisms. Based on their set of experiments and the knowledge in the field, they proposed an exhaustive reaction network for the ionic and free radical mechanisms. They concluded that some products could only be formed through one mechanism (*e.g.* allyl alcohol through the free radical pathway), but acetaldehyde and acrolein were main products in both decomposition mechanisms.

1.5 Catalytic supercritical water gasification

Initial work on SCWG began in the 1970s by Modell at MIT, where they showed that char formation could be limited in biomass gasification when performed in subCW and completely avoided in SCW [62]. They also reported the use of commercial Ni and Co/Mo (and Pt) catalyst mixtures which increased the gas formation. However, very little CH_4 was formed in these conditions. Later, Elliott looked into the effect of homogeneous (Na_2CO_3) and heterogeneous (supported Ni) catalysts for the conversion of wood bio-polymers (cellulose, hemicellulose, lignin and fir wood flour) at 350, 400 and 450°C [63]. The combination of both catalysts led to the highest carbon conversion (X_C) for all feeds. Na_2CO_3 addition favoured H_2 formation at the expense of CO, evidencing its effect on the WGS reaction. The use of Ni led to increased CH_4 yields at the expense of CO again, and a complete disappearance of C=C gases. These initial results led to further research on stable and active gasification catalysts for their process

named thermochemical environmental energy system (TEES). Elliott evaluated the effect of different base and noble metal catalysts for the conversion of 10 wt% *p*-cresol at 350 °C and 20 MPa [64]. The metals tested included Cu/ZnO, Co, Zn/Cr, Cr, W, Mo, supported on SiO₂ or Al₂O₃. Among these catalysts, only Cu/ZnO showed some activity (although very limited) for the conversion of *p*-cresol and CH₄ formation, other catalyst were inactive. Catalyst oxidation was the main reason behind the low activity as only Cu remained reduced. The focus was then set on evaluating the activity and stability of "innovative" nickel catalysts, such as unsupported Ni (Raney) or nickel salt (nitrate) solutions, which did not require a stable support. Other Ni catalysts were supported on ZrO₂ or Al₂O₃. Nickel nitrate exhibited some activity, but it was only due to the nitrates oxidising the organics as no further activity was observed. Ni in solution was later confirmed inactive with an acetate salt having no activity [65]. Raney nickel and Ni/Al₂O₃ were the only catalysts to show promising gasification and methanation activities. A variety of commercial Ni catalysts were also assessed by Elliott, namely some benchmark gasification, hydrogenation, methanation and steam reforming catalysts [64]. Ni remained reduced (by X-ray diffraction (XRD)), however the Al₂O₃ supports underwent phase change to böhmite, α - or η -Al₂O₃. Nickel crystal size growth was also observed in this environment.

Noble metals such as Ru, Rh, Pt and Pd were also investigated in the same system, being supported on different materials (γ -Al₂O₃, δ -Al₂O₃, ZrO₂ or carbon). Elliott concluded that Ru was a very active catalyst in TEES also showing good methane selectivity. Rhodium exhibited some activity, whereas Pt and Pd did not show any kind of activity and were very prone to carbon deposition. Another important learning from their study was that Ru did not undergo crystallite growth after 250 h of time on stream (TOS), whereas Ni sintered significantly. Elliott also looked into the stability of the different commercial supports used within his studies. Surprisingly, very few materials were stable during the process. All aluminas (except α -Al₂O₃) underwent phase change to böhmite, which was accompanied by substantial decreases in specific surface area (SSA) and crush strength. Carbon was stable, as was zirconia in the monoclinic phase, silica was prone to dissolution and titania did exhibit some physical changes. The pioneering research from Elliott's group laid the foundations for catalytic SCWG, highlighting the numerous constraints of this system in terms of useful active metals and supports. The main findings were that Ru and Ni were active catalysts and that stable supports included α -Al₂O₃, ZrO₂ and carbon.

1.5.1 State-of-the art catalysts for SCWG

Continued research on SCWG catalysts aimed at improving the activity and more importantly the catalyst lifetime. Most of the research still focussed on Ni or Ru, the former because of its lower costs, the latter thanks to its excellent stability. Waldner and Vogel showed that

wood at high feed concentrations (10–30 wt%) could be gasified to thermodynamic yields of methane over Raney nickel at 404 °C and 31 MPa for reaction times of 90 min [66]. The final liquid phase did not contain tars and very little residual carbon (<2 wt%), but carbon deposition occurred on the catalyst. Elliott *et al.* tried to stabilise nickel catalysts by doping a commercial steam-reforming catalyst with other metals (Ru, Cu, Re, Sn or Pb). The doping significantly limited Ni sintering, but high GE_C were only recorded for Ru-doped Ni catalysts [67]. They also looked at Ru/TiO₂ catalysts to evaluate the stability of the two phases (anatase and rutile). Mixed-phase TiO₂-based catalysts systematically ended in the low-SSA rutile phase. Long-term stability tests were also performed and showed that Ru-stabilised nickel catalysts could completely gasify 10 wt% phenol for more than 24 weeks. Ruthenium (3 wt%) supported on ZrO₂, mixed-TiO₂, rutile-TiO₂ and carbon (8 wt%) also exhibited complete feed gasification for over 6 weeks. Ru/r-TiO₂ managed to sustain long-term gasification activity for more than 3000 h. Based on these results, Waldner also tried to stabilise Raney Ni with other metals (Ru, Fe, Mo, Cu) for synthetic liquefied wood (SLW) gasification experiments, but was unsuccessful [68]. Only the Ru-doped catalyst was tested on a continuous setup and exhibited similar lifetime and activity as the non-doped one, with the presence of Ru not preventing Ni sintering (from 9 to 45 nm). Other Ni catalyst synthesis attempts were reported by Nakagawa *et al.* who carbonised a resin after adding nickel by ion-exchange [69]. This led to a catalyst of high Ni loading (47 wt%) and interesting SSA (170 m² g⁻¹), unfortunately sintering was still an issue with this formulation [70]. Waldner *et al.* compared the activity between Raney nickel and a commercial 2%Ru/C catalyst [71]. The latter maintained full conversion and thermodynamic gas equilibrium for 220 h of SLW gasification. They concluded that skeletal Ni catalysts were not suited to HTG processes because of their rapid activity loss.

Sato *et al.* investigated the activity of supported noble metal catalysts for SCWG of alkylphenols (lignin model compounds) in batch at 400 °C [72]. They reported GE_C in the order Ru/ γ -Al₂O₃ \gg Ru/C > Rh/C, with Pt/ γ -Al₂O₃, Pd/ γ -Al₂O₃ and Pd/C showing no activity. Osada *et al.* looked at the stability of Ru-based catalysts for SCWG of lignin at 400 °C and reported activities in the order Ru/a-TiO₂ > Ru/ γ -Al₂O₃ > Ru/C [73]. The SSA of the a-TiO₂-based catalyst was not affected after three consecutive runs of 3 h, whereas Ru/C lost 65 %. Ru/ γ -Al₂O₃ lost 95 % of its SSA after 3 h in SCW due to transformation to Ru/ α -Al₂O₃. Hence, the high activity reported for Ru/ γ -Al₂O₃ was biased by the batch testing conditions, as the activity may have stopped after several minutes only. Their results confirmed this as the gas yield only slightly increased between 15 and 120 min and the yield was four times lower after the third repetition, suggesting that the lost Ru did not participate in the reaction. Osada *et al.* also looked at the effect of water density (0–0.5 g cm⁻³) when gasifying lignin or 4-propylphenol at 400 °C [74]. They reported that the GE_C linearly increased between 0.33–0.5 g cm⁻³ water density for lignin conversion, but was unaffected by water density with the model compound, suggesting

that the heterolytic pathway of lignin hydrolysis was catalysed by water in these conditions. Peng *et al.* also compared the activity of ruthenium catalysts supported on activated carbon and metal oxides during 50 h continuous isopropanol gasification (450 °C, 30 MPa) [75]. The 2 %Ru/C catalyst exhibited the best activity with full conversion at a high space velocity, whereas initial conversions were lower ($\approx 70\%$) for 2 %Ru/TiO₂, 1 %Ru/ZrO₂ and 1 %Ru/ α -Al₂O₃. Of these three catalysts, Ru/ZrO₂ exhibited a better stability and they concluded that high dispersions were necessary for improved catalyst stability. In another study they were also able to link the activity to the dispersion by synthesising Ru/C catalysts of different nanoparticle (NP) sizes by changing the preparation method [76]. Minor Ru sintering and coke deposition were reported, which led to the decrease in activity. As AC started to attract substantial interest due to its good performance as catalyst support, Yamaguchi *et al.* compared the activity of AC-impregnated Ru catalysts for lignin gasification at 400 °C [77]. AC was also used as catalyst and showed low GE_C (8 %). Impregnated (non-reduced) Ru/AC catalysts (RuCl₃/AC and RuNO(NO₃)₃) were assessed with the former exhibiting a low activity ($GE_C = 24\%$) and the latter showing a good activity ($GE_C = 75\%$), similar to a commercial Ru/AC catalyst. Interestingly, the chloride catalyst only achieved low CH₄ selectivity compared to the other catalysts 17 % vs. $\approx 45\%$, while all catalysts were confirmed to be reduced after the reaction. They suggested that the residual chloride inhibited the catalyst activity, which was confirmed by an additional experiment with equimolar amounts of HCl. Focussing on AC as catalyst support, Peng *et al.* investigated the effect of surface functional groups on the catalyst activity [78]. Treatment in HNO₃ led to ten times more acidic functional groups (carboxylic and lactonic) at the surface, whereas a subsequent thermal treatment in He at 500 °C only removed a small fraction of the carboxylic acid groups. After impregnation they were able to link the metal dispersion to the concentration of acidic groups, suggesting that they help in a better anchoring of the Ru NPs on the support. However, the activity of the untreated, acid-treated, acid and thermally-treated catalysts were similar (although these tests were performed at near-total conversion *i.e.* 94–99 %).

Even though AC is a very interesting catalyst support, its high surface area mainly arises from micropores which can rapidly be blocked by coke deposits. Hence, more open carbon structures were investigated to try and circumvent this. Yu *et al.* mentioned good stability and activity of Ru supported on a graphitised carbon black for phenol gasification at 400–500 °C [79]. Furthermore, they managed to synthesise small Ru NPs that underwent minor sintering (2.0 nm to 3.4 nm). de Vlieger *et al.* were the first to report the stability of carbon nanotubes (CNT) in SCW and evaluated the activity of Pt/CNT for continuous SCWG of ethylene glycol and acetic acid (450 °C, 25 MPa, 6 h) [80]. They showed that the catalyst did not undergo deactivation and that unsupported CNT were relatively inert with 5 % and 3 % conversion of ethylene glycol and acetic acid, respectively. They later used a CNT-supported Ru catalyst for

continuous SCWG of bio-based acetic acid (450 °C, 25 MPa, 7 h), showing that the morphology (surface area, degree of graphitisation) and the Ru particle size remained intact [81]. Although the results were promising, very few carbon nanofibers (CNF)-based catalysts were reported in literature for SCWG.

1.5.2 Active Ru species

The SCWG reaction environment makes it difficult to probe the catalyst during the reaction (*i.e. in situ* or *operando*). For this reason, it was not clear which Ru species was active and what the catalytic mechanism was. A first mechanism was postulated by Park and Tomiyasu after naphthalene gasification over RuO₂ in supercritical D₂O [82]. As the major products were the completely deuterated isotopes CD₄ and D₂, they concluded that the former would be formed through methanation reactions with partial oxidation of naphthalene by the catalyst. This implied that the partially reduced RuO was re-oxidised by the heavy water, thus forming D₂. The presented mechanism was a redox cycle between Ru^{IV} and Ru^{II} where methane was formed from CO and H₂. This was a first glimpse into what might happen in SCWG environments. Later, Ketchie *et al.* evaluated several ruthenium catalysts in H₂-saturated water (4 MPa, 200 °C) by *in situ* X-ray absorption spectroscopy (XAS) and found Ru in the metallic state [83]. These findings were confirmed by Yamaguchi *et al.* who performed extended X-ray absorption fine structure (EXAFS) during lignin gasification (400 °C, 37 MPa) over AC-supported Ru salts [77]. They reported the *in situ* reduction of the Ru salts, confirming earlier findings. Rabe *et al.* tried to further understand the role of Ru by *operando* X-ray absorption near edge structure (XANES) studies during ethanol gasification over 2 % Ru/C [84]. They showed that the as-received catalyst (oxidised by air) reduced between 125 °C and 150 °C at 25 MPa and remained reduced up to 390 °C. They also confirmed that ruthenium remained in metallic form after flushing water over the catalyst at 350 °C. All these findings strongly confirmed that ruthenium was active in the metallic state and that the presence of organics would readily reduce the passivation (*i.e.* oxide) layer at low temperatures.

Looking at the reaction mechanism in more detail, Peterson *et al.* coupled density functional theory (DFT) calculations with batch experiments to understand methane formation as well as its interaction with water [85]. They calculated the free energy pathway for the adsorption and subsequent dehydrogenation of methane on a stepped ruthenium surface. They performed the same calculations for the adsorption of water at the catalyst surface and showed that adsorbed CH_x species would rather easily scramble (rapid H interchange) and that water would have a relatively low energy barrier to overcome to adsorb on the Ru surface. The modelling was confirmed by experimental data, showing that the presence of Ru/C led to scrambling with CD₄, CHD₃, CH₂D₂ and CH₃D detected in decreasing concentrations. More

operando SCWG studies were performed by Dreher *et al.* who investigated the mechanism of ethanol gasification (400 °C, 24.5 MPa) as well as poisoning by sulfur species [86]. The Ru/AC catalyst was activated by the organics at around 150 °C and the Ru NPs underwent minor sintering from 1.0 to 1.5 nm. They also used methanol in batch tests to investigate the reforming mechanism and were able to draw the same conclusions as in previous works – CD₄ and CHD₃ were the main gases formed, showing that C* and CH* have the lowest free energy on a Ru surface. They concluded that methanation occurs by direct hydrogenation of the adsorbed C* and CH* species.

1.5.3 Continuous SCWG of biomass

Many catalytic studies in SCWG were performed in batch conditions, which is good to screen new materials, catalyst formulations or types of feed. However, there are some limitations and batch-test results cannot be extrapolated for continuous systems since the residence time considerably changes. Also, the pressure is built up through heating in batch experiments, which makes the feed and catalyst go through the HTC, HTL and subCW regimes before reaching the desired SCWG conditions. The rapid changes in water properties (as discussed in Section 1.3) can thus significantly bias the interpretation of the results. Hence, continuous SCWG assessment is vital to gather enough knowledge for the commercialisation of this technology.

The first continuous HTG experiment was reported by Elliott's group, who greatly contributed to SCWG catalyst development. The first test was performed in a stirred tank reactor with a Ni catalyst to convert several biomass feedstocks (sorghum, cheese whey or spent grain) [87]. They confirmed high conversions and methane selectivity, but suffered rapid deactivation because of poisoning/fouling by minerals and catalyst decomposition. They then used different scales of fixed-bed tubular reactors (0.03 to 33 Lh⁻¹) to convert model and real biomass feeds, while assessing the best-performing catalysts from the batch tests [88]. As for the batch tests, Ru-based catalysts showed increased stability with Ru/ZrO₂ achieving 83 % gasification efficiency after 860 h of phenol gasification. The conversion of nitrates and chlorinated hydrocarbons was also assessed with the latter catalyst leading to corrosion. Food processing wastes, organic chemical wastes and brewer's spent grain (barley) were efficiently gasified on their setups. However, minerals present in the feedstock deposited in the lines and on the catalyst during the process. Magnesium, calcium, phosphorus and sulfur were detected on the Ru/C catalyst after continuous HTG of dried distiller's grain with solubles [89]. Ca, P and Mg were mainly found on the outside of the catalyst grains, but sulfur was located throughout the grain suggesting its high affinity to Ru.

Boukis's group at the Karlsruhe Institute of Technology developed the first high-throughput SCWG pilot plant (VERENA) in the early 2000s [90]. Their aim was to better exploit agricultural waste by converting it to H_2 at 600 °C and 28 MPa. They successfully managed to gasify model compounds into H_2 without or in the presence of homogeneous alkali catalysts. They also showed the plant's ability to convert agricultural wastes, as well as sewage sludge in the high-temperature regime with an alkali catalyst, or at lower temperatures (423 °C) with a sulfur absorber (ZnO) and a Ru/C catalyst to target CH_4 formation [91]. A salt separator developed at the Paul Scherrer Institute (PSI) was also tested in this study and was successful in removing more than 50 % of the ash contained in the feed. Furthermore, phosphorus and potassium were separated from the feed stream at 470 °C, with a better efficiency for P than for K. Sulfur was not completely separated, but the fraction reaching the reactor was not sufficient to poison the Ru/C catalyst. More recently, a successful algae gasification campaign was performed on PSI's demonstration unit *Konti-C* with over 100 h of operation [92]. They used a salt separator developed by our group at PSI [93], [94] to continuously remove a mineral-rich brine effluent and thus avoid poisoning of the catalyst bed downstream. A sulfur absorber (ZnO) was also used to protect the catalyst from sulfur poisoning. Subsequent analysis of the absorber and catalyst showed that some coking, slight sintering and fouling by minerals occurred after 55 h [95]. Sulfur poisoning was reportedly the main deactivation mechanism.

Up to now two pilot-scale plants are in operation, one being the VERENA plant in Germany and the other located in Japan with throughputs of 2 and 1 t d⁻¹, respectively. However, both operate at high temperatures (600 °C) with either alkali or AC as catalyst [96]. At PSI, a pilot plant (100 kg h⁻¹) was developed for the conversion of sludges into CH_4 at around 400–500 °C, with the use of a salt separator and a sulfur absorber to protect the Ru/C catalyst.

1.6 Deactivation mechanisms in SCWG

As mentioned in Section 1.5.1, biomass conversion in SCW is a demanding environment for catalysts as most conventional supports undergo dissolution or phase change. Even when stable, catalysts are still prone to deactivation through different mechanisms [97], namely:

- dissolution of the active metal *i.e.* leaching.
- particle growth *i.e.* sintering.
- fouling by carbon *i.e.* coking.
- fouling by minerals.
- poisoning by chlorine or sulfur.

Working in model conditions allows to narrow down the possible deactivation mechanisms to leaching, sintering and coking, and are discussed in more detail below. Fouling by salts and poisoning by sulfur can only occur during processing of real biomass. For instance, the former was observed after 100 h of continuous algae conversion, where Peng *et al.* reported the presence of minerals on the catalyst surface [95]. However, it seemed to arise from the sulfur absorber (ZnO binder matrix) rather than from the feed. Elliott *et al.* showed that minerals deposited on the catalyst too, but originating from the algae feed this time [98]. Sulfur was also detected on the catalyst, as their attempt to use Raney Ni as sulfur trap did not work. Waldner *et al.* gave a nice overview of the potential deactivation mechanisms occurring during SCWG [71].

1.6.1 Ru loss

Loss of active metal from fixed-bed reactors can occur through dissolution (*i.e.* leaching) or through mechanical losses because of catalyst breakdown, friction or attrition. The scheme in Figure 1.7 represents those different loss mechanisms, with support self-gasification by Ru also potentially contributing to the loss of carbon-supported Ru NPs.

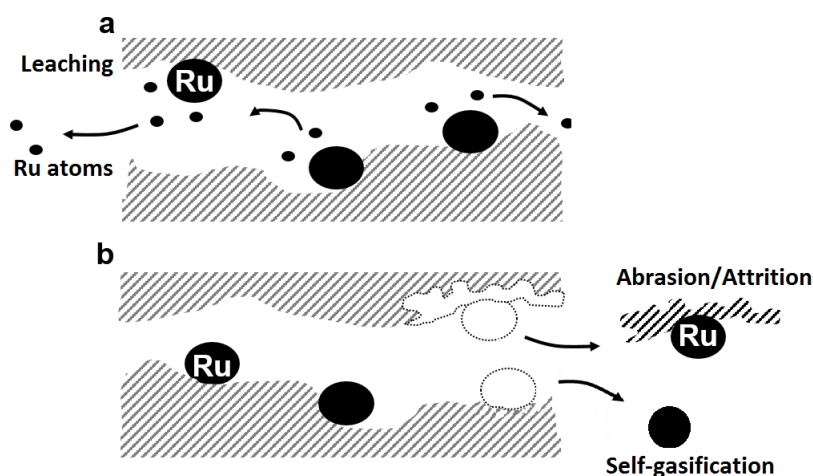


Figure 1.7 – Potential Ru loss mechanisms from activated carbon during SCWG, leaching (a) and attrition, self-gasification (b).

Very little is known on mechanical Ru loss, Waldner however reported dust being flushed out of his continuous SCWG reactor at the beginning of experiments, mentioning attrition as the main cause [68]. Self-gasification of the carbon support by Ru was reported in several works [68], [99], but is thought to have a minor contribution towards Ru loss. The main metal losses reported in literature are linked to leaching.

Unfortunately, the data available on Ru leaching during continuous SCWG is very scarce, as most publications report concentrations below the limit of detection with inductively coupled plasma - optical emission spectroscopy (ICP-OES). X-ray fluorescence (XRF) is also often employed to quantify leaching, but also faces limitations due to matrix effects when several elements are present in the sample, or because of dilution effects [95], [98]. However, this does not mean that leaching does not occur. On a continuous rig, CNF-based catalysts exhibited no metal loss for Pt in SCW (<5 wt%), but for Ru it amounted to 10 % during acetic acid reforming in subCW and increased to 20 % during SCWG [80], [81]. Higher subCW temperatures led to slightly higher losses. However, the catalytic activity was not influenced by the loss of active phase, suggesting that the least stable Ru NPs get washed out at the beginning of the process.

More data is available on Ni, mainly because of its considerably higher solubility in SCW *i.e.* $10^{-5} \text{ mol kg}^{-1}$ for Ni vs. $10^{-12} \text{ mol kg}^{-1}$ for Ru (400 °C, 30 MPa) according to thermodynamic dissolution models [100]. Wang *et al.* reported steady-state Ni concentrations of 1 mg L^{-1} for Ni/AC and Ni/ $\gamma\text{-Al}_2\text{O}_3$ [101]. For a Ni/ $\alpha\text{-Al}_2\text{O}_3$ catalyst, steady state concentrations reached 10 mg L^{-1} (280 mg L^{-1} at the start of the experiment) [102].

1.6.2 Sintering

Growth of active metal particles during SCWG is a serious problem for Ni-based catalysts, as mentioned in Section 1.5.1. For example, Cardoso *et al.* reported sintering of Ni/CNF in SCW (from 18 nm to 36 nm in 15 min) showing that the dispersion loss could be due to the SCW environment only [103]. Fortunately, Ru is much more stable in this environment but still prone to sintering as shown in several studies. In model conditions, Peng *et al.* mentioned very minor increases in Ru NP size for a 0.5 %Ru/AC catalyst [76]. Waldner *et al.* reported minor Ru NP growth (1 to 2 nm) after gasifying SLW for 220 h over 2 %Ru/AC. During 100 h continuous gasification of algae, a 5 %Ru/AC catalyst sintered from 2 to 13 nm. Although more pronounced, it still remains better than in most reported cases for Ni. In our recent paper on Ru leaching, we reported no notable Ru particle growth from two commercial 5 %Ru/AC catalysts after glycerol and sewage sludge gasification [104]. The high Ru NP stability reported by many groups could be due to the support, as AC contains many defects and a variety of surface functional groups which increase the wettability of the carbon and can act as strong anchoring sites through covalent bonding to surface oxygen groups [78], [105]–[107]. On more inert supports like CNF, de Vlieger reported high Ru NP stability with stable sizes in the range 3–5 nm for the fresh Ru/CNF and spent ones (in subCW and after SCWG) [81].

1.6.3 Coking

Coke formation can lead to catalyst deactivation in many catalytic reactions. Different types of coke can be formed depending on the conditions and the metal used. Ochoa *et al.* presented different coking pathways for biomass reforming and pyrolysis, leading either to filamentous coke or encapsulating coke [108]. The former typically occurs on Ni catalysts through adsorption and diffusion of carbon through the metal particle and deposition on the support, being the same process as for CNF formation. This filamentous coke is not reported to induce catalyst deactivation as the metal particle sits on top of the filament/fibre and can still freely adsorb reactants. However, the filament could break off and carry away the NP sitting on top of it. Encapsulating coke however is more problematic, as its name suggests. Strong carbon adsorption will gradually cover the active site or the support and condense, thus hindering the access to the metal active site or blocking the pores of the support [108]. Filamentous coke is generally only formed with transition metals, as carbon does not dissolve in noble metals. In SCW, degradation reactions occur also in the absence of catalysts, meaning that organics will be hydrolysed or decomposed to tars and/or coke. Müller and Vogel showed that glycerol and glucose formed coke when treated in hydrothermal media without catalyst [60]. Coke formation was significant in subCW for both glycerol and glucose, but suppressed for the former in SCW. Glucose was already mostly converted during the heating up procedure in batch, whereas glycerol was stable. These results gave further insights into coking during catalytic conversion, demonstrating that stable carbon species are likely formed when the organics are not fully converted by the catalyst. Many studies on SCWG report coke formation as a main deactivation mechanism, mainly through pore filling/blocking leading to a significant loss in surface area [66], [73], [76], [95], [109]–[111]. Unfortunately, it is difficult to quantify coke deposits on a carbon support and also complicated to regenerate coked Ru/C catalysts. Recently, our group attempted to understand coke formation mechanisms on a spent Ru/AC SCWG catalyst with the help of neutron scattering and liquid chromatography-mass spectrometry (LC-MS) [112]. Extraction of the deactivated catalysts led to a regain in activity, showing that a mild regeneration procedure could work. These results also gave first insights on the nature of the deposited carbon species.

Although coke and char formation were shown to be suppressed with given compounds in SCWG [60], [62], coking still remains a widely-reported deactivation mechanism as soon as the process drifts away from total carbon conversion in continuous systems. The main challenge is thus to protect the catalyst from coking by using more inert materials (*e.g.* CNF) or by delaying this deactivation mechanism for as long as possible. Solvent-based regeneration techniques could also be further developed as calcination is not an option for carbon-supported catalysts.

1.6.4 Poisoning

As sulfur is well-known catalyst poison, a lot of work has been done to better understand the poisoning mechanism and develop potential regeneration techniques for HTG catalysts. Osada *et al.* performed lignin gasification in batch at 400 °C in the presence of different sulfur compounds (elemental sulfur, sulfuric acid, thiophene, a propanethiol as well as some thiophenols) [113]. The gasification efficiency dropped with increasing sulfur, showing that it poisoned the catalyst. S^{2-} , SO_3^{2-} , SO_4^{2-} as well as different Ru oxidation states (0, IV, VI, VIII) were detected at the catalyst surface by X-ray photoelectron spectroscopy (XPS), suggesting that different Ru-S complexes were formed. They also tried to elucidate the reaction pathway of lignin gasification over poisoned Ru/C catalysts with 4-propylphenol and formaldehyde as model compounds [114]. The former was not gasified in the presence of sulfur, whereas the latter was. Higher H_2 concentrations were also linked to sulfur poisoning. They concluded that sulfur poisoned the active sites responsible for C–C bond cleavage, as formaldehyde gasification and the WGS reaction were not affected. Waldner *et al.* drew similar conclusions from SLW gasification in the presence of sulfate [71]. A few years later, Dreher *et al.* showed sulfur poisoning of Ru/AC catalysts by using labelled compounds and *operando* XAS [86]. The addition of dimethyl sulfoxide during SCWG of ethanol led to a considerable decrease in gas production, accompanied by loss of CH_4 (60 to 20 vol%) and CO_2 selectivity, replaced mainly by H_2 and CO. They found a Ru-S coordination number of 1 by EXAFS and thus postulated a mean poisoned catalyst composition of $RuS_{0.33}$. Sulfur poisoning also led to facilitated D_2O dissociation at the catalyst surface at the expense of CH_x dehydrogenation. Catalyst regeneration was attempted with dilute H_2O_2 at 125 °C, which oxidised Ru and led to the removal of adsorbed sulfur [115]. The regenerated catalyst regained full activity initially, but started deactivating again after a few hours – the reason for this drop in activity not being clear.

Chloride is another potential poison, with several works mentioning this issue. Yamaguchi *et al.* compared the activity of Ru trivalent salts impregnated on charcoal for SCWG of lignin at 400 °C and found that the chloride salt led to only 24 % gas yield, compared to 80–90 % yields for the nitrosil nitrate salt and a reduced Ru/C [77]. Methane formation was also decreased with the chloride salt. Although the impregnated salts got reduced during the process, the generated Ru NPs were larger for the chloride salt which could lead to a lower activity. However, Cl was responsible for the activity drop upon HCl addition as the gas yield only reached 30 % with Ru/C. Peng *et al.* also reported lower isopropanol conversions with a catalyst exhibiting some residual chloride as well as a lower dispersion after synthesis from $RuCl_3$ [76]. The lower dispersion coincided with the aforementioned results of Yamaguchi *et al.* . For this reason, nitrate salts were preferentially used as Ru precursors.

1.7 Size sensitivity of supported metal catalysts

The reactivity of metal NPs can change with particle size depending on which chemical bond needs to be activated in a given reaction [116]. Three different trends were observed for a variety of catalytic reactions, as presented in Figure 1.8.

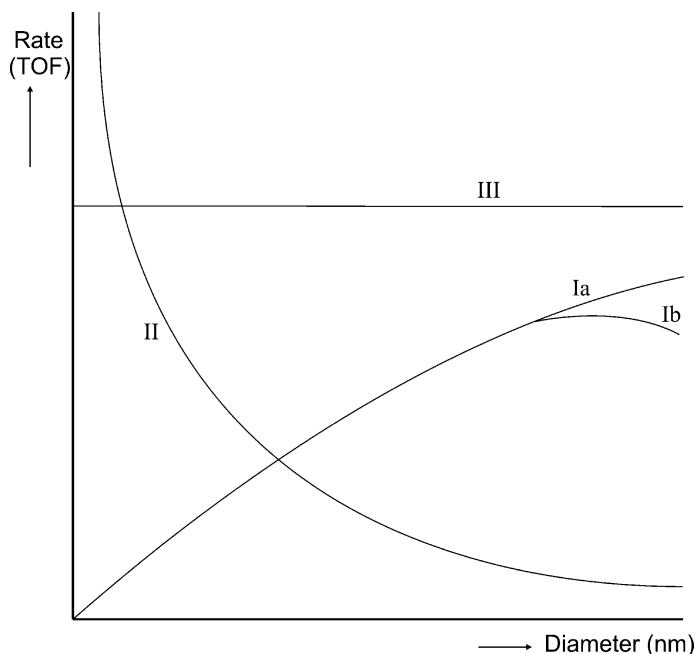


Figure 1.8 – Size sensitivity of catalytic reactions. Re-used from [116].

Type III reactions are size insensitive and comprise hydrocarbon hydrogenation for example. Type II exhibit increased rates for smaller diameters as in CH_4 activation. Finally, type I behaviour shows a maximum or plateau above a given particle diameter and generally involves the dissociation or formation of π bonds, as for CO or N_2 dissociation. The reactivity tends to zero for decreasing particle sizes because special atom arrangements are required *i.e.* step and edge atoms. These special sites are called B_5 sites, being combinations of five under-coordinated "step-edge" atoms creating a three-dimensional adsorption site for a reactive species (*i.e.* CO or N_2), according to the early work of van Hardeveld [117], [118]. Since these are purely geometrical features, the site concentration exhibits a maximum at a given particle diameter, leading to the size sensitivity of some reactions. This was shown by Jacobsen *et al.* for the ammonia synthesis reaction, as higher concentrations of B_5 sites were expected on Ru NPs of 1–3 nm in diameter [119]. They suggested that the increase in NH_3 synthesis activity was due to the disappearance of the smallest NPs (<1 nm) due to sintering, which led to larger crystals containing more B_5 sites. Ru NPs smaller than 0.8 nm exhibited very few B_5 sites as there were not enough atoms available to form these special ensembles.

Detailed studies have investigated the size sensitivity of important catalytic reactions. A lot of work on FT synthesis has been performed in the group of de Jong, evaluating the particle size effect of supported Co catalysts [120]–[122]. They showed a type Ia (Figure 1.8) behaviour for the FT synthesis reaction over a Co/CNF catalyst, with decreasing turnover frequencies below 6 and 8 nm at 1 and 35 bar, respectively [121]. Baudouin *et al.* showed that the rate of methane dry reforming was insensitive to the Ni particle size in the range 1.6–7.3 nm [123]. Cu catalysts for methanol synthesis also exhibited structure sensitivity, with the activity decreasing for particles smaller than 8 nm [124].

Ru is also known to exhibit structure sensitivity in several catalytic reactions such as FT synthesis [125], ammonia synthesis [119], [126], and ammonia decomposition [127]–[129]. This is also the case for the methanation reaction, where size sensitivity was observed with Ru/TiO₂ [130], [131], Ru/C [132] and single crystals [133]. During methanation, CO dissociation seems to be the rate-limiting step and occurs preferentially at under-coordinated sites, as shown over a Ni surface [134]. On Ru, the computational study of Shetty *et al.* showed a lower CO dissociation energy barrier at "hollow" Ru sites than on stepped surfaces, indicating that these specific B_5 sites are highly active for CO activation [135]. Czekaj *et al.* performed DFT calculations and showed that Ru clusters only stabilised in given geometries on graphite, indicating that 1.5 nm Ru NPs contained more B_5 sites (*i.e.* 12) than 1.0 nm Ru NPs (*i.e.* 6) [136]. These modelling results were compared to spectroscopic data from ethanol SCWG over Ru/AC, linking the enhanced Ru activity to its small Ru NPs (1.2–1.4 nm) [86].

1.8 Problem statement

A lot of effort was put into the development and optimisation of SCWG processes and materials. The main outcomes are that there are very few stable materials for catalysis in SCW, the most interesting one being AC because of its relatively good mechanical stability and high surface area. The same applies to active metals, with mainly Ni and Ru being used, although the former is limited by its stability in SCW. At lower SCWG temperatures favouring CH₄ formation, a catalyst is required to efficiently convert the feed into gas. With Ru being the most active and stable metal, this comes at increased costs. For this reason, it is vital to further develop and optimise Ru-based catalysts. As the technology is nearing commercialisation, it is pivotal to ensure high gasification activity and long-term stability for the catalyst. To achieve this, more knowledge is required on deactivation mechanisms and how to delay or suppress them.

Up to now, most of the research on catalytic SCWG has been performed in batch conditions, which does not reflect the reality of continuous systems. Even though batch tests are very important for material activity and stability screenings, many limitations arise when deactivation mechanisms are studied. Typically the catalyst and feed go through the different hydrothermal conversion regimes (carbonisation, liquefaction and eventually gasification), which could already lead to deactivation before even reaching the desired process conditions. Also, it becomes very tricky, if not impossible, to discriminate between the different deactivation mechanisms. Hence, more data is required from continuous SCWG experiments.

Working in model systems can also be criticised, as they do not represent the reality of biomass with all of its impurities. However, pure systems are a required step to gain more insight on purely catalytic properties before moving on to prototypes and pilot scales with biomass. Initially, the majority of the work on SCWG catalysts was performed in model conditions, allowing an efficient screening of active metals and supports. Since then, more in-depth studies were performed to understand the effect of catalyst supports, synthesis methods and metal dispersion on the activity and stability of SCWG catalysts, as discussed before. Recent investigations also elucidated the active Ru phase in SCWG as well as gasification and poisoning mechanisms. Although tremendous progress has been made in the field recently, some questions still remain unanswered in these challenging conditions:

- Carbon was shown to be the best support for Ru catalysts, but very little is known on its role in SCWG and influence towards coking. A better understanding of the intrinsic gasification activity of different carbon support types and the effect of the pore structure is needed to guarantee longer catalyst lifetimes.

- A few studies related the Ru catalyst activity to the metal dispersion, however no systematic particle size study has been performed in SCWG. Since the methanation reaction is known to be structure sensitive, a thorough study on particle size effects in SCWG would generate valuable learnings on the Ru NP size to target. The learnings would also be of great benefit in other fields using Ru-based catalysts (FT synthesis, hydrogenation).
- SCWG catalysts could be prone to dissolution in SCW, potentially leading to significant losses of active phase. Several studies have reported metal losses for Ni, but very little is known for Ru. A better comprehension on the stability of Ru NPs in SCWG is needed to ensure long-term operation and avoid process water contamination.
- CNF was shown to be an interesting support material for SCWG applications because of its stability and open pore structure. Unfortunately, very few studies were dedicated to CNF-based catalysts in SCW. The use of this support could be an alternative to the more conventional AC. It would also allow performing more detailed studies on sintering and coking by transmission electron microscopy (TEM) due to improved contrasts.

1.9 Scope of the thesis

This doctoral thesis aims at further improving the Ru/C catalyst used for SCWG of biomass to bio-SNG in order to have an active and robust catalyst for this process. To do so, the properties of carbons are investigated in order to select an optimal support for catalyst synthesis. Different synthesis techniques are applied with the goal of achieving very small Ru NPs (≈ 1 nm) and evaluating their stability during SCWG. Then the Ru NP size is varied to better understand the different catalytic effects during SCWG. The catalyst activity and stability is assessed in model conditions, by converting glycerol solutions on a continuous SCWG setup (*Konti-I*). The global SCWG performance of new Ru catalysts synthesised during this work is compared to industrial benchmark catalysts. Gasification experiments are coupled to high-end analytical techniques to investigate the different deactivation mechanisms. The detailed structure of the thesis is the following:

1. Finding an optimal carbon support for Ru-based SCWG catalysts (Chapter 3):

Carbon supports exhibiting different properties (surface area, ash content, pore volume, pore structure) are characterised and tested on a continuous SCWG setup with glycerol to evaluate their intrinsic gasification activity. Their resistance to coking is assessed by physisorption analyses of the spent samples. The stability of CNF is also investigated as it is a newer material with very few related studies. Selected supports are used for ruthenium impregnation, the activity and stability of the synthesised Ru/C catalysts is

then evaluated during glycerol conversion and compared to our commercial benchmark catalyst (Ru/AC-BM).

2. Assessing and understanding ruthenium loss during SCWG (Chapter 4):

The gasification activity of two new commercial catalysts is compared, with the goal of replacing our benchmark catalyst (Ru/AC-BM). The process waters (PWs) are analysed by time-resolved inductively coupled plasma - mass spectrometry (ICP-MS) in order to quantify ruthenium in the exit stream. The effect of SCWG-relevant process parameters on the Ru loss is evaluated and compared to thermodynamic modelling data. The best-performing commercial catalyst is selected for further catalytic testing on larger SCWG rigs to evaluate the scale effect on Ru loss. The catalyst is also assessed for its sewage sludge gasification activity, with the Ru loss being monitored during biomass gasification too. Eventually, the Ru loss is compared between the conventional Ru/AC catalyst and SCW-stable metal oxide-based catalysts. For this, a series of 2 %Ru catalysts is synthesised on AC, α -Al₂O₃, monoclinic - ZrO₂ and rutile - TiO₂ and evaluated during glycerol gasification.

3. Using Ru/CNF as improved system to investigate catalyst deactivation (Chapter 5):

CNF are used for their low density, high pore volume and lack of micropores, making TEM characterisation much easier thanks to an enhanced contrast compared to AC. Ru/CNF catalysts of very small Ru NPs are synthesised, characterised (physisorption, TEM, thermogravimetric analysis (TGA)) and assessed during SCWG of glycerol. Ru NPs of different particle size distributions are synthesised to investigate the effect of dispersion on the gasification activity as well as the stability. Turnover frequencies are determined and related to the Ru NP size. Deactivation mechanisms such as sintering, coking and leaching are evaluated too. The most active Ru/CNF catalyst is eventually compared to our commercial benchmark catalyst.

2 Methods and materials

2.1 Catalyst support preparation

2.1.1 Sieving

Prior to catalyst synthesis, all supports were crushed and sieved to the fraction of interest (0.5–0.8 mm) to respect a reactor-to-catalyst diameter ratio $d_R d_{cat}^{-1} \geq 10$. After sieving, the supports were washed in deionised (DI) H₂O to get rid of the generated dust, which can be significant for AC. The washing procedure was performed in a round-bottom flask under continuous stirring for 1 h, and repeated until the water was clear. After washing, the supports were dried in an oven overnight (110 °C). The supports were then ready for impregnation. The α -Al₂O₃ support did not undergo this procedure as it was provided as 0.8 mm beads.

2.1.2 CNF purification

CNF were purified before Ru impregnation to get rid of the residual silica from the synthesis. They were washed for 2 h in 1 M KOH at reflux under agitation in a round-bottom flask equipped with a condenser, as shown in Figure 2.1. The purified support was then filtered and washed with DI H₂O until the filtrate was neutral (pH = 6–7), before being dried overnight at 110 °C in air. The purified, dried support was eventually sieved to 0.5–0.8 mm again before impregnation.

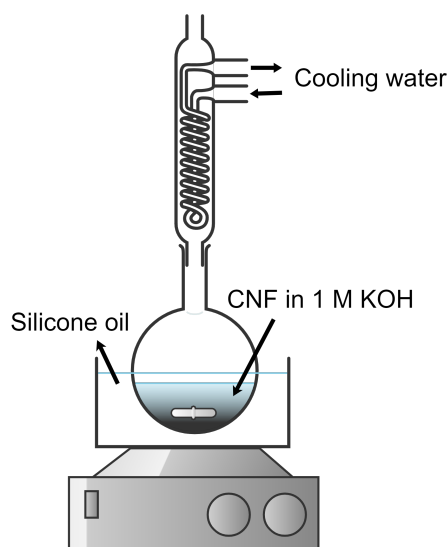


Figure 2.1 – Apparatus used to purify the CNF in KOH (1 M) at reflux.

2.2 Catalyst synthesis

2.2.1 Wet impregnation

For catalysts synthesised by the wet impregnation (WI) method, the support of interest was suspended in a $\text{RuNO}(\text{NO}_3)_3$ solution (1.5 % wt/vol) in a round-bottom flask. The amount of precursor solution was added in 20 % excess based on the final catalyst loading to account for losses on the flask walls. The suspension was continuously rotated on a rotary evaporator for 4 h at 40 °C first, before increasing the temperature to 60 °C and slowly decreasing the pressure to 350 mbar. Afterwards, the pressure was further decreased to 150 mbar (2 h). Eventually, the catalysts were left overnight at room temperature (RT) and 150 mbar to fully evaporate the solvent. The impregnated supports were then dried overnight in air at 110 °C before being calcined and/or reduced.

2.2.2 Incipient wetness impregnation

For the incipient wetness impregnation (IWI) method, the available support pore volume (V_p) was determined by adding DI H_2O until saturation of the support. Due to the possibility of air being blocked in the pores upon water addition, the pore volume determined by H_2O uptake was compared to the one measured by N_2 physisorption. Both volumes were in good agreement, suggesting that the presence of trapped air was negligible. Ru precursor solutions were prepared by dissolving $\text{RuNO}(\text{NO}_3)_3$ or $\text{RuCl}_3 \cdot x\text{H}_2\text{O}$ salts in DI H_2O by adding the solution concentration to the support pore volume (determined by H_2O , based on the desired loading). The supports were impregnated by drop-wise addition of the Ru precursor

solution until they were saturated *i.e.* shiny and sticking together. The theoretical loading was then determined by the volume of precursor solution added. The impregnated support was then dried overnight in air at 110 °C before being reduced.

2.2.3 Calcination

After impregnation, the catalysts synthesised on metal oxides were calcined for 4 h in a quartz tube (i.d. =45 mm, L =600 mm, with a fritted disc in the middle) at 450 °C (10 °Cmin⁻¹) in O₂/N₂ (20:80, 250 mLmin⁻¹), similarly to what was done by Zöhrer *et al.* [109] and Peng [137]. Carbon-based catalysts were not calcined, but directly reduced after the impregnation.

2.2.4 Reduction

All synthesised catalysts (after impregnation for carbon-supported catalysts, after calcination for the metal oxide-based ones) were reduced in a quartz reactor (same as for the calcination) in H₂ with a 5 °Cmin⁻¹ heating ramp. CNF-supported catalysts were reduced at 300 °C for 4 h in H₂/N₂ (5:95, 150 mLmin⁻¹) to ensure the stability of the CNF material. All other catalysts were reduced at 400 °C for 6 h in H₂/N₂ (20:80, 250 mLmin⁻¹). After reduction, the catalysts were passivated by letting air diffuse through the tubular reactor overnight. The CNF-based catalysts were sieved again to the fraction of interest (0.5–0.8 mm) before being used, whereas the other catalysts were ready to be used without further treatment.

2.3 Catalyst characterisation methods

2.3.1 N₂ physisorption

Physisorption measurements were performed on an Autosorb-1 (Quantachrome) in liquid N₂ (77 K). The samples were outgassed in dynamic vacuum for a minimum of 3 h at 300 °C. The SSA was calculated according to the Brunauer-Emmett-Teller (BET) model [138], the total pore volume was determined at a relative pressure $pp_0^{-1} \geq 0.99$. The micropore volume V_{MP} was determined by the t-method developed by Lippens and de Boer [139]. The non-microporous volume is defined here as external volume V_{Ext} and was calculated by subtracting the micropore volume from the total pore volume: $V_{Ext} = V_p - V_{MP}$. The same calculation applies for the external surface area SSA_{Ext} , defining the sample surface area without the micropore contribution. Pore size distributions were generated from the Barrett-Joyner-Halenda (BJH) model [140].

2.3.2 CO pulse chemisorption

CO pulse titration was performed on a TPD/R/O 1100 (Thermo Scientific). First, a temperature-programmed reduction (TPR) was performed in 5 %H₂/Ar (300 °C, 5 °Cmin⁻¹, 1 h hold), followed by a treatment in He 6.0 (400 °C, 1 h hold) to remove the remaining H₂, eventually the catalyst was cooled down to 25 °C and titrated with pulses of 20 %CO/He. Although commonly used, a CO:Ru stoichiometric factor of 1 is debated, as CO adsorption was reported to vary with the Ru NP size [141], [142]. To validate CO:Ru = 1, a control measurement by static H₂ chemisorption was performed on a commercial 5 %Ru/AC catalyst (Ru/AC-BM) yielding the same dispersions within the errors of the methods (H₂: 28 ± 2 %, CO: 32 ± 4 %). Hence, a CO:Ru stoichiometric factor of 1 was used. $d_{p,CO}$ was calculated from D_{CO} with the equations developed by Borodziński and Bonarowska [143]. A detailed description can be found in the work of Peng *et al.* [75].

2.3.3 X-ray diffraction

XRD spectra were acquired on a D8 Advance diffractometer (Bruker) with a Cu K α_1 radiation source ($\lambda = 1.5406 \text{ \AA}$) equipped with a 1D-LynxEye detector. The samples were crushed in a ball mill and sieved (<0.2 mm) before being placed on the sample holder.

2.3.4 Thermogravimetric analysis

TGA was performed on TGA/SDTA 851e (Mettler Toledo), coupled to a ThermoStar mass spectrometer (MS). Approximately 10 mg of sample was loaded in an Al₂O₃ crucible. The samples were first heated up to 110 °C (5 °Cmin⁻¹, 30 min hold) to remove the moisture content, the temperature was then increased to 900 °C (5 °Cmin⁻¹). Analyses were performed in air (temperature-programmed oxidation (TPO)) or H₂/Ar (5:95) (TPR) as reactive gas (10 mLmin⁻¹). Ar (10 mLmin⁻¹) was used as protective gas. The evolved gases flowed to the MS where the following masses were analysed: 2 (H₂), 12 (C), 16 (CH₄), 18 (H₂O), 28 (N₂ or CO), 40 (Ar) and 44 (CO₂).

2.3.5 Diffuse reflectance infrared Fourier transform spectroscopy

Diffuse reflectance infrared Fourier transform spectroscopy (DRIFTS) spectra were measured on a Vertex 80 V (Bruker) FTIR spectrometer between 800 and 2000 cm⁻¹ at a resolution of 10 cm⁻¹. The final spectra are averages of 30 scans per catalyst sample. The spectra were normalised to the highest peak. The samples were measured as grains (0.5–0.8 mm) without further preparation.

2.3.6 Raman spectroscopy

Raman spectra were collected on a Labram HR800 (Horiba Jobin Yvon) instrument using a He-Ne laser ($\lambda = 633$ nm), at a power of 2 mW. Spectra were recorded between 800 and 2000 cm^{-1} with a resolution of 10 cm^{-1} and an exposure time of 30 s. The final spectra are an average of 10 measurements. The catalyst samples were measured as grains (0.5–0.8 mm) without further preparation.

The acquired spectra were deconvoluted into the different modes of carbon vibrations representing a perfectly-organised graphene sheet (G-band) and its structural defects (D-bands). The spectra were first baseline-corrected and normalised to the highest peak intensity (D-band), and then fitted with Lorentzian peaks for bands D1, D2, D4, G and a Gaussian peak for band D3, according to [144], [145]. The peak width, height and position were optimised through a Levenberg-Marquardt algorithm.

2.3.7 Scanning electron microscopy - energy dispersive X-Ray spectroscopy

Scanning electron microscopy (SEM) measurements were carried out on a Zeiss ULTRA 55 field emission gun SEM and energy dispersive X-ray spectroscopy (EDX) scans or mappings were performed with an EDAX APOLLO XV. The investigated samples were placed on a conductive carbon tape. SEM images were acquired with a secondary electron detector at an acceleration voltage of 16.0 kV.

2.3.8 Transmission electron microscopy

TEM images were collected with a JEOL JEM 2010 microscope operated at 200 keV and equipped with a LaB₆ cathode. Images were recorded by a slow-scan CCD camera (4008×2672 pixels, Orius Gatan Inc.). Samples were prepared on lacey carbon grids using ethanol to disperse the ground catalysts.

2.3.9 High-resolution transmission electron microscopy

High-resolution transmission electron microscopy (HR-TEM) images were acquired using a probe-corrected JEOL JEM-ARM200F (NeoARM) microscope equipped with a cold-field emission gun operated at 200 keV and a Gatan OneView camera. The instrument could be operated in TEM or STEM mode (with EDX). Sample preparation was exactly the same as described in Section 2.3.8.

2.3.10 Particle size distributions

For catalysts supported on CNF, particle size distributions (PSDs) were performed to determine the metal dispersion based on TEM micrographs (D_{TEM}). Representative regions of different micrographs were selected to perform the PSD, the Ru NP sample size was kept above 200. The PSD bin size was selected in order to represent the data in a statistically-relevant manner [146]. Since the PSDs did not always observe normal distributions, the main mode of the Ru NP diameter was reported. All PSDs exhibited mono-modal distributions. $d_{p,TEM}$ was corrected for the oxide layer that forms in the presence of oxygen (Equation 2.1) at ambient conditions, with the layer thickness reported to reach 0.6 nm [147],

$$d_{p,TEM,corr} = \begin{cases} 2 \cdot \left[\left(\frac{d_{p,TEM}}{2} \right)^3 \cdot \frac{V_{m,Ru}}{V_{m,RuO_2}} \right]^{\frac{1}{3}} & \text{if } d_{p,TEM} \leq 0.6 \\ 2 \cdot \left[\left(\frac{d_{p,TEM} - 0.6}{2} \right)^3 \cdot \left(1 - \frac{V_{m,Ru}}{V_{m,RuO_2}} \right) + \left(\frac{d_{p,TEM}}{2} \right)^3 \right]^{\frac{1}{3}} & \text{if } d_{p,TEM} > 0.6 \end{cases} \quad (2.1)$$

where $d_{p,TEM,corr}$ is the reduced Ru NP size, $d_{p,TEM}$ is the observed Ru NP size by TEM and V_m is the molar volume of Ru or RuO₂. For simplification, all mentions of $d_{p,TEM}$ in the results chapters already include the oxide-layer correction.

D_{TEM} was calculated from the corrected Ru NP diameter ($d_{p,TEM,corr}$) as shown in Equation 2.2, assuming the NPs organise in a hexagonal close-packed (hcp) structure,

$$D_{TEM} = \frac{\sum Ru_{sf,i}}{\sum Ru_{tot,i}} \quad (2.2)$$

where the total ($Ru_{tot,i}$) and surface ($Ru_{sf,i}$) Ru atoms were calculated from the geometrical equations published by van Hardeveld and Hartog for a truncated bipyramid [118]. The bulk and surface atoms were computed for each additional Ru atom layer as shown in Figure 2.2 and a polynomial (Equation 2.3) was fitted to relate the total and surface atoms ($M_{Ru} = y$) as a function particle diameter ($d_{Ru} = x$) for a truncated bipyramid.

$$y = A_0 + A_1 \cdot x + A_2 \cdot x^2 + A_3 \cdot x^3 + A_4 \cdot x^4 + A_5 \cdot x^5 \quad (2.3)$$

The coefficients A_i are summarised in Table 2.1 for both the surface and total Ru atoms.

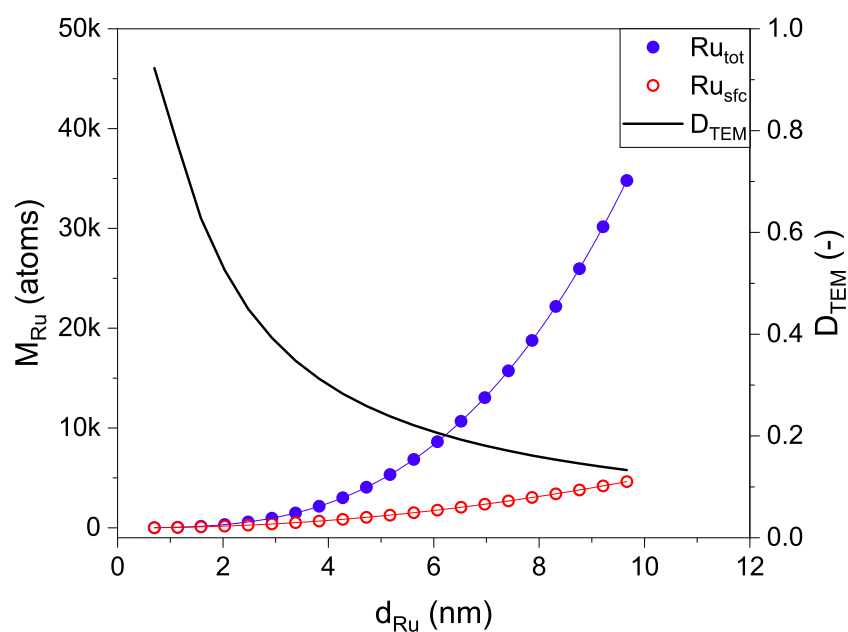


Figure 2.2 – Relationship between total (Ru_{tot}), surface (Ru_{sfc}) Ru atoms and dispersion (D_{TEM}) as a function of Ru NP diameter, assuming a truncated bipyramid shape [118]. The lines represent the fitted 5th-degree polynomial.

Table 2.1 – Polynomial coefficients relating the total and surface Ru atoms to the particle diameter

	A_0	A_1	A_2	A_3	A_4	A_5
Bulk Ru	$-9.2 \cdot 10^{-11}$	$3.3 \cdot 10^{-10}$	$-2.4 \cdot 10^{-10}$	38.6	$-7.8 \cdot 10^{-12}$	$3.2 \cdot 10^{-13}$
Surface Ru	3.6	-24.2	52.3	$-7.2 \cdot 10^{-2}$	$7.3 \cdot 10^{-3}$	$-2.9 \cdot 10^{-4}$

2.4 Analytical methods

2.4.1 Organic carbon determination

A Dimatoc2000 (DIMATEC) was used to analyse the carbon contents of the feed and process waters. The instrument measured the total carbon (TC) by oxidising carbon species into CO₂ at 850 °C in a quartz reactor containing a 5 % Pt/SiO₂ catalyst. The total inorganic carbon (TIC) was determined by converting the carbonates to CO₂ at 160 °C by adding phosphoric acid (42 %) in a quartz reactor containing porous silica gel beads. The CO₂ evolution was measured with an infrared (IR) detector. The total organic carbon (TOC) was eventually determined by subtraction (TOC = TC - TIC). The carbon conversion was calculated from Equation 2.4:

$$X_C (\%) = \frac{\dot{m}_{TOC,feed} - \dot{m}_{TOC,out}}{\dot{m}_{TOC,feed}} \cdot 100 \% \quad (2.4)$$

where $\dot{m}_{TOC,feed}$ and $\dot{m}_{TOC,out}$ are the mass flows of organic carbon entering (feed) and exiting the system (PW), respectively.

2.4.2 Gas chromatography

The gas generated during SCWG experiments was measured online with an μ GC 3000 series (Inficon), equipped with two columns with a thermal conductivity detector (TCD) each. The first column (Molsieve, 10 m x 320 μ m x 30 μ m) was for analysing H₂, O₂, N₂, CH₄ and CO in He carrier gas, at 120 °C and 25 psi. The second column (PLOTQ, 8 m x 320 μ m x 30 μ m) analysed CO₂, H₂S, C₂H₄, C₂H₆, C₃H₆ and C₃H₈ in Ar carrier gas, at 70 °C and 20 psi. The carbon gasification efficiency (GE_C), indicating the fraction of carbon ending up in the gas phase (as CH₄, CO, CO₂, C₂ and C₃) was calculated with Equation 2.5

$$GE_C (\%) = \frac{\dot{n}_{C,gas}}{\dot{n}_{C,feed}} \cdot 100 \% \quad (2.5)$$

by knowing the total amount of carbon in the gas phase ($\dot{n}_{C,gas}$) and the flow of carbon entering the system ($\dot{n}_{C,feed}$) per unit of time.

2.4.3 Elemental analysis

The mass fraction of carbon, hydrogen, nitrogen and sulfur were quantified on a Vario EL Cube (Elementar) by calcining the samples at 1150 °C in a quartz tube filled with a WO₃ catalyst. Another quartz reactor reduced NO_x species over a Cu catalyst. Carbon was oxidised to CO₂ and together with N₂, H₂ were detected with a TCD. Sulfur was detected as SO₂ by an IR detector. The oxygen content was determined by difference to 100 %. Sulfanilamide was used

as standard before each series of measurements, yielding a daily correction factor through the theoretical and measured element fraction in the standard.

2.4.4 ICP-MS

ICP-MS (7700x, Agilent) was used to determine the loading of the catalysts synthesised by the WI method. After impregnation, the glass vial was washed with 20 ml MilliQ H₂O to dissolve the remaining Ru salts. The ruthenium loading was then determined by mass balance (Equation 2.6)

$$x_{Ru} (\%) = \frac{m_{Ru,i} - m_{Ru,ICP}}{m_{cat}} \cdot 100 \% \quad (2.6)$$

where x_{Ru} is the final loading, $m_{Ru,i}$ is the mass of elemental Ru used for the impregnation, $m_{Ru,ICP}$ is the Ru loss determined by ICP-MS and m_{cat} is the final mass of the catalyst.

For carbon-supported Ru catalysts, only Ru and Al were targeted to monitor the loss from the catalyst bed as well as the α -Al₂O₃ filling material. For the metal oxide-supported catalysts, the corresponding elements were also measured *i.e.* Al, Ti and Zr. The process water samples (non-filtered) were acidified with high-purity HNO₃, the final acid concentration was 1 %. Single-element standards (Ru, Al, Ti, Zr) as well as 1 % HNO₃ were used for calibration. The calibration range was 0–50 $\mu\text{g L}^{-1}$ for Al, Ti, Zr, and up to 2000 ng L^{-1} for Ru, depending on the analysis. For samples of Ru concentrations above the calibration range, dilutions steps were performed with 1 % HNO₃. Whenever ICP-MS measurements were carried out with ²⁷Al, ⁴⁷Ti, ⁴⁹Ti, ⁹⁰Zr and ⁹¹Zr, all elements (including Ru) were measured in normal mode (0.2 s integration time). When only Ru was targeted, ⁹⁹Ru and ¹⁰¹Ru isotopes were measured in time-resolved mode (transient signal, 50 s average) in order to more accurately quantify the low concentrations. The residual standard deviation (RSD) of all standards measured in time-resolved mode were below 5 %. The limit of detection (LoD) for ¹⁰¹Ru was 0.0011 $\mu\text{g L}^{-1}$.

To validate the measured Ru concentrations from the PWs, a blank experiment was performed by feeding 10 wt% glycerol over AC only, in SCWG conditions. The analysed Ru concentrations amounted to $0.012 \pm 0.007 \mu\text{g L}^{-1}$.

2.4.5 Ash content determination

The ash content and catalyst loading were determined by calcination in a muffle oven (Naber-therm) in static air at 900 °C for 12 h (10 °C min⁻¹ ramp). For the loading determination, the ash content of the support was subtracted from the total ash and then corrected by the molar mass ratio of Ru and RuO₂, since the remaining ruthenium in the ash is completely oxidised.

2.4.6 Error estimation and propagation

For all quantities presented with a standard deviation, a minimum of three independent measurements were performed for the average and standard deviation determination.

The errors arising from the μ GC gas measurement were <5 % for all gases with concentrations above 0.5 vol%. The used calibration faced limitations at very low gas concentrations, where the error amounted to 25 % for 0.4 vol% CO. This issue was solved above 0.5 vol% (error <1 % for CO).

For the organic carbon determination in process waters (TOC), between 5 and 7 measurements were performed per sample, leading to an average value with standard deviation. The RSD was systematically below 5 %.

Error propagation for calculated values were performed according to Equation 2.7 for sums of the type $z = x \pm y$ and according to Equation 2.8 for multiplications in the form $z = x \cdot y$ or $z = x/y$, where Δx and Δy refer to the standard deviations.

$$\Delta z = \sqrt{(\Delta x)^2 + (\Delta y)^2} \quad (2.7)$$

$$\frac{\Delta z}{z} = \sqrt{\left(\frac{\Delta x}{x}\right)^2 + \left(\frac{\Delta y}{y}\right)^2} \quad (2.8)$$

The error propagation for the carbon conversion (X_C) calculation (Equation 2.4) is shown in Equation 2.9 with simplified variables ($I = \dot{m}_{TOC,feed}$ and $O = \dot{m}_{TOC,out}$) as example.

$$\Delta X_C = X_C \sqrt{\left(\frac{\sqrt{(\Delta I)^2 + (\Delta O)^2}}{I + O}\right)^2 + \left(\frac{\Delta I}{I}\right)^2} \quad (2.9)$$

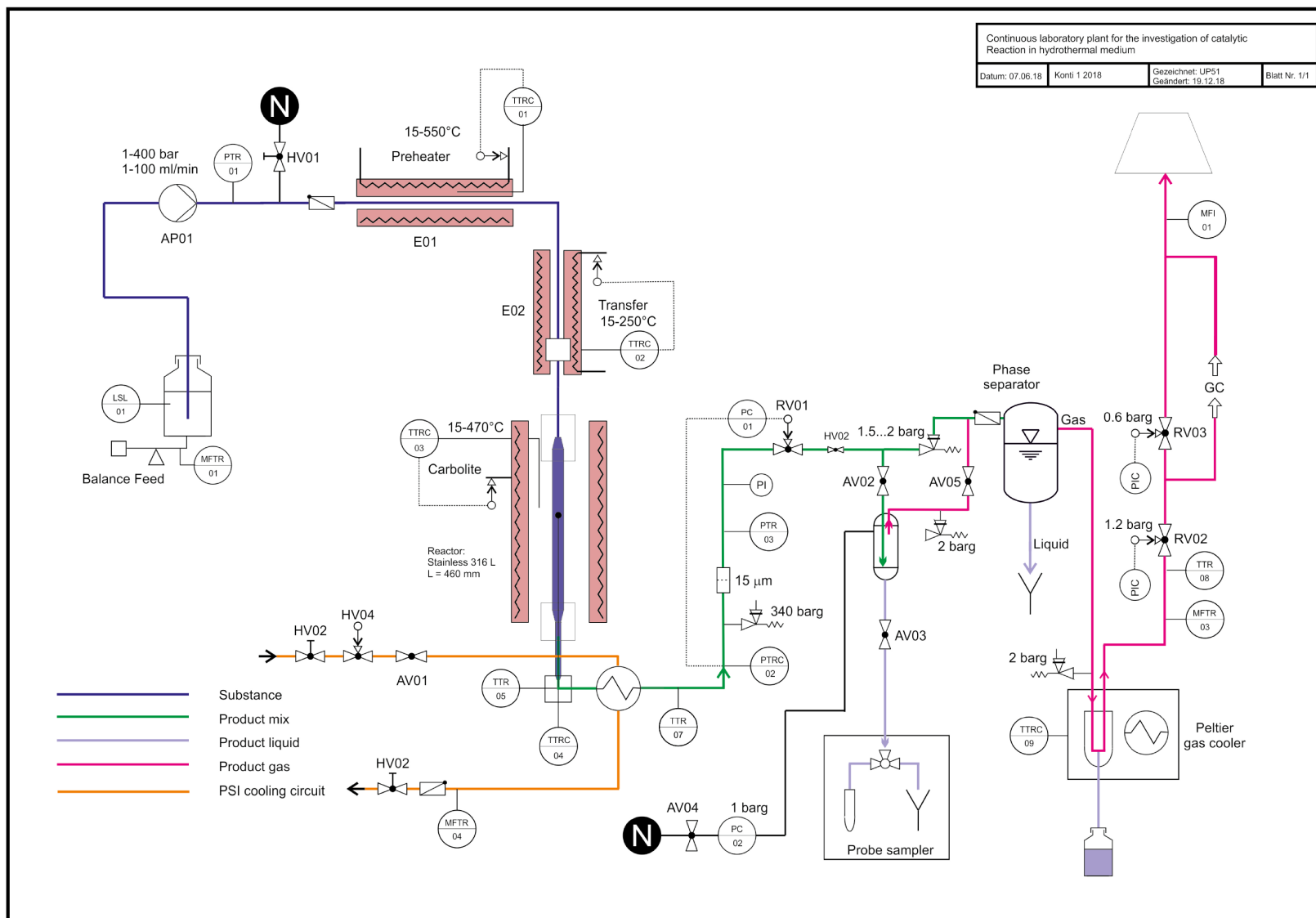
2.5 Continuous SCWG test rigs

2.5.1 Konti-I

The main continuous SCWG setup used during this thesis was named *Konti-I* and was optimised and upgraded from the versions published in previous works [71], [109]. The piping and instrumentation diagram (P&ID) is presented in Figure 2.3. The setup is described below with all of the components referred to as in Figure 2.3.

A DI H₂O tank (for heating, cooling, or flushing) or feed tank (for the reaction) (LSL-01)

was placed on a scale (MFTR-01), which calculated the mass flow rate pumped into the system by the HPLC pump (AP01). A pressure sensor was placed after the pump (PTR-01). A manual valve (HV01) enabled flushing N₂ through the system for drying, before or after experiments. A pre-heater (E01) with temperature control (TTRC-01), followed by a transfer heater (E02) with temperature control (TTRC-02) and eventually the main reactor heater (Carbolite) with temperature control (TTRC-03) heated the pressurised feed to the desired temperature in the reactor. A thermocouple (TTRC-04) placed in a lance inside the reactor allowed monitoring the temperature at different reactor bed heights manually, by sliding the thermocouple upwards and downwards. Another thermocouple (TTR-05) measured the reactor exit temperature. A heat exchanger (in house) cooled the reactor effluent down with cooling water from the building, which was controlled by manual (HV02) and automated (HV04) valves. A flow controller (MFTR-04) was built in as an additional safety measure to ensure that cooling water was flowing during experiments. After the heat exchanger, a thermocouple (TTR-07) monitored the cooled-down reactor effluent, before it entered a 15 µm frit (Swagelok). Pressure sensors were placed before (PTRC-02) and after (PTRC-03) the frit to monitor potential pressure drops due to clogging, in the event of material loss from the catalyst bed. A pressure safety release valve (34 MPa) was placed before the frit. A back pressure regulator (BPR) (Tescom) (RV01) controlled the rig pressure. After the BPR, an automated sampling module could sample at defined time intervals by opening a valve (AV02) and filling the sample tank below (also functioning as phase separator, the gas could exit through another line equipped with a valve (AV05)). After the desired waiting time, vials on the sampling carousel were filled after the valve (AV03) was opened. If the sampling module was not used, the reactor effluent bypassed it and entered the phase separator from where the PW was collected in a tank. The gas then flowed through a Peltier element (temperature controller TTRC-09) to condense the water. A gas flow meter (Brooks) (MFTR-03) and a thermocouple (TTR-08) monitored the generated gas flow and temperature. Two manometers (RV02, RV03) set to 1.2 and 0.6 bar respectively were placed before the µGC and the bypass line. Eventually, both lines flowed through a gas counter (Wohlgroth) (MFI-01), before exiting through the vent.

Figure 2.3 – PID of the *Konti-I* setup (drawn by Pascal Unverricht).

A corresponding picture of the setup is shown in Figure 2.4 with the main units described below:

1. HPLC pump (Knauer 80P), $5\text{--}100\text{ mL min}^{-1}$, 1–400 bar.
2. DI H₂O or feed tank (10 L) placed on a scale calculating the mass flow rate. A suction lance equipped with a level switch was used to protect the pump against air.
3. Carbolite oven controller.
4. Pre-heater.
5. Transfer heater.
6. Carbolite oven (around the reactor).
7. BPR (Tescom).
8. Sample extraction tank ($V_{max} = 150\text{ mL}$).
9. Gas flow meter (Brooks).
10. Phase separator ($V = 160\text{ mL}$).
11. Heat exchanger to cool the reactor effluent (closed-loop building cooling water).
12. Peltier element to condense the water out of the gas stream.
13. Condensate collector.
14. Reactor thermocouple and scale to measure the temperature at different reactor heights.
15. Automated sampling carousel (12 positions).

The *Konti-I* rig was completely automated and controlled by a LabVIEW™ programme. Some screenshots of the different interfaces can be found in Figures A.1 to A.3 in Appendix A. In general, the tubings in high-pressure and high-temperature zones were from SITEC-Sieber Engineering AG, the ones in high-pressure zones only were Swagelok tubings. Prior to each experiment, the stainless-steel (316L) fixed-bed plug-flow reactor (PFR) ($L = 460\text{ mm}$, $d_i = 8\text{ mm}$, SITEC-Sieber Engineering AG) was prepared by filling the catalyst and $\alpha\text{-Al}_2\text{O}_3$ beads (inert filling material) on top (see Figure 2.5). The reactor was then tightly mounted on the setup. A ceramic lubricant paste (Klüber) was applied on all metal-metal connectors to seal the connections and avoid alloying. The reactor was flushed for 30 min (10 g min^{-1}) with DI H₂O (ambient conditions) to remove fine dust particles generated by the filling procedure. The

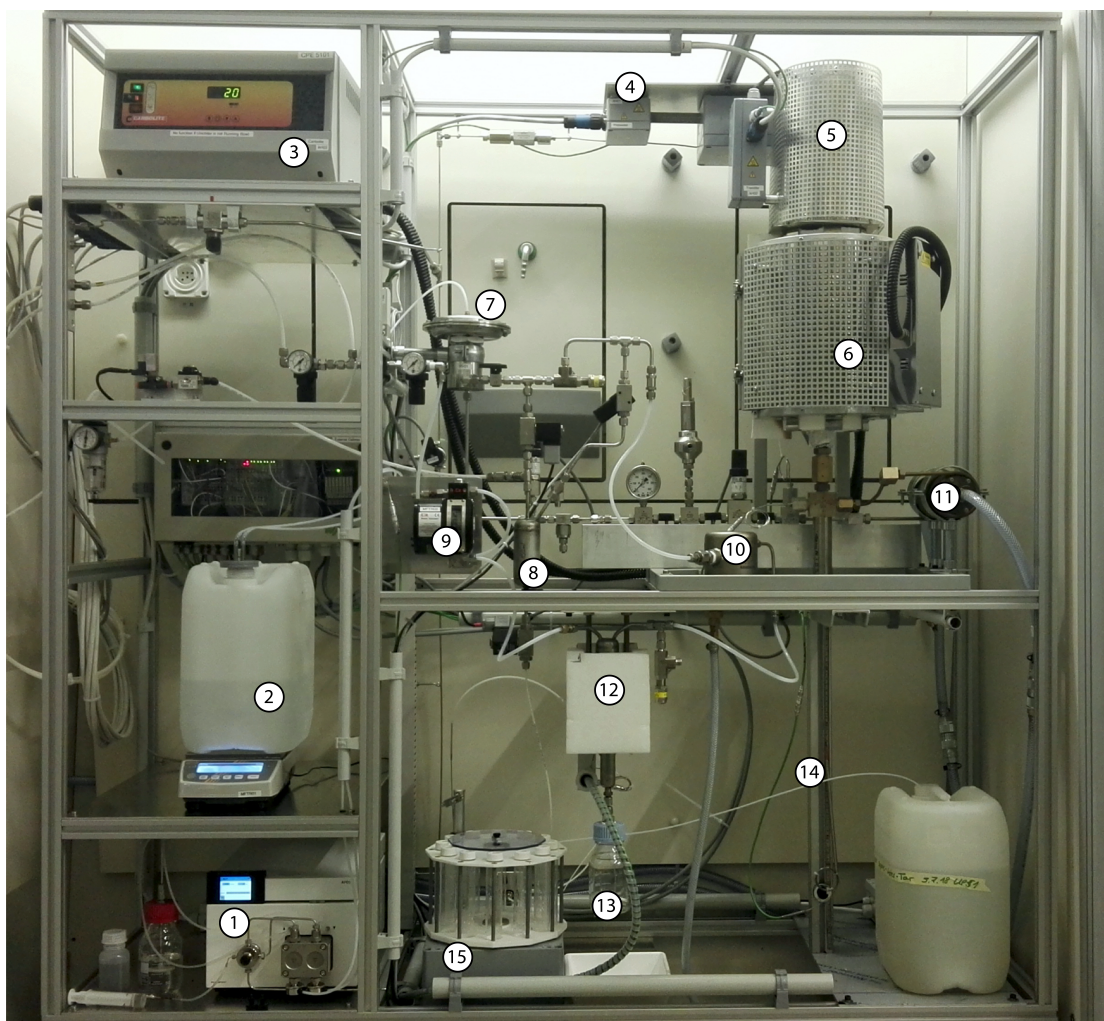


Figure 2.4 – Picture of the lab-scale continuous SCWG rig *Konti-I*.

setup was bypassed before the 15 μm frit to avoid clogging of the frit or damage to the BPR.

Afterwards, the system was first pressurised with DI H_2O and heated up until the reactor temperature at the top of the catalyst bed reached 400 $^{\circ}\text{C}$. The water tank was then exchanged with the glycerol solution and fed into the system, marking the start of the gasification experiment. The heater temperatures were adapted to maintain the desired temperature in the catalyst bed. After 10–15 min, the produced gas built up to 1 bar and gas chromatography (GC) acquisition was started. The autosampler was started with the first sample taken after 20 min with a sampling time of 2 min. The reactor effluent was cooled down by a heat exchanger and flowed through a 15 μm frit before reaching the BPR. After, the depressurised effluent passed the sampling module before reaching the phase separator. From there, the PW was collected to be discarded and the gas flowed through the Peltier element to remove the water.

The gas flow was then measured online with a Brooks gas flow meter (calibrated between 0.3 and 3.0 Lh⁻¹) before reaching manometers set to 1 bar. The gas was split into two lines, one leading to the μ GC and the other bypassing it. Both lines were merged again before reaching the gas counter (Wohlgroth) and exiting through the vent (see Figure A.4). The gas counter had a lower resolution, as an impulse was sent to the LabVIEWTM programme for every 10 L produced. The gas volume was monitored manually during daytime operation to guarantee more precise data.

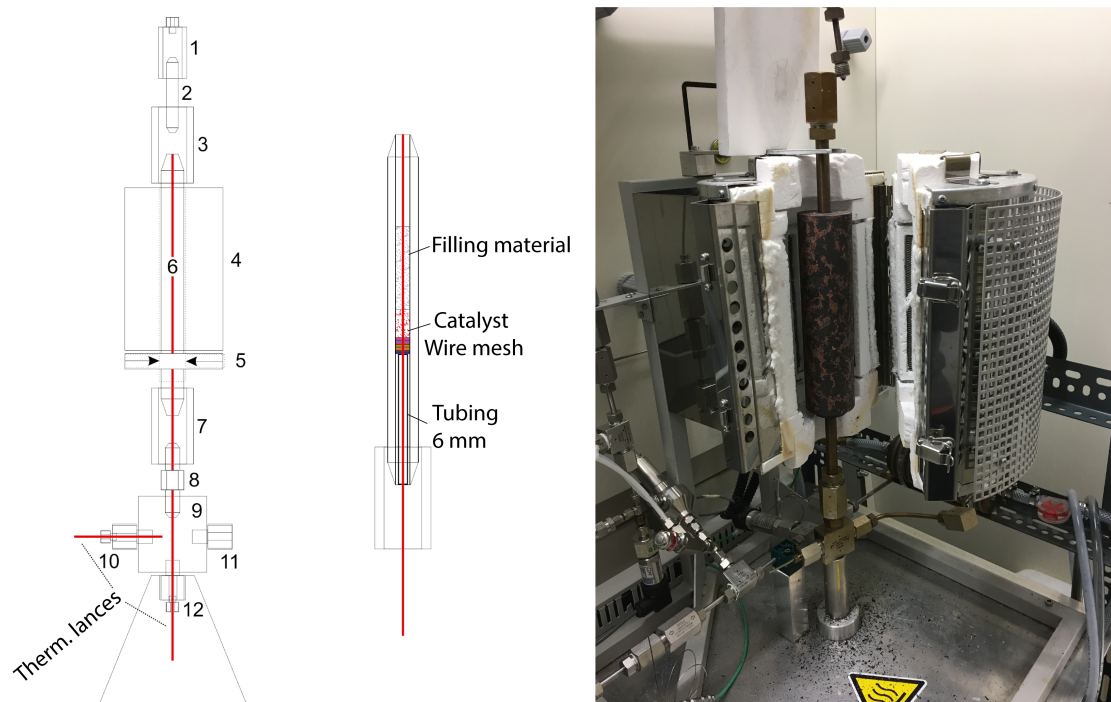
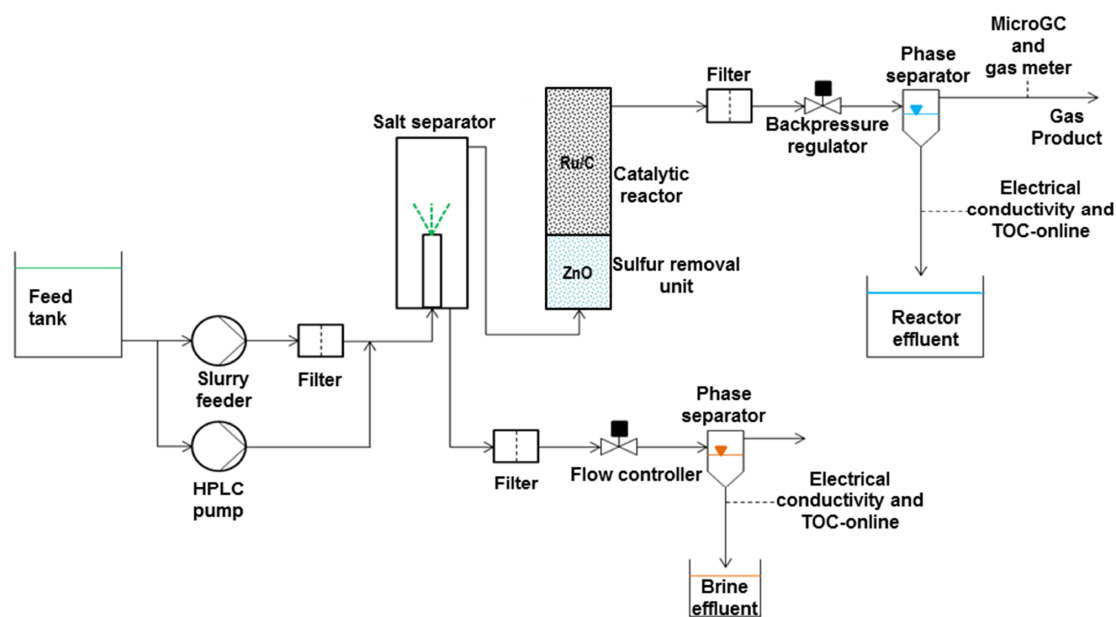


Figure 2.5 – Scheme of the PFR with the different elements (left), and mounted on *Konti-I* (right).



The main difference to the *Konti-I* setup is the presence of a salt separator, developed in our group at PSI [93], [94], and a ZnO-based sulfur absorber bed to protect the catalyst from impurities and sulfur, respectively. For the *intermediate* setup, the reactor used had an inner diameter $i.d.$ = 12 mm and length L = 1435 mm, whereas the *Konti-C* reactor was larger with $i.d.$ = 36 mm and L = 1515 mm. The flow rate for both reactors was set to F = 1 Lh⁻¹.

2.6 Materials

Table 2.2 – Materials and chemicals used throughout this work

Substance	Purity	Supplier
MilliQ H ₂ O	>18 MΩ cm	not applicable (n.a.)
Ethanol	>99 %	Fischer Scientific
Glycerol	85 %	Kuhn AG
Glycerol	99.7 %	Roth
KOH pellets	>85 %	Sigma Aldrich
HNO ₃	Ultratrace grade	Fischer Scientific
Phosphoric acid	85 %	VWR Chemicals
RuNO(NO ₃) ₃	1.5 % (wt/vol)	Alfa Aesar
RuNO(NO ₃) ₃	>31.3 % Ru	Alfa Aesar
RuCl ₃ · xH ₂ O	>38.0 % Ru	Alfa Aesar
Sulfanilamide	>99.0 %	Sigma Aldrich
Sodium borohydride	>98 %	Sigma-Aldrich
CNF	90 %	Nanocyl
AC-A	n.a.	Proprietary
AC-BASF	n.a.	BASF
AC-CGRAN	n.a.	Cabot
AC-H ₂ S	n.a.	Cabot
AC-Spher	n.a.	Dolder
Ru/AC-A	n.a.	Proprietary
Ru/AC-B	n.a.	Proprietary
Ru/AC-BM	n.a.	BASF
α-Al ₂ O ₃	n.a.	Alfa Aesar
m-ZrO ₂	n.a.	Norpro Saint-Gobain
r-TiO ₂	n.a.	Norpro Saint-Gobain
Katalco™ 32-5	n.a.	Johnson Matthey

3 Optimal carbon supports for Ru-based SCWG catalysts

Using activated carbon as catalyst support for Ru is known to be the most active and stable system for SCWG [75], [148]. Although AC is interesting due to its high surface area (SSA), this can also be seen as a drawback. Indeed, the high SSA is mostly generated by the presence of micropores (<2 nm), which are thought to be undesired. Mass transfer limitation for the organics can be an issue as pore blockage induced by carbon deposits can hinder the access to Ru NPs, of which only the smallest could be located in micropores [80]. Also, ACs originate from a variety of sources like renewable biomass (olive stones, coconut shells, wood), peat or coal [149], [150]. The different precursors used can have an effect on the pore structure and mineral content of the final AC. Hence, it is a heterogeneous material (mainly in terms of texture and structure) which contributes to gasification in SCW conditions. This makes it complicated to discriminate between the different effects in SCWG. To get a better understanding, different carbon supports will be analysed and used for SCWG of glycerol in order to look at their intrinsic gasification activity. Selected supports were impregnated with ruthenium to monitor the catalyst activity and stability.

3.1 Carbon support selection

A series of carbon supports were first characterised and then chosen based on their physical properties. The carbons chosen for this study are summarised in Table 3.1. The goal was to have a selection of carbon materials exhibiting completely different properties. AC-BASF is a catalyst-grade support of low ash content and high SSA mainly arising from micropores. AC-Spher is a synthetic AC in the form of small beads made from a resin. AC-CGRAN possesses a high SSA with a considerable fraction of mesopores. AC-H₂S contains significant amounts of iron and is designed for H₂S removal from gas streams.

The supports were then evaluated for their intrinsic glycerol gasification activity as well as

Table 3.1 – Characteristics of selected carbon materials

Support	Ash (%)	SSA	SSA _{MP}	V _p (cm ³ g ⁻¹)	V _{MP} V _p ⁻¹ (-)
		(m ² g ⁻¹)			
AC-BASF	1.8 ± 0.1	1255 ± 115	1172 ± 116	0.60 ± 0.04	0.81 ± 0.02
AC-Spher	0.0 ± 0.1	1329	1260	0.7	0.81
AC-CGRAN	4.1 ± 0.2	1539	1000	1.3	0.62
AC-H2S	41 ± 12	504 ± 80	366 ± 82	0.42 ± 0.03	0.63 ± 0.01
CNF ^a	1.6 ± 0.3	330	5	3.6	0

^a Purified in KOH.

for their coking resistance. Standard experimental conditions were 29 MPa, 400–405 °C, with a 10 wt% glycerol feed pumped at a rate of 5 gmin⁻¹. The concentration of organics was measured in the PWs to determine the conversion. The type of molecule (*i.e.* glycerol or degradation products) was not monitored, since the global carbon conversion was evaluated, regardless of species. All experiments performed within this chapter are summarised in Tables A.1 and A.2. The carbon conversion and the gas flow generated by the experiments are summarised in Figure 3.1. At first, one can see that all ACs exhibited non-negligible initial conversions, with AC-CGRAN being the highest. After the initial decrease in X_C , all samples stabilised to values in the range 0–10 %. AC is known to efficiently catalyse the gasification of organics at higher temperatures (600 °C) in SCW [151], however its effect is limited at lower temperatures as shown here. The gas flow data exhibited the same trend as X_C , confirming that CNF had a very low gasification activity from the start. The large fluctuations in the gas flow data arise from the very low amounts produced, generating larger errors when reading out the gas volume from the counter.

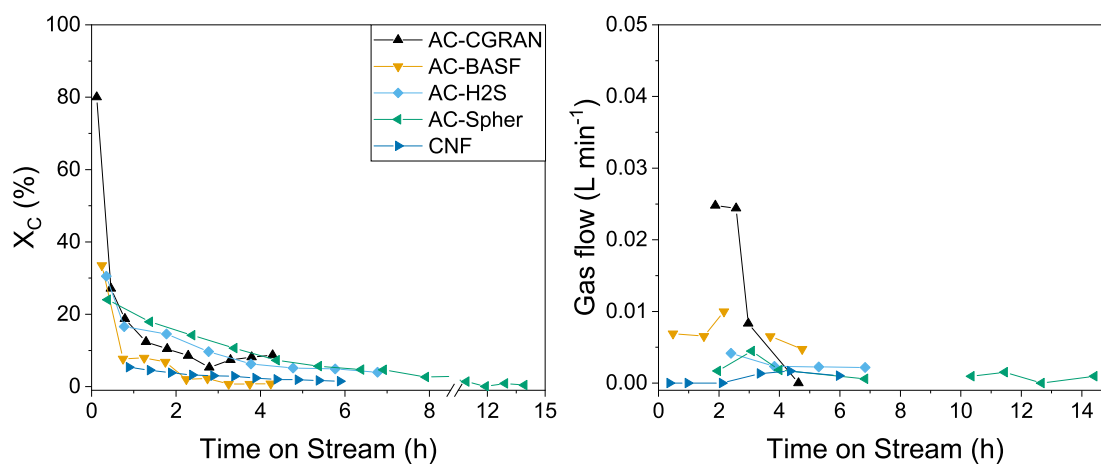


Figure 3.1 – Carbon conversion (left) and gas flow (right) during SCWG over carbon materials.

The rate of carbon conversion was determined at the beginning of the experiment (TOS = 0.3–0.8 h, averaged to 0.5 h) and after TOS = 4 h. The activity of the different carbons significantly dropped (Figure 3.2), as the SCWG activity of AC was reported to arise from its surface functional groups reacting with the feed to produce H₂, CO_x and coke [76]. Physisorption (Table 3.2) and gas composition (Figure B.1) data are in line with these findings, with significant SSA losses due to pore filling/blockage by coke. The highest initial conversion rates were achieved by both AC supports exhibiting a lower fraction of microporosity ≈ 40 %. As the gasification activity could be linked to the surface area, an area-normalised rate was plotted for the different supports in Figure 3.3. The CNF support showed the highest normalised conversion. It must be noted that for the CNF support the mass loaded in the reactor was considerably lower *i.e.* 0.50 g for CNF (because of its lower bulk density), compared to 3.2–4.5 g for the other supports. This might be the reason for these higher values. Furthermore, it is not straightforward to compare CNF to ACs as the surface chemistry and morphology of the material are not the same. For this reason, the focus is set to ACs only. Even normalised by the total surface area in the reactor, the supports exhibiting a more open pore structure (*i.e.* meso- and macropores) had a higher activity. It should also be noted that the high ash content of AC-H2S is mainly due to iron, which can be used as a catalyst in SCWG. The slightly higher carbon conversion rate of AC-H2S compared to AC-CGRAN could be due to the presence of Fe. However, the activity of iron at low temperatures (500 °C) was reported to be low [152]. The gas composition at the end of the experiments reported in Figure B.1 in Appendix B, showed no clear effect from the presence of iron. The methanation reaction was not catalysed by any of the supports, as the CH₄ concentration in the gas stream remained low (4 vol%). The main gases produced were H₂, CO and CO₂ and were thought to arise from the decomposition of glycerol on the support with surface functional groups. Peng *et al.* obtained similar results by gasifying isopropanol over a carbon support exhibiting mesopores ($SSA = 802 \text{ m}^2 \text{ g}^{-1}$, $V_{Ext} = 0.69 \text{ cm}^3 \text{ g}^{-1}$, $V_{MP} = 0.14 \text{ cm}^3 \text{ g}^{-1}$), with initial conversions above 80 % and decreasing down to 12 % after 6 h (remaining constant up to 24 h) [76]. They reported a 90 % loss in SSA and a complete loss of micropores because of carbon deposition from the feed.

N₂ physisorption analyses were performed on spent samples and showed drastic decreases in SSA for carbons exhibiting high microporosity, as highlighted in Table 3.2. Both highly microporous supports lost more than 80 % of their surface area. AC-Spher suffered the highest decrease, mainly because it was run for almost 15 h, compared to the 4–7 h of the other supports. For the supports having some mesopores, the loss in SSA was less pronounced (20–24 %). Although the AC-CGRAN SSA is high and made up of 60 % micropores ($SSA_{MP} = 1000 \text{ m}^2 \text{ g}^{-1}$), its SSA was less affected, suggesting that the presence of larger pores help in avoiding rapid pore blockage leading to a rapid activity loss. However, one can extrapolate that longer times will lead to complete pore filling or blockage of the AC support, independent of pore size as shown by Peng *et al.* [76]. The most striking learning was the inertness and stability

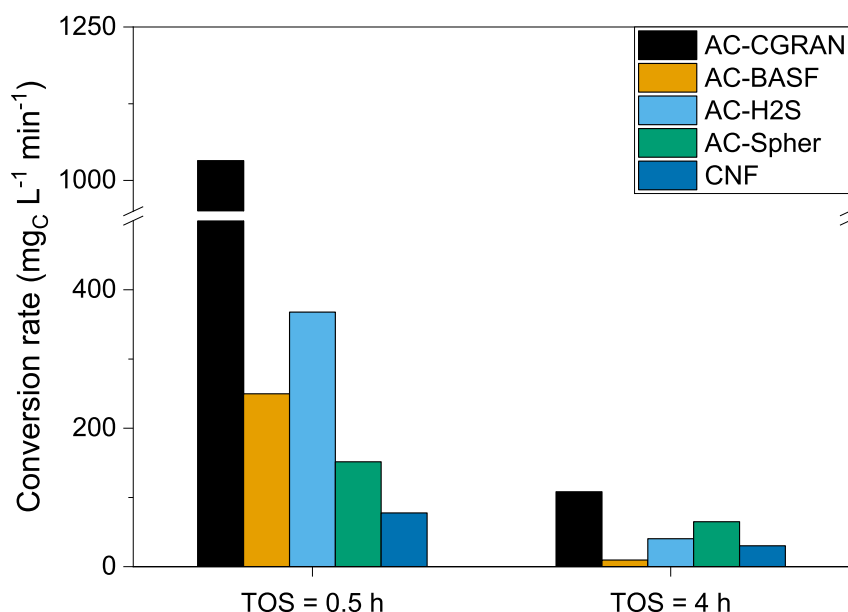


Figure 3.2 – Carbon conversion rate of the different supports at the start and after 4 h of gasification.

of CNF. Due to its completely open structure, no pore blockage occurred and the SSA was almost unaffected (6 % loss). CNF being highly structured materials, there are considerably less defects (surface functional groups) at the surface, thus decreasing the probability of glycerol reacting with the CNF surface. The evolution of the pore size distributions of the supports shown in Figure 3.4 truly highlighted the negative effect of carbon deposition on microporous samples. For all samples, the micropore fraction of the volume decreased (being worst for AC-BASF and AC-Spher) and was slightly shifted towards mesopores. CNF obviously only had a negligible micropore contribution, but the main pore radius mode increased from ≈ 32 nm to ≈ 65 nm. This could be due to minor opening of the CNF, since treatment of multi-walled carbon nanotubes (MWCNT) in SCW (400 °C, 27.6 MPa) can induce tube thinning and opening [153]. On the contrary, de Vlieger showed that the morphology and structure of CNF was unaffected by SCW (450 °C, 25 MPa) after a treatment of 6 h [80]. The higher temperatures and hence lower ion product of the solvent is thought to decrease the degradation of the carbon surface, as the opening is thought to be initiated by H^+ [153].

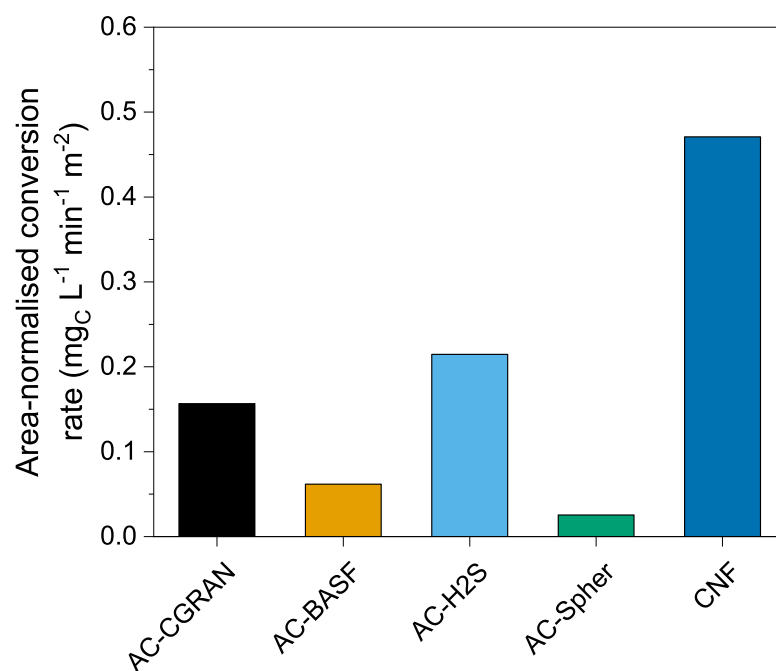


Figure 3.3 – Rate of carbon conversion normalised by the total surface area of the supports loaded in the reactor (TOS = 0.5 h).

Table 3.2 – Surface area and pore volume of the fresh and spent carbon materials used for SCWG of glycerol

Exp.	Support	fresh			spent			ΔSSA (%)
		SSA	SSA_{MP}	V_p	SSA	SSA_{MP}	V_p	
		$(\text{m}^2 \text{g}^{-1})$		$(\text{cm}^3 \text{g}^{-1})$	$(\text{m}^2 \text{g}^{-1})$		$(\text{cm}^3 \text{g}^{-1})$	
S1	AC-BASF	1255	1172	0.6	236	205	0.2	-81
S2	AC-Spher	1329	1260	0.7	100	16	0.1	-93
S3	AC-CGRAN	1539	1000	1.3	1236	791	1.1	-20
S4	AC-H2S	504	366	0.4	445	219	0.6	-24
S5	CNF	330	5	3.6	310	26	3.9	-6

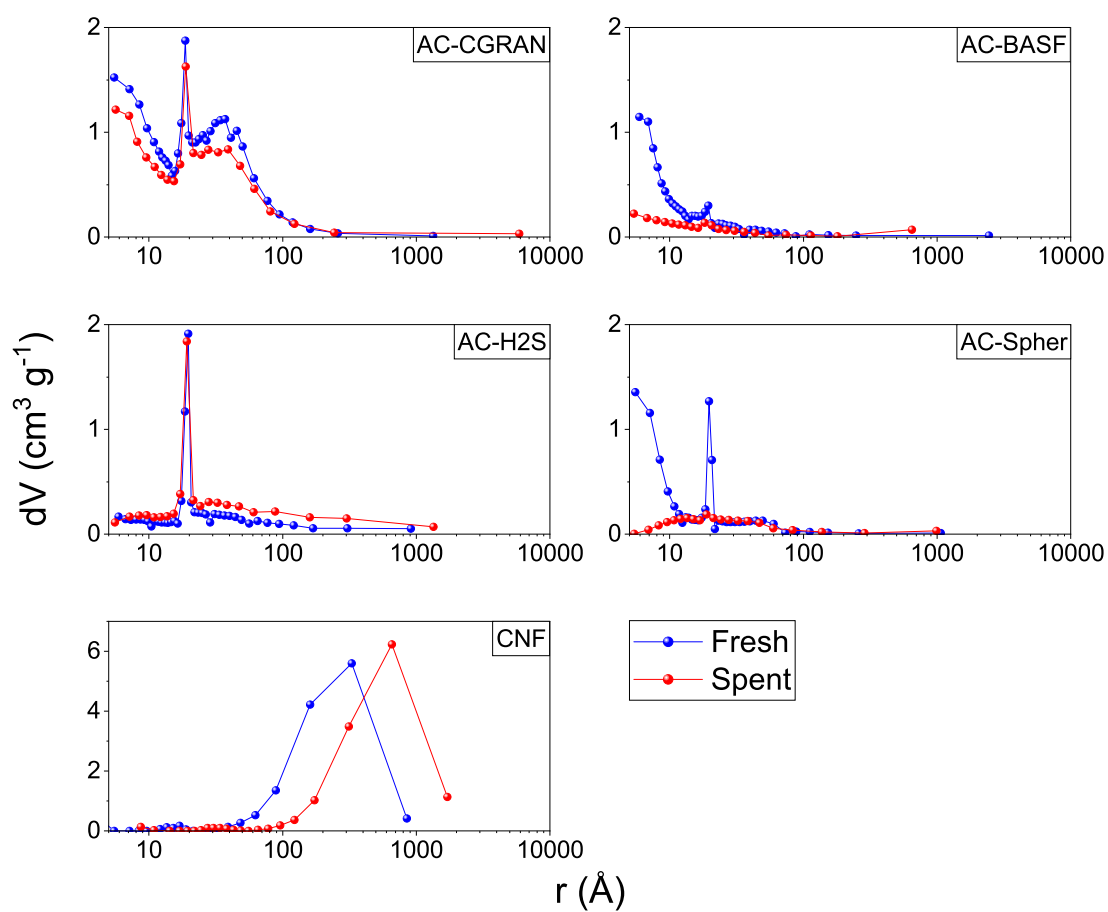


Figure 3.4 – Pore size distributions (differential volume dV as a function of pore radius r) of the fresh and spent (after exposure to 10 wt% glycerol) carbon supports.

3.2 Influence of carbon support on catalyst activity

With a better understanding of the behaviour of carbons during SCWG of glycerol, selected supports were used for impregnation of Ru and their activity was then assessed on *Konti-I*. CNF drew significant interest due to its tendency not to form coke in the presence in glycerol. CNF-supported catalysts had never been used before for catalyst synthesis and catalytic tests on *Konti-I*, hence some stability tests were required beforehand. Sieved CNF (0.50–0.80 mm) were first dispersed in DI water and stirred for 3 h, before being filtered and dried in an oven at 110 °C. Afterwards, the CNF were sieved again and the grain size distribution was measured again as well. This method was applied with three different samples for statistical evaluation. For all three evaluations, 55 % of CNF remained in the same size range (0.50–0.80 mm), the rest was mainly found in the smaller fraction 0.25–0.50 mm. Although the grain size distribution shifted to lower values, it was still encouraging as these grain sizes are compatible with the *Konti-I* reactor. To completely validate CNF as catalyst support to be tested on the continuous rig, 0.6 g support (0.50–0.80 mm) was loaded in the reactor and tested in SCW (400 °C, 28.5 MPa) for 4 h. The support was recovered, dried and sieved as described before. The loaded support mass was completely recovered, showing already a good stability of CNF grains in SCW. Also, 70 % of the grains kept their initial size, whereas 30 % were found in the fraction 0.25–0.50 mm. This confirmed the results from dispersion in water and validated the use of CNF as potential SCWG catalyst on our continuous rig. The surface and porosity properties were also relatively well preserved with a minor decrease in SSA from 330 to 308 m² g⁻¹ and in V_p from 3.6 to 2.7 cm³ g⁻¹, confirming earlier reports on CNF stability [81].

Table 3.3 – Characteristics of the catalysts synthesised on the supports of interest and the benchmark catalyst used as reference

Catalyst	x_{Ru}	SSA	SSA_{MP}	V_p
	(%)	(m^2g^{-1})		(cm^3g^{-1})
Ru/AC-BM	5	1172	1106	0.6
Ru/AC-Spher	5	1196	1130	0.6
Ru/AC-CGRAN	5	1077	604	0.9
Ru/AC-H2S	5	395	292	0.3
Ru/CNF	22	288	24	1.0

The catalysts were synthesised by wet impregnation and reduced in H₂ at 400 °C (300 °C for Ru/CNF for stability reasons). The catalyst characteristics are presented in Table 3.3. Initially, the targeted loading was 5 wt% Ru. It was significantly higher on the CNF support because of its very high pore volume. The synthesis had not been optimised yet at that stage, hence more

solution was required to completely soak the support. For catalytic experiments, 1 g catalyst was loaded in the *Konti-I* reactor (except 0.6 g for Ru/AC-CGRAN), the testing conditions were 400–405 °C and 28.5 MPa.

Figures 3.5 to 3.8 give an overview of the catalyst performances, assessed at different $WHSV_{gRu}$ to investigate their stability. The top part of the graphs show the measured gas composition, the bottom part shows the conversion (X_C , connected by a line for easier reading) and gas flow, when it was possible to accurately measure it (small leaks appeared on the gas line for the Ru/AC-Spher, Ru/AC-CGRAN and Ru/AC-BM experiments). Changes in experimental conditions (*i.e.* $WHSV_{gRu}$) are represented by vertical dashed lines. The horizontal dashed lines represent the thermodynamic equilibrium gas composition for the given species [109].

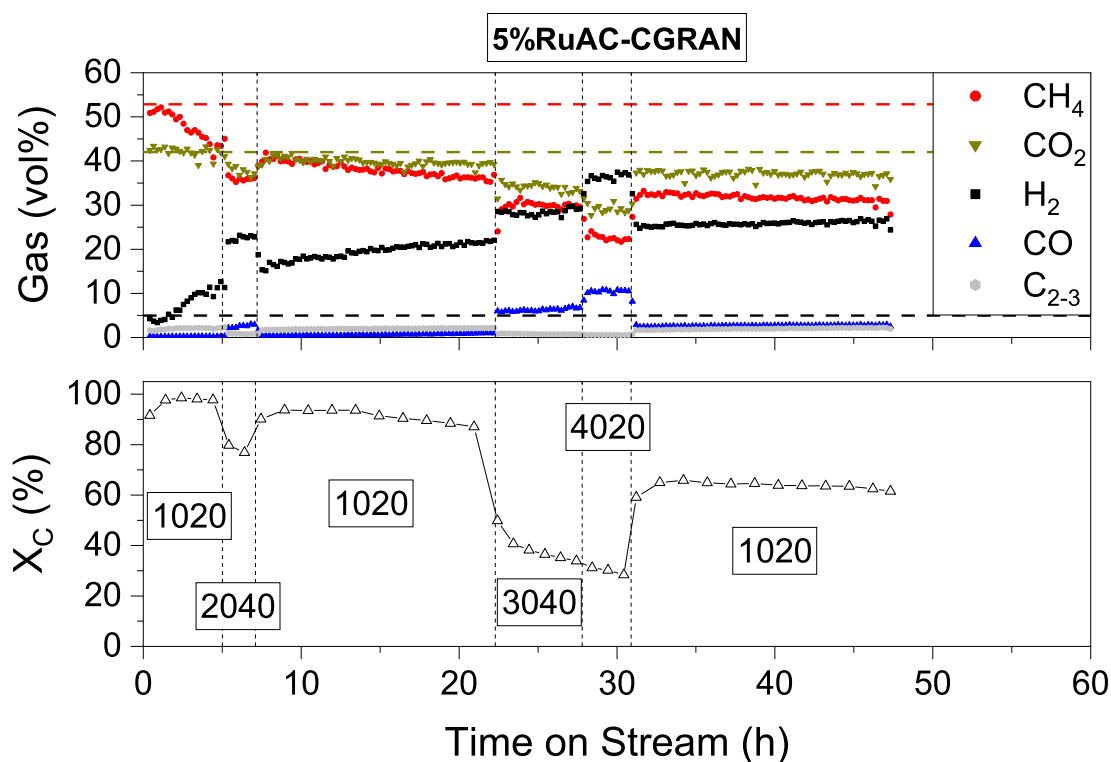


Figure 3.5 – Catalytic testing of 5 %Ru/AC-CGRAN with 10 % glycerol. $WHSV_{gRu}$ ($g_{org}g_{Ru}^{-1}h^{-1}$) is indicated in the boxes (Exp. C3).

All catalysts exhibited good initial activities with total carbon conversion and thermodynamic equilibrium gas composition at moderate $WHSV_{gRu}$ ($\approx 500 g_{org}g_{Ru}^{-1}h^{-1}$). With increasing $WHSV_{gRu}$, X_C began to drop for Ru/AC-CGRAN and Ru/AC-Spher. The former exhibited better stability as the conversion drop started at $WHSV_{gRu} \approx 2000 g_{org}g_{Ru}^{-1}h^{-1}$ compared to $\approx 1000 g_{org}g_{Ru}^{-1}h^{-1}$ for the latter. Furthermore, the decrease in X_C at higher $WHSV_{gRu}$

3.2. Influence of carbon support on catalyst activity

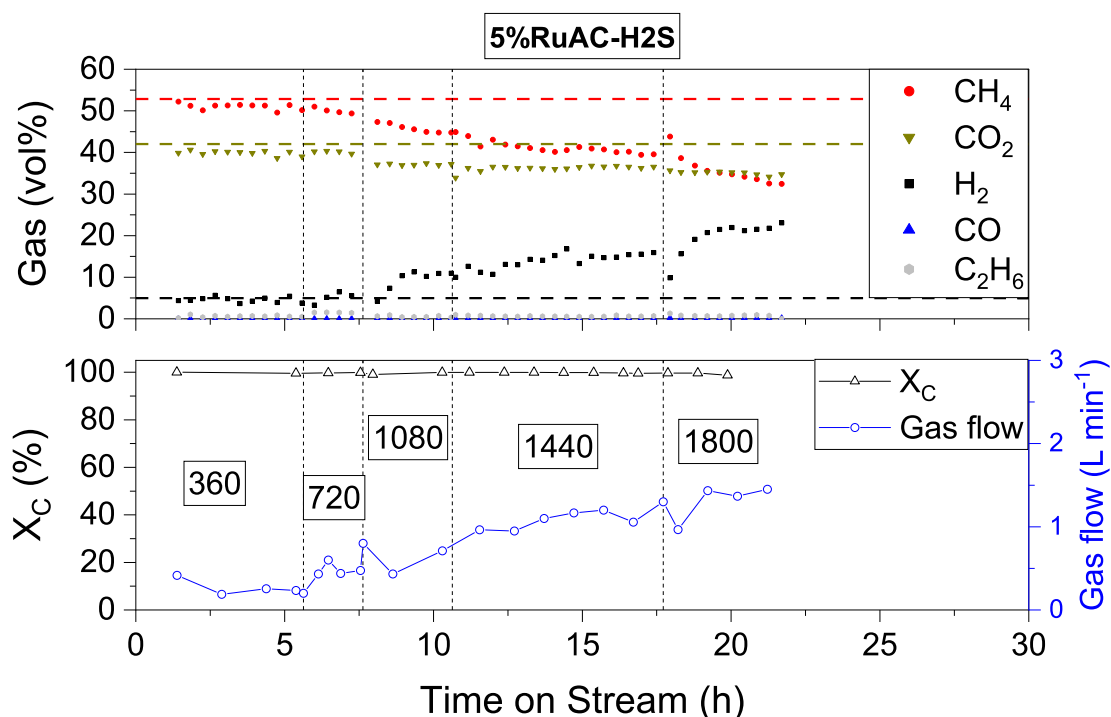


Figure 3.6 – Catalytic testing of 5 %Ru/AC-H2S with 10 % glycerol. $WHSV_{gRu}$ ($g_{org}g_{Ru}^{-1}h^{-1}$) is indicated in the boxes (Exp. C4).

was slower for Ru/AC-CGRAN and it also managed to stabilise to $X_C \approx 60\%$ after having experienced high space velocities. This was not the case for Ru/AC-Spher, for which the conversion rapidly dropped in the last section of testing. Ru/AC-H2S and Ru/CNF also proved to be stable, with changes in gas composition arising at $WHSV_{gRu} \approx 1000 g_{org}g_{Ru}^{-1}h^{-1}$ and the conversion remaining high throughout the experiments. Compared to our commercial benchmark catalyst (Ru/AC-BM, Figure 3.9) used for gasification campaigns at PSI [92], Ru/AC-CGRAN and Ru/AC-H2S showed a better overall stability, although the conversion was not complete for the former and the gas composition shifted from equilibrium for the latter. Ru/CNF was not assessed at high enough $WHSV_{gRu}$ to conclude on its stability. The stability trends of the tested catalysts are in line with glycerol conversion on the neat supports, the ones with less micropores (Ru/AC-CGRAN, Ru/AC-H2S) exhibited better stability.

Physisorption data reported in Table 3.4 show decreases in SSA for all catalysts except Ru/AC-H2S, which surprisingly saw its surface area increase by almost 80 %. Slight increases have been reported in literature after SCWG [76], but nothing of this magnitude. Possible reasons could be the formation of new carbon domains at the catalyst surface generating increased porosity and surface area, however it is unlikely that this was the only reason, as the figures are almost double. Due to its high ash content, some minerals could have been washed out after dissolving in SCW, as the results from glycerol conversion over the neat support

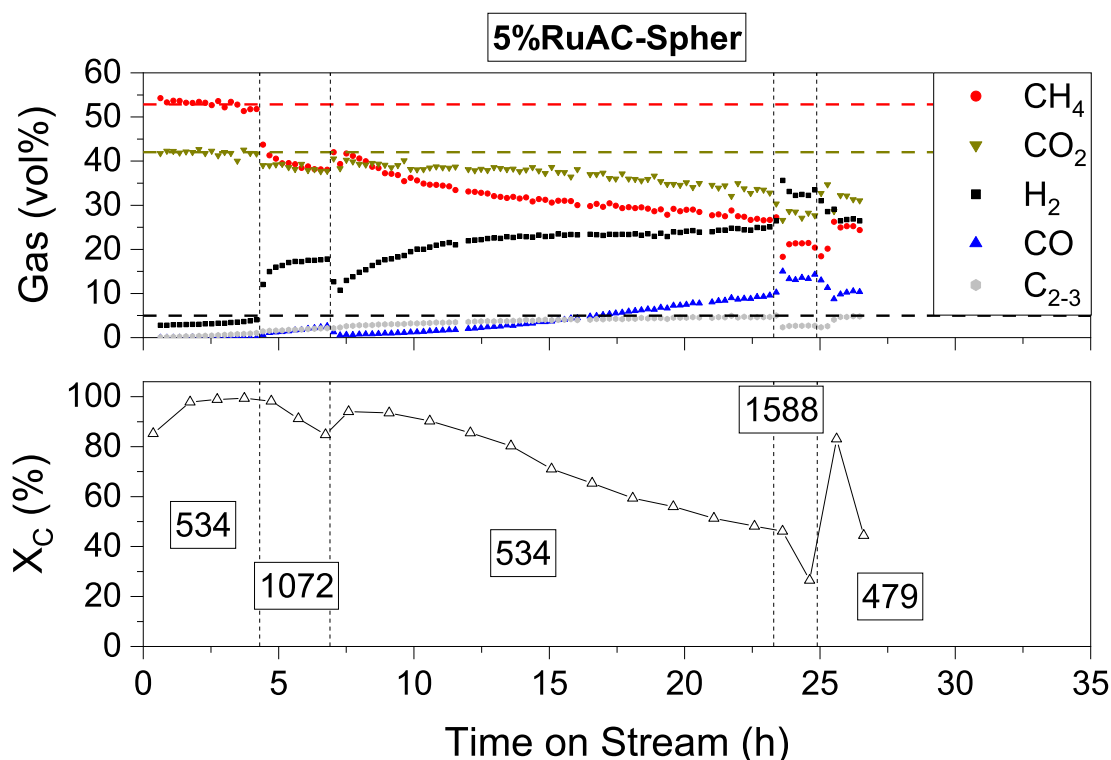


Figure 3.7 – Catalytic testing of 5 %Ru/AC-Spher with 10 % glycerol. WHSV_{gRu} ($\text{g}_{\text{Org}}\text{g}_{\text{Ru}}^{-1}\text{h}^{-1}$) is indicated in the boxes (Exp. C2).

also increased the pore volume (by 35 %, see Table 3.2). Another reason may be the strong sample heterogeneity because of its high ash content. Ru/AC-CGRAN showed limited SSA loss and Ru/CNF showed none. The conversion was high during the Ru/CNF experiment, which led to a lower probability of finding coke deposits. The very microporous Ru/AC-Spher only underwent minor SSA loss although the conversion rapidly decreased during the experiment. One would have predicted a significant surface area loss. Possible explanations to this behaviour could be the pore structure of the synthetic material. The average pore diameter remained constant (2.0 nm) for the fresh and spent Ru/AC-Spher, suggesting that no pore filling/blockage occurred. The presence of Ru NPs blocking the access or completely gasifying the carbon around micropores could be a reason. Compared to Ru/AC-BM, which exhibited a significant loss in SSA, the average pore diameter increased from 1.8 to 2.8 nm, showing a decreased stability of the pore network. The increase in the average pore size could be an indication of micropore blockage, and/or a contribution from deposited coke species. Hence, the AC-Spher prepared synthetically may have beneficial properties towards the inhibition of coke formation, maybe through the homogeneous pore size and purity of the carbon. The difference in surface chemistry (functional groups) from the synthesis may affect the produced gases. Figure B.1 shows that the gas selectivities were similar between AC-Spher and AC-BASF for H_2 , CO , CH_4 , but not for CO_2 , C_2 , C_3 . AC-Spher generated less CO_2

3.2. Influence of carbon support on catalyst activity

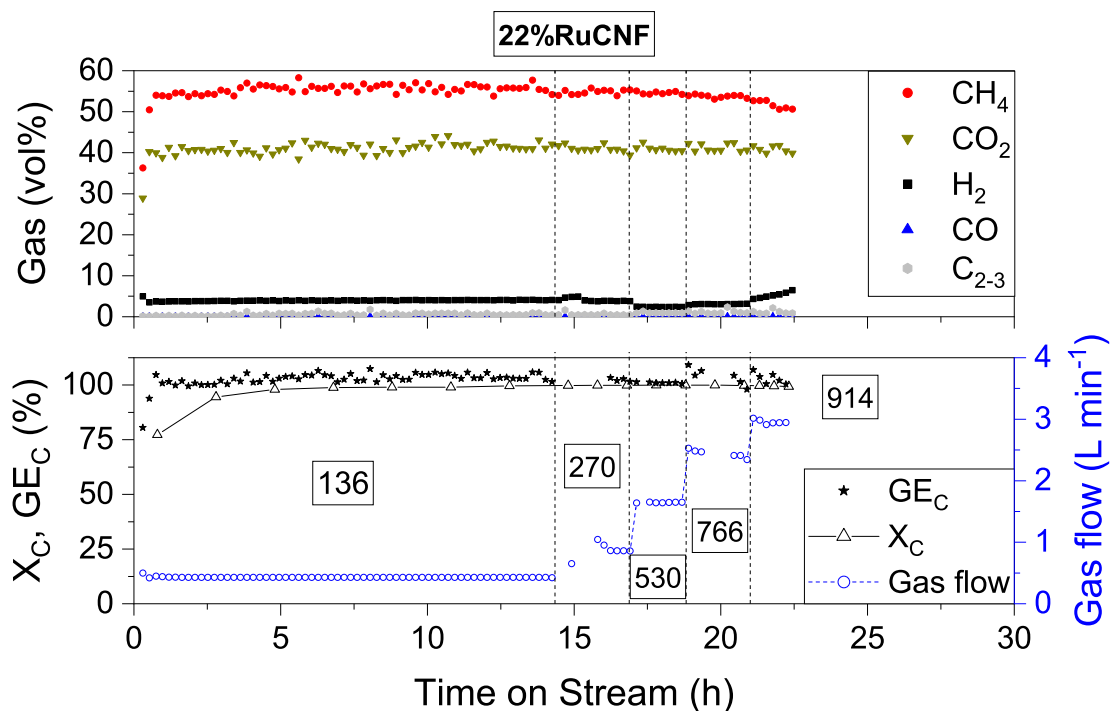


Figure 3.8 – Catalytic testing of 22 %Ru/CNF with 10 and 20 % glycerol (changed at TOS = 17 h). $WHSV_{gRu}$ ($g_{Org}g_{Ru}^{-1}h^{-1}$) is indicated in the boxes (Exp. C5).

compared to AC-BASF, while the trend was opposite for the C_2 and C_3 gases. These figures could indicate a higher decomposition of surface oxygen groups through reaction with the feed molecules, leading to higher concentrations of CO_2 . In analogy, the C_2 and C_3 gases were present in lower concentrations, meaning that they may have reacted further leading to potential carbon deposition. However, the gas composition was similar (at the same X_C) in both catalytic tests with 5 % Ru. Unfortunately, not enough data is available to further conclude on the difference between Ru/AC-BM and Ru/AC-Spher. It must be noted that the measured dispersions D_{CO} for Ru/AC-Spher and Ru/AC-BM were similar (32–40 %), ruling out the effect of particle size on the activity. These results highlight the complexity generated when working with AC-based materials, as many different effects come into play, especially in SCW conditions.

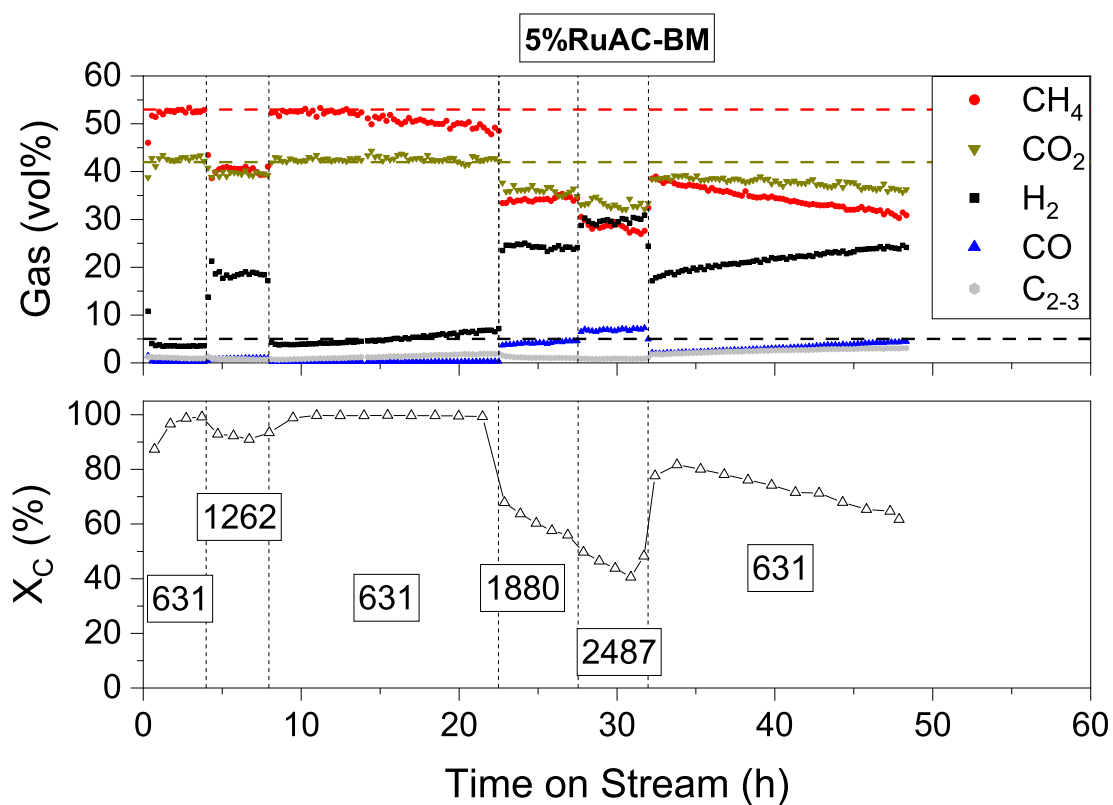


Figure 3.9 – Catalytic testing of 5 %Ru/AC-BM with 10 % glycerol. $WHSV_{gRu}$ ($g_{Org}g_{Ru}^{-1}h^{-1}$) is indicated in the boxes (Exp. C1).

Table 3.4 – Surface area and pore volume of the fresh and spent Ru/C catalysts

Exp.	Catalyst	fresh			spent			ΔSSA (%)
		SSA	SSA_{MP}	V_p	SSA	SSA_{MP}	V_p	
		$(m^2 g^{-1})$		$(cm^3 g^{-1})$	$(m^2 g^{-1})$		$(cm^3 g^{-1})$	
C1	Ru/AC-BM	1172	1106	0.6	605	527	0.4	-48
C3	Ru/AC-CGRAN	1077	604	0.9	882	405	0.7	-18
C2	Ru/AC-Spher	1196	1130	0.6	1112	1047	0.5	-7
C4	Ru/AC-H ₂ S	395	292	0.3	705	511	0.7	79
C5	22 %Ru/CNF	288	24	1.0	287	12	1.3	0

3.3 Summary

Commercial carbon materials exhibiting different properties (SSA , SSA_{MP} , V_p , ash content) were assessed for their suitability as catalyst support for the conversion of glycerol to bio-SNG by SCWG. The carbons were first tested alone for their intrinsic activity in SCWG of glycerol, before being impregnated with Ru and tested for their SCWG activity and stability. The main results are reported below:

- All ACs showed activity in SCWG of glycerol with initial conversions in the range 20–35 % (80 % for the high- SSA AC-CGRAN). The activity then rapidly dropped before stabilising to 1–12 %. CNF was relatively inert with conversions remaining below 5 %.
- Initial conversions normalised by surface area showed two distinct groups, with supports of more open pore structure (*i.e.* less micropores) having a higher initial activity than highly microporous samples. However, the latter group was prone to severe SSA losses of up to 93 %, most probably due to coking. On the contrary, the other group of supports exhibiting smaller fractions of micropores only lost ≈ 20 % of surface area, highlighting the negative effect of micropores.
- The activity of highly microporous carbons was rapidly affected, most probably due to the rapid decrease in SSA . The presence of meso-/macropores may have helped in avoiding complete blockage of the pores, suppressing or delaying a rapid activity loss.
- CNF looked like a promising support, showing good mechanical stability on the *Konti-I* rig, as well as very little absolute gasification activity and a pore structure remaining unaffected by SCWG conditions.
- Ru supported on selected carbon supports showed good initial gasification activities. In a similar trend to the neat supports, microporous samples exhibited rapid decreases in conversion during the accelerated ageing procedure at high $WHSV_{gRu}$. More open structures led to a better stability at similar SCWG conditions.
- Ru/AC-CGRAN seemed to slightly outperform the available benchmark catalyst, with increased stability after ageing at high $WHSV_{gRu}$ and similar CH_4 selectivity.
- Ru/CNF proved to be a very interesting catalyst, sustaining complete carbon conversion up to $900 \text{ g}_{org} \text{ g}_{Ru}^{-1} \text{ h}^{-1}$ and thermodynamic equilibrium gas composition. Also, the SCWG conditions did not alter the catalyst surface area, suggesting that the completely open structure of CNF suppressed or delayed coke formation.

4 Ru loss during SCWG

In this chapter, the stability of the Ru NPs on supports stable in SCW was evaluated with the help of ICP-MS. First, three commercial 5 wt% Ru catalysts were tested for their gasification activity and stability with the aim of replacing our former benchmark catalyst (Ru/AC-BM) which is no longer produced. Potential candidates are Ru/AC-A and Ru/AC-B (both proprietary). In addition to the activity assessment, the collected PW samples were analysed by time-resolved ICP-MS to quantify the Ru loss. The catalysts were tested at different $WHSV_{gRu}$ on *Konti-I* (1 g catalyst) to compare industrially-relevant conditions (*i.e.* thermodynamic regime, $X_C = 100\%$) to kinetic conditions ($X_C \ll 100\%$). Then, the best performing candidate was selected for further testing on a larger reactor (*i.e. intermediate*, 50 g catalyst), where real biomass (sewage sludge) was also gasified. PWs from a gasification campaign on PSI's demonstration unit *Konti-C* were also analysed for their Ru content and compared to the results obtained on the lab-scale rigs. Eventually, the Ru NP stability was compared between the stable catalyst supports used in SCWG by synthesising 2 wt% Ru catalysts on AC, ZrO₂, TiO₂ and α -Al₂O₃.

The results presented within this chapter were submitted and accepted in *Catalysis Science & Technology* as C. Hunston, D. Baudouin, M. Tarik *et al.*, 'Investigating Active Phase Loss from Supported Ruthenium Catalysts during Supercritical Water Gasification', *Catalysis Science & Technology*, 2021. DOI: 10.1039/d1cy00379h.

4.1 Commercial Ru/C catalysts

The benchmark catalyst (Ru/AC-BM) used to perform gasification campaigns on PSI's demonstration unit was no longer produced, which led to the search and validation of a similar catalyst (5 wt% Ru/AC) for future research and development within our group at PSI. The goal

was to use this new catalyst for the HTG pilot plant which was under construction at PSI at the time. The characteristics of the tested commercial catalyst are summarised in Table 4.1 and the different rigs in Table 4.3.

Table 4.1 – Main characteristics of the fresh 5 wt% Ru/AC catalysts

Catalyst	x_{Ru}^a (%)	D_{CO} (%)	$d_{p,CO}^b$ (nm)	SSA ($m^2 g^{-1}$)	SSA_{MP} ($m^2 g^{-1}$)	SSA_{Ext} ($m^2 g^{-1}$)
5%Ru/AC-BM	5.0	32 ± 4	3.6 ± 0.6	1172 ± 8	1107 ± 13	66 ± 15
5%Ru/AC-A ^c	5.3	40 ± 5	2.7 ± 0.5	1145 ± 26	1114 ± 26	31 ± 37
5%Ru/AC-B ^c	5.0	13	9.7	1258	1202	56

^a Metal loadings from the suppliers' product specification.

^b Calculated from D_{CO} [143].

^c Proprietary catalysts, the producer cannot be disclosed.

Measurements for standard deviation estimation – SSA : $n = 3$, $n = 6$ for D_{CO} .

Initial validation experiments were performed in model conditions (glycerol) on the *Konti-I* setup. The experiments performed within this chapter are summarised in Table A.2. Figure 4.1 shows the overview for the former benchmark catalyst Ru/AC-BM. The gas composition is shown in the top part of the graph and the conversion and Ru concentration are reported in the bottom part. The horizontal dashed lines represent thermodynamic gas equilibrium data for 10 wt% glycerol (400 °C, 28.5 MPa [109]). The vertical dashed lines represent the different sections (*i.e.* space velocity) at which the catalyst was evaluated and are defined in the following way:

1. $WHSV_{gRu} \approx 500\text{--}600 \text{ g}_{org} \text{ g}_{Ru}^{-1} \text{ h}^{-1}$
2. $WHSV_{gRu} \approx 1200 \text{ g}_{org} \text{ g}_{Ru}^{-1} \text{ h}^{-1}$
3. $WHSV_{gRu} \approx 1800 \text{ g}_{org} \text{ g}_{Ru}^{-1} \text{ h}^{-1}$
4. $WHSV_{gRu} \approx 2400 \text{ g}_{org} \text{ g}_{Ru}^{-1} \text{ h}^{-1}$

Assessing the catalyst at higher $WHSV_{gRu}$ can be seen as an accelerated ageing procedure and is hence important to verify the catalyst's long-term stability [137]. Figure 4.2 and Figure 4.3 show the performance assessment for both new catalysts. There was a clear activity difference between Ru/AC-B and the two other catalysts, which showed good activity, stability and CH_4 production throughout the experiment. Ru/AC-BM and Ru/AC-A sustained high conversions in sections 1 and 2, whereas the conversion of Ru/AC-B already significantly dropped (65 %) in section 2, most probably due to its low dispersion (13 %). Furthermore, it is important to note that the conversion did not reach 100 % when going back to the lowest $WHSV_{gRu}$. X_C

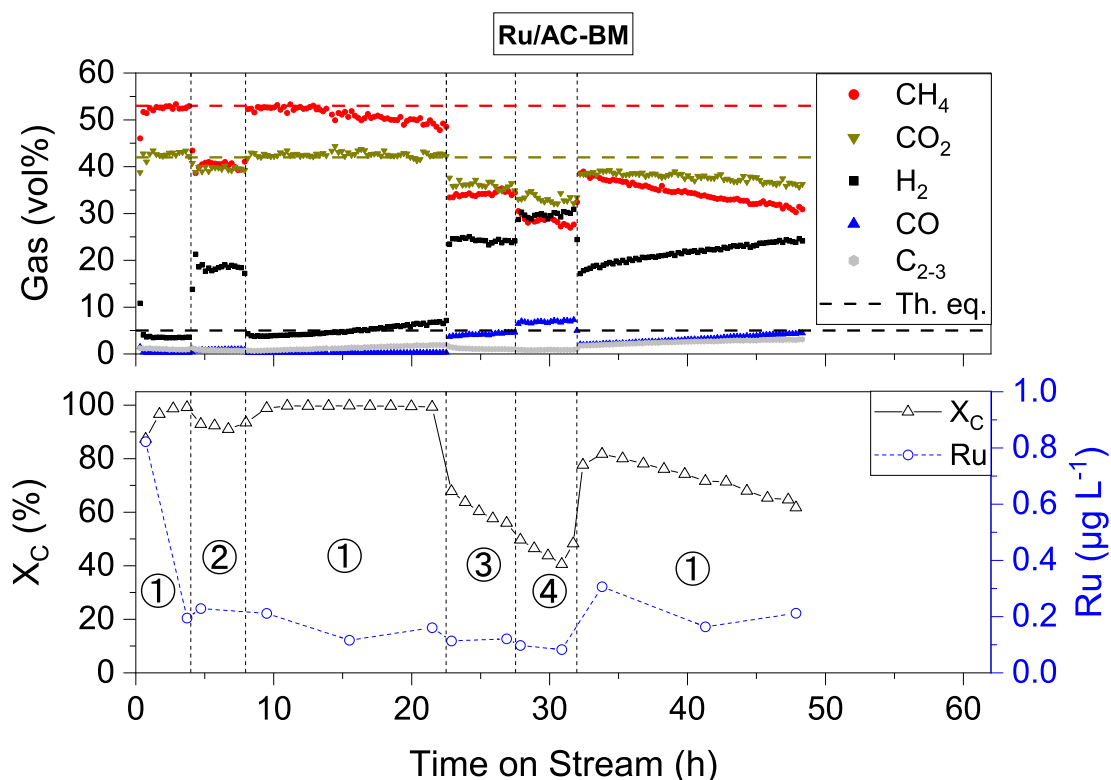


Figure 4.1 – Catalyst testing overview for Ru/AC-BM. The produced gas (top part of the graphs) and both the carbon conversion and Ru concentration (bottom part of the graphs) are shown as a function of the time on stream (Exp. C1).

continued decreasing from this point. Although the conversion was very low for Ru/AC-B in section 4, a pump failure (Figure 4.3, TOS =29–30 h) leading to a rapid increase in density (340 °C, 12 MPa) did not seem to affect the catalyst. On the contrary, Ru/AC-BM and A reached total conversion after sections 2 and 3 respectively, and maintained high conversions throughout the experiment. Ru/AC-A seems more active than our benchmark catalyst, however the loading as well as the dispersion are slightly higher (see Table 4.1) which can explain this difference. The catalyst surface area is a good indicator for coking and was thus measured before and after testing (Table 4.2). Interestingly, only Ru/AC-A managed to resist the loss in SSA, the reason could be the higher conversions throughout the test leading to less carbon deposition.

The Ru quantified (limit of quantification (LoQ) = $0.007 \mu\text{g L}^{-1}$) in the PW exhibited different trends between the different catalysts. A sharp initial decrease is observed for Ru/AC-BM, but the Ru concentration then seemed to stabilise around $0.20 \pm 0.06 \mu\text{g L}^{-1}$. This may mainly be due to the least strongly bound Ru NPs that are washed out when the feed is changed. The concentrations are much lower for Ru/AC-A and B with $0.03 \pm 0.01 \mu\text{g L}^{-1}$ and $0.08 \pm 0.05 \mu\text{g L}^{-1}$,

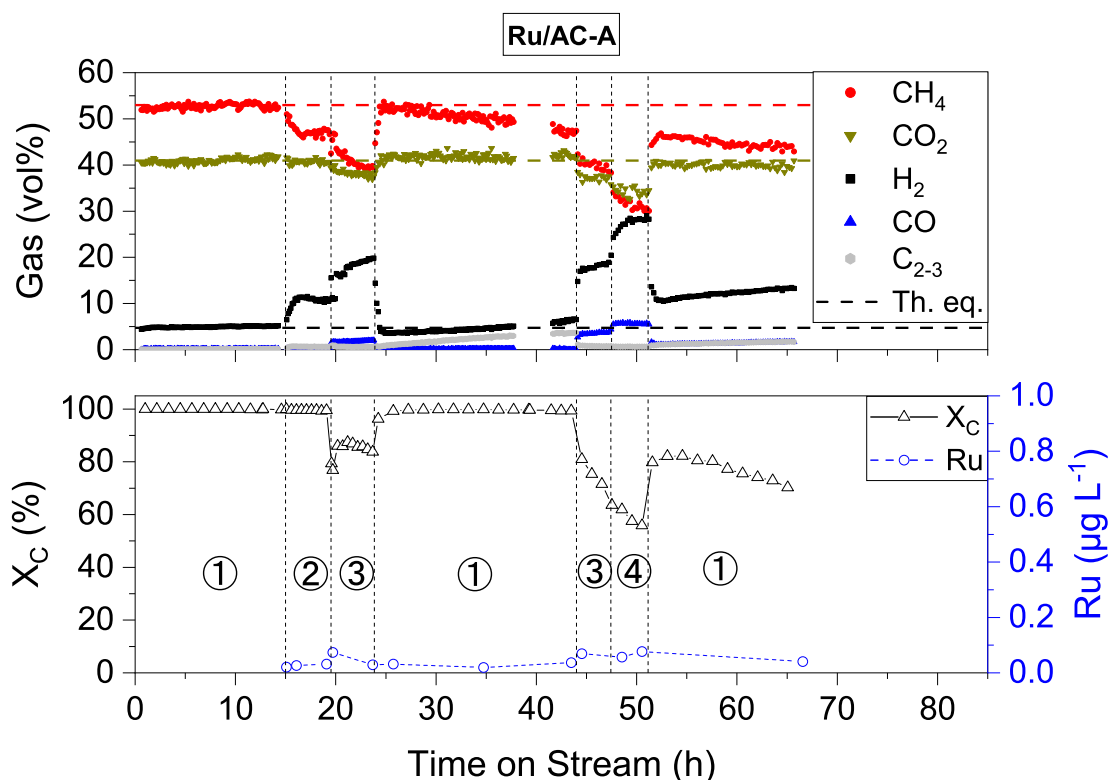


Figure 4.2 – Catalyst testing overview for Ru/AC-A. The produced gas (top part of the graphs) and both the carbon conversion and Ru concentration (bottom part of the graphs) are shown as a function of the time on stream (Exp. C7).

respectively. By normalising the loss to the amount of Ru loaded in the reactor for each experiment, it amounted to 1.2 ± 0.4 , 0.19 ± 0.05 and $0.4 \pm 0.3 \mu\text{g}_{\text{Ru}} \mu\text{g}_{\text{Ru,bed}}^{-1} \text{h}^{-1}$ for Ru/AC-BM, Ru/AC-A and Ru/AC-B respectively. These figures were calculated for section 1 as it was closest to industrial operation. Unfortunately, almost no data has been reported for Ru loss in SCWG. In many publications, leaching is not thought to occur because it is measured by ICP-OES, which is not suited to these very low concentrations. Scarce data exist for nickel however, with Wang *et al.* reporting similar loss trends for Ni during phenol gasification (480 °C, 25 MPa) with O₂ [101]. Initial concentrations were in the range 10–15 mgL⁻¹ and stabilised to 1 mgL⁻¹ after 30 h TOS. For glycerol gasification over a Ni/ α -Al₂O₃ catalyst, Li *et al.* showed initial Ni leaching of 280 mgL⁻¹, eventually stabilising to 10 mgL⁻¹ [102]. It is known that Ni has a higher solubility in SCW than Ru, which is very stable metal [100], [154]. However, the difference in measured metal concentrations is significant, at least 10⁴ times higher for Ni.

The reported metal losses from the catalyst bed could still be active for gasification and hence bias the assessment of deactivation due to active phase loss. However, Ni salts dissolved in H₂O were shown to be inactive [65]. For Ru, losses were reported from Ru/ γ -Al₂O₃ because

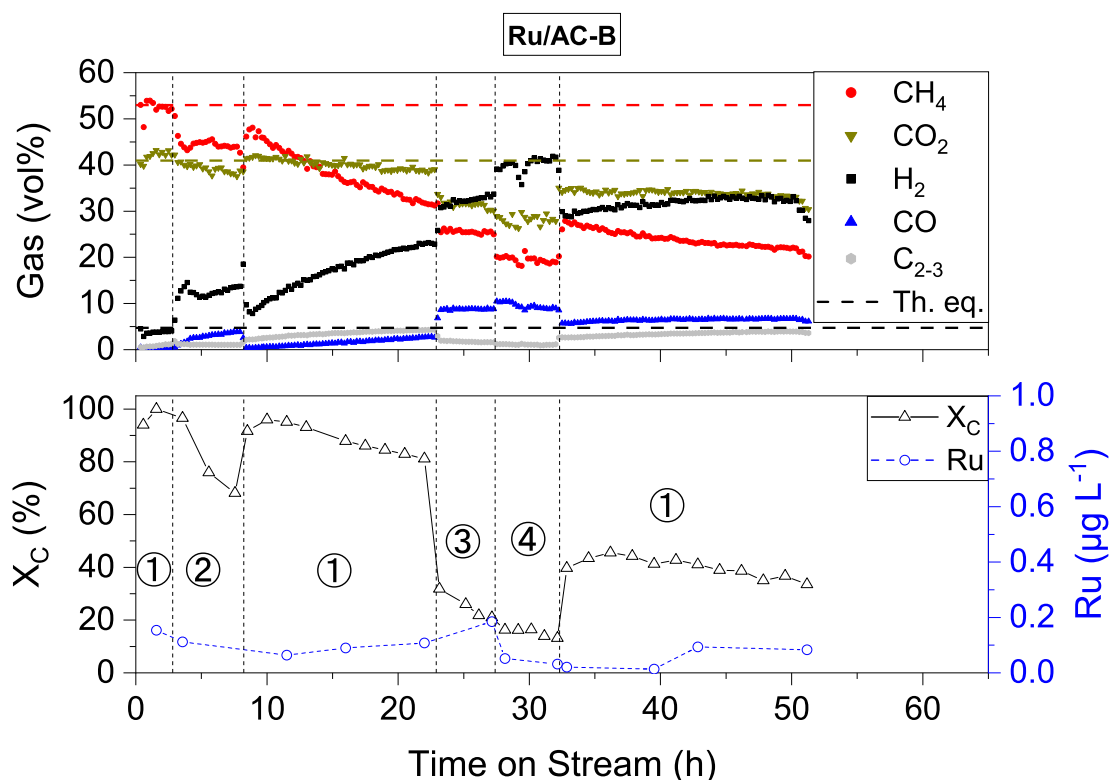


Figure 4.3 – Catalyst testing overview for Ru/AC-B. The produced gas (top part of the graphs) and both the carbon conversion and Ru concentration (bottom part of the graphs) are shown as a function of the time on stream (Exp. C8).

of phase transformation of the support leading to a drastic loss in SSA [73]. The lost Ru (still present in the batch reactor) was not reported to contribute to the gasification activity, as it stopped after 15 min (of a 240 min test. Hence, the reported Ru losses here are not thought to be active for the gasification of organics.

As mentioned previously, the ICP-MS measurements were performed in time-resolved mode because of the very low Ru concentrations. The complete profiles are shown in Figures C.1 to C.3 for Ru/AC-BM, A and B, respectively. The signals were all relatively stable (low RSD) except for two samples which exhibited sudden signal increases. The outliers can clearly be seen in an RSD-concentration plot (Figure C.4). This was most probably due to the presence of Ru particles or agglomerates, as purely ionic solutions exhibit low RSDs (<5 %) as shown with the measured Ru standards (Figure C.5). Unfortunately, no information on the size of the agglomerates can be extracted, as it would require measuring in single-particle ICP-MS mode, as performed by Lee *et al.* for instance [155].

Table 4.2 – SSA comparison between the fresh and spent catalysts after SCWG of glycerol

Catalyst	fresh			spent			ΔSSA
	SSA	SSA_{MP}	SSA_{Ext}	SSA	SSA_{MP}	SSA_{Ext}	
	$(m^2 g^{-1})$			$(m^2 g^{-1})$			
5%Ru/AC-BM ^a	1172 ± 8	1107 ± 13	66 ± 15	605	527	78	-50
5%Ru/AC-A ^b	1145 ± 26	1114 ± 26	31 ± 37	1086	950	136	-5
5%Ru/AC-B ^c	1258	1202	56	621	467	157	-51

^a Exp. C1.

^b Exp. C7.

^c Exp. C8.

Measurements for standard deviation estimation: n = 3.

For the three catalysts investigated, the Ru loss appeared to be different in terms of concentrations, but also in terms of profile as some sudden increases were observed. This was especially the case right after changes in process conditions (feed rate). To better understand the governing mechanisms of ruthenium loss from the support and try to minimise it, further experiments were performed with Ru/AC-A as the new benchmark catalyst for SCWG.

4.2 Effect of process parameters

To understand what governs the loss of ruthenium in SCW conditions, the most relevant process parameters were varied. Temperature, feed concentration and feed rate were systematically varied during SCWG of glycerol solutions over a Ru/AC-A catalyst. The experiments were performed at 29 MPa and at $WHSV_{gRu} = 540\text{--}570 \text{ g}_{org} \text{ g}_{Ru}^{-1} \text{ h}^{-1}$. As it is not easy to vary only one parameter at a time, $WHSV_{gRu}$ was kept constant so that the Ru atoms are exposed to the same amount of organics per unit time. This implied adapting the feed rate when the concentration was changed, and vice-versa. The collected PW was analysed by ICP-MS to quantify Ru and Al too this time, as the filling material ($\alpha\text{-Al}_2\text{O}_3$) may leach and affect the catalyst bed downstream. Figure 4.4 gives an overview of this process parameter screening. Two different catalyst loads were tested, the first one (Figure 4.4, left) was only subject to temperature variations with 10 wt% glycerol, the second one (Figure 4.4, right) experienced temperature changes in SCW, concentration changes (and feed rate) and temperature changes in glycerol again. Al concentration seemed to stabilise around $10 \mu\text{g L}^{-1}$, close to the modelled dissolution equilibrium in SCW ($4 \mu\text{g L}^{-1}$, see Table C.1 [100]). Ru again exhibited sharp decreases after setup restarts and changes in process parameters, however the variations were more pronounced than with Al. Several Ru concentration spikes were observed, which can lead to 100-fold increases in PW Ru concentration. Although the Ru concentration stabilised

after each process parameter change, it remained approximately ten times above the modelled equilibrium data ($0.003 \mu\text{g L}^{-1}$, Table C.1).

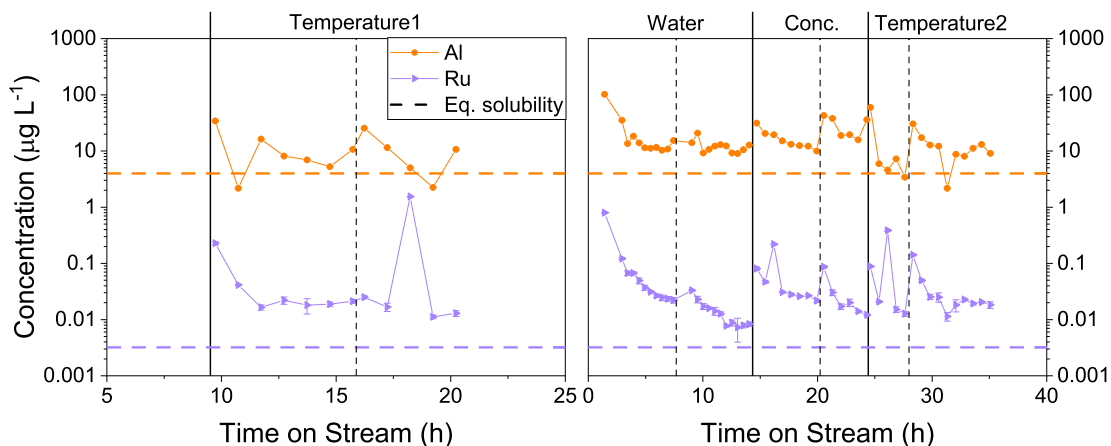


Figure 4.4 – Effect of process parameters on Ru loss from Ru/AC-A catalyst. 1st catalyst load (left, Exp. C9), 2nd catalyst load (right, Exp. C10-C12). Horizontal dashed lines represent the thermodynamic equilibrium solubility of Al and Ru (400 °C, 30 MPa), respectively [100]. A change in the varied parameter is indicated by a vertical dashed line, whereas a full vertical line indicates a complete setup restart.

For the different parameters evaluated, the Ru concentration in the PW stabilised towards similar values *i.e.* $0.01\text{--}0.03 \mu\text{g L}^{-1}$ as shown in Figure 4.5, independent of process conditions. Varying the feed rate also meant changes to the residence time τ and the superficial velocity u_s . However, there were no obvious correlations to the Ru loss (see Figure C.6). It is important to note that the steady-state Ru concentrations were calculated without the contributions of the initial concentration decreases or spikes. In the investigated range of temperature, the density and dielectric constant are known to rapidly decrease, hence one could expect a similar decrease in Ru concentration. This was not the case however, and actually follows the model from Jocz *et al.* predicting constant Ru concentrations over this range [100]. They claimed that the main Ru species present in these conditions is RuO and is not affected by the dielectric constant decrease because it is not ionic. Other ionic species observe this drop in concentration around the critical point. Although the experimental data presented here is one order of magnitude above the modelled concentration, it still remains close as the model is for pure SCW. The effect of glycerol being converted to light gases (CH_4 , CO_2 , H_2) was not taken into account and has an impact on the SCW density [156]. Our experimental data showed the opposite as the Ru concentration was similar in SCW and when converting glycerol. The concentration equilibrium could also be affected by glycerol degradation products forming chelating anions with Ru species. Again, this does not seem to be a valid reason as metal-acetate complexes were shown to undergo decomposition into the corresponding hydroxide and oxide in SCW [157].

The data thus suggests thermodynamically-governed leaching until solvent saturation as main Ru loss mechanism, with minor contributions from Ru NPs. The latter being in the form of support self-gasification by Ru, or through losses of small carbon domains because of friction within the catalyst bed.

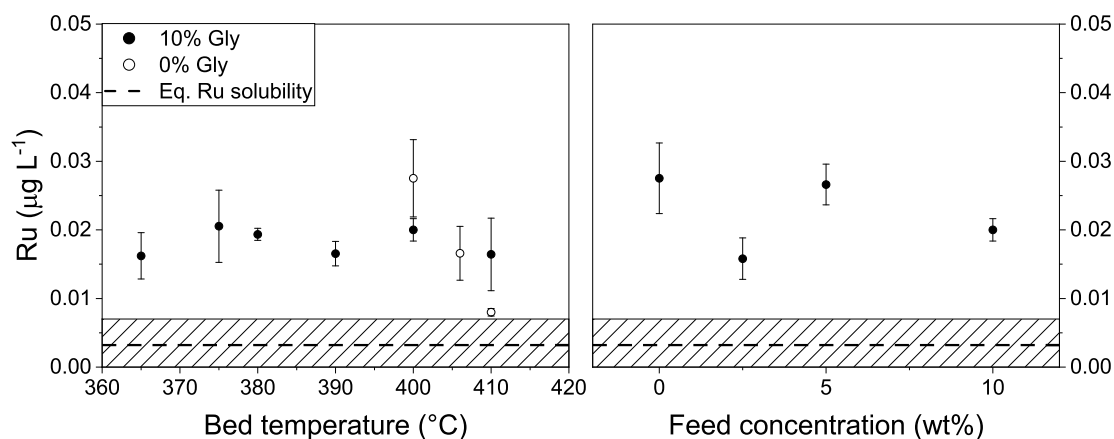


Figure 4.5 – Mean Ru concentration in the process waters for different reaction temperatures (left, Exp. C9,C10,C12) and glycerol concentrations (right, Exp. C11). Hatched area: below Ru LoQ ($=0.007 \mu\text{g L}^{-1}$).

4.3 Intentional pressure and feed variations

The results from the previous section indicated that the Ru loss was generally very low, but some concentration increases spikes could occur. These increases were often recorded after changing process parameters or after setup restarts. The hypothesis was that changes in pressure or feed rate could generate movement within the catalyst bed and lead to friction. As carbon is a brittle material with a relatively low crushing strength ($\approx 10 \text{ MPa}$ [158]), collisions between catalyst grains could lead to the loss of small carbon domains containing Ru NPs.

To confirm this, intentional pressure and feed rate variations (Figure 4.6) were applied on the same catalyst (Ru/AC-A). The quantified Ru was six times higher than the average of the tests performed before as summarised in Figure 4.7. In addition, the frit ($15 \mu\text{m}$) downstream of the catalytic reactor was sonicated in DI H_2O after each set of experiments. The series of experiments prior to the intentional fluctuations ($>250 \text{ h SCWG}$) led to $29 \text{ ng}_{\text{Ru}}$ being quantified in the frit. After the fluctuation control experiment, $298 \text{ ng}_{\text{Ru}}$ were quantified for a TOS of only 4 h. These results emphasised the negative effect of process parameter fluctuations, inducing loss of support domains (presumably through friction) containing Ru NPs. Compared to steady-state Ru concentrations measured in Section 4.2, 95 % of the Ru loss from the fluctuations experiment could be ascribed to a mechanical loss. SEM was performed on the fresh catalyst and the one having experienced fluctuations, but no significant differences in mor-

4.3. Intentional pressure and feed variations

phology were observed (Figure 4.8). A few cracks in some catalyst grains were observed after the intentional fluctuations experiment as shown in Figure 4.9, which could have appeared due to collisions within the reactor. However it must be noted that the observation of cracks was not representative of the whole analysed sample, as only few of them were observed.

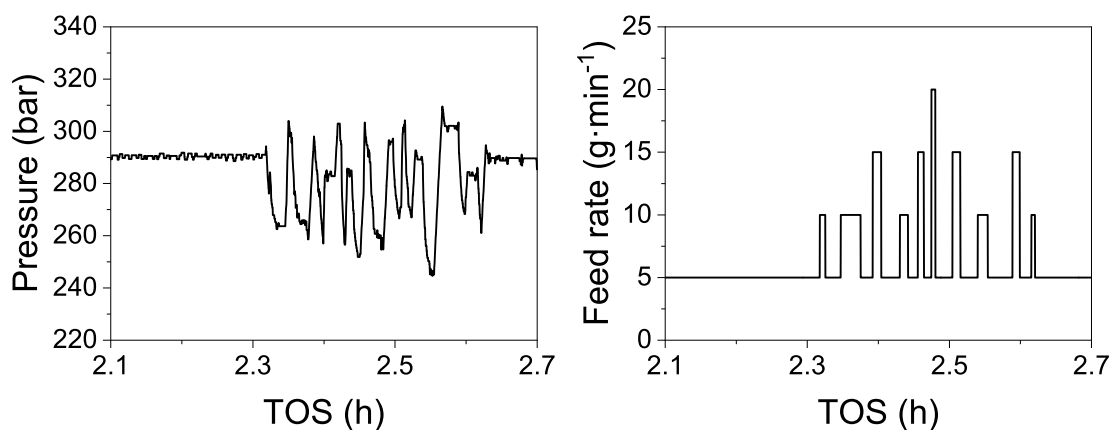


Figure 4.6 – Pressure (left) and mass flow rate (right) variations during the intentional fluctuations test (Exp. C13).

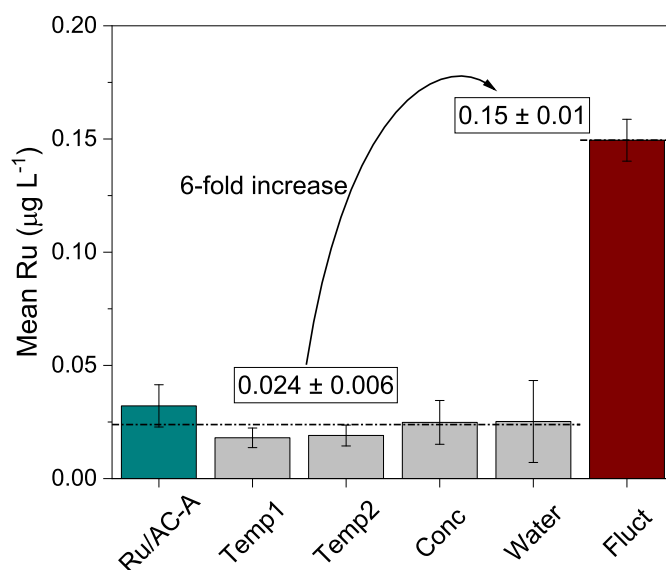


Figure 4.7 – Ru loss comparison between the different process parameters assessed.

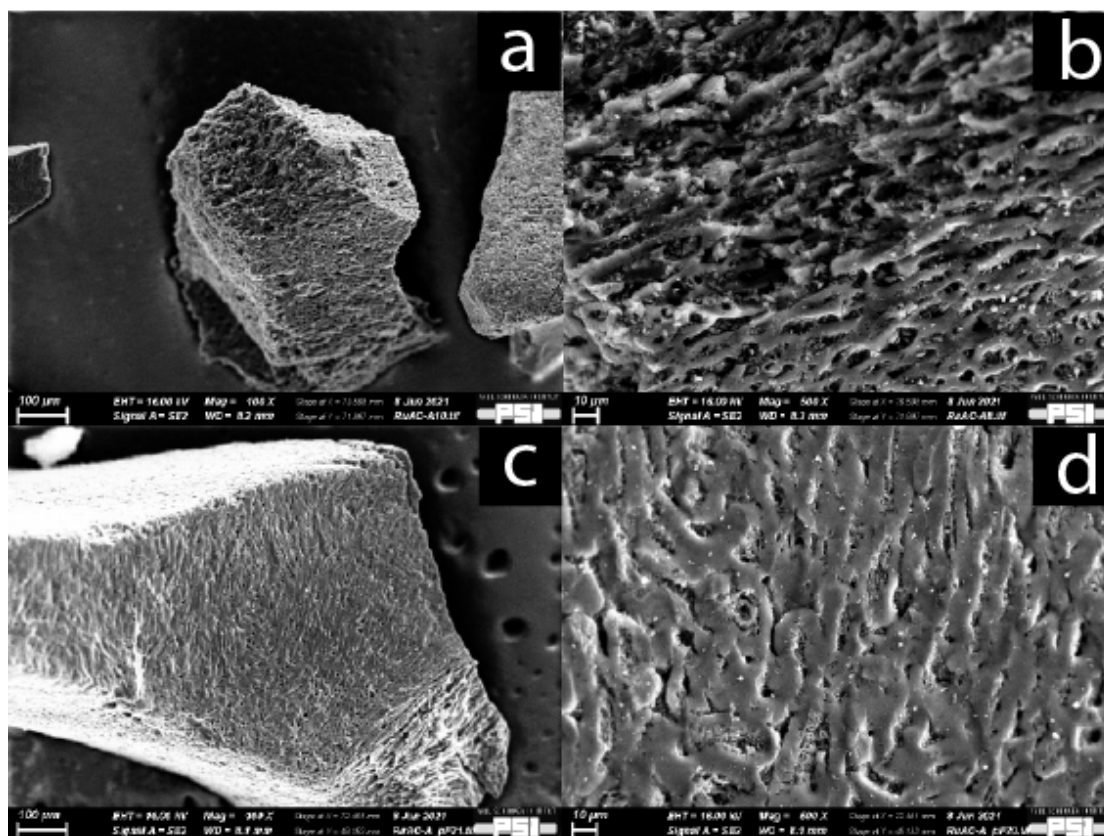


Figure 4.8 – SEM images of the fresh Ru/AC-A catalyst (a: 100x, b: 500x) and spent having experienced fluctuations (c: 100x, d: 500x).

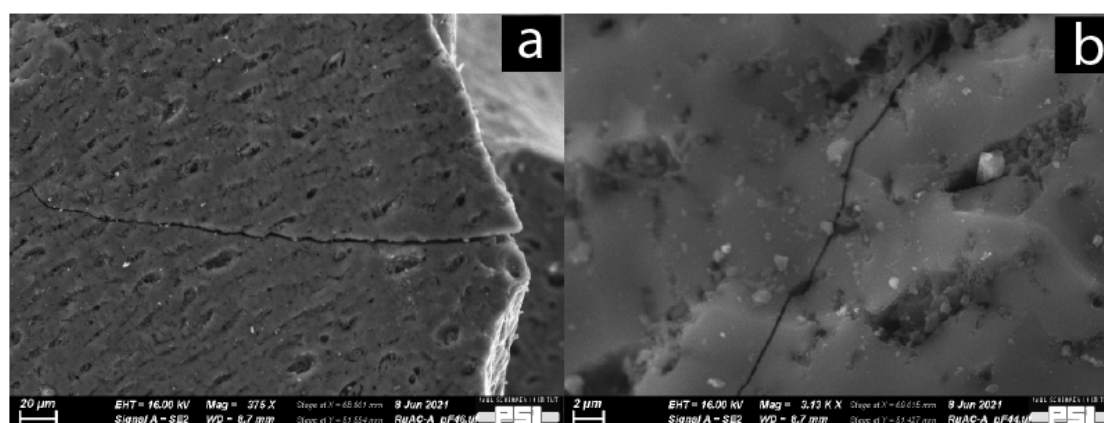


Figure 4.9 – SEM images of the Ru/AC-A catalyst having experienced pressure and flow rate fluctuations (a: 375x, b: 3130x).

4.4 Impact of feed type and setup size

Table 4.3 – Characteristics of the different SCWG setups and main experimental conditions used

Setup	Reactor		Catalyst		WHSV _{gRu}		T (°C)	p _{avg} (MPa)	X _C (%)
	i.d. / L (mm)	F (L h ⁻¹)	mass (g)	grain size (mm)	gly (g _{Org}	SS ^a g _{Ru} ⁻¹ h ⁻¹)			
Konti-I	8 / 460	0.3 ^b	1	0.5 – 0.8	600 ^c	-	400	29	99.9
Intermediate	12 / 1435	1	50	0.8 – 1.25	16	5	400	25	99.9
Konti-C	36 / 1515	1	550	2.0 – 4.0	-	0.4	400 ^c	26	99.9

^a gly = glycerol, SS = sewage sludge.

^b Value at the start of an experiment, before variation (lowest feed rate and $WHSV_{gRu}$).

^c Average between inlet and outlet temperatures, $T_{in} = 390^\circ\text{C}$, $T_{out} = 410^\circ\text{C}$.

Looking ahead towards commercialisation of this catalytic HTG technology, it is important to quantify the Ru loss on larger scales and when exposed to real biomass. To investigate this, Ru/AC-A was tested on the *intermediate* setup (see Table 4.3) with glycerol first (3 h steady state operation), followed by sewage sludge (3 h steady state operation, total solids = 2.6 %, TOC = 11.7 g L⁻¹, TIC = 0.66 g L⁻¹, pH = 6.9). During sewage sludge gasification, there were some pump issues that affected the experiment and is thought to have led to the destruction of the sulfur absorber bed, inducing catalyst deactivation. This is discussed below in Section 4.4.1. Additional PW samples were taken from another sewage sludge gasification campaign on PSI's demonstration unit *Konti-C* for comparison with the acquired data. The Ru loss rates from the different setups are highlighted in Figure 4.10. The gas composition from the conversion of glycerol ($X_C > 99.9\%$) and sewage sludge ($X_C > 99.9\%$) on the *intermediate* setup is shown in Figure C.7. Ru/AC-A showed normalised Ru loss rates in the same order of magnitude, be it for experiments on *Konti-I* or on the *intermediate* setup. Converting glycerol or sewage sludge did not seem to affect the loss rate too much. However, it must be noted that the loss rate doubled between glycerol and sewage sludge on the *intermediate* setup. This could be due to the presence of other organic or inorganic compounds which might change the Ru solubility, or form complexes. Typically nitrates, sulfides and sulfates are strong oxidisers which could lead to increased Ru dissolution, as shown for Ni [159]. Several works reported the formation of stable Ru-S complexes while investigating the sulfur poisoning of Ru-based catalysts [71], [86], [113]. XRD was performed to check whether other phases or complexes formed during sewage sludge gasification. XRD spectra of selected catalyst samples exhibit no phases other than Ru (Ru/AC-BM treated with glycerol). These very small reflections indicate minor NP sintering. Other catalysts showed no sign of phase change or sintering (<4–5 nm). Another encouraging sign is that Ru/AC-A remained stable during treatments with glycerol, during strong process parameter variation and during the conversion of sewage sludge (also after the

poisoning phase!).

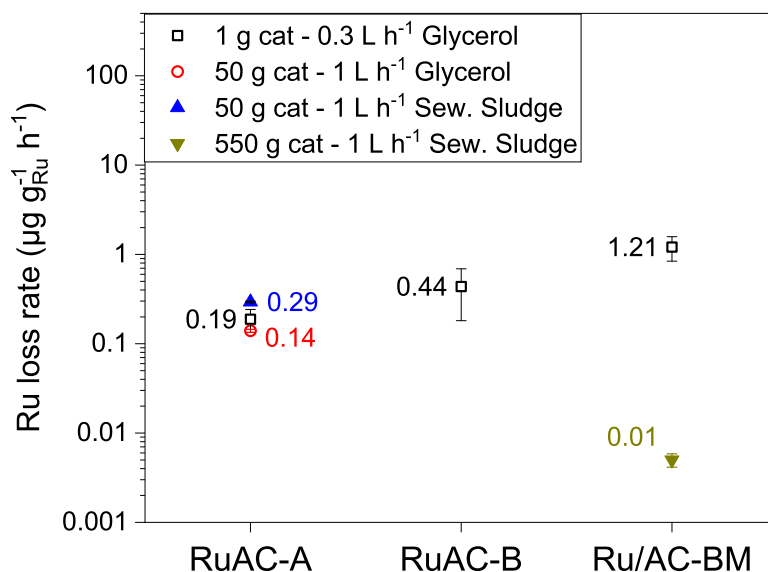


Figure 4.10 – Normalised Ru loss rate for the commercial Ru/AC catalysts on the different SCWG setups. Empty symbols: 10 wt% glycerol (Exp. C1,C7,C8,C14), full symbols: sewage sludge (Exp. C15).

The Ru loss rate of Ru/AC-BM was considerably lower than for Ru/AC-A during sewage sludge gasification. Here, we have to keep in mind the the reactor do not have the same design (height and diameter, see Table 4.3), nor the same amount of catalyst loaded in the reactor. The static pressure from the reactor filling on the lowest part of the bed (calculated with Equation C.1) amounted to 0.002, 0.007 and 0.008 MPa for the *Konti-I*, *intermediate* and *Konti-C* setups respectively, being orders of magnitude below the crushing strength of AC (≈ 10 MPa [158]). The catalyst is thus not expected to be damaged from this. However, small pressure and flow variations can lead to increased Ru loss as shown in Section 4.3, even though the experiment ran smoothly. The static pressures on the catalyst bed were similar for the *Konti-C* and *intermediate* setups, but the Ru loss was higher on the latter setup. To take the different reactor designs into account, the Ru loss rate was plotted as a function of catalyst bed aspect ratio $H_{cat}d_R^{-1}$. Figure 4.12 shows an increase in Ru loss rate as a function of $H_{cat}d_R^{-1}$. This can be explained by higher collisions forces in reactors of larger $H_{cat}d_R^{-1}$ caused by small vertical movements in the catalyst bed, which in turn lead to additional friction and attrition between the catalyst grains.

The Ru loss did not correlate to the feed rate (F), residence time τ or superficial velocity u_s . Furthermore, no correlation was observed between the Ru loss and the amount of catalyst (*i.e.* Ru) loaded in the reactor. This is a strong indication that leaching was the main loss mechanism at steady state.

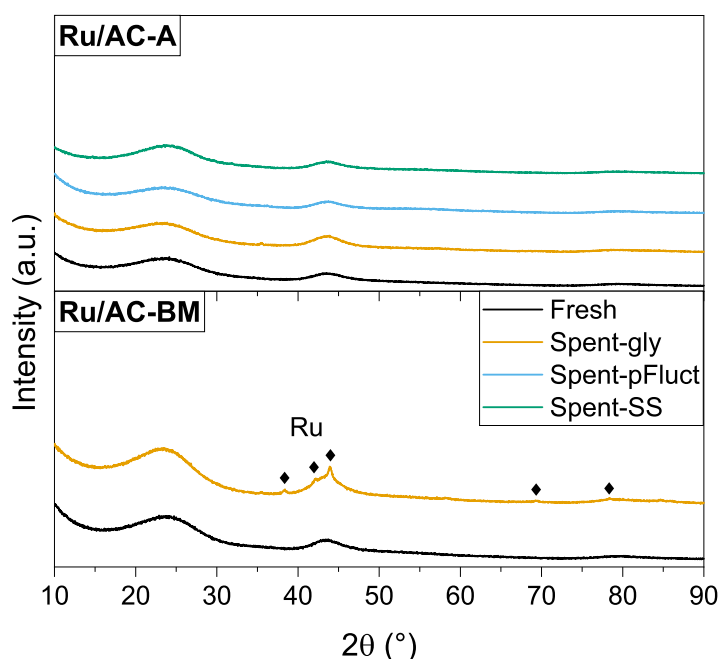


Figure 4.11 – XRD spectra of fresh and spent samples of Ru/AC-A (top) and Ru/AC-BM (bottom). Spent-gly (Exp. C1,C7) and Spent-pFluct (Exp. C13) refer to catalysts treated with glycerol on *Konti-I* in normal operation and during the deliberate fluctuations test, respectively. Spent-SS refers to the experiment on the *intermediate* setup with sewage sludge (Exp. C15).

AC is known to be a stable support in SCW conditions, however it remains a brittle material and can lose some carbon domains through collisions or friction if there are some strong flow or pressure fluctuations. Although the quantified Ru loss was very low for AC-based catalysts, it was compared to metal oxides (Section 4.5) which remain stable in SCW, to see whether these supports could further decrease the Ru loss.

4.4.1 Sewage sludge gasification on the *intermediate* setup

Several issues were encountered during the gasification experiment on the *intermediate* setup. The whole run is summarised in Figure C.7. First, pumping the sewage sludge feed sieved at 0.5 mm did not work well because the check valves constantly got clogged with accumulated particles. For this reason the feed was sieved down to 0.25 mm, which solved the pumping problem. The second issue was a pump failure during night operation with water only. This led to a significant temperature drop ($T_{min} = 196\text{ °C}$) and pressure loss ($p_{min} = 9\text{ MPa}$). When wanting to continue the test on the following day, the PW had a yellowish colour and a bed smell (sulfur-containing compounds). The methane composition was much lower compared to the stable 3 h section the day before, *i.e.* $\approx 10\%$ vs. $\approx 30\%$. Furthermore, the concentration of

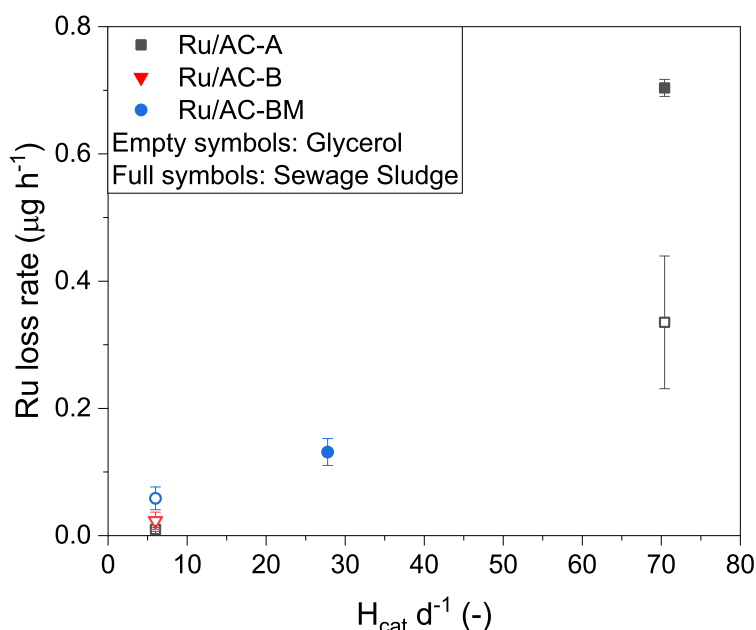


Figure 4.12 – Ru loss rate as a function of catalyst bed aspect ratio $H_{cat}d_R^{-1}$. Empty symbols: 10 wt% glycerol, full symbols: sewage sludge.

C_2 and C_3 gases increased, indicating that the catalyst was not able to break down the organics. However, the CO composition remained low which is unusual when deactivation occurs. Also, a peak started to appear at the H_2S retention time of the μGC , but the compound was not calibrated and thus not quantified. The hypothesis was that the sulfur trap protecting the catalyst bed did not survive the "steaming" phase that occurred because of the pump failure, leading to poisoning of the catalyst. Saturation of the sulfur absorber by the sulfur present in the feed was ruled out, as only 0.8 g S were fed through the system before the pump failure and the absorber bed has a theoretical capacity of 10 g S, supposing a S:ZnO ratio of 1. The catalyst bed was recovered from the reactor and separated into five fractions of similar quantities (fraction 1 being at the reactor exit, fraction 5 being right after the sulfur absorber bed). CHNS analyses Figure C.8 showed that sulfur was present in similar amounts for all fractions of the spent catalyst bed *i.e.* 0.78 ± 0.04 wt% whereas the fresh catalyst had 0.09 ± 0.01 wt% S. These results strongly suggest that the ZnO-based sulfur trap did not survive the pressure loss, hence poisoning the catalyst bed downstream when the experiment was restarted. Nitrogen was also observed in larger concentrations. The SSA of the recovered catalyst fractions was also evaluated and showed a significant decrease along the flow direction in the reactor (Figure C.9). Interestingly, the quantified Ru from the "poisoned" PW was in the same range as for the fully active catalyst ($0.77 \mu\text{g L}^{-1}$ vs. $0.71 \mu\text{g L}^{-1}$, respectively), suggesting that the change in chemistry around the catalyst did not affect Ru leaching.

4.5 Ru loss from metal oxide-supported catalysts

AC was compared to m-ZrO₂, r-TiO₂ and α -Al₂O₃ to see if Ru supported on metal oxides exhibited a better stability. For this set of experiments, the catalysts were synthesised in-house with a target loading of 2 wt%. The loading was decreased because of the very low pore volume and surface area of titania and alumina. The characteristics of the synthesised catalysts are reported in Table 4.4.

Table 4.4 – Characteristics of the in-house 2 %Ru catalysts and experimental conditions

Exp.	Catalyst	x_{Ru}^a (%)	D_{CO} (%)	$d_{p,CO}^b$ (nm)	SSA ($m^2 g^{-1}$)	SSA_{Ext} ($m^2 g^{-1}$)	$WHSV_{gRu}$ ($g_{Org} g_{Ru}^{-1} h^{-1}$)
C16	2%Ru/AC	2.30	62	1.6	1354	136	1370
C17	2%Ru/ α -Al ₂ O ₃	1.74	2.5	52	6.6	5.7	1511
C18	2%Ru/TiO ₂	1.74	1.3	104	4.5	3.7	1724
C19	2%Ru/ZrO ₂	1.80	40	2.6	27	22	1604

^a Loading determined by Ru mass balance.

^b Calculated from D_{CO} according to [53].

The results are summarised in Figure 4.13, showing the Ru concentrations in the PW for all four catalysts (left) and the conversion, Al and Ru concentrations for the 2 %Ru/AC catalyst (right). Individual graphs for the metal oxide-based catalyst are shown in Figures C.10 to C.12. $WHSV_{gRu}$ was set to $\approx 1500 g_{org} g_{Ru}^{-1} h^{-1}$ to hopefully observe some conversion loss for the Ru/AC catalyst. However this did not work, as the AC-based catalyst managed to fully convert the feed over more than 20 h at $WHSV_{gRu} = 1370 g_{org} g_{Ru}^{-1} h^{-1}$. The space velocity was lower than for the other catalysts because of the higher Ru loading. The Ru loss was significantly higher from the metal oxide-supported catalysts, stabilising around $1 \mu g L^{-1}$ compared to $0.04 \mu g L^{-1}$ for Ru/AC. The latter concentration is again in the same range as for the commercial 5 %Ru/AC catalysts investigated in Section 4.1. In terms of normalised loss rates, they reached 10.3 ± 3.7 , 24.3 ± 5.6 and $10.2 \pm 2.9 \mu g g_{Ru}^{-1} h^{-1}$ for Ru/TiO₂, Ru/ α -Al₂O₃ and Ru/ZrO₂, respectively. These figures are between 20 and 50 times higher than for Ru/AC ($0.5 \pm 0.1 \mu g g_{Ru}^{-1} h^{-1}$). Li *et al.* reported slightly different Ni loss rates for Ni/ α -Al₂O₃ and Ni/CNT (10^{-3} and $0.5 \times 10^{-3} g g_{Ni}^{-1} h^{-1}$, respectively) during SCWG of glycerol [102]. Their hypothesis was that smaller NPs have more atoms in contact with the support (proportionally) and thus leach less. For Ru/ZrO₂, the results were in contradiction with this statement as the small Ru NPs exhibited higher Ru loss compared to Ru/AC. Interestingly, the initial Ru concentrations of the metal oxide catalysts (flushed with H₂O at ambient conditions) followed an opposite trend to Ru/AC. As mentioned previously, the least strongly bound Ru NPs and carbon domains get flushed out of the system by the initial wash. Since the metal oxide catalysts are considerably more stable (1000–5000 MPa [160]–[162] vs. 10 MPa for AC [158]),

they did not undergo this initial loss. However, SCWG conditions induced an increase in Ru loss for the metal oxide-based catalysts, whereas it decreased for Ru/AC. Concerning Ru/AC, the Al concentrations remained very stable around $10 \mu\text{g L}^{-1}$ as for previous experiments, highlighting the repeatability of these experiments. Also, the steady-state Al concentration is close to the modelled data. For these experiments, no concentrations spikes were observed.

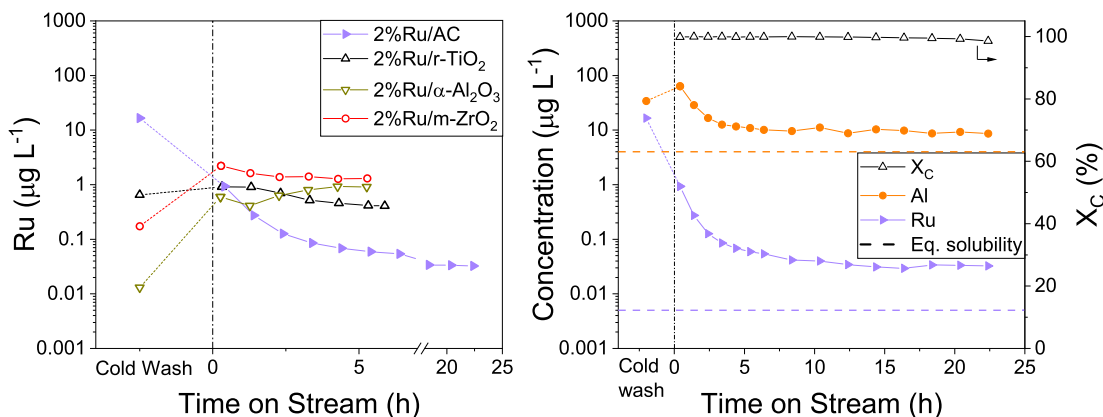


Figure 4.13 – Ru concentration in the effluent stream during SCWG of glycerol over 2 wt% Ru catalysts (left). Conversion and concentration profiles of Al and Ru for 2 %Ru/AC.

In terms of gasification activity, Ru/AC clearly outperformed its metal oxide analogues, with a minor drop in conversion appearing after 20 h TOS. For the metal oxides, none of them achieved total feed conversion at similar conditions as shown in Figure 4.14, right. Ru/TiO₂ was the most active at the start of the experiment ($X_C \approx 80\%$), but the activity loss was very rapid. Ru/ α -Al₂O₃ and Ru/ZrO₂ exhibited a similar initial activity ($X_C \approx 60$ and 50% respectively), but the latter was more stable as the conversion decrease was less pronounced. Ru/AC was expected to perform well because of its small Ru average NP diameter ($d_{p,CO} = 1.3$ nm) and reached thermodynamic CH₄ yields ($28 \text{ g}_{\text{CH}_4} \text{ g}_{\text{Gly}}^{-1}$ [109]) for over 10 h. Nevertheless, Ru/ZrO₂ also exhibited relatively small Ru NPs ($d_{p,CO} = 2.6$ nm), but was much less active. The exact reason for this is unknown, but could be due to several factors: a synergistic effect between Ru and AC, or the positive effect of higher SSA. Zöhrer *et al.* showed that 2 %Ru supported on TiO₂ and ZrO₂ were able to completely gasify a glycerol solution for 24 h (400 °C, 28.5 MPa) [109]. However, this was at a $WHSV_{gRu}$ of only $30 \text{ g}_{\text{org}} \text{ g}_{\text{Ru}}^{-1} \text{ h}^{-1}$. Peng *et al.* also compared Ru/AC to metal oxide-based catalysts by gasifying isopropanol for 50 h at much higher space velocities ($WHSV_{gRu} = 5200 \text{ g}_{\text{org}} \text{ g}_{\text{Ru}}^{-1} \text{ h}^{-1}$) and observed the same activity trends [75]. Interestingly, Ru/TiO₂ also exhibited the fastest initial activity loss. The results shown here confirm their earlier findings with Ru/AC > Ru/ZrO₂ > Ru/ α -Al₂O₃ \approx Ru/TiO₂. Peng *et al.* showed that Ru/ZrO₂ was more resistant to coking with TPO profiles showing no CO₂ evolution, whereas the other catalysts did [75]. This could be an explanation for the increased stability of Ru/ZrO₂.

The catalysts did not undergo significant property changes after the SCWG experiments,

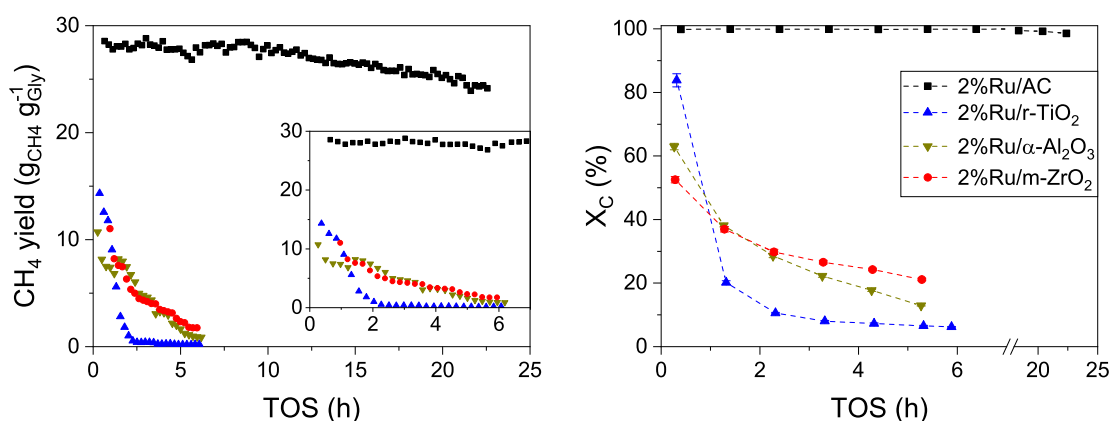


Figure 4.14 – CH₄ yield (left) and carbon conversion (right) for the 2 %Ru catalysts during SCWG of 10 wt% glycerol.

Table 4.5 – SSA comparison between the fresh and spent catalysts after SCWG of glycerol

Catalyst	fresh			spent			$X_{C,end}^a$ (%)
	SSA	SSA_{Ext}	V_p	SSA	SSA_{Ext}	V_p	
	($m^2 g^{-1}$)		($cm^3 g^{-1}$)	($m^2 g^{-1}$)		($cm^3 g^{-1}$)	
2%Ru/AC	1354	38	0.6	1147	43	0.5	100
2%Ru/ α -Al ₂ O ₃	6.6	5.7	0.1	6.2	5.9	0.1	13
2%Ru/TiO ₂	4.5	3.7	0.1	5.2	4.1	0.1	7
2%Ru/ZrO ₂	27	22	0.2	29	25	0.2	21

^a After TOS = 5.3 h.

as highlighted in Table 4.5. For Ru/AC this was expected because of the almost-complete conversion of glycerol throughout the run. SSA and V_p decreased slightly, certainly due to some deposited carbon species blocking the access to micropores. For the metal oxide-based catalysts no big differences were observed. The low SSA and lack of micropores may be the reason for this, as unconverted carbon species have less probability of depositing on a low-SSA support. Interestingly, a slight increase in SSA_{Ext} was observed for all four catalysts.

4.6 Summary

The activity and stability of different Ru-based catalysts were investigated in this chapter, with a special focus on Ru loss from the catalytic reactors. Continuous SCWG rigs of different size were used to assess the Ru loss and understand the different mechanisms governing Ru loss. The main findings are summarised below:

- A new commercial Ru/AC catalyst was found in Ru/AC-A, matching the performance of the previous benchmark catalyst Ru/AC-BM for industrially-relevant conditions. The new catalyst was then assessed on a larger setup (*intermediate*, 50 g catalyst) where it fully converted 10 wt% glycerol for 3 h and sewage sludge for 3 h as well.
- Ru was detected in the PWs and was successfully quantified by ICP-MS, showing that different commercial 5 wt%Ru/AC catalysts led to different steady-state Ru concentrations in the PW: 0.20 ± 0.06 , 0.03 ± 0.01 and $0.08 \pm 0.05 \mu\text{g L}^{-1}$ for Ru/AC-BM, Ru/AC-A and Ru/AC-B, respectively. Converted to normalised loss rates, they amounted to 1.2 ± 0.4 , 0.19 ± 0.05 and $0.4 \pm 0.3 \mu\text{g}_{\text{Ru}} \mu\text{g}_{\text{Ru,bed}}^{-1} \text{ h}^{-1}$ for Ru/AC-BM, Ru/AC-A and Ru/AC-B, respectively.
- The temperature, feed concentration and feed rate had no effect on the Ru concentration in the PW for Ru/AC-A. The concentration systematically stabilised in the range 0.01 – $0.03 \mu\text{g L}^{-1}$, independent of the varied process conditions. The absence of an effect is in line with thermodynamic equilibrium models.
- The feed rate and pressure were constantly varied, resulting in a six-fold increase in Ru quantified in the PWs, as well as ten times more Ru quantified in the frit ($15 \mu\text{m}$) downstream of the catalytic reactor in 4 h only, compared to >250 h of steady state operation. These intentional fluctuations hence damaged the Ru/AC catalyst through collisions leading to friction and abrasion inside the catalyst bed. These results show the importance of smooth plant operation, especially for larger scales in the near future.
- Ru/AC-A was assessed on larger setups too, with glycerol and sewage sludge. The Ru loss rates were of the same order of magnitude, be it from *Konti-I*, the *intermediate* setup with glycerol, or with sewage sludge. The loss rates from the different setups did not correlate to the feed rate, residence time, superficial velocity or the mass of catalyst loaded in the reactor. However, it did correlate with the $H_{\text{cat}} d_R^{-1}$ aspect ratio.
- Temperature and pressure drops due to a pump failure seriously damaged the sulfur absorber bed, as the catalyst was unable to fully convert the sewage sludge feed afterwards. H_2S was detected on the μGC and the PW was yellowish and smelly. The Ru loss was not affected, however the recovered catalyst bed showed higher N and S concentrations, and a considerable decrease in SSA along the catalyst bed.
- 2 wt% Ru catalysts supported on metal oxides exhibited higher Ru loss rates (10.2 – $24.3 \mu\text{g g}_{\text{Ru}}^{-1} \text{ h}^{-1}$) and a considerably lower activity than for 2 %Ru/AC ($0.5 \mu\text{g g}_{\text{Ru}}^{-1} \text{ h}^{-1}$). The absolute Ru concentration in the PW ($0.04 \mu\text{g L}^{-1}$) of the latter was similar to the 5 %Ru/AC commercial catalysts. Ru/AC hence remains the most active and most stable catalyst for SCWG.

- Leaching was shown to be the main Ru loss mechanism, governed by thermodynamics with steady-state Ru concentrations close to theoretical values. Concentration spikes induced by fluctuating process parameters were ascribed to a mechanical Ru loss through friction/abrasion.
- The very low Ru concentrations reported did not lead to catalyst deactivation on the assessed time scale.

5 Ru/CNF as SCWG catalyst

In Chapter 3, we showed that CNF was a promising support in the search of active and stable SCWG catalysts. CNF was used for catalyst impregnation because of its inertness and high pore volume, enabling the synthesis of high-loading catalysts. The former is important too, as ACs were shown to be initially very active in SCWG (see Chapter 3). Furthermore, working with AC-based catalysts makes it difficult to perform a thorough characterisation, as their high heterogeneity and density add considerable limitations to TEM, for the analyses of Ru NP sizes (PSDs) or the observation of coke deposits. By working with this type of material, the goal was to assess the activity of Ru/CNF and see whether they can outperform commercial Ru/AC catalysts. The limits of a CNF-based catalytic system were assessed by looking at the stability of Ru NPs, as well as trying to maximise/optimize the Ru loading without generating large NPs. The aim was also to synthesise Ru/CNF catalysts of different particle size distributions to investigate the size sensitivity of Ru during SCWG of glycerol. With this model system, different deactivation mechanisms could be analysed in more detail such as sintering and coking, which is not easily feasible on Ru/AC because of its higher density and heterogeneity.

5.1 Synthesis and characterisation of Ru/CNF catalysts

Before synthesising the catalysts, the CNF support was purified in KOH to get rid of the residual silica from the synthesis. The ash content of the as-received material amounted to 7.6 ± 0.6 %. This was decreased to 1.8 ± 0.3 % by washing the support in KOH at reflux for 2 h. The washing step did not alter the support properties as shown in Table 5.1. The catalysts were then synthesised by the IWI method on the purified CNF support. TEM images of the synthesised Ru/CNF catalysts are presented in Figures D.1 to D.7 in Appendix D.

The catalyst properties are summarised in Table 5.1. When comparing the as-received support

Table 5.1 – Support and catalyst characteristics

Material ^a	SSA ($m^2 g^{-1}$)	V_p ($cm^3 g^{-1}$)	x_{Ru} (%)	D_{TEM} (%)
CNF_AR ^b	288	3.9	n.a.	n.a.
CNF ^c	311 ± 19	3.3 ± 0.3	n.a.	n.a.
1%Ru/CNF_1	285 ± 12	2.8 ± 0.1	1.4 ± 0.3	67
1%Ru/CNF_2	297 ± 14	2.4 ± 0.1	1.1 ± 0.3	71
5%Ru/CNF_1	263 ± 16	2.0 ± 0.1	4.6 ± 0.3	67
5%Ru/CNF_Cl ^d	297	2.2	5.1 ± 0.3	69
10%Ru/CNF	283	1.81	10.4 ± 0.3	59
15%Ru/CNF	287 ± 11	1.8 ± 0.1	16.0 ± 0.3	47
20%Ru/CNF	268	1.58	20.6 ± 0.8	51
30%Ru/CNF	226	1.05	32.3 ± 0.5	35

^a Catalysts synthesised from RuNO(NO₃)₃ unless stated otherwise.

^b As-received material.

^c Purified material.

^d Synthesised from RuCl₃ · xH₂O.

Standard deviations: n = 3.

(CNF_AR) and the purified one (CNF), one can see that treatment in KOH did not alter the support properties, as the surface area and pore volume remained in the same range. The same findings were reported in another study [163]. The pore volume (V_p) and the surface area (SSA) of the synthesised catalysts decreased with increasing loading. Due to the increasing density of the higher-loading catalysts, both measured parameters were biased by the additional mass of Ru. For this reason, the uncorrected and loading-corrected V_p and SSA were plotted in Figure 5.1 to show the effect of Ru loading. From there, one can see that the loading-corrected V_p still decreased, highlighting the volume taken up by the Ru NPs. For the 30%Ru/CNF catalyst however, the corrected pore volume decrease was more significant. This could arise from the Ru NPs taking up or blocking most of the inner CNF volume. Winter *et al.* demonstrated the presence of Co and Pd NPs inside CNF by combined TEM and XPS studies [164]. They reported up to 15 and 34 % of NPs inside the tubes for Pd (1–4 nm) and Co (3–4 nm), respectively. Calculations from TEM images in this thesis suggested that approximately 10 % of the pore volume would arise from the inner core of the tubes. Since the impregnation method is considered homogeneous (no concentration gradient), 10 % of the Ru NPs could be located inside the tubes. For higher loadings, the access to this volume may be blocked by the increased metal content, which may partly explain the decrease in V_p for 30%Ru/CNF. For the SSA no significant difference was observed, indicating that the synthesis method did not affect the CNF support. The Ru loading measured by calcination was close to the theoretical loading, showing that this characterisation method could safely be used.

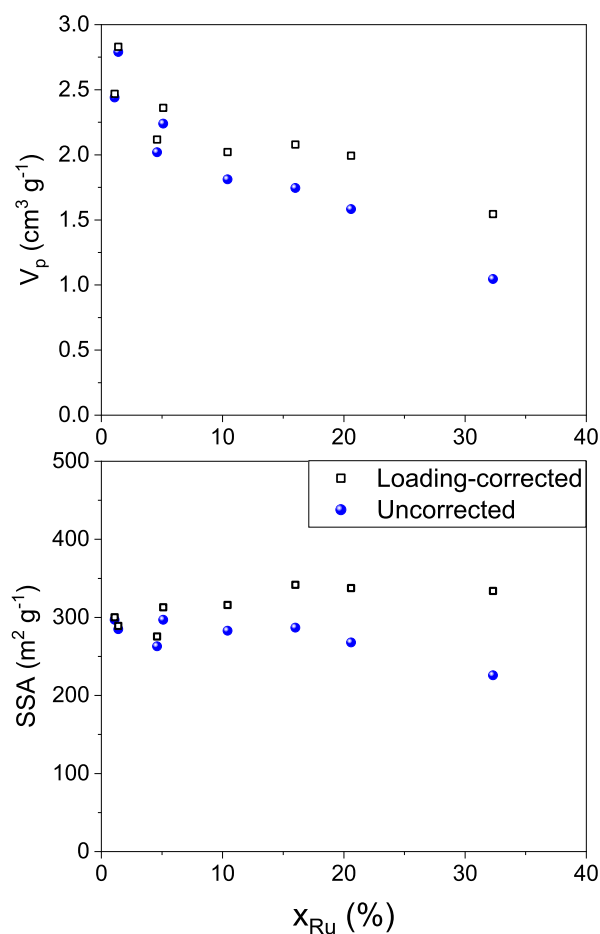


Figure 5.1 – Evolution of the uncorrected (blue spheres) and loading-corrected (black squares) Ru/CNF pore volume (top) and surface area (bottom) as a function of Ru loading.

The catalyst synthesis method yielded very small Ru NPs of mono-modal distributions, with D_{TEM} reaching 71 and 67 % for both 1 %Ru/CNF catalysts ($d_{p,TEM} = 1.0$ and 1.2 nm), 69 and 67 % for the 5 %Ru/CNF catalysts ($d_{p,TEM} = 0.9$ and 1.1 nm). These figures also highlight the good reproducibility of the synthesis method. Examples of HR-TEM images are shown in Figure 5.2 for 1%Ru/CNF_2 (left) and 5%Ru/CNF_1 (right).

Very small Ru NPs (≤ 1.1 nm) were achieved with catalyst loadings up to 5 %, higher Ru contents led to a decrease in D_{TEM} , from 59 % for 10 %Ru/CNF down to 35 % for 30 %Ru/CNF. However, even the high loading of the latter catalyst yielded mean Ru NP diameters of 2.2 nm, remaining relatively small. The increase in $d_{p,TEM}$ as function of Ru loading is shown in Figure 5.3. These results show that small Ru NPs can easily be achieved on CNF with a facile synthesis method, even at high loadings.

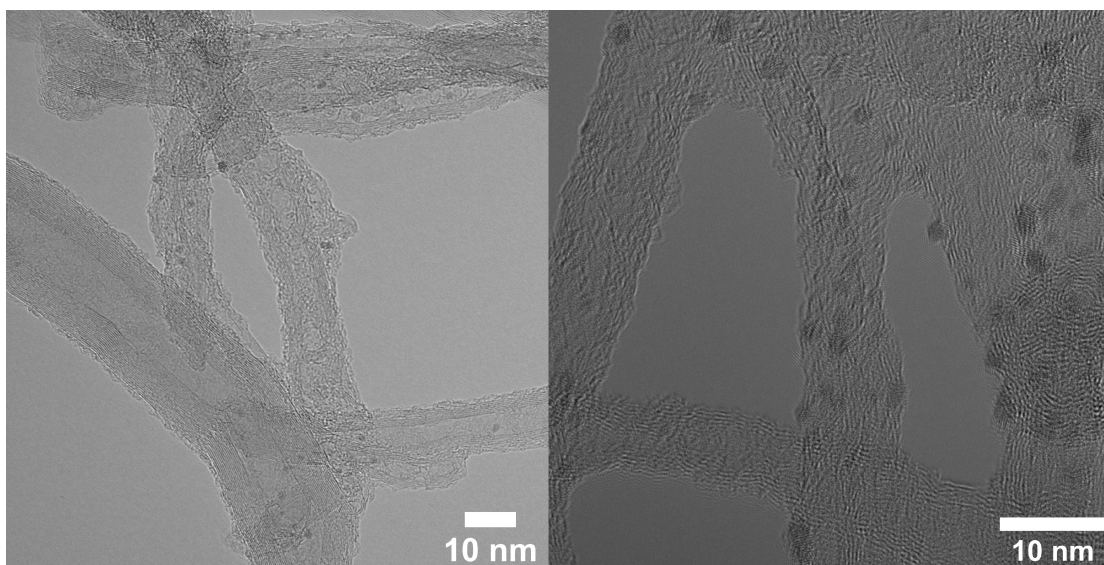


Figure 5.2 – High-resolution micrographs of the fresh 1%Ru/CNF_2 (left) and 5%Ru/CNF_1 (right) catalysts. The small Ru NPs are seen as darker spots. Magnification: 250kX left, 600kX right.

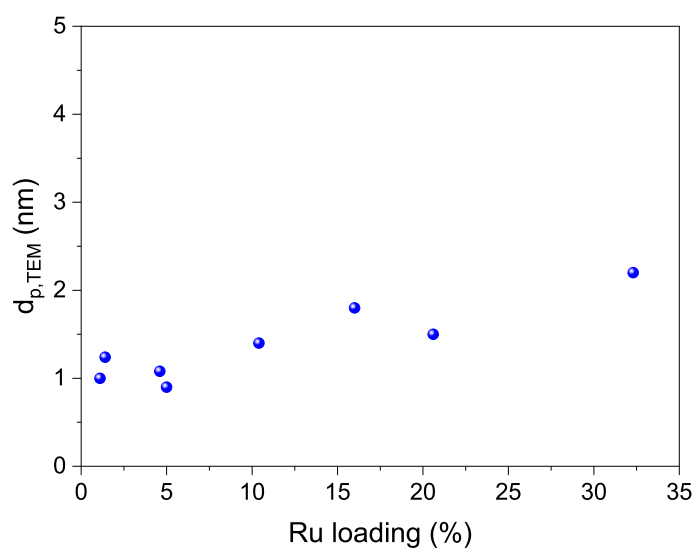


Figure 5.3 – Mean Ru NP diameter ($d_{p,TEM}$) as a function of Ru loading for the synthesised catalysts.

5.2 Catalytic testing of Ru/CNF

To obtain valuable activity and stability information, the synthesised Ru/CNF catalysts were assessed at high $WHSV_{gRu}$ ($\approx 4000 \text{ g}_{org} \text{ g}_{Ru}^{-1} \text{ h}^{-1}$) to target $X_C < 50\%$ and hence have an unbiased turnover frequency estimation. The experiments performed in this chapter are summarised in Table A.3. Ideally, lower conversions should be reached for such catalytic studies, but we are limited by the SCWG process. At very low conversions (5–10 %), there is an increasing share of support activity. Also, supports of highly microporous nature tend to be coked more rapidly, inducing a drastic activity loss which is not related to the Ru NPs themselves. For this reason, the catalyst activity was investigated at higher conversions, around 30–50 %. Due to the higher Ru loadings in the series of catalysts tested here, 20 wt% glycerol was used as feed solution, except for both 1%Ru/CNF catalysts (6 and 8 wt% for the experiments at 3000 and 9000 $\text{g}_{org} \text{ g}_{Ru}^{-1} \text{ h}^{-1}$, respectively).

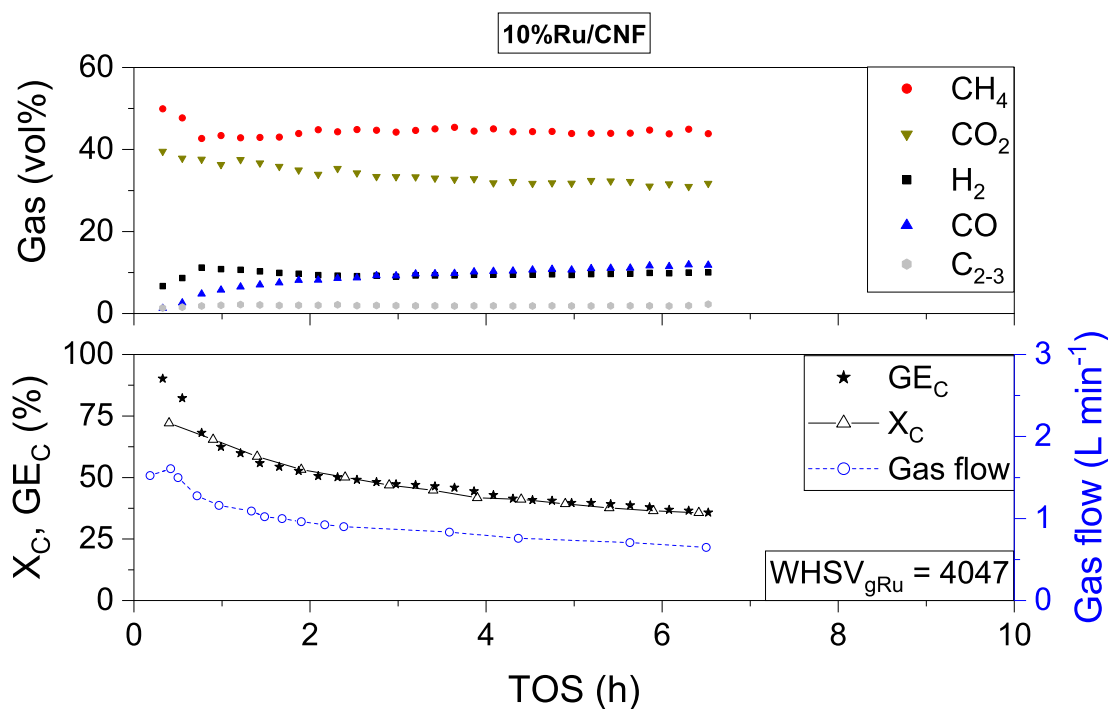


Figure 5.4 – SCWG of glycerol (20 %) over 10 %Ru/CNF. The gas composition is shown in the top graph, the carbon gasification efficiency (GE_C , stars) and conversion (X_C , triangles) are shown in the bottom graph together with the produced gas flow (blue circles). $p = 28.5 \text{ MPa}$, $T = 404 \text{ }^\circ\text{C}$, $WHSV_{gRu} = 4047 \text{ g}_{org} \text{ g}_{Ru}^{-1} \text{ h}^{-1}$ (Exp. C24).

Figure 5.4 serves as an example for the catalytic SCWG experiments performed within this study. Here, the experiment overview is shown for 10 %Ru/CNF, with the generated gas composition in the top graph and the gas flow, X_C , GE_C in the bottom graph. The stable gas

composition was also observed for all other tests performed in the same conditions (see Figures D.8 to D.14). In Figure 5.4, X_C and GE_C overlap throughout the experiment indicating that the fraction of feed converted ended up in the gas phase. Hence, no significant coke deposition occurred during the gasification experiment. An example of carbon flow during the 10 %Ru/CNF experiment is presented in Figure 5.5, which shows that the carbon balance was closed during the experiment. The minor difference appearing at the start of the experiment is due to the initial gas build up in the system, and not to carbon accumulation in the system.

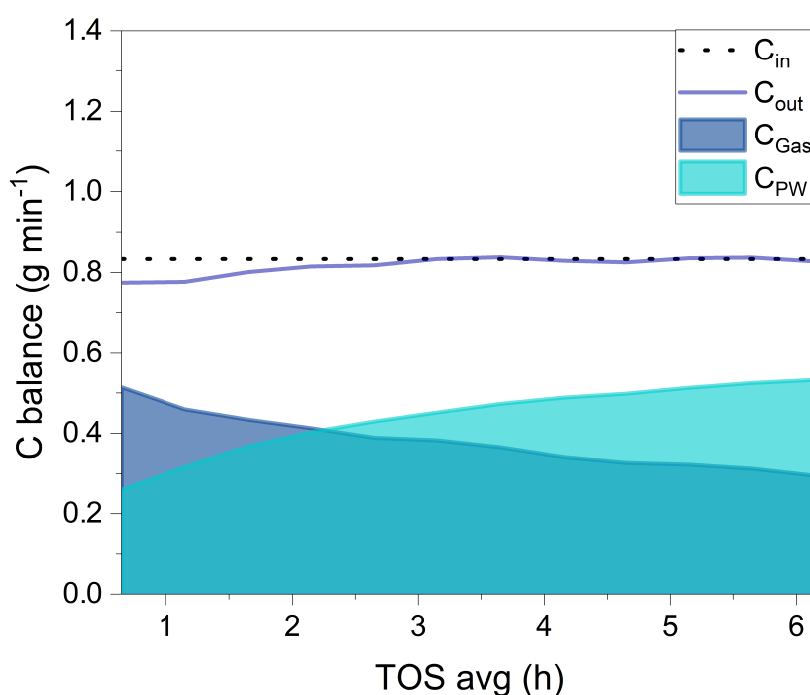


Figure 5.5 – Carbon flow during SCWG of glycerol over 10 %Ru/CNF. The carbon fed into the system (black dashed line) and the total carbon exiting the system (blue line) are shown, the latter being the sum of the carbon in the PW (grey area) and gas (blue area) phases.

As seen in Figure 5.4, 10 %Ru/CNF exhibited a high initial activity, before decreasing similarly to an exponential decay. Unfortunately, no steady state could be achieved during daytime operation of the rig, as it required longer TOS to stabilise. In order to have an accurate estimation of the steady-state X_C and TOF data, as well as to ensure a correct comparison between the different catalysts evaluated, both parameters were fitted with an exponential decay function (optimised through a Levenberg-Marquardt iteration algorithm), shown as example in Figure 5.6 for the 10 %Ru/CNF catalyst. The TOF, relating the amount of glycerol

converted per unit time and per active site, was calculated with Equation 5.1,

$$TOF \left(\frac{mol_{gly}}{mol_{Ru,afc} \cdot min} \right) = \frac{\dot{n}_{gly,fed} \cdot X_C}{n_{Ru} \cdot D_{TEM}} \quad (5.1)$$

where $\dot{n}_{gly,fed}$ is the moles of glycerol fed per unit time, X_C the carbon conversion, n_{Ru} the Ru loading in moles and D_{TEM} the catalyst dispersion.

The function used to fit the data is described in Equation 5.2, where A_1 is the amplitude, t_1 the time constant and y_0 is the offset, or steady-state value of interest (X_C or TOF).

$$y = A_1 \cdot \exp\left(\frac{-x}{t_1}\right) + y_0 \quad (5.2)$$

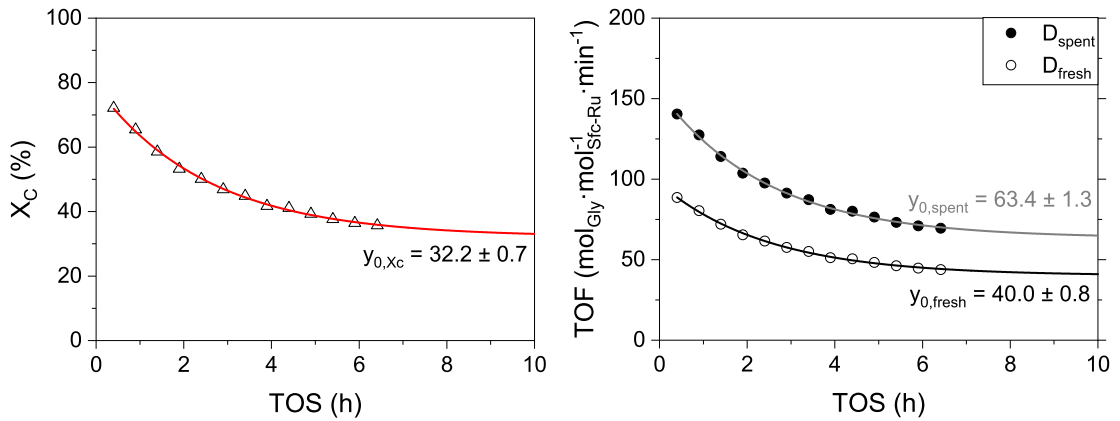


Figure 5.6 – Exponential decay fits for the conversion (left, red line) and the TOF (right) calculated from the fresh (black line) and spent (grey line) dispersions of the 10%Ru/CNF catalyst.

The SCWG activity of the different Ru/CNF catalysts was compared in Figure 5.7, where the left-hand side graph regroups the experiments performed at $WHSV_{gRu} \approx 4000 \text{ g}_{\text{org}} \text{ g}_{\text{Ru}}^{-1} \text{ h}^{-1}$ and the right-hand side graph shows the 1 %Ru/CNF catalysts tested at different conditions ($WHSV_{gRu} = 3000$ and $9000 \text{ g}_{\text{org}} \text{ g}_{\text{Ru}}^{-1} \text{ h}^{-1}$). In Figure 5.7 (left), all catalysts showed a similar activity trend throughout the experiments. The highest activity was recorded for 5 %Ru/CNF_Cl, which also exhibited a very high dispersion (69 %). The catalyst achieved total feed conversion over the first hour before starting to decrease in a similar trend as the other catalysts. The other 5 %Ru/CNF_1 catalyst was less active at the beginning of the experiment, but eventually stabilised to a TOF in the same range as the former catalyst (TOF = 55 and 47 min^{-1} , respectively). The activity of 10 %Ru/CNF was slightly lower than the 5 %Ru/CNF

catalysts, but still significantly higher than the higher-loading catalysts. For the 15, 20 and 30 % Ru/CNF catalysts, the initial loss in activity was more pronounced and final TOFs were consequently lower 26–28 min⁻¹. Looking at the 1 %Ru/CNF catalysts (Figure 5.7, right), the catalyst activation time took longer, as the conversion was lower in the early stage of the experiment. A reason for this could be the very high dispersion, meaning that more organics were required to fully reduce the passivation layer. Once the Ru NPs were fully active (*i.e.* reduced), the initial activity was much higher for 1 %Ru/CNF_9000 (TOF = 150 min⁻¹). However, the TOF loss was very rapid for both 1 %Ru/CNF experiments, leading to low final values overlapping after TOS = 4 h and stabilising at ≈ 11 min⁻¹. The final TOFs were reported as a function of the spent catalyst dispersions in Figure 5.8. The superiority of the 5 %Ru/CNF catalysts is highlighted even more clearly.

Previous works reported the negative effect of chloride precursors on the Ru/C catalyst activity because of some residual chloride poisoning the active sites or leading to lower dispersions [76], [77]. Here, the catalyst synthesised from ruthenium chloride exhibited very high dispersions and the best stability with a steady-state TOF of 55 min⁻¹. This is in contradiction with the results of Peng *et al.* who measured residual chloride on a Ru/AC catalyst impregnated in water (and not with acetone) [76]. They reported a lower activity, related to the incomplete removal of chlorides and maybe the subsequent lower dispersion. Even though the CNF-based catalyst used here was reduced at a lower temperature (300 vs. 450 °C), no chloride seemed to be present due to the enhanced activity of 5 %Ru/CNF_Cl. This difference could arise through the support properties, as AC's micropores and surface functionality may hinder complete Cl removal.

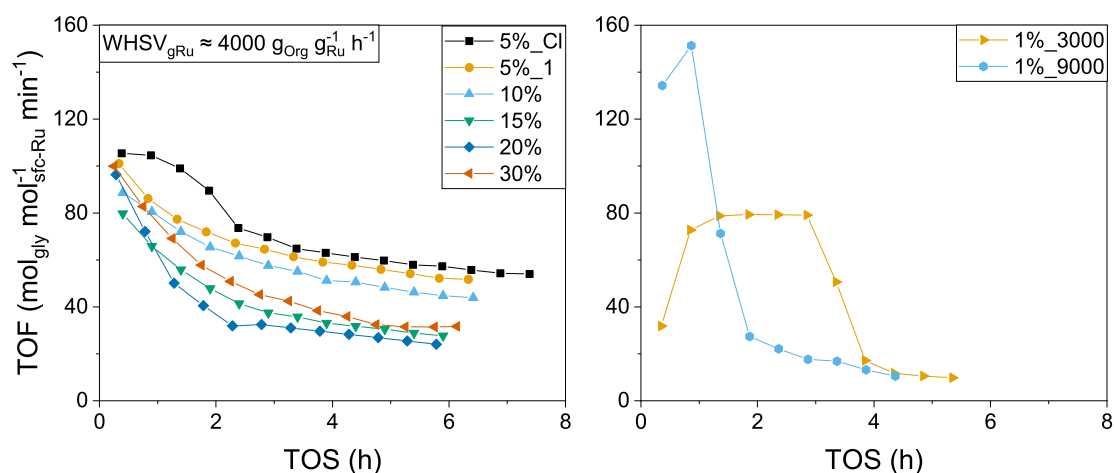


Figure 5.7 – TOF overview after SCWG of glycerol (6–20 wt%) over Ru/CNF catalysts of different loadings. The left-hand side graph shows Ru/CNF (5–30 %) catalysts treated at $WHSV_{gRu} \approx 4000 \text{ g}_{org} \text{ g}_{Ru}^{-1} \text{ h}^{-1}$ (Exp. C22-C27). The right-hand side graph shows the 1 %Ru/CNF catalysts treated at $WHSV_{gRu}$ of 3000 and 9000 $\text{g}_{org} \text{ g}_{Ru}^{-1} \text{ h}^{-1}$ (Exp. C20,C21). The shown TOFs were calculated with the fresh catalyst dispersion. $F = 9.4\text{--}11.6 \text{ g min}^{-1}$, $p = 28.5 \text{ MPa}$, $T = 400\text{--}408 \text{ }^{\circ}\text{C}$.

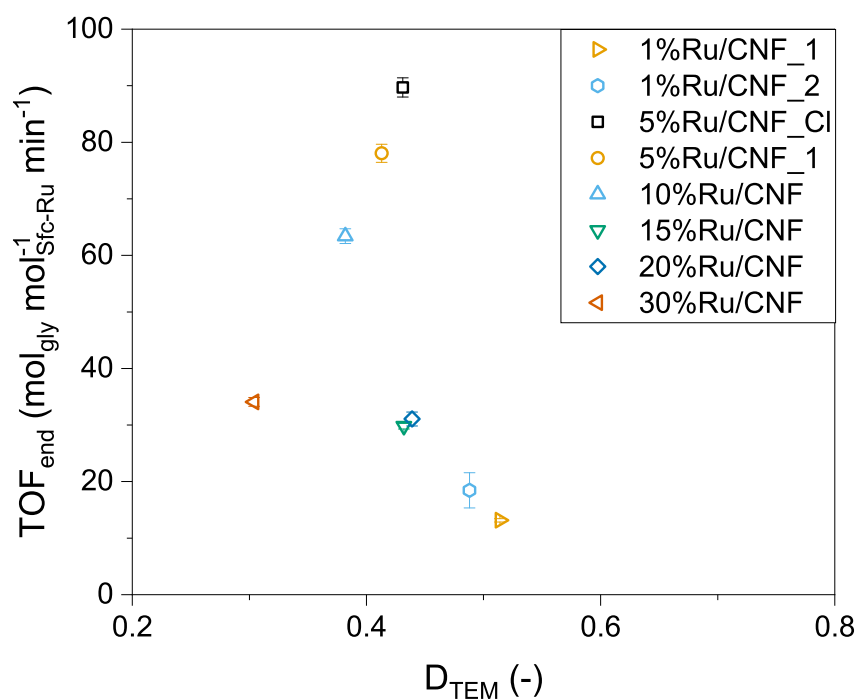


Figure 5.8 – Final fitted turnover frequency (TOF_{end}) calculated from the spent dispersion for the different Ru/CNF catalysts.

Table 5.2 – Catalyst characteristics before and after glycerol conversion

Exp.	Catalyst	fresh				spent				TOF_{ini}^a	TOF_{end}	ΔD_{TEM}	ΔTOF
		SSA	V_p	D_{TEM}	$d_{p,TEM}$	SSA	V_p	D_{TEM}	$d_{p,TEM}$				
		($m^2 g^{-1}$)	($cm^3 g^{-1}$)	(%)	(nm)	($m^2 g^{-1}$)	($cm^3 g^{-1}$)	(%)	(nm)	(min^{-1})		(%)	
C20	1%Ru/CNF_1	286	2.3	67	1.2	285	2.8	51	1.6	66	13	-23	-80
C21	1%Ru/CNF_2	297	2.4	71	1.0	273	2.7	49	1.9	220	18	-31	-92
C22	5%Ru/CNF_1	263	2.0	67	1.1	274	2.3	40	2.2	128	78	-40	-39
C23	5%Ru/CNF_Cl	297	2.2	69	0.9	271	2.4	42	2.1	107	90	-40	-16
C24	10%Ru/CNF	283	1.8	59	1.4	252	1.9	37	2.4	113	63	-37	-44
C25	15%Ru/CNF	287	1.8	47	1.8	265	2.0	42	2.1	89	30	-11	-67
C26	20%Ru/CNF	268	1.6	51	1.5	250	1.8	43	2.1	116	31	-17	-73
C27	30%Ru/CNF	226	1.1	35	2.2	224	1.4	30	2.9	120	34	-17	-72

^a Initial TOF calculated at X_C =50–64 % depending on the available data points, from the spent catalyst dispersion.

Since the 1 %Ru/CNF catalysts exhibited a very high dispersion (67 and 71 %), one can think of the loss in dispersion as main deactivation cause. To check this, the initial TOF (TOF_{ini}) was determined for all catalysts. As some experiments began at relatively high conversions $>75\%$, TOF_{ini} was calculated at $X_C = 50\text{--}64\%$ depending on the data points available for the different catalysts. From there, the TOF loss percentage could be calculated. Figure 5.9 shows that the loss in TOF was not explained by the loss in D_{TEM} alone, suggesting that other factors influenced the catalyst activity. All catalysts were prone to sintering (although limited as shown in Table 5.2). Furthermore, the 1 %Ru/CNF catalysts still exhibited the highest dispersion after SCWG. Cardoso *et al.* reported that Ni/CNF underwent rapid sintering in SCW (from 18 to 36 nm in 15 min), showing that the dispersion loss could be due to the SCW environment only [103]. However, this was not the case for Ru/CNF as no growth was observed for 5 %Ru/CNF after spending 4.5 h in SCW (28.5 MPa, 400 °C), see Figure 5.10. Hence, this rules out the effect of a thermodynamically-driven particle growth in SCW and shows that the particle growth happened during the catalytic reaction. The good Ru NP stability could be due to the spacing of the NPs on the high-SSA support. Yin *et al.* showed that a critical distance between NPs existed, below which significant sintering occurred [165]. Particle growth could be mitigated up to 900 °C with higher Pt NP spacing, either through the use of supports of higher surface area or by decreasing the loading. Due to the limited sintering observed in this work, it is supposed that none of the synthesised catalysts exceeded this critical distance.

As stated before, the loss in TOF did not correlate with the loss in D_{TEM} (Figure 5.9). One reason for the improved activity of both 5 %Ru/CNF catalysts (and the 10 %Ru/CNF catalyst to a lesser extent) could be the density of active sites, as the mean Ru NPs are in the same size range, but present in higher concentrations. Peng *et al.* reported a higher activity during SCWG of isopropanol with a 2 %Ru/AC of lower dispersion than a 0.5 %Ru/AC catalyst ($D_{\text{TEM}} = 14$ and 26 % respectively), showing that the density of Ru NPs on the catalyst support could be an even more important parameter than the dispersion [76].

To verify this hypothesis, the final TOF (TOF_{end}) was plotted as function of the surface Ru atom density (Ru_{sfc}) of the spent materials (Figure 5.11). One can distinguish a clear optimum in Ru_{sfc} density between 0.4 and 0.7 $\text{atom}_{\text{Ru,sfc}} \text{ nm}^{-2}$. To put these figures into perspective, a maximum theoretical density of 17.7 $\text{atom}_{\text{Ru,sfc}} \text{ nm}^{-2}$ could be calculated assuming a mono-layer coverage of the CNF support by Ru (*i.e.* 48 % loading). Lu *et al.* synthesised stable ultra-high-density single-atom catalysts up to high loadings (20 wt%), showing improved efficiencies in the eletrocatalytic reduction of CO_2 [166]. However, the usefulness of this work only applies to reactions which are not prone to structure sensitivity. For methanation, under-coordinated step-edge sites are required, hence showing the need for Ru NPs and not

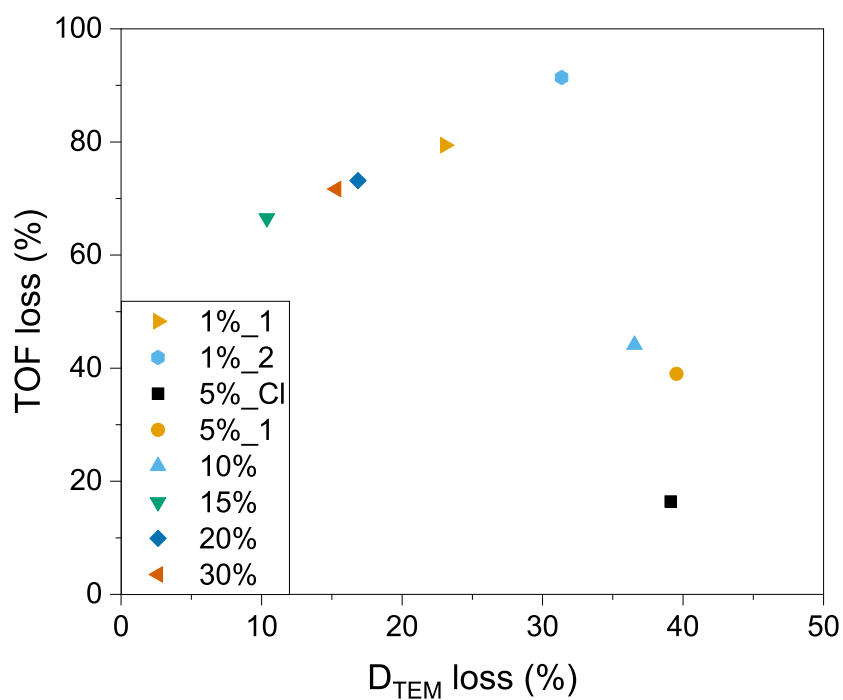


Figure 5.9 – TOF loss as a function of D_{TEM} loss for Ru/CNF catalysts tested for SCWG of glycerol.

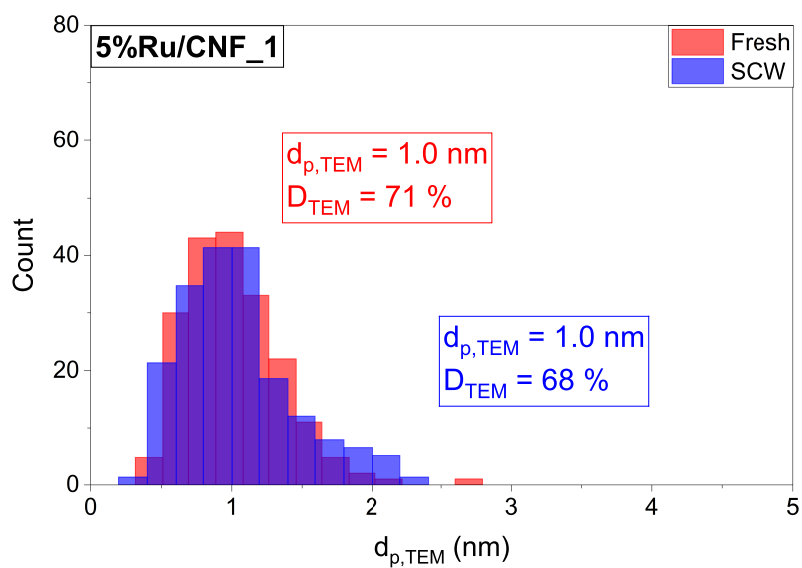


Figure 5.10 – PSD of a fresh 5 %Ru/CNF catalyst (red) and after treatment in SCW (blue). The main mode for $d_{p,TEM}$ as well as D_{TEM} are reported next to the histograms.

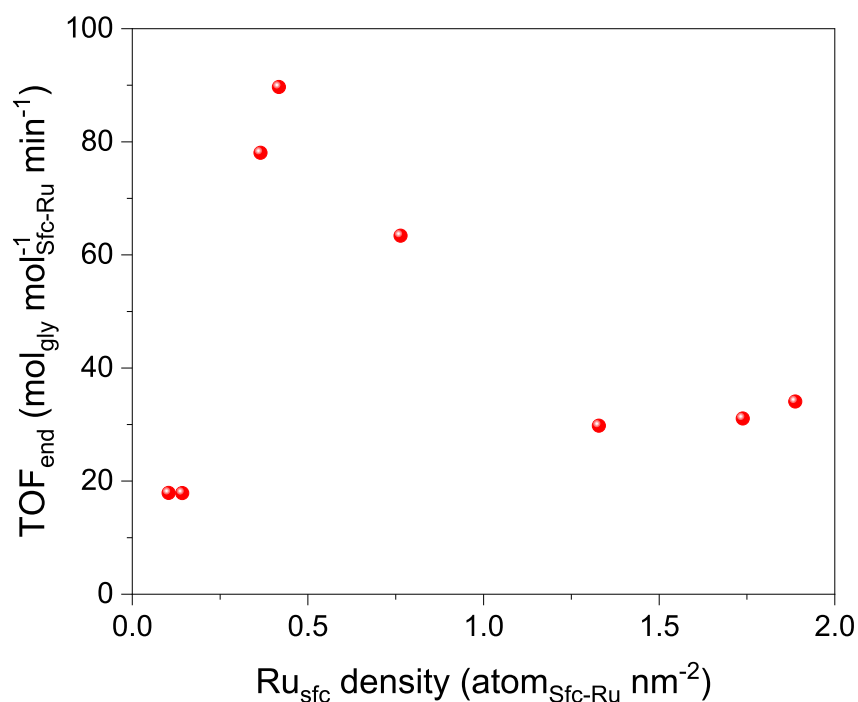


Figure 5.11 – Final TOF after SCWG of glycerol over Ru/CNF catalysts as a function of Ru_{sfc} density. The reported TOF and Ru_{sfc} density relate to the spent catalysts.

single atoms. Higher efficiencies or activities could thus be tailored through stable NPs of high density.

The results presented here indicated that the presence of small Ru NPs (1.0 nm) was not the only reason to ensure high gasification activity over several hours. As evidenced by the 1 %Ru/CNF catalysts, the activity losses were very rapid, suggesting that the observed sintering (Table 5.2) and the coking measured by TGA (Figure 5.12) may have led to this very rapid deactivation. This was not observed for the 5 %Ru/CNF catalysts, hence the higher density of small Ru NPs may hinder or delay deactivation through coking.

Higher Ru NP densities on the catalyst surface could lead to increased sintering, as suggested by Finney *et al.* [167]. However, higher surface Ru atom densities led to lower dispersion losses than for lower surface Ru atom densities. Campbell *et al.* showed that small MgO-supported Pb NPs were more prone to sintering, as their stability drastically decreased below 1 nm [168], which is in line with the Ru/CNF sintering data presented here. However, another study contradicts these results showing that mono-modal PSDs suppressed the Ostwald ripening sintering process for Pt NPs [169]. In our case, the broadest PSD (30 %Ru/CNF) underwent the lowest D_{TEM} loss.

High Ru dispersions are beneficial for high SCWG activities, however catalysts of lower loadings may undergo faster deactivation. As the ratio of Ru NP to CNF surface is significantly lower for 1 %Ru/CNF catalysts, there would be a higher probability of glycerol decomposing at the carbon surface, supposing that coking could be the reason for the loss in activity.

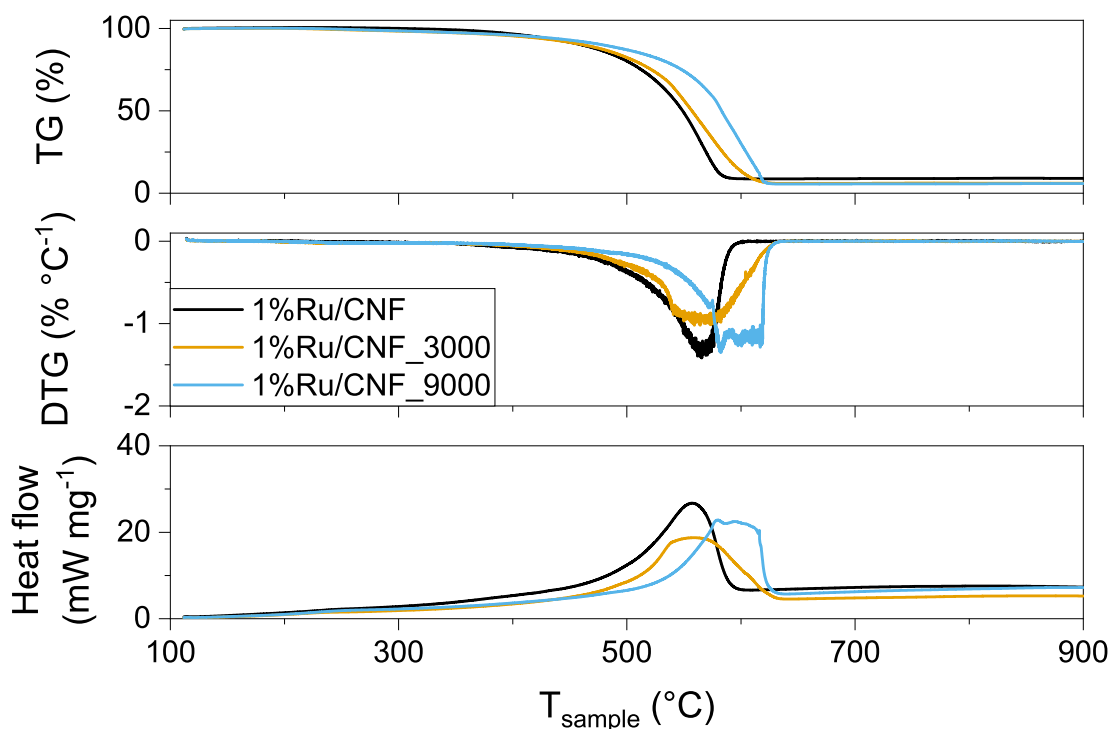


Figure 5.12 – Thermogravimetric (TG, top), differential weight loss (DTG, middle) and heat flow (bottom) analyses for the fresh and spent 1%Ru/CNF catalysts (Exp. C20,C21).

TGA analyses (Figure 5.12) revealed that the weight loss patterns were completely different for the fresh and both spent (1 %Ru/CNF_3000 and 1 %Ru/CNF_9000) catalysts. The former underwent constant weight loss, with one clear contribution in the differential thermogravimetric analysis (DTG) graph. The spent catalysts exhibited broader DTG profiles, with the weight-loss offset higher in temperature for 1 %Ru/CNF_9000 (≈ 510 °C vs. ≈ 460 °C). This decreased activity for oxidising the support could be ascribed to coke deposits encapsulating the Ru/CNF structure and maybe the NPs too. Peng *et al.* observed a similar trend for AC treated in SCW with isopropanol, with the maximum loss rate was shifted to a higher temperature for the spent material [76]. Harsher testing conditions led to increased coke deposits and/or cokes of higher chemical stability.

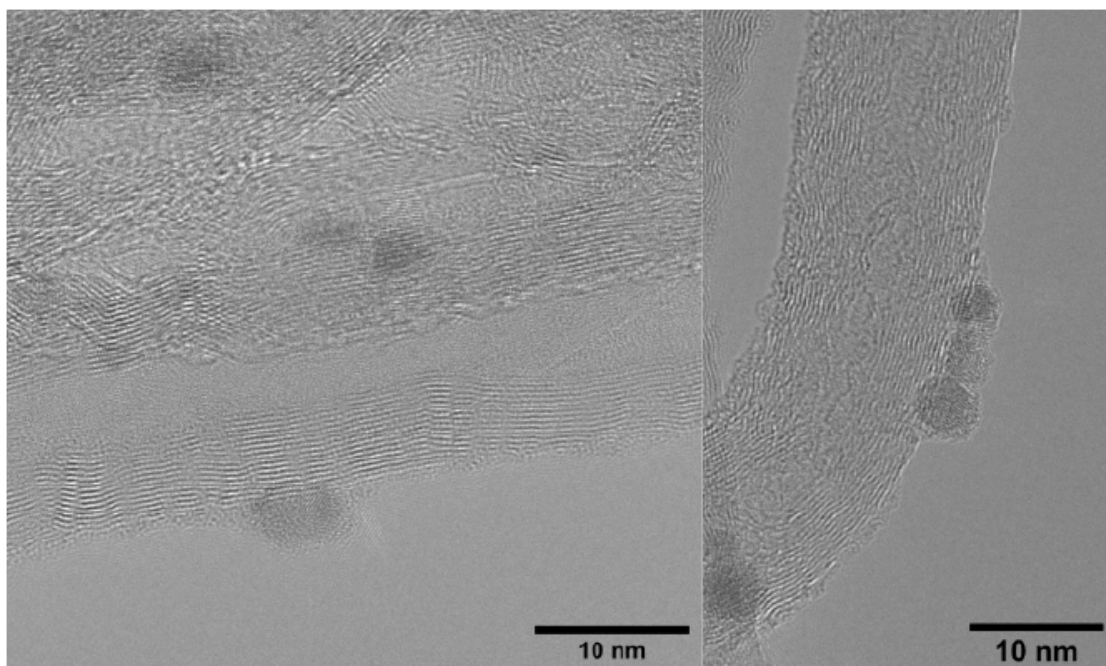


Figure 5.13 – HR-TEM images of the spent 1 %Ru/CNF_2 catalyst ($=9000 \text{ g}_{\text{org}} \text{g}_{\text{Ru}}^{-1} \text{h}^{-1}$, Exp. C21). Magnification: 800kX left, 600kX right.

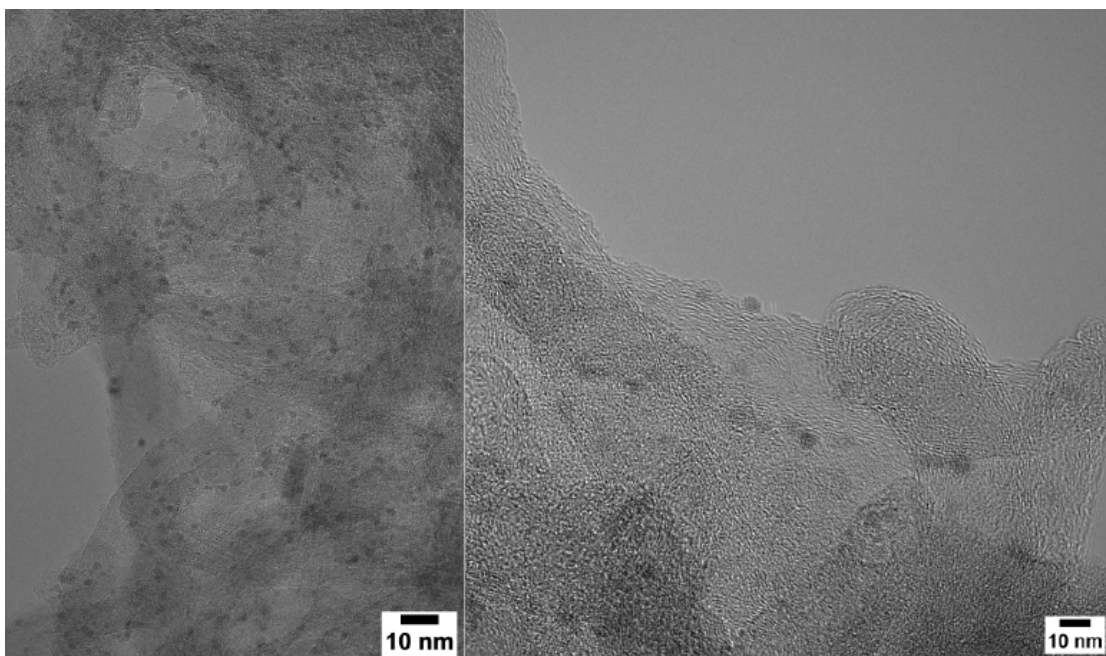


Figure 5.14 – HR-TEM images of the fresh 5 %Ru/CNF_1 catalyst. Magnification: 500kX left, 600kX right.

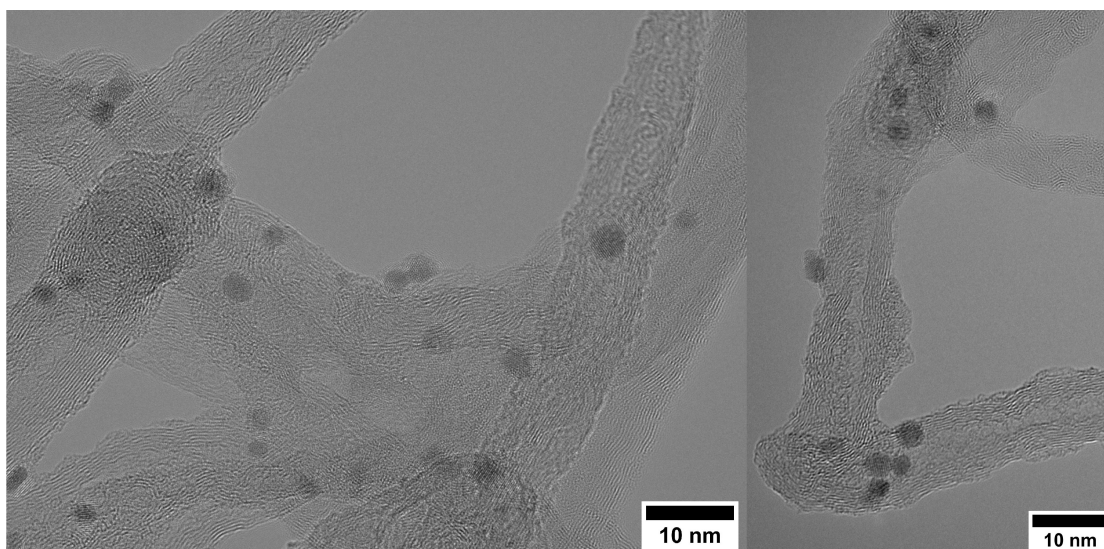


Figure 5.15 – HR-TEM images of the spent 5 %Ru/CNF_1 catalyst ($=4000 \text{ g}_{\text{org}} \text{ g}_{\text{Ru}}^{-1} \text{ h}^{-1}$, Exp. C22). Magnification: 500kX.

However, conventional TEM and even HR-TEM analyses were not very conclusive as no significant coke deposits were observed. The fresh 1 %Ru/CNF_2 catalyst (Figure D.1) and the one treated at $WHSV_{\text{gRu}} = 9000 \text{ g}_{\text{org}} \text{ g}_{\text{Ru}}^{-1} \text{ h}^{-1}$ (Figure 5.13) exhibited no striking differences. The same applied to the 5 %Ru/CNF_1 catalyst (Figures 5.14 and 5.15). To try and elucidate this potential deactivation mechanism, additional experiments were performed in the hope of favouring coke deposition.

5.3 Coking on Ru/CNF catalysts during SCWG

To study the coking deactivation mechanism on CNF-based catalysts during SCWG of glycerol, a new batch of 5 %Ru/CNF catalyst was synthesised. The characteristics of the fresh catalyst are shown in Table 5.3. Again, the main characteristics are very close to the previously-synthesised 5 %Ru/CNF catalysts (Table 5.1), showing the good reproducibility of the synthesis method.

Table 5.3 – Characteristics of the 5 %Ru/CNF_C catalyst

Catalyst	SSA ($m^2 g_{-1}$)	V_p ($cm^3 g_{-1}$)	x_{Ru} (%)	D_{TEM} (%)
5%Ru/CNF_C	278 ± 10	2.0 ± 0.1	4.4	69

Standard deviation: n = 3.

The 5 %Ru/CNF catalyst was then evaluated at different $WHSV_{gRu}$ to investigate the effect of space velocity on sintering and coking. Results from Section 5.2 (Table 5.1) showed a slight increase in $d_{p,TEM}$ for the 1 %Ru/CNF catalyst treated at 3000 and 9000 $g_{org} g_{Ru}^{-1} h^{-1}$. Hence, a similar growth was expected. The experimental conditions are summarised in Table 5.4.

Table 5.4 – Experimental conditions for the 5 %Ru/CNF_C catalyst

Exp.	Conditions	$WHSV_{gRu}$ ($g_{org} g_{Ru}^{-1} h^{-1}$)	m_{cat} (g)	F ($g min^{-1}$)	T (°C)	p (MPa)	x_{gly} (%)
C29	SCW	0	0.31	10.0	400	28.5	0
C30	Thermo ^a	1530	0.32	7.2	403	28.5	5
C31	Far-kin ^b	11120	0.31	12.6	410	28.5	20

^a Thermodynamic regime: $X_C = 100\%$.

^b Far kinetic, or deactivating regime: $X_C < 20\%$.

For the experiment in thermodynamic conditions (Figure 5.16), all the feed was converted to the thermodynamic gas equilibrium composition, as expected. The carbon flow during the experiment is shown in Figure 5.17. For the far-kinetic experiment (deactivating conditions, Figure 5.18), a very high $WHSV_{gRu}$ was applied in order reach lower conversions. This was performed because of the 5 %Ru/CNF catalysts exhibiting high activities and stability due to their small Ru NPs and optimal NP density, as highlighted in the previous section. Conversions reached $\approx 50\%$ at $WHSV_{gRu} \approx 4000 g_{org} g_{Ru}^{-1} h^{-1}$ (see Figure D.10), which can be described as a stable kinetic regime.

This time however, too many organics were fed to the catalyst for it to sustain high conversions. As seen in Figure 5.18, the gas composition changed rapidly with the conversion (decreasing CH_4 , increasing H_2 and CO) up to ≈ 3 h. CH_4 increased again afterwards, however very little

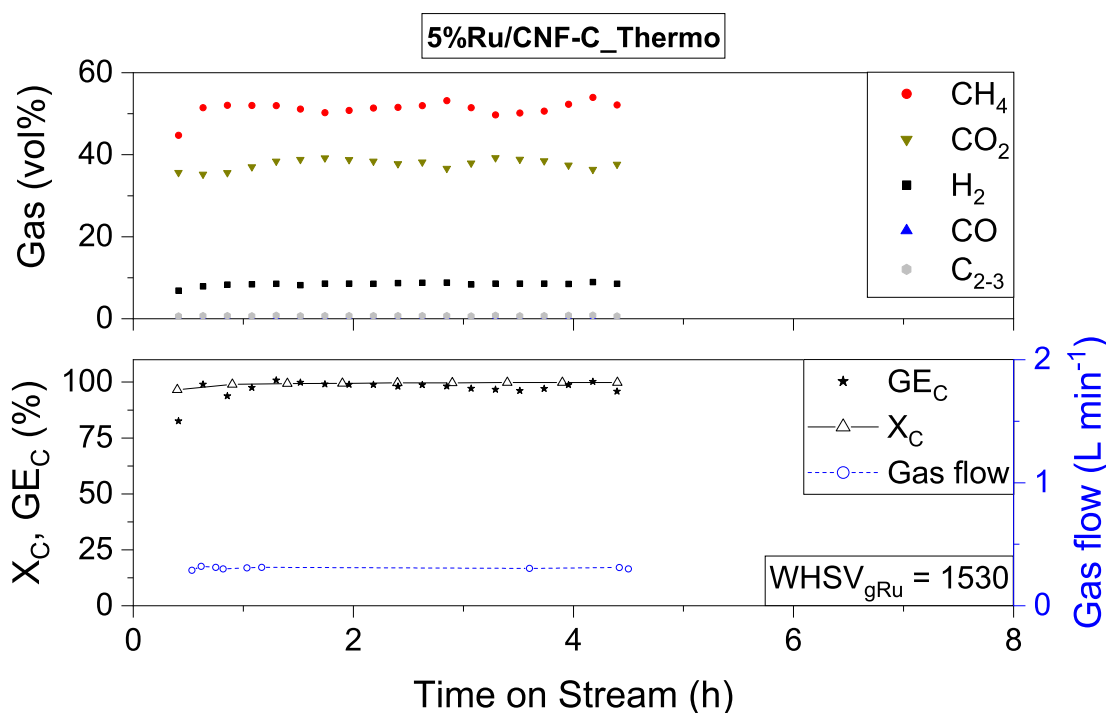


Figure 5.16 – SCWG activity of 5 %Ru/CNF_C at thermodynamic conditions *i.e.* $X_C = 100\%$ (Exp. C30).

gas was produced at this point, suggesting that this behaviour arose from GC measurement inaccuracies because of the very low gas flow. X_C dropped to $\approx 5\%$ and GE_C started decreasing even further after 2.5 h TOS. At this point only little glycerol was converted to the gas phase, indicating a carbon accumulation in the system in the form of coke deposits. This is highlighted with the carbon flow depicted in Figure 5.19.

The spent catalyst samples were analysed by TEM to evaluate the dispersion and coke deposits. The Ru NPs underwent minor sintering (summarised in Figure 5.20), similarly to what was observed with the 1 %Ru/CNF catalyst ($d_{p,TEM} = 1.9$ nm, $WHSV_{gRu} = 9000$ g_{org} g_{Ru}⁻¹ h⁻¹) in Section 5.2. However, the growth was limited small with final Ru NP diameters below 2 nm. From TEM (Figure 5.21), no significant differences were observed between the fresh (a), SCW-treated (b) and spent at $WHSV_{gRu} = 1530$ g_{org} g_{Ru}⁻¹ h⁻¹ (c) samples. Surprisingly, the sample treated at $WHSV_{gRu} = 11\,120$ g_{org} g_{Ru}⁻¹ h⁻¹ (Figure 5.21, d and e) showed the presence of thin sheets or agglomerates covering the CNF. The Ru NP size was not badly affected, however the fibres seemed embedded in these deposits. EDX confirmed that it was carbon as no other heavier elements were detected, supporting the hypothesis that these deposits are indeed coke. It is important to note that some regions were less affected by these deposits, suggesting a non-homogeneous deposition and/or growth around the catalyst. These deposits were

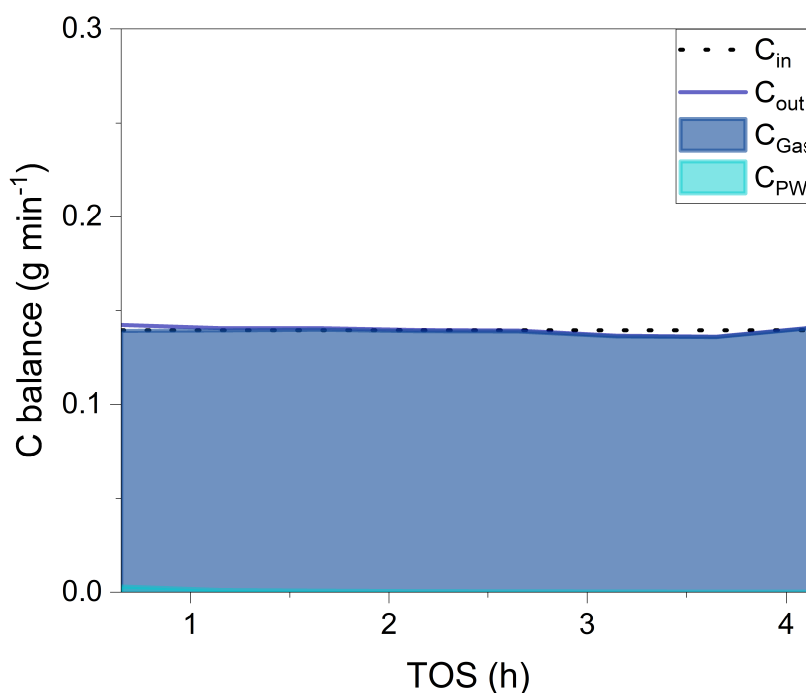


Figure 5.17 – Carbon flow during glycerol SCWG over 5 %Ru/CNF_C at $X_C = 100\%$ (Exp. C30).

only observed at very high $WHSV_{gRu}$, showing the robustness of Ru/CNF catalysts towards deactivation by coking.

Other characterisation techniques were attempted to distinguish coke on the Ru/CNF catalysts, although it is a tricky task to measure carbon species (coke) on other carbon species (CNF). Since coke and CNF do not exhibit the same properties, infrared (DRIFTS) and Raman spectroscopy were attempted with the hope of seeing differences in the carbonyl region (for DRIFTS) and graphitisation degree (for Raman). All DRIFTS spectra looked the same, from the CNF support, to the fresh (5%Ru/CNF_C) and spent ($WHSV_{gRu} = 1530$ and $11\,120\text{ g}_{org}\text{ g}_{Ru}^{-1}\text{ h}^{-1}$) catalysts (see Figure D.15). Concerning the Raman measurements, the spectra were successfully deconvoluted into the different modes (Figure D.16). However, no significant difference could be observed from the different intensity ratios (Figure D.17). This again shows the challenging task of working with carbon-based catalysts.

TGA analyses were also performed on the fresh and spent ($WHSV_{gRu} = 11\,120\text{ g}_{org}\text{ g}_{Ru}^{-1}\text{ h}^{-1}$) 5 %Ru/CNF_C catalysts. Figure 5.22 shows the considerable difference in weight loss patterns. Although the fresh and spent catalysts underwent a similar initial loss pattern with a main mode at $\approx 500^\circ\text{C}$, the spent sample was less active and required higher temperatures to get fully oxidised. A second contribution was observed at $\approx 600^\circ\text{C}$, which was probably due to coke deposits. The difference between both 5 %Ru/CNF samples was less striking than for

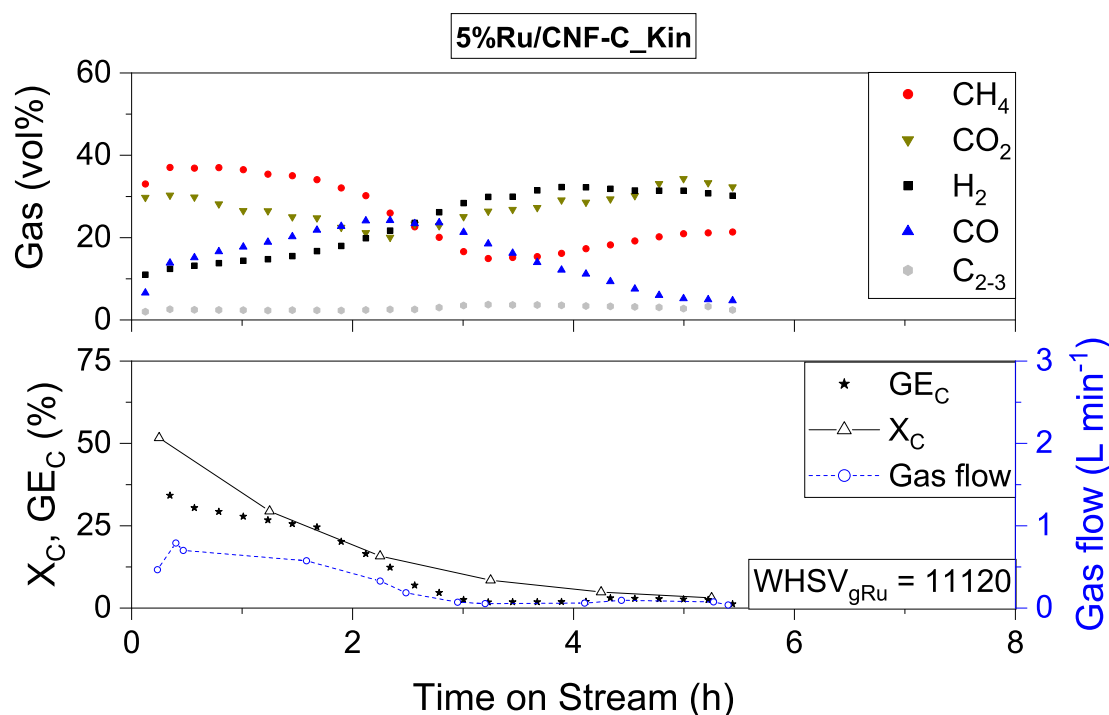


Figure 5.18 – SCWG activity of 5 %Ru/CNF_C at kinetic conditions *i.e.* $X_C < 50\%$ (Exp. C31).

the 1 %Ru/CNF_2 (Figure 5.12) because of the difference in Ru loading. Although no coke deposits were observed on the different regions analysed of the 1 %Ru/CNF_2 catalyst, it does not mean that they were not present since only a small fraction of the sample is analysed by TEM. The lower space velocity (9000 vs. 11 000 $\text{g}_{\text{org}} \text{g}_{\text{Ru}}^{-1} \text{h}^{-1}$) could also be a reason.

In a effort to understand the mechanisms as well as the molecules involved in coking and eventually catalyst deactivation, a parallel project was initiated within our research group. The goal was to couple the catalytic experiments to high-performance, high-resolution LC-MS analytical techniques. For this, the spent catalyst samples were extracted in a mix of solvents (methanol, acetone, toluene, chloroform), the extracts together with the PWs were analysed by LC-MS, this procedure was described in a recent study from our group [112]. The very first results showed different types of compounds for the different testing conditions, with molecules of higher unsaturation measured in the PWs of the high- $WHSV_{\text{gRu}}$ experiments. More aromatic species were also observed, showing the potential pathway towards coke formation and catalyst deactivation. Blank experiments on CNF yielded no aromatics, showing that the Ru catalyst was active (directly or indirectly) in the formation of aromatics at low X_C . The analysed catalyst extracts contained mainly aromatic species, suggesting that coke deposits could partially be removed. Again, blanks were performed to validate the data. TEM was performed on the extracted Ru/CNF samples (Figure 5.23) and confirmed that these coke deposits could be removed. Although the deposits were not totally removed, they appeared

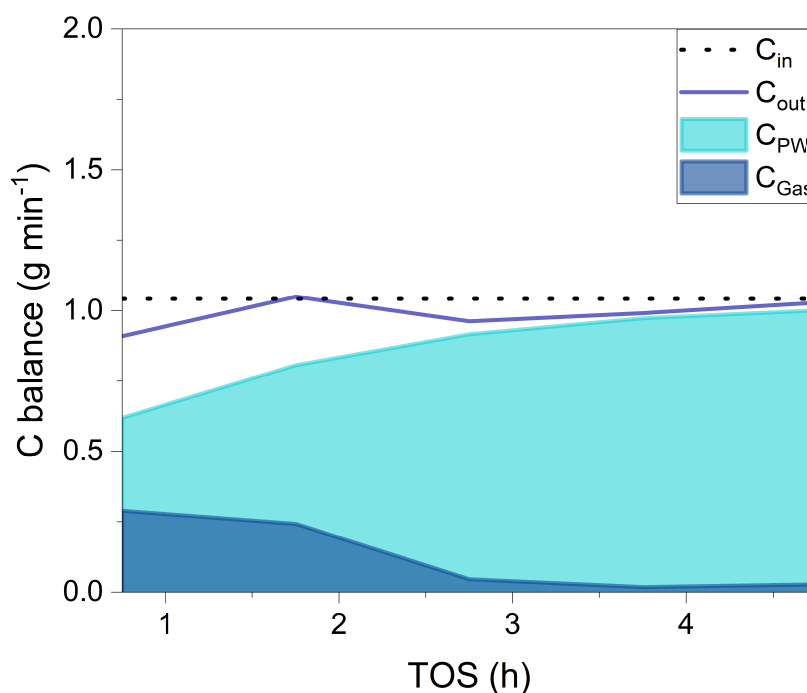


Figure 5.19 – Carbon flow during glycerol SCWG over 5 %Ru/CNF_C at $X_C < 50\%$ (Exp. C31).

considerably thinner (increased transparency). Furthermore, the CNF and Ru NPs seemed unaffected in terms of morphology and size.

These are the very first results of this parallel study, therefore limited data is available at the time of writing. Further analyses on the main compounds present in PWs and in catalyst extracts are ongoing. However, the extraction procedure successfully removed parts of the deposits, which is a very promising result for the ongoing study and potential catalyst regeneration in mild conditions.

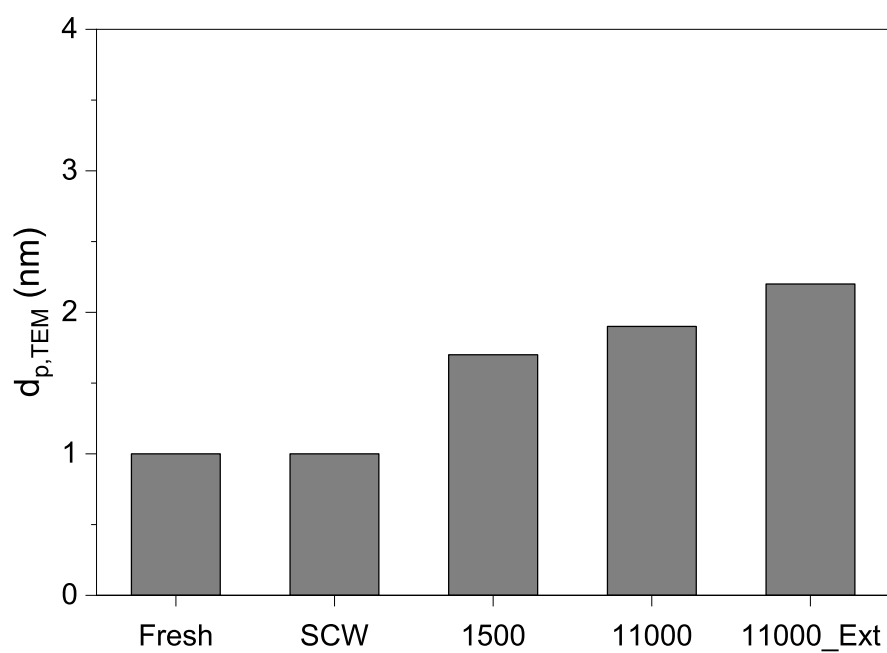


Figure 5.20 – Evolution of $d_{p,TEM}$ for the different experiments with 5 %Ru/CNF_C and for the extracted catalyst sample.

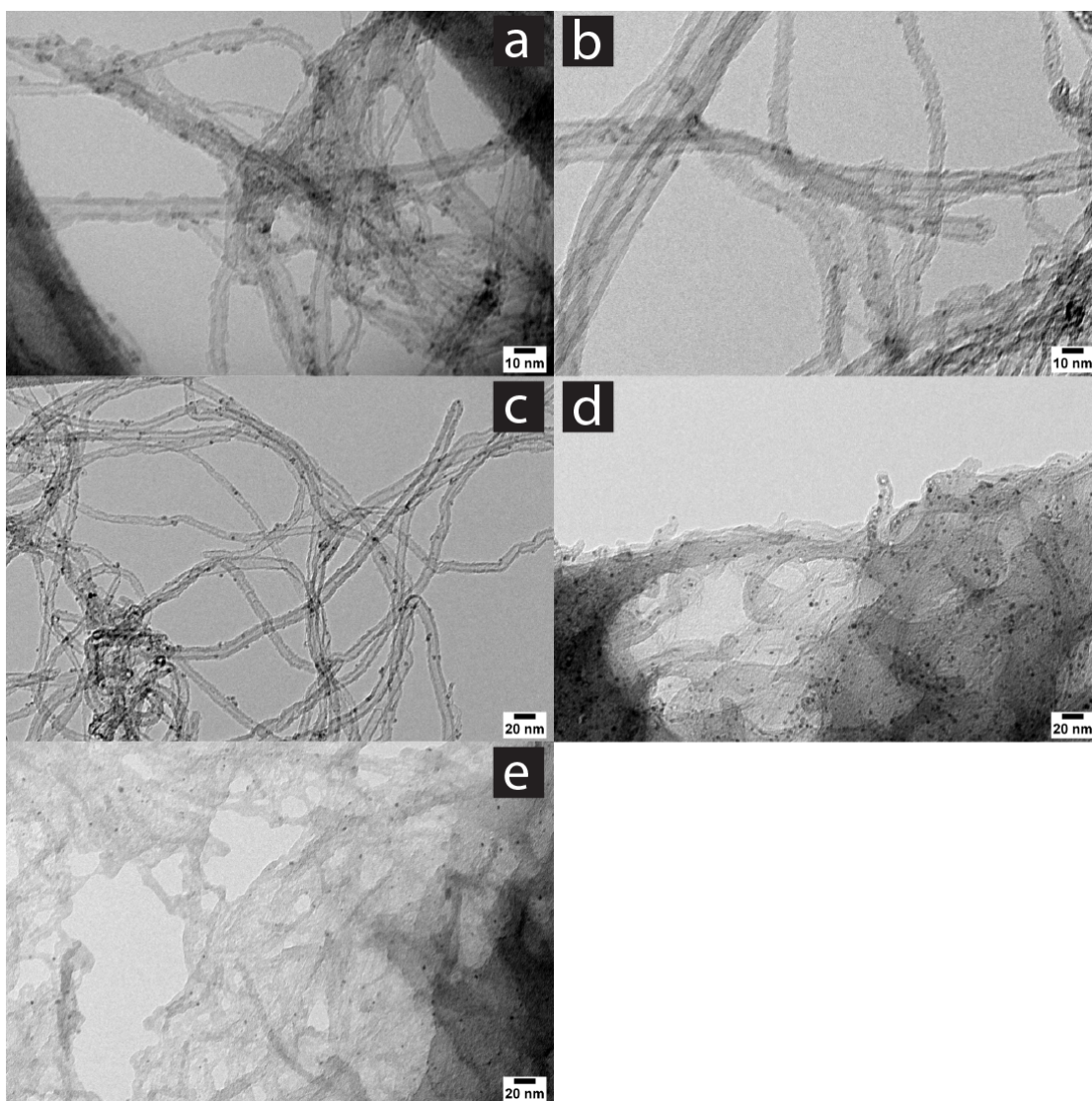


Figure 5.21 – TEM images of the fresh 5 %Ru/CNF_C catalyst (a), treated in SCW (b), spent at 1500 g_{org} g_{Ru}⁻¹ h⁻¹ (c), spent at 11000 g_{org} g_{Ru}⁻¹ h⁻¹ (d, e). 100kX magnification for a and b, 50kX for c, d and e.

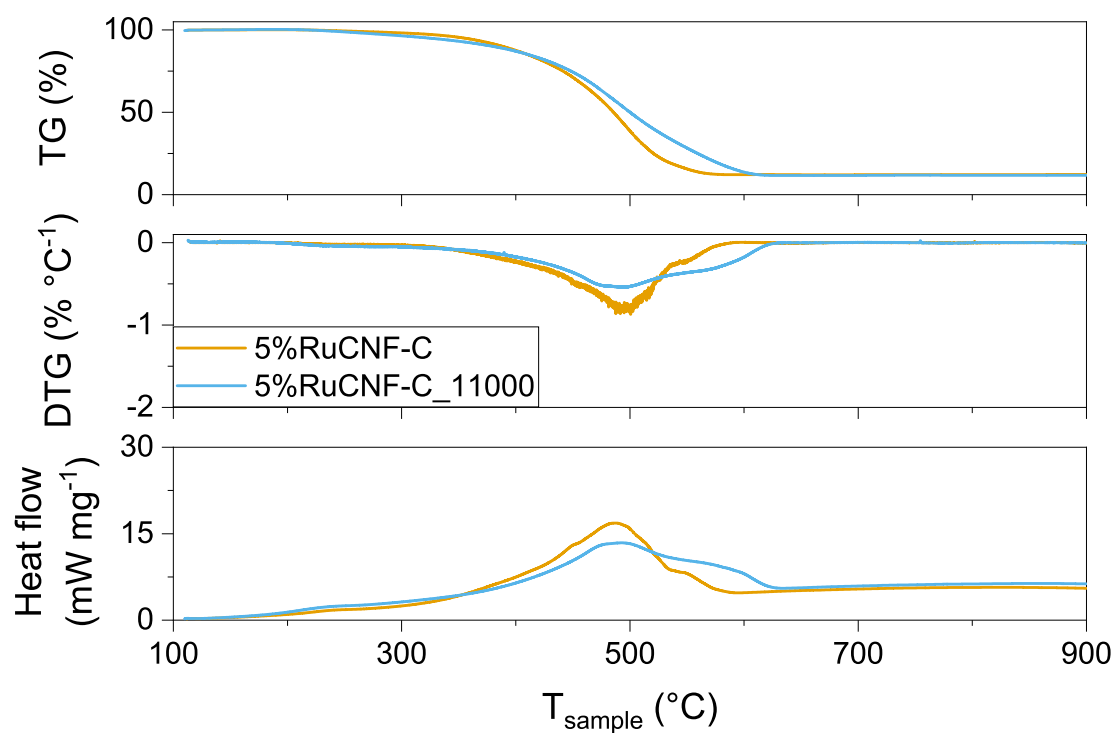


Figure 5.22 – Thermogravimetric (TG, top), differential weight loss (DTG, middle) and heat flow (bottom) analyses for the fresh and spent (Exp. C31) 5 %Ru/CNF catalysts. Conditions: 10 mg sample, air (10 mL min^{-1}), $5^\circ \text{C min}^{-1}$ ramp.

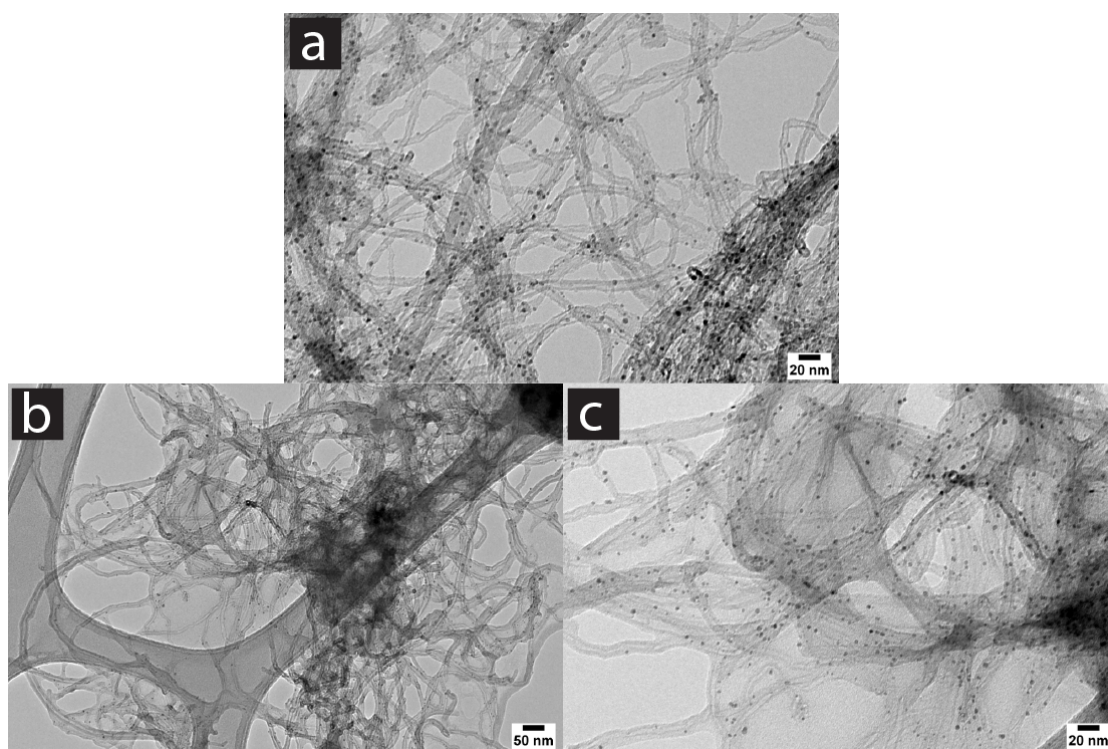


Figure 5.23 – TEM images of the 5%Ru/CNF_C catalyst treated at $11000 \text{ g}_{\text{org}} \text{g}_{\text{Ru}}^{-1} \text{h}^{-1}$ and extracted in a mix of solvents (MagicMix). 50kX magnification for a and c, 20kX for b.

5.4 Ru loss from CNF-supported catalysts

The stability of the Ru/CNF catalysts was also investigated by quantifying Ru in the process waters by time-resolved ICP-MS on selected catalysts. The high stability of Ru on activated carbon was shown in Chapter 4, with measured concentrations ($0.02\text{--}0.2\ \mu\text{g L}^{-1}$) being close to thermodynamic models [104]. However, CNF is more inert than ACs due to its well-defined structure and could lead to weaker metal-support interactions [170], [171]. For this reason the Ru loss was also quantified from Ru/CNF catalysts, with the results presented in Figure 5.24.

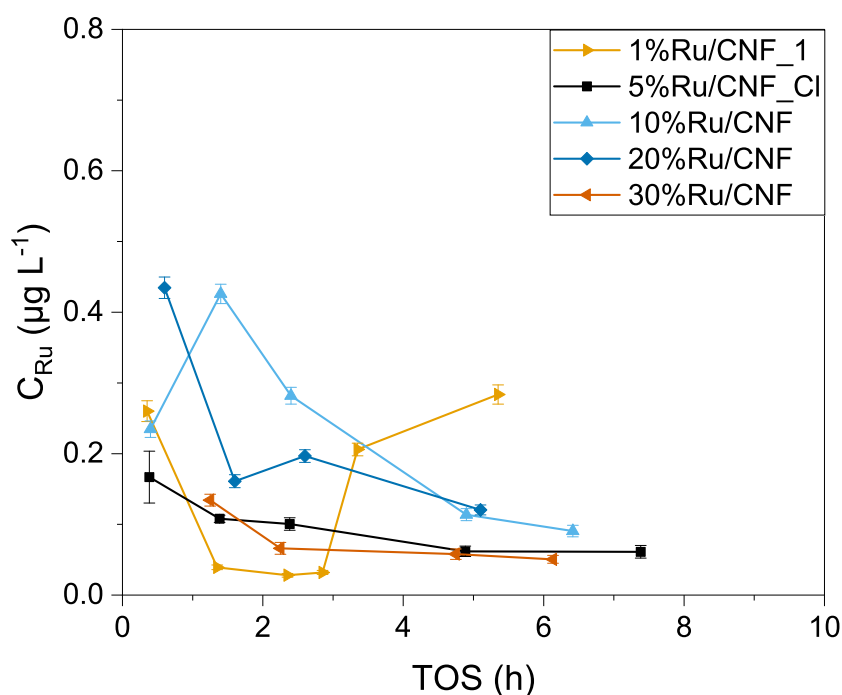


Figure 5.24 – Ru loss as a function of time on stream for selected Ru/CNF catalysts (Exp. C20,C23,C24,C26,C27).

All catalysts exhibited the same Ru loss trend *i.e.* higher amounts at the start that stabilised in the range $0.06\text{--}0.12\ \mu\text{g L}^{-1}$, except for 1 %Ru/CNF_1. The measured concentrations were in the same range as what was measured for Ru/AC, showing the good stability of Ru/CNF as well. For the 1 %Ru/CNF_1 catalyst, although the initial Ru loss followed the same trend as for the other ones, the Ru loss suddenly increased after 3 h TOS. Interestingly, the Ru loss trend mirrored the carbon conversion (Figure 5.25). However, this was only the case for the 1 %Ru/CNF_1 catalyst as the other samples underwent exponential-like decreases in conversion as well as in Ru loss. The reason for this behaviour could either be linked to the sudden loss in activity, or vice-versa. The cumulated Ru loss during the whole run only amounted to 0.004 % (and 0.002 % up to the sudden increase) of the Ru loaded in the reactor, suggesting that the rapid deactivation led to an increased Ru loss and not the other way round. The chemistry around

the NPs changed very rapidly, with a decreased gasification ability replacing the produced gas by glycerol and its degradation products as well as carbon deposits at the catalyst surface.

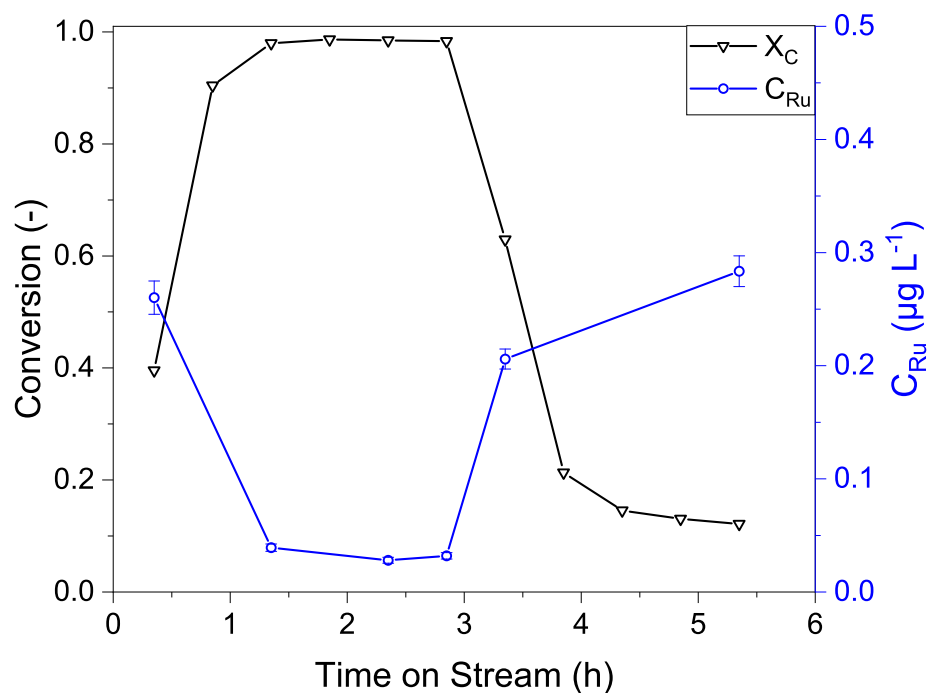


Figure 5.25 – X_C and Ru loss as a function of time on stream for 1 %Ru/CNF_1 (Exp. C20).

5.5 Comparison Ru/CNF vs. Ru/AC

CNF-based catalysts showed interesting gasification activities and good stability. However, as the goal of this work was to find a catalyst exhibiting an enhanced activity and stability in comparison to the previous AC-based catalysts, it was compared with the new benchmark catalyst Ru/AC-A. The latter was tested in similar conditions as shown in Figure 5.26. The benchmark catalyst exhibited a good gasification activity and overall stability. The methane selectivity remained high (≈ 45 vol%) and X_C stabilised at ≈ 30 %. Also, the GE_C and X_C overlapped during the whole run, indicating no carbon accumulation in the system during the experiment. The carbon balance is fully closed as shown in Figure 5.27 with the carbon flow.

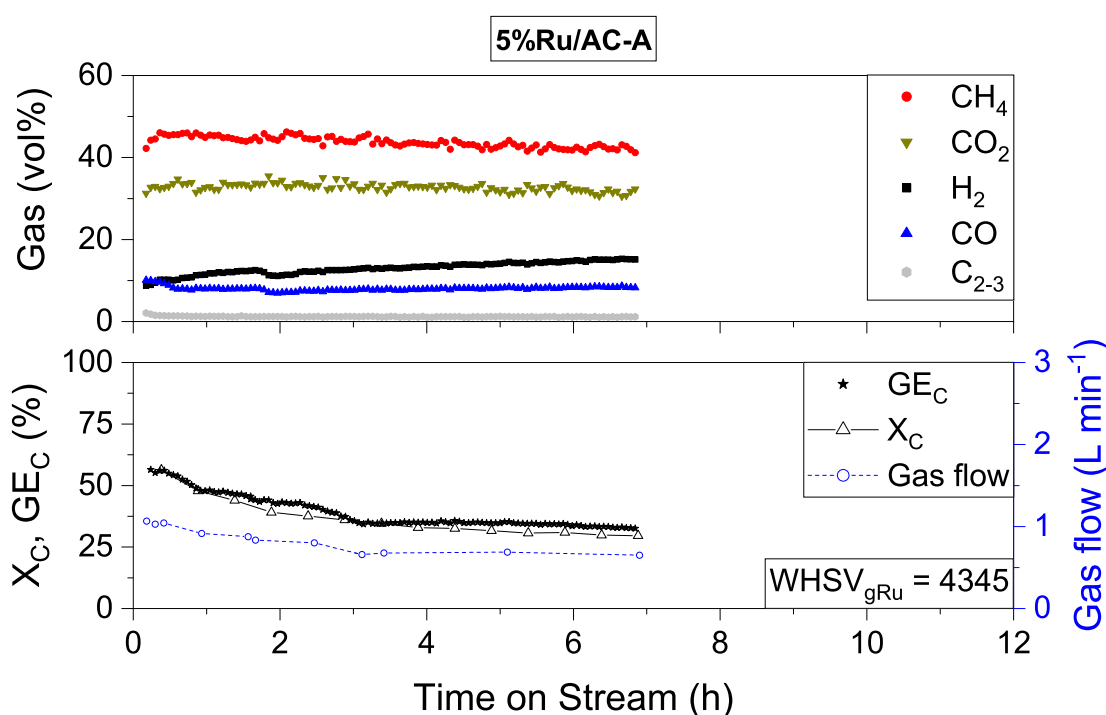


Figure 5.26 – SCWG activity of 5 %Ru/AC-A. Conditions: 20 % glycerol, $F = 10.6 \text{ g min}^{-1}$, $p = 28.5 \text{ MPa}$, $T = 405^\circ \text{C}$ (Exp. C28).

Compared to the 5 %Ru/CNF catalysts evaluated in Section 5.2, Ru/AC-A stabilised at lower X_C but still maintained a high CH_4 selectivity. A more exhaustive comparison is shown in Table 5.5. In terms of TOF, all three catalysts exhibited similar values in the range $52\text{--}59 \text{ min}^{-1}$, with Ru/AC-A being the most active catalyst. It is important to note that the Ru/AC-A dispersion was significantly lower than the ones of Ru/CNF. Unfortunately, the quality of the TEM data available for Ru/AC was not good enough to perform a thorough PSD, certainly because of the high AC density leading to lower contrasts in bright-field mode. For this reason, D_{CO} was reported.

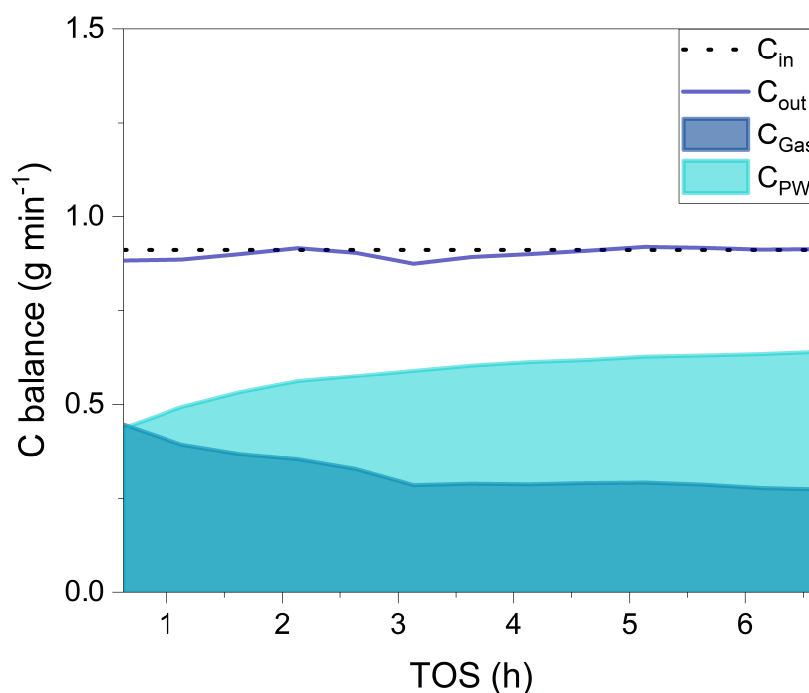


Figure 5.27 – Carbon flow during SCWG of glycerol over 5 %Ru/AC-A in kinetic regime (Exp. C28).

Finally, 5 %Ru/CNF and 5 %Ru/AC-A exhibited similar activity and stability. The CNF-based catalysts seemed slightly more active and more stable, which could be expected because of their high Ru dispersions. Ru/AC-A was considerably more stable than its CNF-based analogues of lower D_{TEM} , showing why AC-supported catalysts remain of such interest for SCWG.

Table 5.5 – Comparison between Ru/CNF and Ru/AC catalysts

Exp.	Catalyst	D_{TEM}	$WHSV_{gRu}$	$X_{C,end}$	TOF_{end}^a	y_{CH_4}	y_{CO}	x_{gly}
		(%)	($g_{Org} g_{Ru}^{-1} h^{-1}$)	(%)	(min^{-1})	(vol%)		(%)
C28	5 %Ru/AC-A	40 ^b	4345	30	59	42	8	20
C22	5 %Ru/CNF_1	67	4228	42	52	44	11	20
C23	5 %Ru/CNF_Cl	69	4160	51	54	37	8	10

^a Calculated from the fresh catalyst dispersions.

^b D_{CO} instead of D_{TEM} .

5.6 Summary

In this chapter, CNF-supported Ru catalysts were investigated as potential SCWG catalysts. CNF was used for its inertness, facilitated study by TEM and also for the possibility of achieving high metal loadings. With this catalytic system, deactivation mechanisms were investigated in more detail, such as sintering and coking. Ru loss was also investigated since the more inert support in CNF could lead to a decreased metal-support interaction and hence loss of Ru NPs. The main conclusions are listed below:

- Small Ru NPs (1 nm) of mono-modal distributions were successfully synthesised on a CNF support with a facile synthesis method. High loadings of up to 30 % were achieved with mean Ru NPs of 2.2 nm, showing the very interesting properties of CNF as catalyst support.
- The catalytic activity and stability of Ru/CNF of increasing particle sizes were assessed on *Konti-I*, with the highest dispersions leading to the highest initial TOFs. A particle size effect was clearly observed in SCWG for the first time.
- The dispersion was responsible for the high initial TOFs, but could not sustain a high activity as low-loading catalysts (1 %Ru/CNF) exhibited a poor stability, leading to very rapid deactivation and hence the lowest final TOFs.
- The surface Ru atom density appeared to be a very important parameter too, as 5 %Ru/CNF catalysts (of similar Ru NP size as 1 %Ru/CNF) exhibited the best combined activity and stability. The optimum density was found between 0.4 and 0.7 $\text{atom}_{\text{Ru,sfc}} \text{nm}^{-2}$, representing 5–10 % loading and ≈ 2 nm diameter.
- Minor sintering was observed for all Ru/CNF catalysts and was induced by the catalytic reaction. The SCW environment did not lead to Ru NP growth.
- Ru/CNF synthesised from a chloride precursor exhibited the best catalytic activity, showing that chloride poisoning was not an issue in this system.
- Globally, a similar activity was recorded for both 5 % Ru/CNF and Ru/AC catalysts, with Ru/CNF showing a slightly better stability.
- Coke was observed by TEM after treating Ru/CNF at very high $WHSV_{gRu}$. An extraction procedure by a mix of solvents partly removed the deposited carbon without affecting the CNF structure or Ru NP size, showing a potential regeneration route for Ru/C catalysts.

6 Concluding remarks and outlook

6.1 Achieved results

In this work, we showed the importance of investigating Ru-based catalysts in a model system to acquire more insight on the governing deactivation mechanisms in continuous SCWG. Examining catalysts in SCW conditions is a complex task because of the high temperatures and pressures. Therefore, catalysts are analysed *ex situ* and not *in situ*, making it complicated to discriminate between the different processes leading to the loss of activity. Here, we tried to look at every part of the catalyst individually to isolate the different mechanisms occurring during catalytic SCWG and better understand the intrinsic activity of the support and active phase, within the constraints of a continuous SCWG system. First, the carbon support was assessed with and without Ru in order to find an optimal catalyst support exhibiting increased stability during SCWG. Secondly, the ruthenium loss was investigated from commercial and in-house catalysts. Finally, sintering, coking and particle size effects were investigated on an ideal Ru/CNF system to better understand the implications of these different mechanisms on catalyst activity and stability and see whether this new system can outperform the well-established Ru/AC.

The starting point was set on the carbon support. Coking is known to be a serious deactivation mechanism during SCWG of biomass and also model compounds, as it blocks the pores of AC leading to rapid losses in surface area. The activated carbon support was known to exhibit non-negligible gasification activity, but without truly knowing how it affected a supported catalyst. For this reason, the intrinsic gasification activity of carbon supports of different properties was investigated during SCWG of glycerol. Interestingly, catalyst-grade ACs exhibiting mainly micropores were found to have high initial activities, before deactivating rapidly. The cause was the high surface area generated from the micropores which were rapidly blocked (90 % SSA decrease), leading to a complete loss of activity. On the contrary carbons hav-

ing higher fractions of mesopores were less prone to blockage and exhibited higher carbon conversions normalised per surface area, compared to microporous ACs. The example of AC-CGRAN showed that the presence of mesopores could hinder a rapid deactivation through pore blockage, even though it possessed $\approx 60\%$ micropores. Eventually, CNF was investigated too after initial results from de Vlieger showed that its completely open pore structure may be beneficial as SCWG catalyst support [80], [81]. Our results confirmed these findings, as CNF was almost inert (1–2 % conversion) and its SSA and pore volume unaffected. These initial results demonstrated the undesired effect of micropores in AC supports for SCWG applications. Also, CNF seemed to be a promising catalyst support for its lack of micropores, but also for its inertness and stability in this environment. Impregnation of ruthenium on selected supports and subsequent assessment during SCWG of glycerol confirmed the initial results, with the CNF-based catalyst being significantly more stable. An "active" support in SCWG is not thought to be required and would actually be undesired, as shown with CNF. Indeed, the support inertness did not hinder the SCWG performance of the CNF-based catalyst. Although active supports do participate in the decomposition of organics, this "pre-decomposition" by the carbon surface is not required and would inevitably lead to carbon deposition on the catalyst support. These results show that there is an alternative to AC as catalyst support in CNF, which considerably hinders the coke formation mechanism and can thus lead to more robust catalysts.

Focussing on another deactivation mechanism, the loss of active phase was very rarely investigated for Ru catalysts during SCWG. SCW is known to be a harsh environment capable of oxidising or dissolving metal catalysts. With Ru being one of the least soluble metals in SCW [100], [154], high-end analytical techniques are required to detect Ru in process waters. We were able to show this with low-LoD time-resolved ICP-MS, with which we successfully quantified Ru in the effluent stream of gasification experiments. Steady-state concentrations from Ru/AC catalysts were found to be very low, in the range $0.01\text{--}0.04\text{ }\mu\text{g L}^{-1}$ regardless of temperature, feed concentration, feed rate or catalyst loading. Furthermore, measured Ru concentrations were one order of magnitude higher than thermodynamic equilibrium models, showing that leaching is the main loss mechanisms and that it is governed by thermodynamics. Concentrations spikes leading to 100-fold increases in Ru concentration were also observed and mainly linked to changes in process parameters, suggesting that alterations in flow rate and pressure could lead to increased Ru loss due to collisions between catalyst grains. This was confirmed by intentionally varying the pressure and feed rate, which led to a six-fold increase in Ru in the process waters. Also, non-negligible amounts of carbon (and Ru) were recovered from the $15\text{ }\mu\text{m}$ frit, emphasising the negative effect of non-steady-state operation. The type of Ru loss could clearly be discriminated between leaching (thermodynamic) and mechanical (friction). The commercial Ru/AC-A catalyst tested on *Konti-I* with glycerol and

on the *intermediate* rig with glycerol and sewage sludge underwent similar Ru loss rates, in the range $0.14\text{--}0.29\text{ }\mu\text{g g}_{\text{Ru}}^{-1}\text{ h}^{-1}$. These results confirmed that the Ru/AC catalyst maintained its good stability towards Ru NPs when real biomass was fed. As AC was shown to be limited by its brittleness in non-steady-state operation, metal oxide-supported catalysts were analysed for their activity and stability during glycerol gasification. Not only was Ru/AC the most active and stable catalyst, it also exhibited the lowest Ru loss with 20–40 times less Ru quantified in the PWs in comparison to Ru/ZrO₂, Ru/Al₂O₃ and RuTiO₂. These findings are very relevant to the field of catalytic SCWG, showing that AC-supported Ru catalysts lead to the lowest Ru loss. With this quantified loss being very close, if not at thermodynamic equilibrium, there is almost no room for improvement regarding the stability of Ru NPs on AC. With this study, we are the first to thoroughly analyse Ru loss during catalytic SCWG.

Regarding other deactivation mechanisms such as coking or sintering, they were investigated on Ru/CNF catalysts because of the inertness of the support, its absence of micropores and the higher contrasts for TEM. At first, we were successful in synthesising a series of Ru/CNF catalysts of mono-modal NP size distributions between 0.9 and 2.2 nm with an easy synthesis method. Ru/CNF catalysts proved to be very active in SCWG of glycerol, with the high dispersions being responsible for the good initial activities. However, Ru catalysts of low loading (1 %) deactivated rapidly compared to 5–10 % catalysts, showing that the dispersion is not the only reason for enhanced activity and stability. Indeed, the surface Ru atom density was found to be more important to ensure a good stability. A volcano-shaped trend related the TOF to the surface Ru density, with an optimum between 0.4 and 0.7 atom_{Ru,sfc} nm⁻². Due to high dispersions and optimal surface Ru densities, 5 %Ru/CNF performed extremely well during glycerol gasification at high space velocity. We also showed that all catalysts underwent minor particle growth being due to the gasification conditions, and not the SCW environment. Coke deposition was observed at very high space velocities and could partly be removed by extraction in a mix of solvents, opening a route for a potential regeneration mechanism. The analysis of the PWs and catalyst extracts will generate new insights into coking mechanisms in SCWG conditions in the near future. Globally, we managed to synthesise a new catalyst outperforming a commercial benchmark Ru/AC thanks to its high metal dispersion and optimal active site density, leading to an enhanced stability during SCWG of glycerol. For now, Ru/CNF catalysts have only been synthesised and evaluated on the gram scale. Further experiments on larger scales will hopefully show the usefulness of this new catalyst.

6.2 Conclusions

Besed on the results presented in this thesis, the following conclusions were drawn. The pore network of carbon supports for SCWG catalysts was an important factor regarding carbon deposition. Catalyst supports exhibiting high fractions of micropores (>80 %) were subject to

drastic surface area losses, which was not the case for supports exhibiting larger pore structures (meso-/macropores). When impregnated with ruthenium, the same trend was observed. Indeed, catalysts exhibiting lower fractions of micropores showed an increased stability during SCWG of glycerol. This was the case for a support having $\approx 30\%$ mesopores (AC-CGRAN) and one having only macropores (CNF), evidencing the negative effect of micropores for catalyst stability.

While deactivation mechanisms are difficult to disentangle in SCWG conditions, we managed to show the individual contributions of leaching, sintering and coking. The former was successfully monitored on different types of catalysts (Ru supported on AC, CNF, TiO_2 , ZrO_2 , $\alpha\text{-Al}_2\text{O}_3$). From these results we concluded that carbon-based catalysts exhibited the best Ru NP stability with Ru losses close to thermodynamic equilibrium models, indicating that leaching is the main loss mechanisms at steady state and is only governed by thermodynamics. However, the Ru loss increased when the process conditions were not stable (fluctuating feed rate and pressure) leading to six times more Ru loss versus steady state. Furthermore, sudden peaks in Ru signal showed up to 100-fold increases in Ru concentration. We thus concluded that pressure and flow variations irreversibly damaged the Ru/AC catalyst, inducing the loss of carbon domains containing Ru NPs through friction. The main learning from these results is to operate SCWG plants as smoothly as possible, without flow or pressure variations to protect the catalyst bed. This will become increasingly important on larger-scale units or commercial plants.

To deal with the limitations of ACs in terms of catalyst characterisation, new SCWG catalysts were synthesised on CNF, which already showed promising results for SCWG. Ru/CNF proved to be an alternative to AC-based catalysts, thanks to their good stability in SCW, propensity to form small Ru NPs and lack of micropores. Coke deposits were only observed at very high space velocities, showing the advantage of using a more inert catalyst support without micropores. With this system, we were able to show a particle size effect during SCWG for the first time, with highly dispersed catalysts leading to high initial turnover frequencies. However, due to the different behaviours of the catalysts, the high dispersions alone did not guarantee a high steady-state activity. We thus concluded that the density of surface atoms played an important role in maintaining high gasification activities during the experiment. A combined effect of high dispersion and surface NP density seemed to govern the catalyst stability.

We hereby showed that CNF could be used as SCWG catalyst support, leading to better performances and easier characterisation than conventional Ru/AC catalysts. This work hence opens a new path towards catalyst design for SCWG processes. Tailoring catalysts of optimal

loading and Ru particle size may be an important step to achieve longer lifetimes and hence increase the economic viability of SCWG.

6.3 Recommendations for further research

Although the role of the carbon support is now better understood, an open question still remains regarding the effect of the support graphitisation on the catalyst activity. Several studies linked the graphitisation degree to improved Ru/C activity in the ammonia synthesis reactions [172]–[174]. This effect was not evaluated during this work even though AC and CNF were investigated. The main difficulty would be to synthesise Ru NPs of same sizes on the differently graphitised supports to exclude a particle size effect. A more thorough study could shed some light on the effect of graphitisation.

Ruthenium leaching was mainly investigated in model conditions, hence it would be interesting to broaden this study to other feedstocks to check if Ru remains as stable in the presence of larger amounts of sulfur species for example. Even though the measured Ru loss was in the same range for glycerol and sewage sludge gasification, the latter experiment still exhibited slightly higher losses. A series of experiments with sulfur model compounds could be performed to confirm whether Ru-S complexes would lead to increased Ru losses. Also, the observed Ru loss from 1 %Ru/CNF significantly increased when the catalyst activity drastically dropped, almost mirroring the carbon conversion. This effect is not yet understood and further experiments are required to get additional insight on the effect of a sudden change in chemistry on the Ru NP stability.

Ru/CNF catalysts are a very promising alternative to Ru/AC, as investigated on a 1 g scale with model solutions. To confirm these findings, Ru/CNF synthesis should be attempted on a larger scale to evaluate the feasibility of using such a catalyst in a 50–100 g bed or even larger. If successful, these findings could be very important for the economic viability of catalytic HTG since the catalyst could exhibit considerably longer lifetimes.

The effect of Ru NP density was presented here, however more data would be useful to corroborate these conclusions and find the true optimum between 0.4 and 0.7 atom_{Ru,sfc} nm⁻². Regarding the particle size effect, it would be interesting to see whether very small Ru NPs (single atoms) exhibit a poor activity due to the lack of *B*₅ sites.

Using a chloride salt as ruthenium precursor was reported problematic in terms of larger

Chapter 6. Concluding remarks and outlook

Ru NPs and/or poisoning leading to lower gasification activity [76], [77]. This issue was not encountered with CNF-based catalysts, hence a study linking the removal of chloride to the type of carbon could be performed to check whether the chloride preferentially remains in microporous activated carbons, and whether specific treatments can solve this issue.

A Konti-I setup

A.1 Setup control

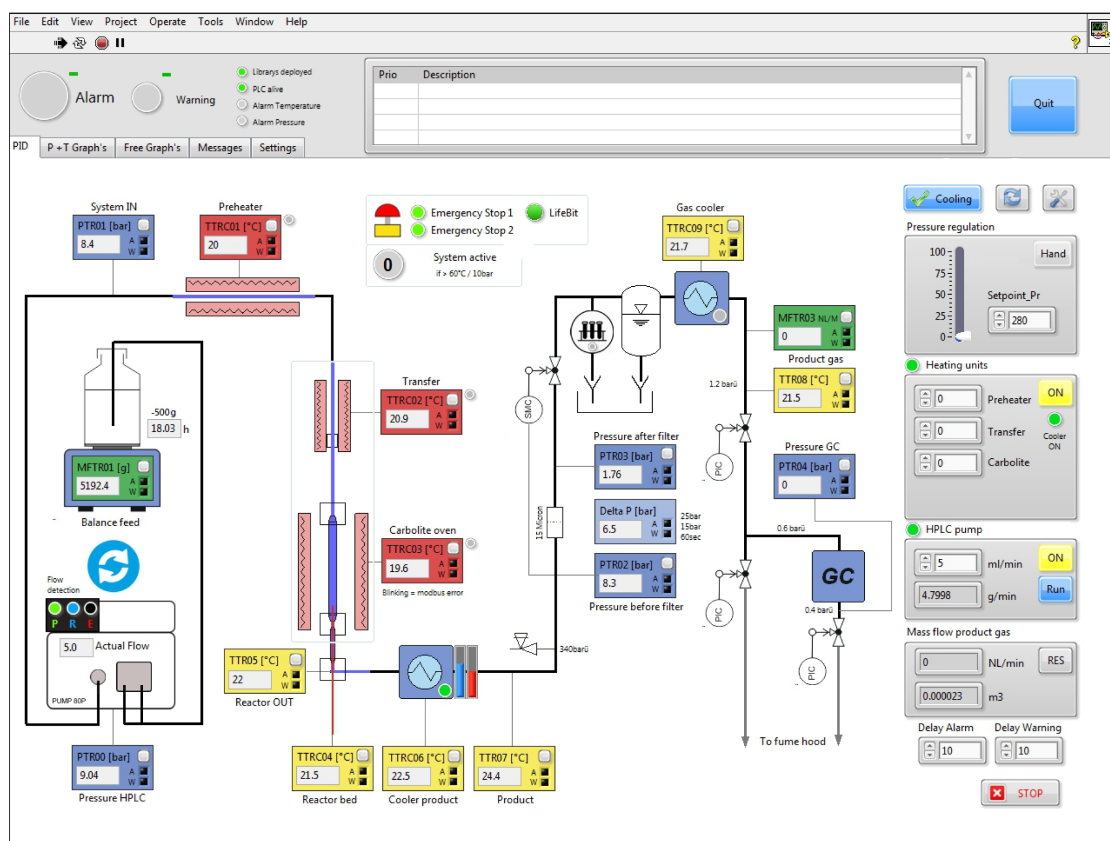


Figure A.1 – Screenshot of the main LabVIEW™ interface controlling *Konti-I*.

A.1. Setup control

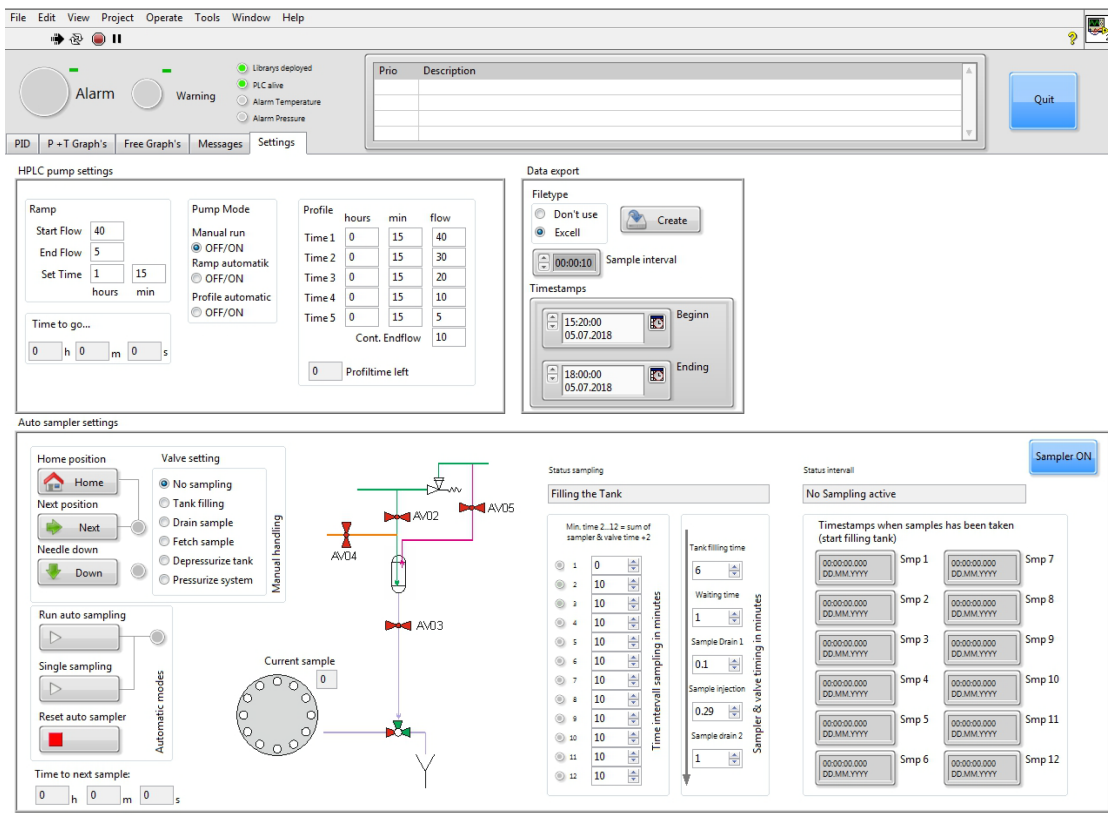


Figure A.3 – LabVIEW™ settings for the automated sampling and data export.

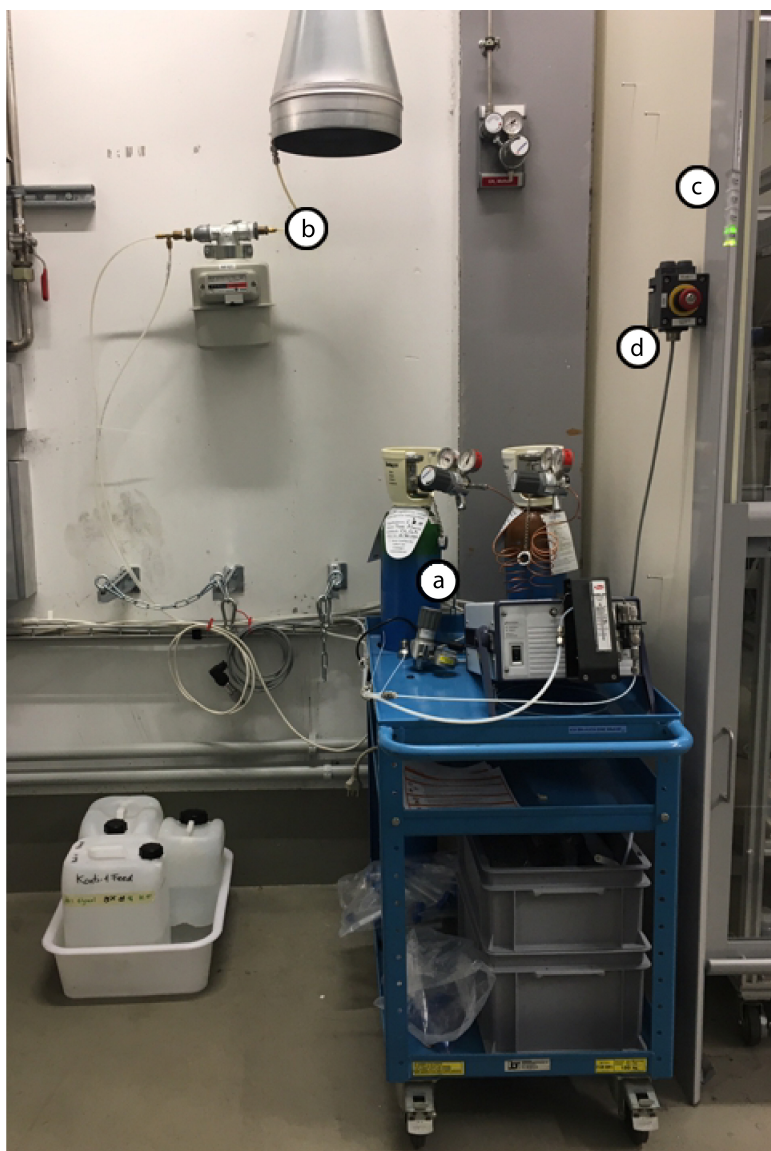


Figure A.4 – Side installations of *Konti-I* : μ GC (a), gas counter (b), fumehood controls (c), emergency stop (d).

A.2 List of experiments

Table A.1 – Experiments discussed in Chapters 3 and 4

Exp.	Material	x_{Ru} (%)	D_{CO} (%)	D_{TEM} (%)	d_p (nm)	m (g)	T (°C)	p (MPa)	x_{Gly} (%)	F ($g\,min^{-1}$)	$WHSV_{gRu}$ ($g_{org}\,g_{Ru}^{-1}\,h^{-1}$)	TOS (h)
B	Blank	-	-	-	-	-	401	29	10	5	-	24
S1	AC-BASF	-	-	-	-	3.22	401	29	9.6	5-10	-	5
S2	AC-Spher	-	-	-	-	4.48	395	29	10	5	-	14
S3	AC-CGRAN	-	-	-	-	4.28	401	29	10	5	-	5
S4	AC-H2S	-	-	-	-	3.40	395	29	10	5	-	7
S5	CNF ^a	-	-	-	-	0.50	403	28.5	10	10.2	-	6

^a Purified in KOH.

Table A.2 – Experiments discussed in Chapters 3 and 4

Exp.	Material	x_{Ru} (%)	D_{CO} (%)	D_{TEM} (%)	d_p (nm)	m (g)	T (°C)	p (MPa)	x_{Gly} (%)	F (gmin ⁻¹)	$WHSV_{gRu}^a$ (g _{org} g _{Ru} ⁻¹ h ⁻¹)	TOS (h)
C1	Ru/AC-BM	5	32	-	3.6	0.97	401	29	10	5-20	2487	48
C2	Ru/AC-Spher	5	40	-	2.7	1.16	400	29	10	5-15	1588	27
C3	Ru/AC-CGRAN	5	-	-	-	0.60	399	29	10	5-20	4020	48
C4	Ru/AC-H2S	5	-	-	-	1.00	405	29	10	3-15	1800	22
C5	Ru/CNF	21.1	-	45	1.7	1.03	400-411	28.5	10,20	5-18	914	23
C7	Ru/AC-A	5.3	40	-	2.7	0.97	399	29	8.3,10	5-20	2391	72
C8	Ru/AC-B	5	13	-	9.7	1.07	400	29	10	5-20	2209	51
C9	Ru/AC-A	5.3	40	-	2.7	1.00	390-410	29	10	5	574	21
C10	Ru/AC-A	5.3	40	-	2.7	1.02	390-411	29	0	5	0	14
C11	Ru/AC-A	5.3	40	-	2.7	1.02	406	29	2.5,5	10-20	550	10
C12	Ru/AC-A	5.3	40	-	2.7	1.02	365-382	29	10	5	563	11
C13	Ru/AC-A	5.3	40	-	2.7	1.07	396-418	24-31	10	5-20	547	4
C14	Ru/AC-A	5.3	40	-	2.7	50	400	25	10	17	16	3
C15	Ru/AC-A	5.3	40	-	2.7	50	400	25	2.6 ^b	17	0.4	13
C16	Ru/AC-A	2.3	62	-	1.6	1.01	402	29	10	5	1370	23
C17	Ru/ α -Al ₂ O ₃	1.9	2.5	-	52	1.06	403	29	10	5	1511	6
C18	Ru/TiO ₂	1.7	1.3	-	104	1.04	406	29	10	5	1721	6
C19	Ru/ZrO ₂	1.8	40	-	2.6	1.06	399	29	10	5	1604	7

^a Maximum $WHSV_{gRu}$ during the experiment.^b Based on sewage sludge total solids (TS = 2.6 %).

Table A.3 – Experiments discussed in Chapter 5

Exp.	Material	x_{Ru} (%)	D_{CO} (%)	D_{TEM} (%)	d_p (nm)	m (g)	T (°C)	p (MPa)	x_{Gly} (%)	F (g min ⁻¹)	$WHSV_{gRu}^a$ (g _{org} g _{Ru} ⁻¹ h ⁻¹)	TOS (h)
C20	1%Ru/CNF_1	1.4	-	71	1.0	0.89	403	28.5	6	10.2	2938	5
C21	1%Ru/CNF_2	1.1	-	67	1.2	0.5	404	28.5	8	10.2	9151	5
C22	5%Ru/CNF_1	4.6	-	67	1.1	0.6	403	28.5	20	10.6	4596	8
C23	5%Ru/CNF_Cl	5.1	-	69	0.9	0.27	408	28.5	20	9.4	4127	8
C24	10%Ru/CNF	10.4	-	59	1.4	0.3	404	28.5	20	10.5	4047	7
C25	15%Ru/CNF	16.0	-	47	1.8	0.2	403	28.5	20	10.5	3928	6
C26	20%Ru/CNF	20.6	-	51	1.5	0.14	400	28.5	20	10.6	4352	6
C27	30%Ru/CNF	32.3	-	35	2.2	0.11	403	28.5	20	11.6	3938	6
C28	5%Ru/AC-A	5.3	40	-	2.7	0.55	405	28.5	20	10.6	4345	7
C29	5%Ru/CNF_C	4.4	-	69	1.0	0.31	398	28.5	0	10	0	5
C30	5%Ru/CNF_C	4.4	-	69	1.0	0.32	403	28.5	5	7.2	1530	5
C31	5%Ru/CNF_C	4.4	-	69	1.0	0.31	407	28.5	20	12.6	11120	5

^a Maximum $WHSV_{gRu}$ during the experiment.

B Carbon supports for SCWG catalysts

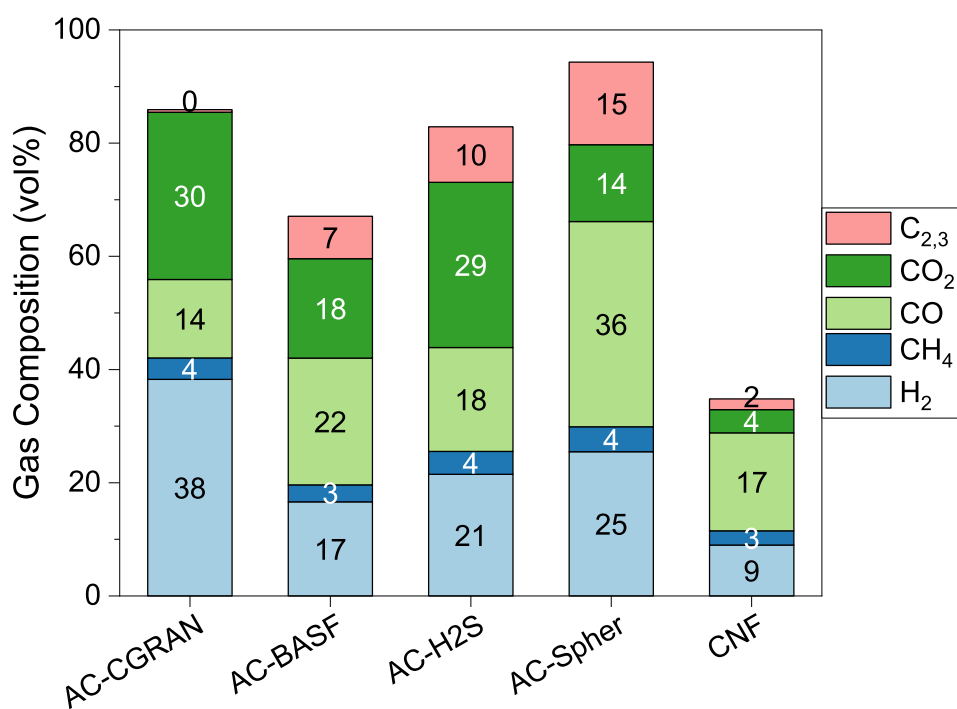


Figure B.1 – Gas composition after glycerol gasification over carbon supports. The total does not close to 100 % because of the low gas flows - the balance is N₂ (Exp. S1-S5).

C Ru loss from SCWG catalysts

The pressure on the lowest layer of the catalyst bed was calculated according to Equation C.1:

$$p(bar) = p_{bed} + p_{H_2O} = \frac{m_{cat+fill} \cdot g}{A_{CS}} + \rho_{p,T} \cdot g \cdot H_{reactor} \quad (C.1)$$

by taking into account the weight of the catalyst and filling material ($m_{cat+fill}$), the reactor cross-section area A_{CS} , as well as the weight contribution from SCW (400 °C, 29 MPa) of density $\rho_{29,400} = 0.31 \text{ g mL}^{-1}$ and the reactor height $H_{reactor}$ (from the top down to the end of the catalyst bed).

Appendix C. Ru loss from SCWG catalysts

Table C.1 – Modelled thermodynamic equilibrium solubilities of different materials in SCW

	Compound	log(Solubility) ^a (mol kg _{H₂O} ⁻¹)	Solubility (g g _{H₂O} ⁻¹)
Calculated	α-Al ₂ O ₃	-7.1	7.6·10 ⁻⁹
	Al	-7.1	4.0·10 ⁻⁹
	RuO ₂	-14.5	4.5·10 ⁻¹⁶
	TiO ₂	-12.7	1.8·10 ⁻¹⁴
	ZrO ₂	-10.0	1.3·10 ⁻¹¹
Extrapolated ^b	Ru	-10.5	3.2·10 ⁻¹²
	RuO ₂	-15	1.3·10 ⁻¹⁶
	TiO ₂	-13	8.0·10 ⁻¹⁵
	ZrO ₂	-10	1.2·10 ⁻¹¹

^a Data from Jocz *et al.* [100].

^b Extrapolated from the graphs in Jocz *et al.* [100].

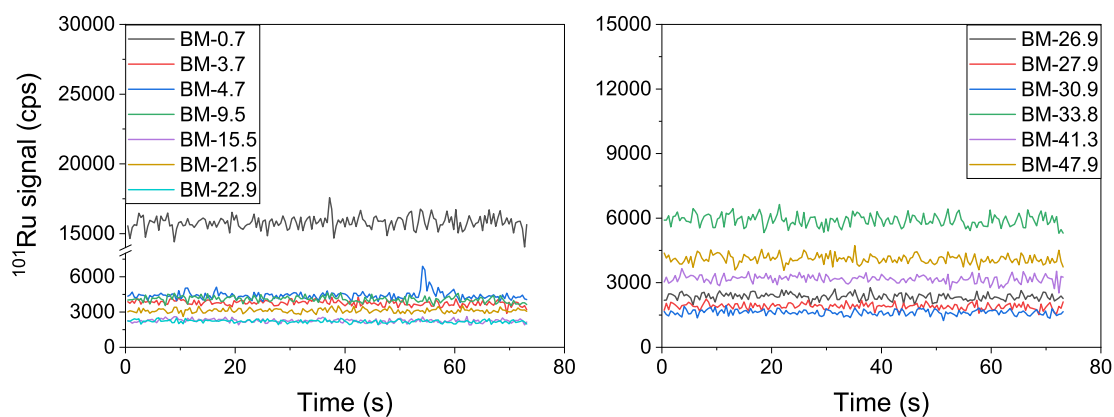


Figure C.1 – ICP-MS time-resolved analysis for selected Ru/AC-BM SCWG samples. BM-xx.x refers to the sample TOS (h) (Exp. C1).

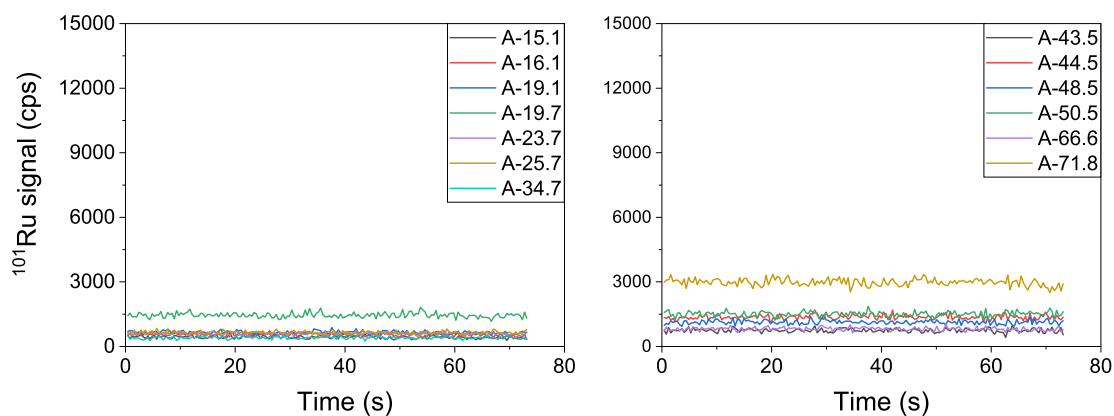


Figure C.2 – ICP-MS time-resolved analysis for selected Ru/AC-A SCWG samples. A-xx.x refers to the sample TOS (h) (Exp. C7).

Appendix C. Ru loss from SCWG catalysts

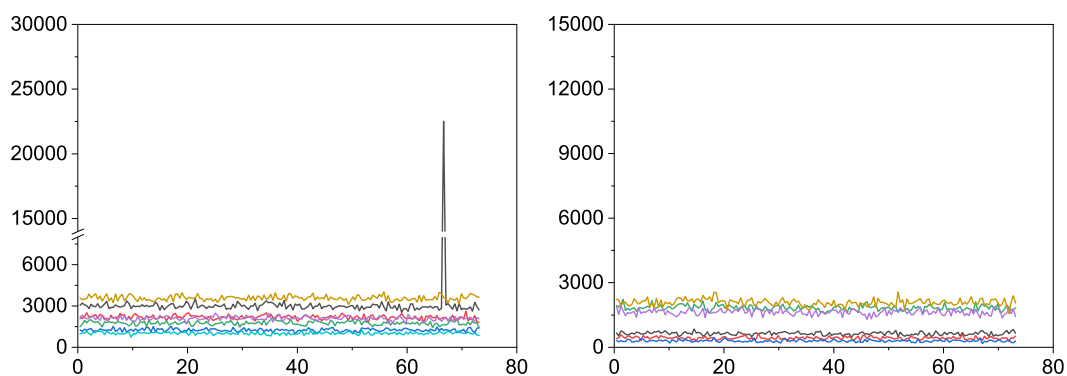


Figure C.3 – ICP-MS time-resolved analysis for selected Ru/AC-B SCWG samples. B-xx.x refers to the sample TOS (h) (Exp. C8).

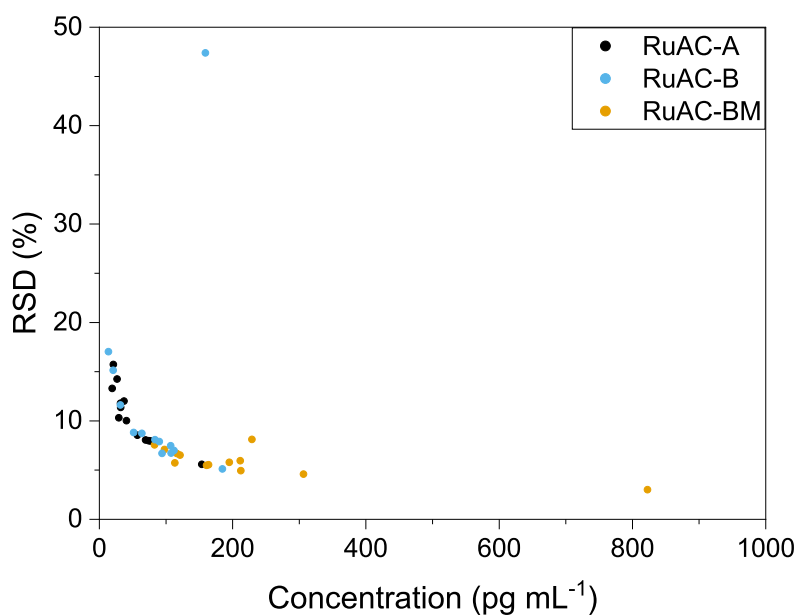


Figure C.4 – RSD of the time-resolved ICP-MS signals as a function of concentration for the three commercial Ru/AC catalysts. A main outlier is seen with Ru/AC-B-1.6 (Figure C.3) and smaller outlier with Ru/AC-BM-4.7 (Figure C.1).

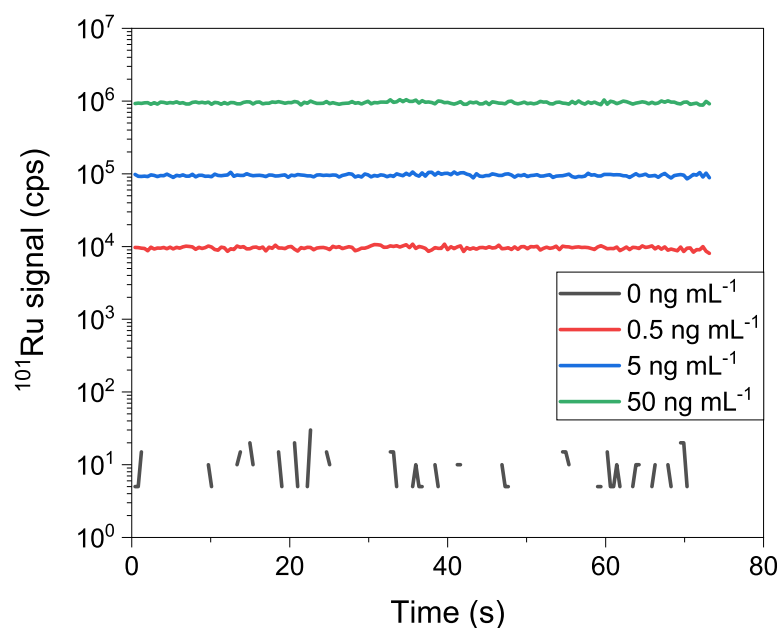


Figure C.5 – ICP-MS time-resolved signal of the ionic Ru standards used for the calibration. RSD = 4.7, 3.9 and 3.5 % for the 0.5, 5 and 50 ngmL⁻¹ standards, respectively. The line of the blank sample (0 ngmL⁻¹) is discontinued because the measured signal is often zero.

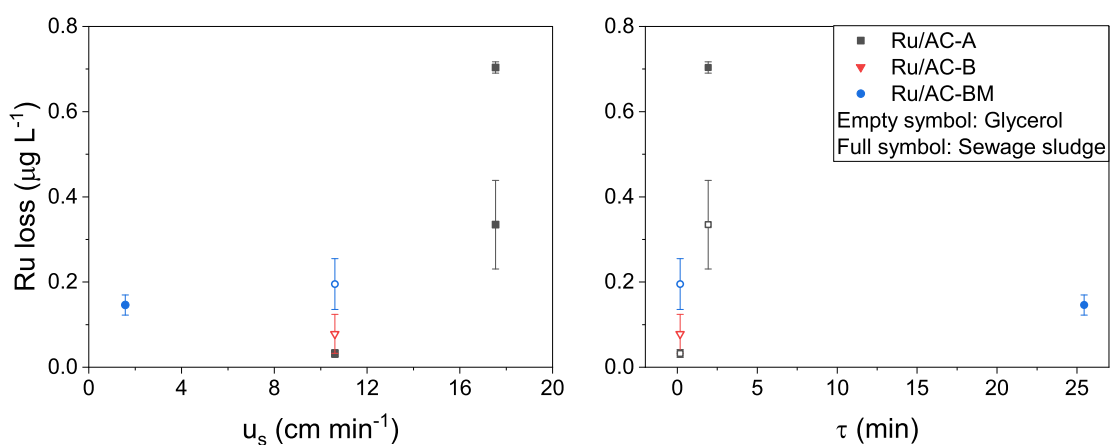


Figure C.6 – Ru concentration as a function of superficial velocity u_s (left) and residence time τ (right) in the catalyst bed for the three SCWG setups.

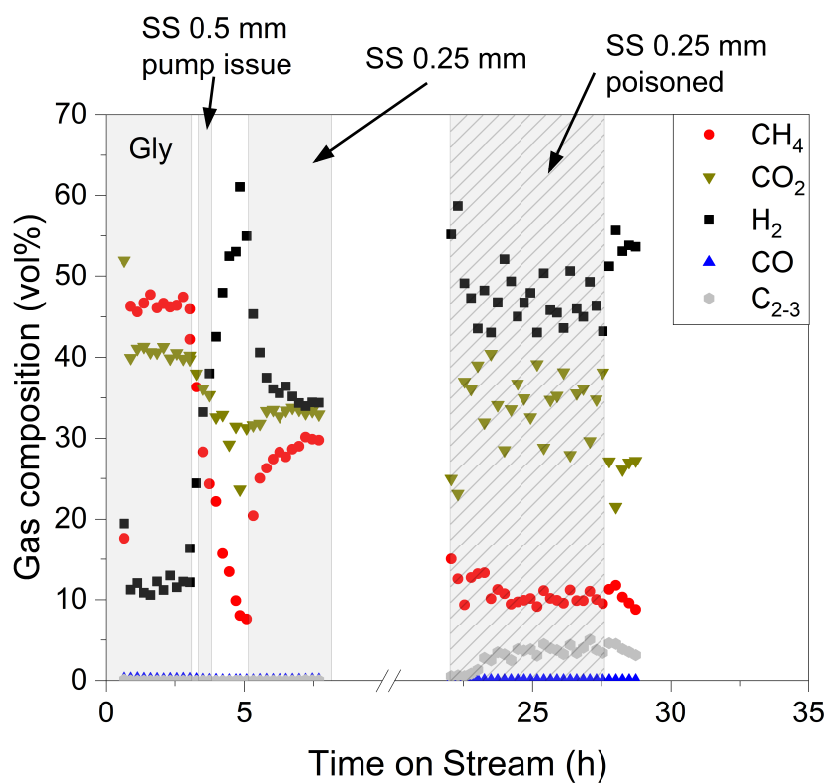


Figure C.7 – SCWG of glycerol and sewage sludge over Ru/AC-A on the *intermediate* setup. The grey areas indicate gasification sections, either with glycerol (gly, Exp. C14) or sewage sludge (SS, Exp. C15). Another pump failure occurred at TOS = 16.8 h leading to $T_{min} = 196^\circ\text{C}$ and $p_{min} = 9\text{ MPa}$.

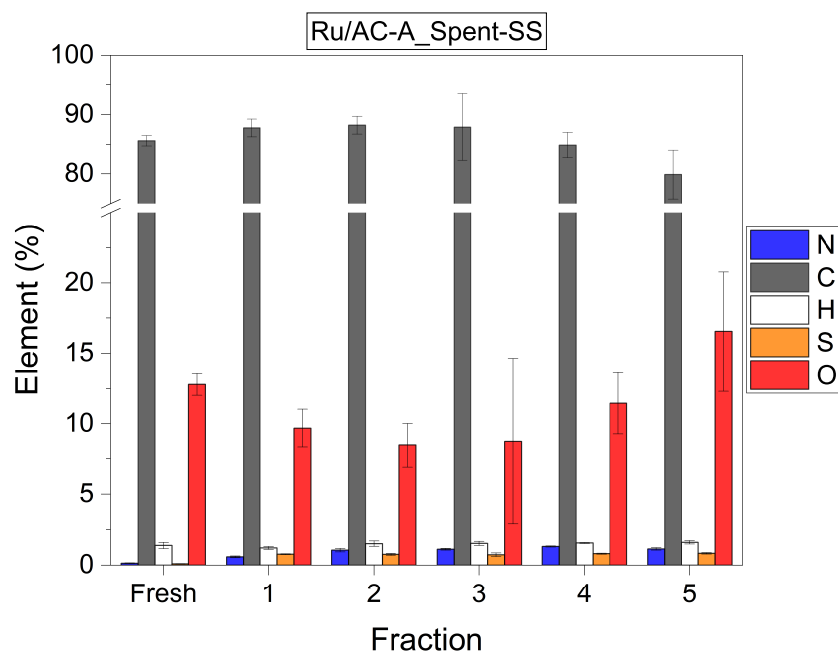


Figure C.8 – Elemental composition of the fresh and spent (sewage sludge) Ru/AC-A catalyst (Exp. C15). The catalyst was recovered in different fractions (1: reactor exit – 5: first catalyst fraction after sulfur absorber bed).

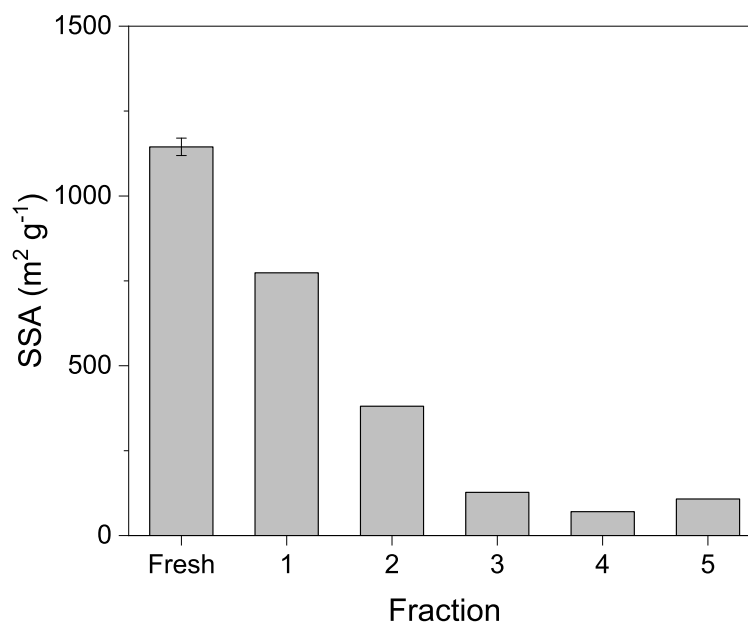


Figure C.9 – SSA of the fresh and spent (sewage sludge) Ru/AC-A catalyst (Exp. C15). The catalyst was recovered in different fractions (1: reactor exit – 5: first catalyst fraction after sulfur absorber bed).

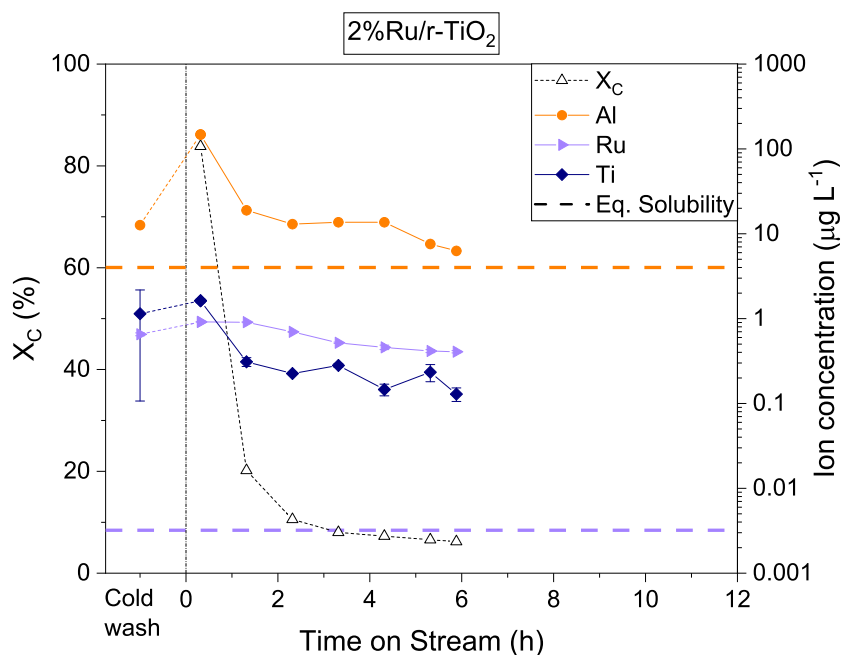


Figure C.10 – Carbon conversion and Al, Ru, Ti concentrations in the process water as a function of TOS for 2%Ru/TiO₂ (Exp. C18). Horizontal dashed lines: metal dissolution equilibrium (Table C.1) for the given species (not shown for Ti because its concentration is too low ($2 \times 10^{-5} \mu\text{g L}^{-1}$)).

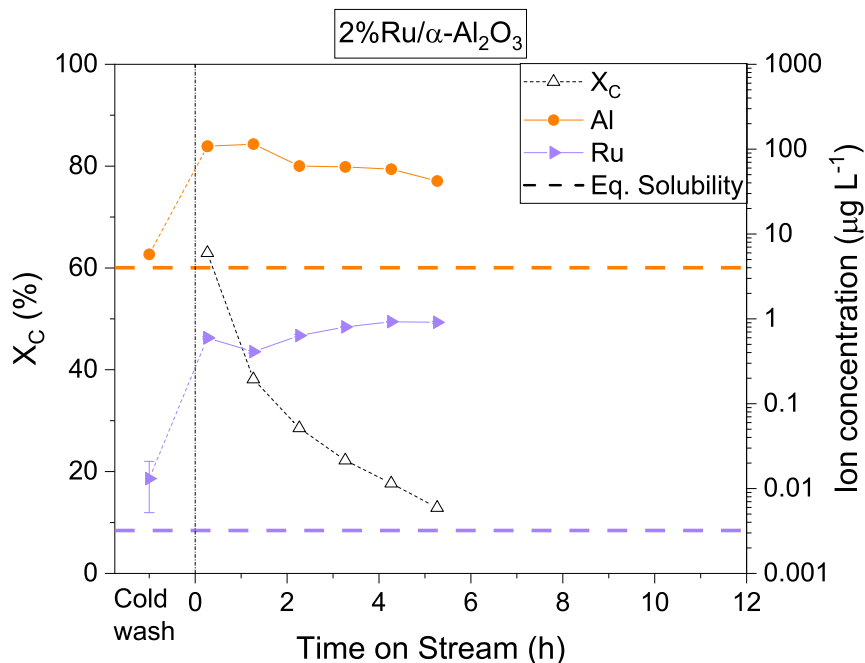


Figure C.11 – Carbon conversion and Al, Ru concentrations in the process water as a function of TOS for 2%Ru/α-Al₂O₃ (Exp. C17). Horizontal dashed lines: metal dissolution equilibrium (Table C.1) for the given species.

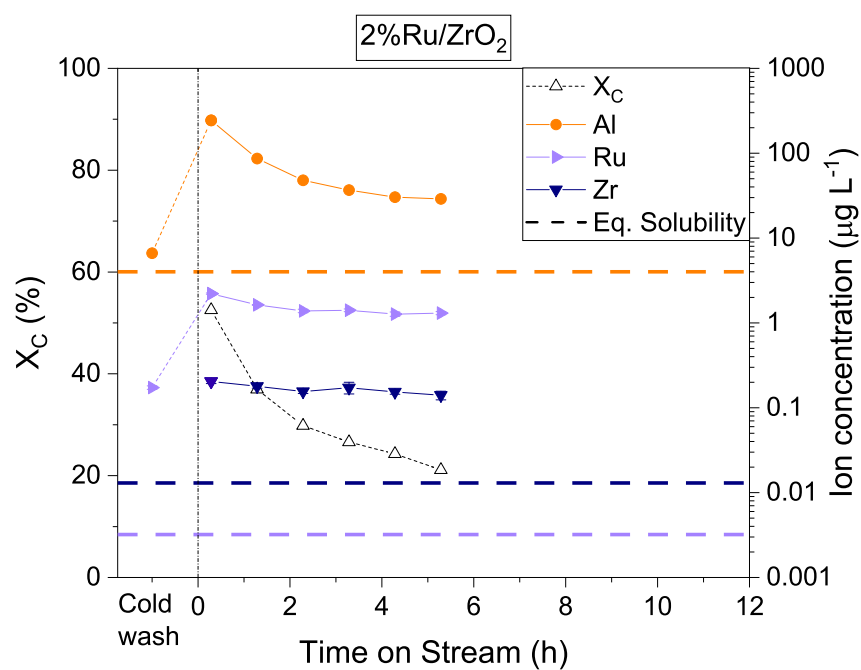


Figure C.12 – Carbon conversion and Al, Ru, Zr concentrations in the process water as a function of TOS for 2%Ru/ZrO₂(Exp. C19). Horizontal dashed lines: metal dissolution equilibrium (Table C.1) for the given species.

D Ru/CNF catalysts

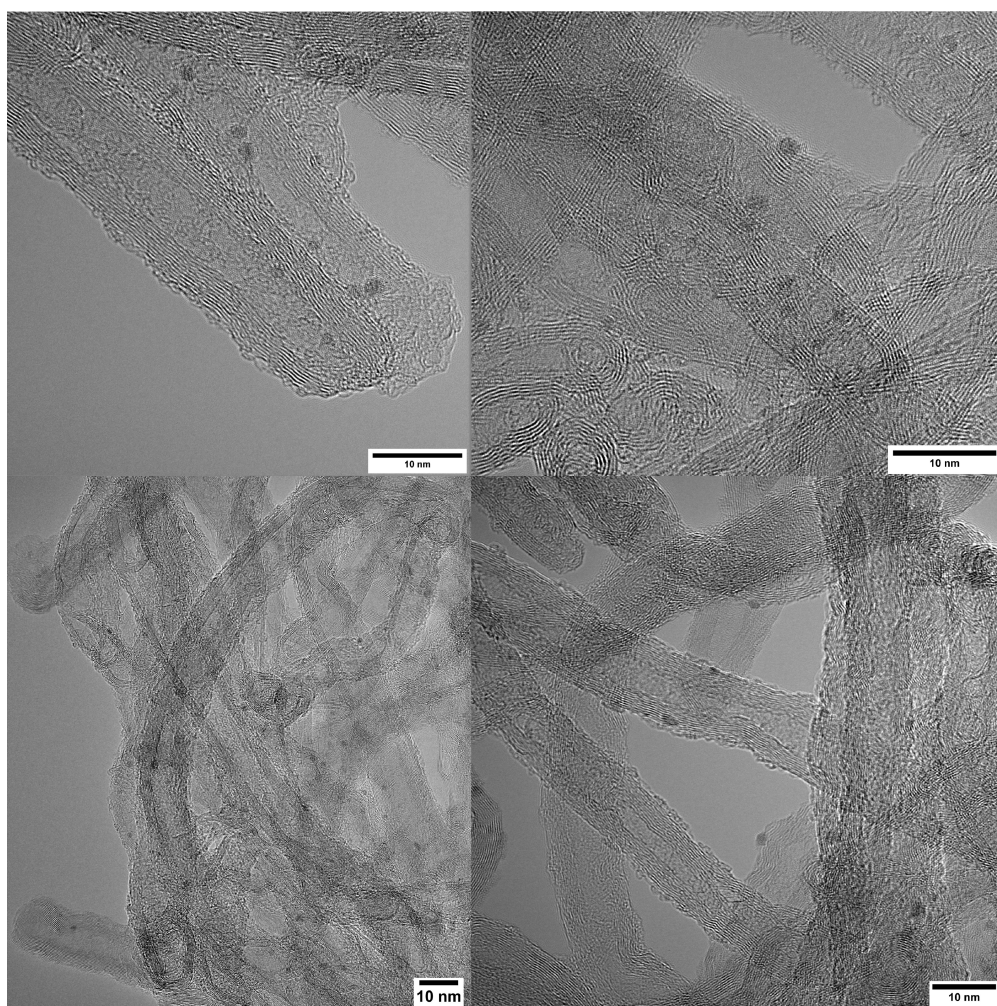


Figure D.1 – High-resolution micrographs of 1%Ru/CNF_2.

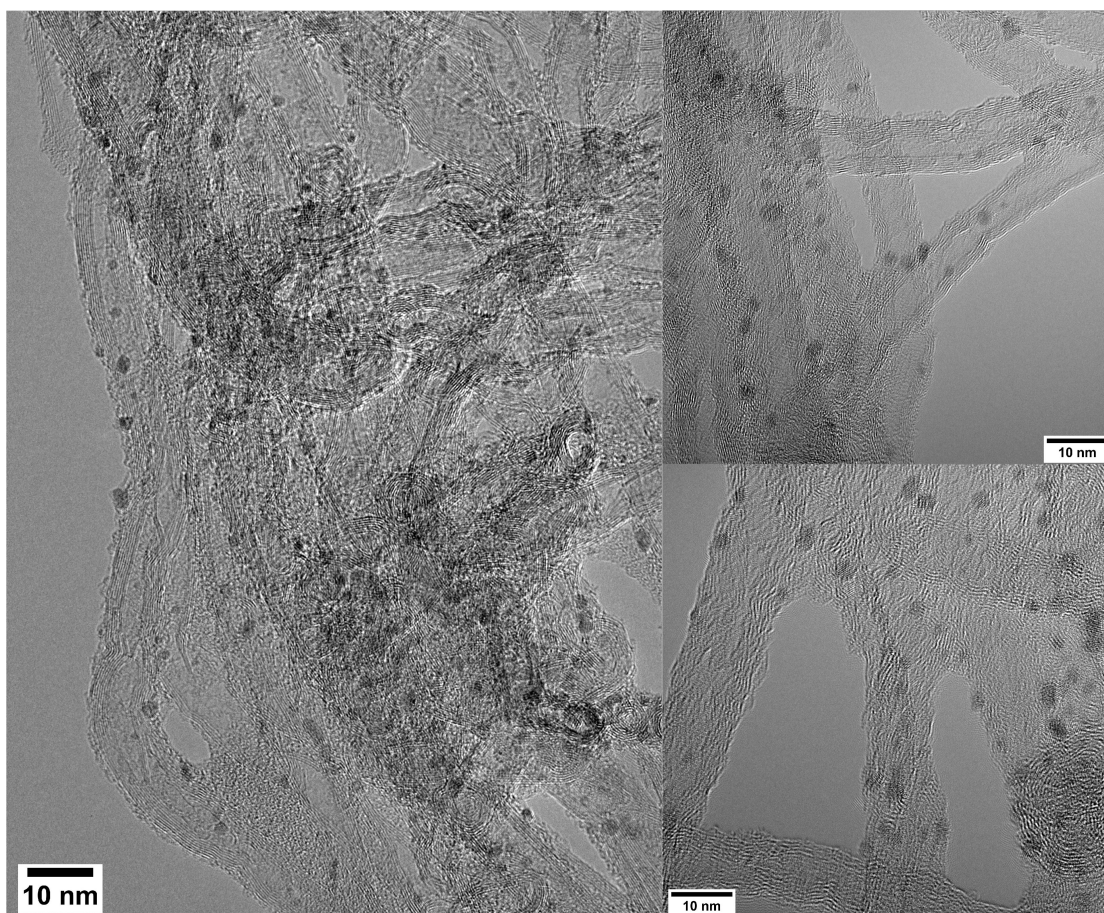


Figure D.2 – High-resolution micrographs of 5%Ru/CNF_1.

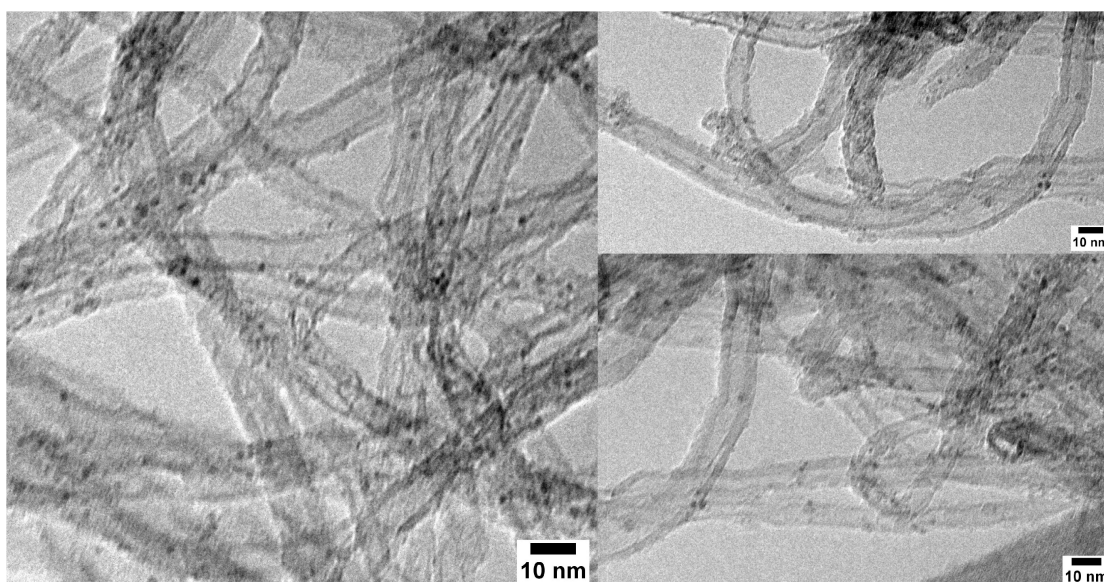


Figure D.3 – Micrographs of 5%Ru/CNF_Cl.

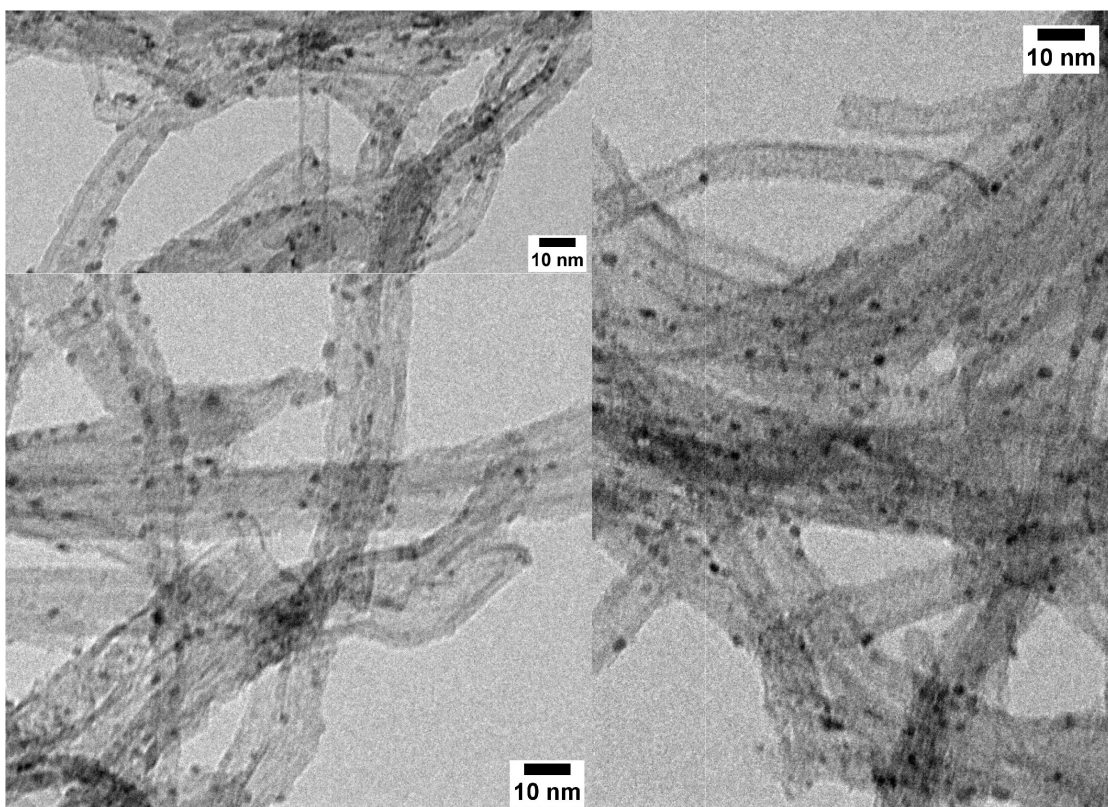


Figure D.4 – Micrographs of 10%Ru/CNF.

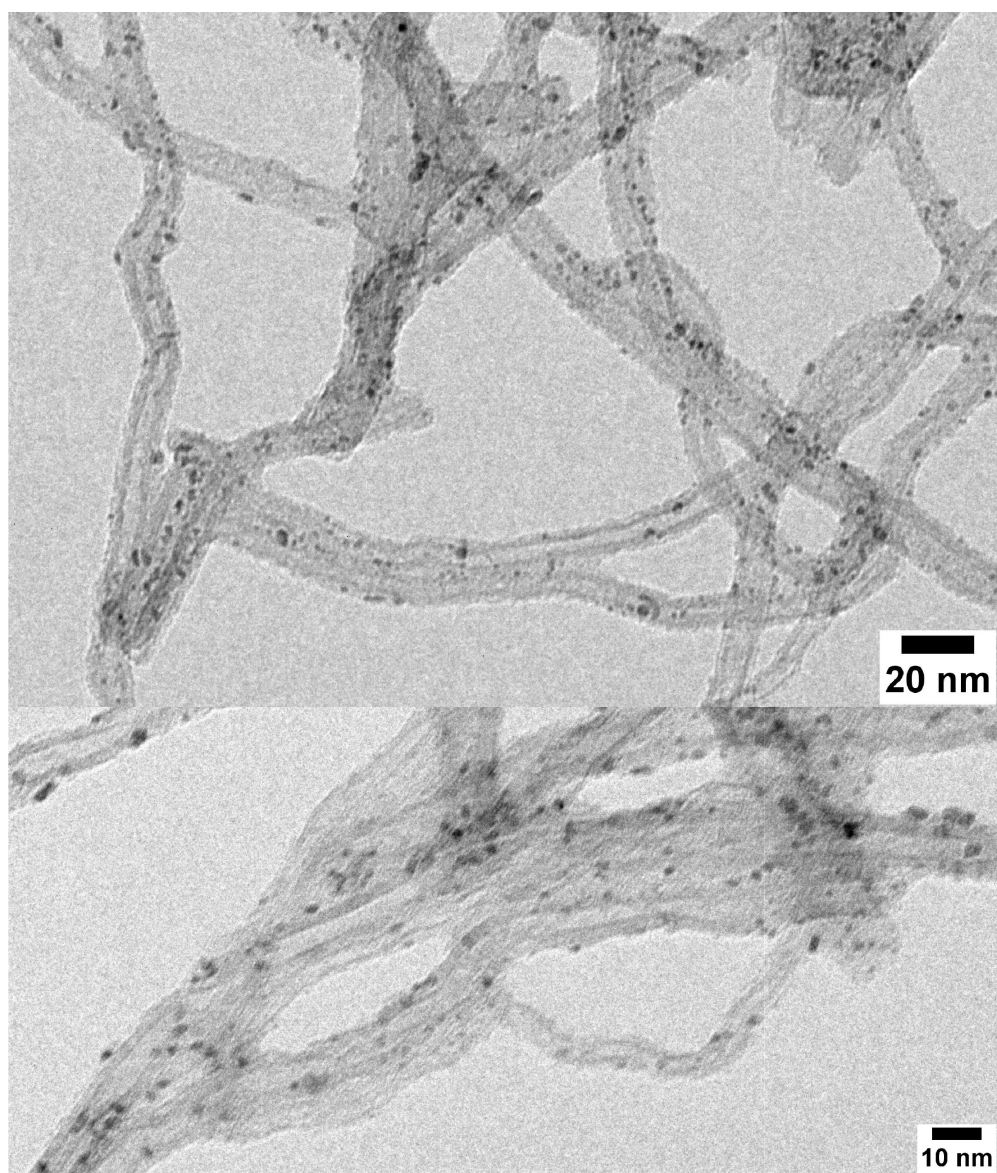


Figure D.5 – Micrographs of 15%Ru/CNF.

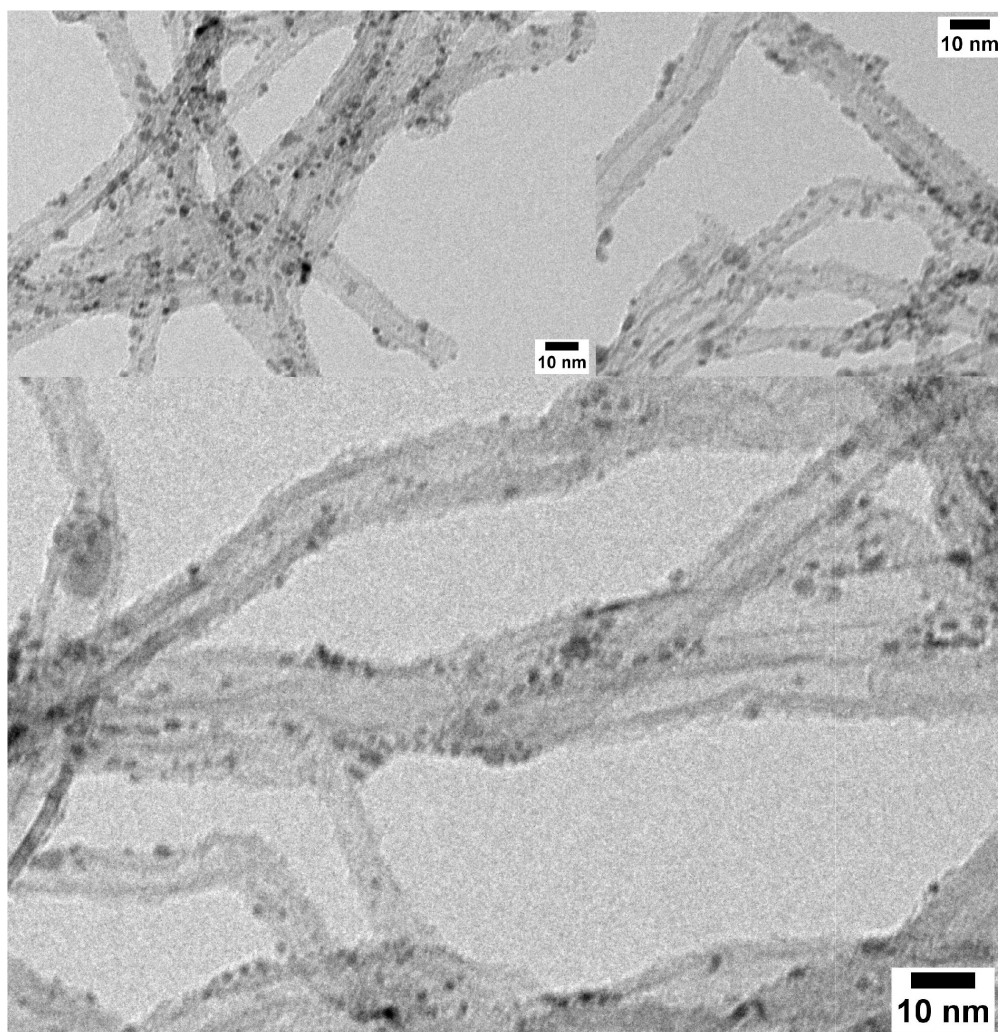


Figure D.6 – Micrographs of 20%Ru/CNF

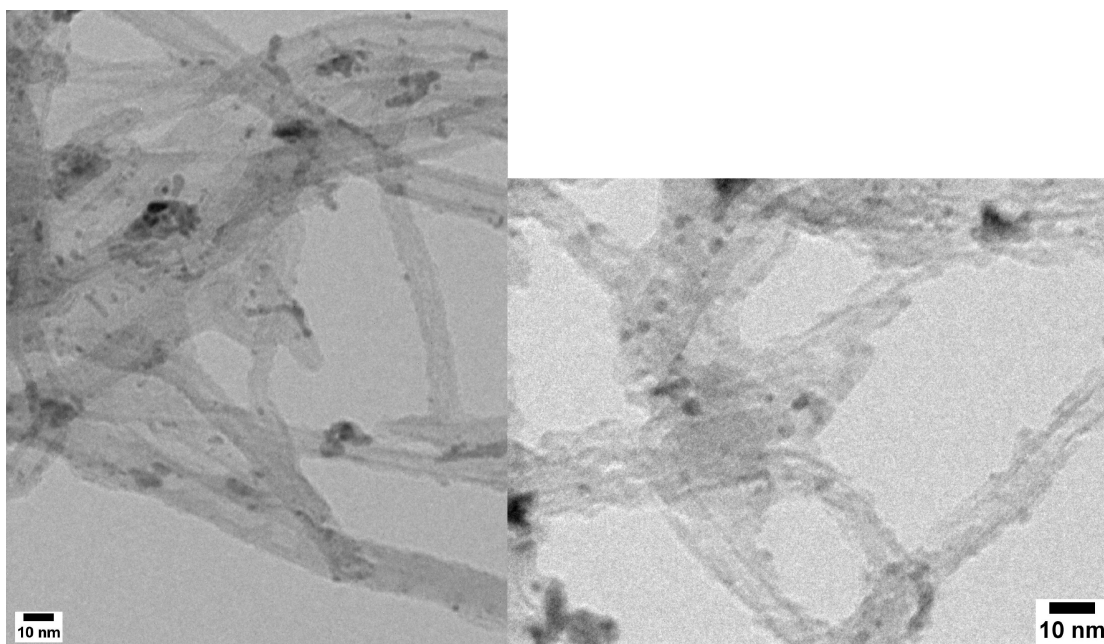


Figure D.7 – Micrographs of 30%Ru/CNF.

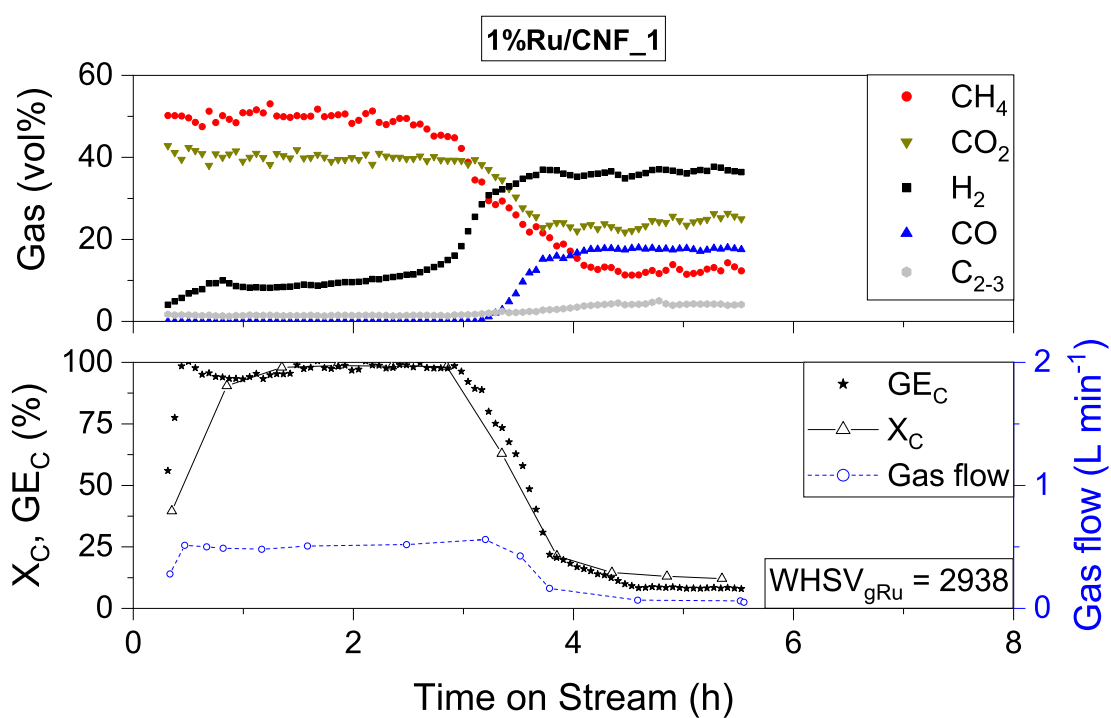


Figure D.8 – Gas composition (top), X_C , GE_C and gas flow (bottom) for 1 %Ru/CNF_1. Feed: 6 wt% glycerol, $m_{cat} = 0.89$ g, $F = 10.2$ gmin⁻¹, $T = 403$ °C, $p = 28.5$ MPa (Exp. C20).

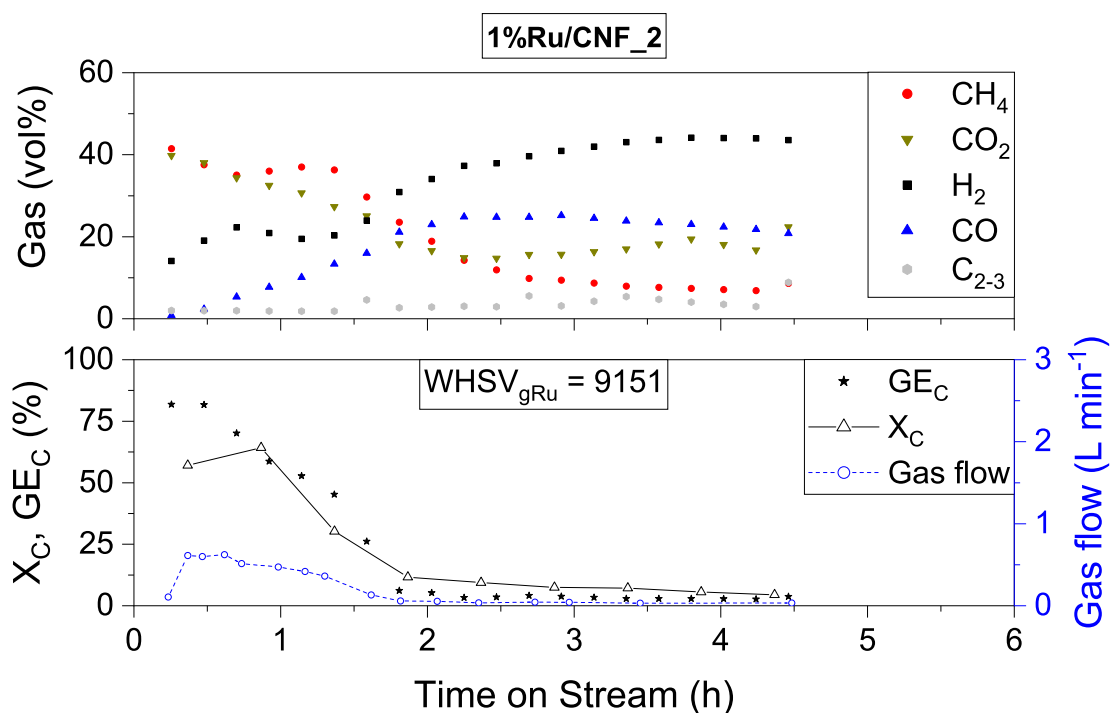


Figure D.9 – Gas composition (top), X_C , GE_C and gas flow (bottom) for 1 %Ru/CNF_2. Feed: 8 wt% glycerol, $m_{cat}=0.50$ g, $F=10.2$ g min⁻¹, $T=404$ °C, $p=28.5$ MPa (Exp. C21).

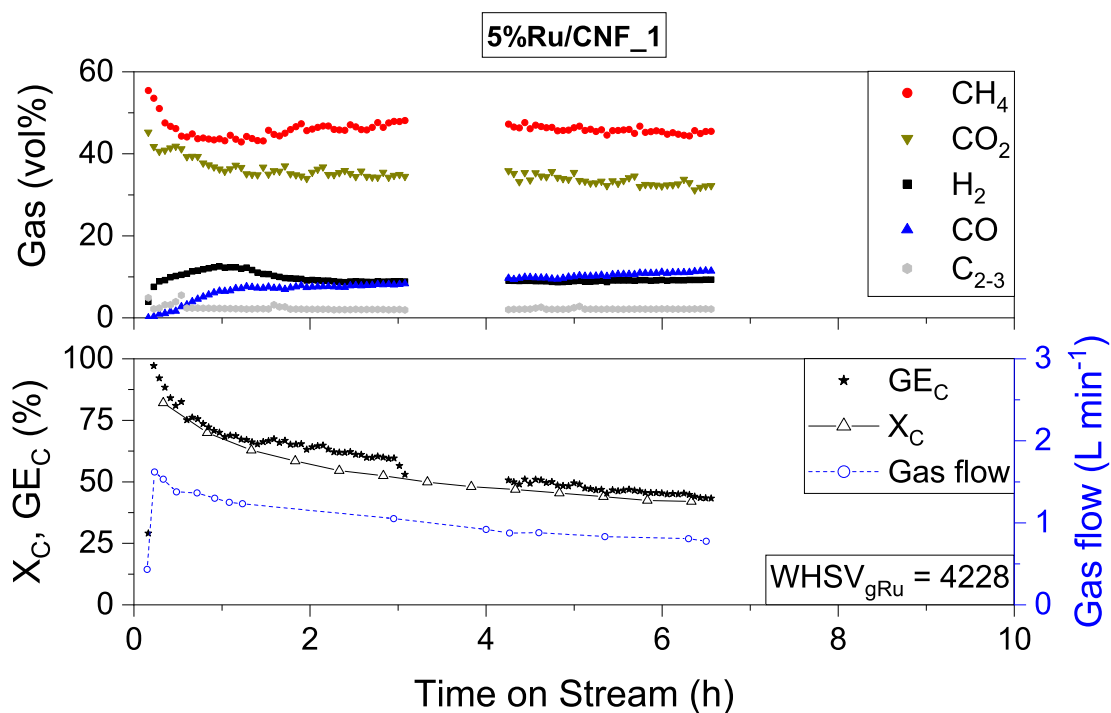


Figure D.10 – Gas composition (top), X_C , GE_C and gas flow (bottom) for 5 %Ru/CNF_1. Feed: 20 wt% glycerol, $m_{cat}=0.60$ g, $F=10.6$ g min⁻¹, $T=403$ °C, $p=28.5$ MPa (Exp. C22).

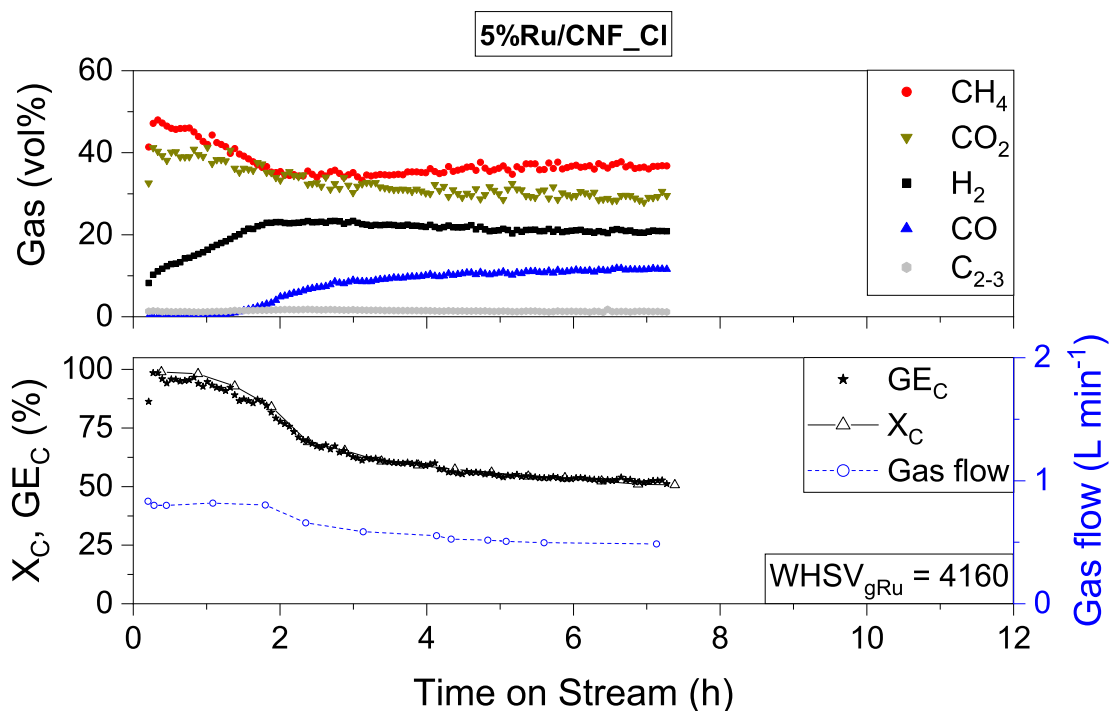


Figure D.11 – Gas composition (top), X_C , GE_C and gas flow (bottom) for 5 %Ru/CNF_Cl. Feed: 10 wt% glycerol, $m_{cat} = 0.27$ g, $F = 9.4$ g min⁻¹, $T = 408$ °C, $p = 28.5$ MPa (Exp. C23).

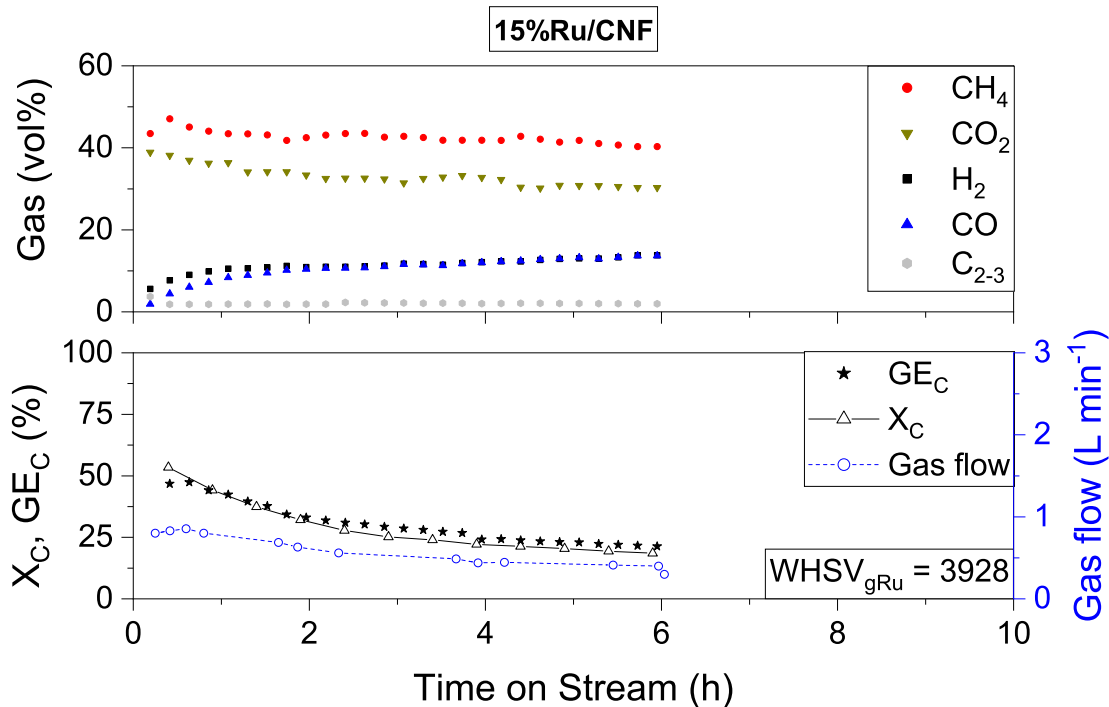


Figure D.12 – Gas composition (top), X_C , GE_C and gas flow (bottom) for 15 %Ru/CNF. Feed: 20 wt% glycerol, $m_{cat} = 0.20$ g, $F = 10.5$ g min⁻¹, $T = 403$ °C, $p = 28.5$ MPa (Exp. C25).

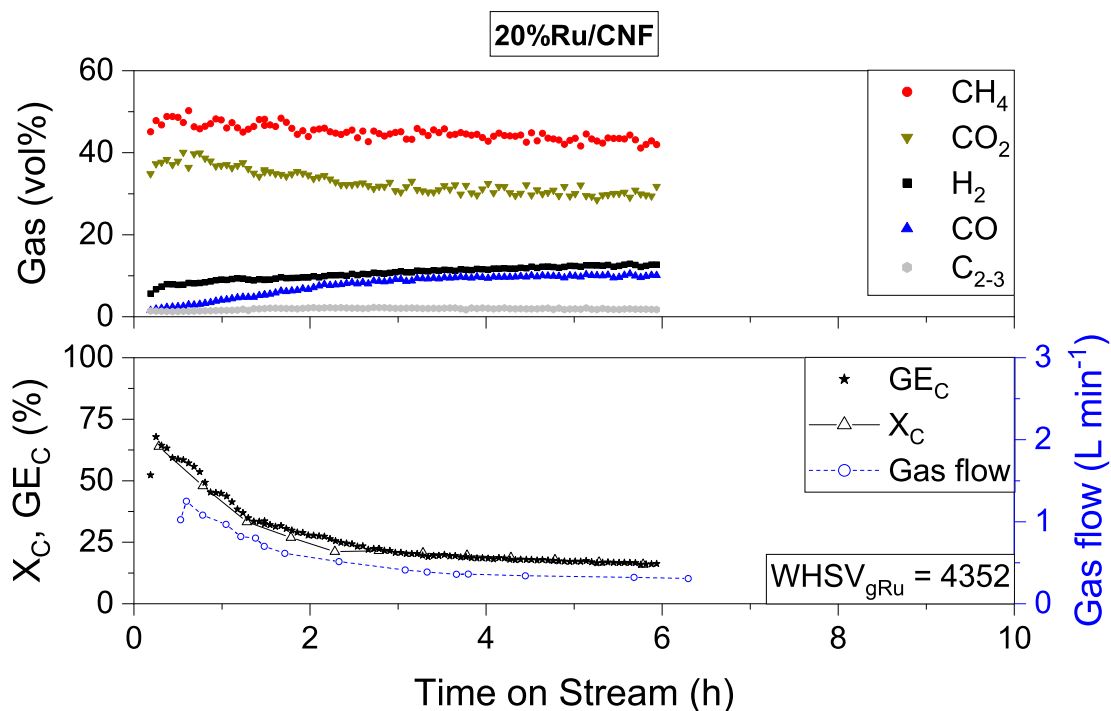


Figure D.13 – Gas composition (top), X_C , GE_C and gas flow (bottom) for 20 %Ru/CNF Feed: 20 wt% glycerol, $m_{\text{cat}} = 0.14 \text{ g}$, $F = 10.6 \text{ g min}^{-1}$, $T = 400^\circ\text{C}$, $p = 28.5 \text{ MPa}$ (Exp. C26).

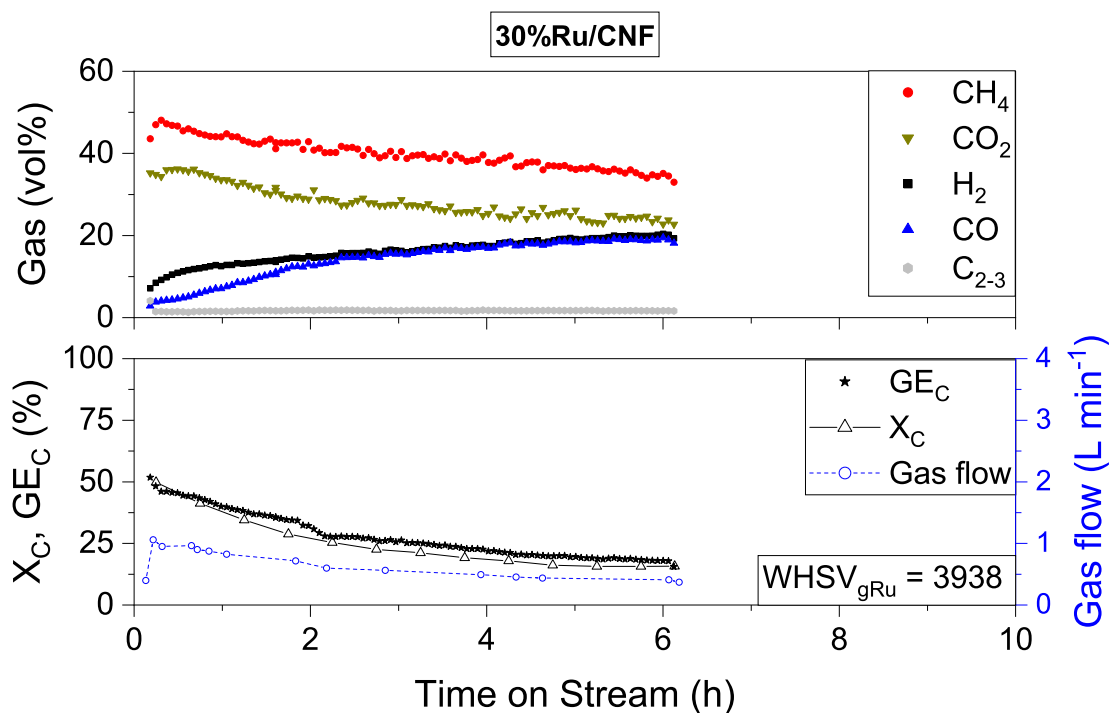


Figure D.14 – Gas composition (top), X_C , GE_C and gas flow (bottom) for 30 %Ru/CNF Feed: 20 wt% glycerol, $m_{\text{cat}} = 0.11 \text{ g}$, $F = 11.6 \text{ g min}^{-1}$, $T = 403^\circ\text{C}$, $p = 28.5 \text{ MPa}$ (Exp. C27).

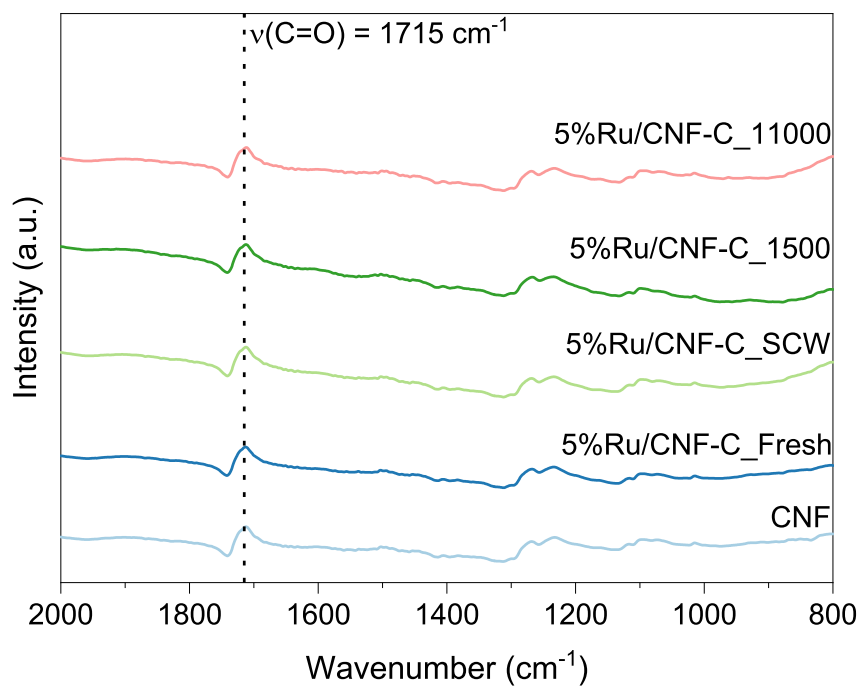


Figure D.15 – DRIFTS spectra of CNF, the fresh and spent (Exp. C29-C31) 5%Ru/CNF_C catalysts.

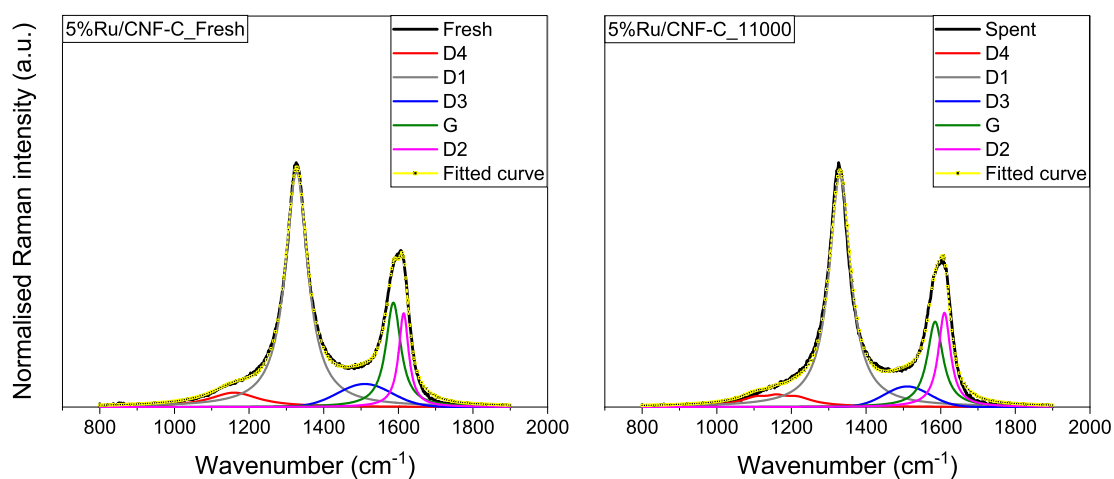


Figure D.16 – Raman spectra of the fresh and spent (Exp. C31) 1%Ru/CNF_2 catalysts, deconvoluted into the different vibration modes.

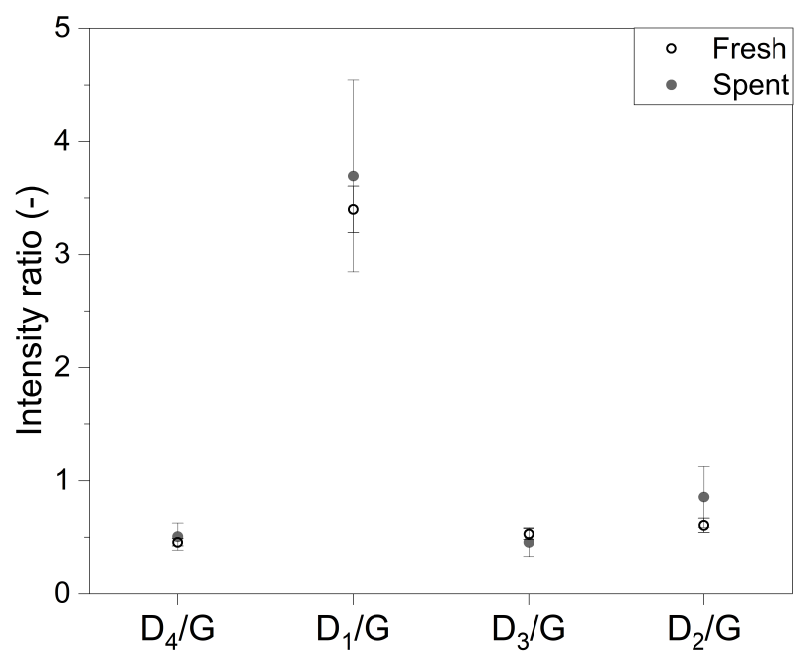


Figure D.17 – Area ratios of the deconvoluted peaks for the fresh and spent (Exp. C31) 1%Ru/CNF_2 catalysts.

Bibliography

- [1] N. Oreskes, 'The scientific consensus on climate change', *Science*, vol. 306, no. 5702, pp. 1686–1686, 2004. DOI: 10.1126/science.1103618.
- [2] 350.org. The science, [Online]. Available: <https://350.org/about/science/> (visited on 13/06/2021).
- [3] Scripps CO₂ Program. Keeling curve lessons, [Online]. Available: https://scrippsco2.ucsd.edu/history_legacy/keeling_curve_lessons.html (visited on 16/06/2021).
- [4] CO₂.Earth. Earth's CO₂, [Online]. Available: <https://www.co2.earth/> (visited on 16/06/2021).
- [5] IPCC (2018), 'Global warming of 1.5 °C', Intergovernmental Panel on Climate Change, Geneva.
- [6] WBA (2019), 'Global bioenergy statistics 2019', World Bioenergy Association, Stockholm.
- [7] IEA (2020), 'World energy balances: Overview', International Energy Agency, Paris.
- [8] IEA (2021), 'Net zero by 2050', International Energy Agency, Paris.
- [9] P. McKendry, 'Energy production from biomass (part 1): Overview of biomass', *Biore-source Technology*, vol. 83, no. 1, pp. 37–46, 2002. DOI: 10.1016/S0960-8524(01)00118-3.
- [10] P. McKendry, 'Energy production from biomass (part 2): Conversion technologies', *Bioresource Technology*, vol. 83, no. 1, pp. 47–54, 2002. DOI: 10.1016/S0960-8524(01)00119-5.
- [11] L. Brennan and P. Owende, 'Biofuels from microalgae — a review of technologies for production, processing, and extractions of biofuels and co-products', *Renewable and Sustainable Energy Reviews*, vol. 14, no. 2, pp. 557–577, 2010. DOI: 10.1016/j.rser.2009.10.009.
- [12] IRENA (2014), 'Global bioenergy supply and demand projections: A working paper for REmap 2030', The International Renewable Energy Agency, Abu Dhabi.
- [13] S. Guran, 'Chapter 8 - Sustainable waste-to-energy technologies: Gasification and pyrolysis', in *Sustainable Food Waste-To-energy Systems*, T. A. Trabold and C. W. Babbitt, Eds., Academic Press, 2018, pp. 141–158. DOI: 10.1016/B978-0-12-811157-4.00008-5.

Bibliography

- [14] V. S. Sikarwar, M. Zhao, P. S. Fennell, N. Shah and E. J. Anthony, 'Progress in biofuel production from gasification', *Progress in Energy and Combustion Science*, vol. 61, pp. 189–248, 2017. DOI: 10.1016/j.pecs.2017.04.001.
- [15] G. Schuster, G. Löffler, K. Weigl and H. Hofbauer, 'Biomass steam gasification – an extensive parametric modeling study', *Bioresource Technology*, vol. 77, no. 1, pp. 71–79, 2001. DOI: 10.1016/S0960-8524(00)00115-2.
- [16] X. Hu and M. Gholizadeh, 'Biomass pyrolysis: A review of the process development and challenges from initial researches up to the commercialisation stage', *Journal of Energy Chemistry*, vol. 39, pp. 109–143, 2019. DOI: 10.1016/j.jechem.2019.01.024.
- [17] J. A. Libra, K. S. Ro, C. Kammann, A. Funke, N. D. Berge, Y. Neubauer, M.-M. Titirici, C. Fühner, O. Bens, J. Kern and K.-H. Emmerich, 'Hydrothermal carbonization of biomass residuals: A comparative review of the chemistry, processes and applications of wet and dry pyrolysis', *Biofuels*, vol. 2, no. 1, pp. 71–106, 2011. DOI: 10.4155/bfs.10.81.
- [18] Q.-V. Bach, K.-Q. Tran, R. A. Khalil, Ø. Skreiberg and G. Seisenbaeva, 'Comparative assessment of wet torrefaction', *Energy Fuels*, vol. 27, no. 11, pp. 6743–6753, 2013. DOI: 10.1021/ef401295w.
- [19] S. A. Nicolae, H. Au, P. Modugno, H. Luo, A. E. Szego, M. Qiao, L. Li, W. Yin, H. J. Heeres, N. Berge and M.-M. Titirici, 'Recent advances in hydrothermal carbonisation: From tailored carbon materials and biochemicals to applications and bioenergy', *Green Chem.*, vol. 22, no. 15, pp. 4747–4800, 2020. DOI: 10.1039/D0GC00998A.
- [20] A. A. Peterson, F. Vogel, R. P. Lachance, M. Fröling, J. Michael J. Antal and J. W. Tester, 'Thermochemical biofuel production in hydrothermal media: A review of sub- and supercritical water technologies', *Energy Environ. Sci.*, vol. 1, no. 1, pp. 32–65, 2008. DOI: 10.1039/B810100K.
- [21] D. López Barreiro, W. Prins, F. Ronsse and W. Brilman, 'Hydrothermal liquefaction (HTL) of microalgae for biofuel production: State of the art review and future prospects', *Biomass and Bioenergy*, vol. 53, pp. 113–127, 2013. DOI: 10.1016/j.biombioe.2012.12.029.
- [22] P. Biller and A. B. Ross, 'Potential yields and properties of oil from the hydrothermal liquefaction of microalgae with different biochemical content', *Bioresource Technology*, vol. 102, no. 1, pp. 215–225, 2011. DOI: 10.1016/j.biortech.2010.06.028.
- [23] P. Duan and P. E. Savage, 'Hydrothermal liquefaction of a microalga with heterogeneous catalysts', *Ind. Eng. Chem. Res.*, vol. 50, no. 1, pp. 52–61, 2011. DOI: 10.1021/ie100758s.
- [24] A. Kruse, 'Supercritical water gasification', *Biofuels, Bioproducts and Biorefining*, vol. 2, no. 5, pp. 415–437, 2008. DOI: 10.1002/bbb.93.
- [25] F. Vogel, 'Catalytic Conversion of High-Moisture Biomass to Synthetic Natural Gas in Supercritical Water', in *Handbook of Green Chemistry*, John Wiley & Sons, Inc., 2010, pp. 281–324. DOI: 10.1002/9783527628698.hgc024.

- [26] M. Osada, T. Sato, M. Watanabe, M. Shirai and K. Arai, 'Catalytic gasification of wood biomass in subcritical and supercritical water', *Combustion Science and Technology*, vol. 178, no. 1, pp. 537–552, 2006. DOI: 10.1080/00102200500290807.
- [27] Y. Lu, L. Guo, X. Zhang and Q. Yan, 'Thermodynamic modeling and analysis of biomass gasification for hydrogen production in supercritical water', *Chemical Engineering Journal*, vol. 131, no. 1, pp. 233–244, 2007. DOI: 10.1016/j.cej.2006.11.016.
- [28] A. G. Haiduc, M. Brandenberger, S. Suquet, F. Vogel, R. Bernier-Latmani and C. Ludwig, 'SunChem: An integrated process for the hydrothermal production of methane from microalgae and CO₂ mitigation', *J Appl Phycol*, vol. 21, no. 5, pp. 529–541, 2009. DOI: 10.1007/s10811-009-9403-3.
- [29] J. S. Luterbacher, M. Fröling, F. Vogel, F. Maréchal and J. W. Tester, 'Hydrothermal gasification of waste biomass: Process design and life cycle assessment', *Environ. Sci. Technol.*, vol. 43, no. 5, pp. 1578–1583, 2009. DOI: 10.1021/es801532f.
- [30] M. Gassner, F. Vogel, G. Heyen and F. Maréchal, 'Optimal process design for the poly-generation of SNG, power and heat by hydrothermal gasification of waste biomass: Thermo-economic process modelling and integration', *Energy Environ. Sci.*, vol. 4, no. 5, pp. 1726–1741, 2011. DOI: 10.1039/C0EE00629G.
- [31] Y. Lin and S. Tanaka, 'Ethanol fermentation from biomass resources: Current state and prospects', *Appl Microbiol Biotechnol*, vol. 69, no. 6, pp. 627–642, 2006. DOI: 10.1007/s00253-005-0229-x.
- [32] E. A. Johnson and C. Echavarri-Erasun, 'Chapter 3 - yeast biotechnology', in *The Yeasts (Fifth Edition)*, C. P. Kurtzman, J. W. Fell and T. Boekhout, Eds., London: Elsevier, 2011, pp. 21–44. DOI: 10.1016/B978-0-444-52149-1.00003-3.
- [33] P. Halder, K. Azad, S. Shah and E. Sarker, 'Chapter 8 - prospects and technological advancement of cellulosic bioethanol ecofuel production', in *Advances in Eco-Fuels for a Sustainable Environment*, K. Azad, Ed., Woodhead Publishing, 2019, pp. 211–236. DOI: 10.1016/B978-0-08-102728-8.00008-5.
- [34] E. Kwietniewska and J. Tys, 'Process characteristics, inhibition factors and methane yields of anaerobic digestion process, with particular focus on microalgal biomass fermentation', *Renewable and Sustainable Energy Reviews*, vol. 34, pp. 491–500, 2014. DOI: 10.1016/j.rser.2014.03.041.
- [35] A. Baiker, 'Supercritical fluids in heterogeneous catalysis', *Chem. Rev.*, vol. 99, no. 2, pp. 453–474, 1999. DOI: 10.1021/cr970090z.
- [36] A. Kruse and E. Dinjus, 'Hot compressed water as reaction medium and reactant: Properties and synthesis reactions', *The Journal of Supercritical Fluids*, vol. 39, no. 3, pp. 362–380, 2007. DOI: 10.1016/j.supflu.2006.03.016.
- [37] F. Maxim, C. Contescu, P. Boillat, B. Niceno, K. Karalis, A. Testino and C. Ludwig, 'Visualization of supercritical water pseudo-boiling at widom line crossover', *Nature Communications*, vol. 10, no. 1, pp. 1–11, 2019. DOI: 10.1038/s41467-019-12117-5.

Bibliography

- [38] NIST chemistry WebBook, [Online]. Available: <https://webbook.nist.gov/chemistry/> (visited on 05/06/2020).
- [39] M. Uematsu and E. U. Frank, 'Static dielectric constant of water and steam', *Journal of Physical and Chemical Reference Data*, vol. 9, no. 4, pp. 1291–1306, 1980. DOI: 10.1063/1.555632.
- [40] A. V. Bandura and S. N. Lvov, 'The ionization constant of water over wide ranges of temperature and density', *Journal of Physical and Chemical Reference Data*, vol. 35, no. 1, pp. 15–30, 2005. DOI: 10.1063/1.1928231.
- [41] J. F. Connolly, 'Solubility of hydrocarbons in water near the critical solution temperatures.', *J. Chem. Eng. Data*, vol. 11, no. 1, pp. 13–16, 1966. DOI: 10.1021/je60028a003.
- [42] N. Akiya and P. E. Savage, 'Roles of water for chemical reactions in high-temperature water', *Chem. Rev.*, vol. 102, no. 8, pp. 2725–2750, 2002. DOI: 10.1021/cr000668w.
- [43] H. Weingärtner and E. U. Franck, 'Supercritical water as a solvent', *Angewandte Chemie International Edition*, vol. 44, no. 18, pp. 2672–2692, 2005. DOI: 10.1002/anie.200462468.
- [44] W. L. Marshall and E. U. Franck, 'Ion product of water substance, 0–1000 °C, 1–10,000 bars - new international formulation and its background', *Journal of Physical and Chemical Reference Data*, vol. 10, no. 2, pp. 295–304, 1981. DOI: 10.1063/1.555643.
- [45] M. J. Antal, A. Brittain, C. DeAlmeida, S. Ramayya and J. C. Roy, 'Heterolysis and homolysis in supercritical water', *Supercritical Fluids*, vol. 329, pp. 77–86, 1987. DOI: 10.1021/bk-1987-0329.ch007.
- [46] X. Xu and M. J. Antal, 'Kinetics and mechanism of isobutene formation from t-butanol in hot liquid water', *AIChE Journal*, vol. 40, no. 9, pp. 1524–1534, 1994. DOI: 10.1002/aic.690400911.
- [47] X. Xu, M. J. Antal and D. G. M. Anderson, 'Mechanism and temperature-dependent kinetics of the dehydration of tert-butyl alcohol in hot compressed liquid water', *Ind. Eng. Chem. Res.*, vol. 36, no. 1, pp. 23–41, 1997. DOI: 10.1021/ie960349o.
- [48] N. Wei, D. Xu, B. Hao, S. Guo, Y. Guo and S. Wang, 'Chemical reactions of organic compounds in supercritical water gasification and oxidation', *Water Research*, vol. 190, p. 116 634, 2021. DOI: 10.1016/j.watres.2020.116634.
- [49] J. Yu and P. E. Savage, 'Decomposition of formic acid under hydrothermal conditions', *Ind. Eng. Chem. Res.*, vol. 37, no. 1, pp. 2–10, 1998. DOI: 10.1021/ie970182e.
- [50] P. E. Savage, 'Organic chemical reactions in supercritical water', *Chemical Reviews*, vol. 99, no. 2, pp. 603–622, 1999. DOI: 10.1021/cr9700989.
- [51] Q. Guan, P. E. Savage and C. Wei, 'Gasification of alga nannochloropsis sp. in supercritical water', *The Journal of Supercritical Fluids*, vol. 61, pp. 139–145, 2012. DOI: 10.1016/j.supflu.2011.09.007.
- [52] R. F. Susanti, L. W. Dianningrum, T. Yum, Y. Kim, B. G. Lee and J. Kim, 'High-yield hydrogen production from glucose by supercritical water gasification without added

- catalyst', *International Journal of Hydrogen Energy*, vol. 37, no. 16, pp. 11 677–11 690, 2012. DOI: 10.1016/j.ijhydene.2012.05.087.
- [53] P. T. Williams and J. Onwudili, 'Composition of products from the supercritical water gasification of glucose: a model biomass compound', *Ind. Eng. Chem. Res.*, vol. 44, no. 23, pp. 8739–8749, 2005. DOI: 10.1021/ie050733y.
- [54] C. M. Huelsman and P. E. Savage, 'Reaction pathways and kinetic modeling for phenol gasification in supercritical water', *The Journal of Supercritical Fluids*, vol. 81, pp. 200–209, 2013. DOI: 10.1016/j.supflu.2013.05.012.
- [55] T. L.-K. Yong and Y. Matsumura, 'Kinetics analysis of phenol and benzene decomposition in supercritical water', *The Journal of Supercritical Fluids*, vol. 87, pp. 73–82, 2014. DOI: 10.1016/j.supflu.2013.12.018.
- [56] A. G. Chakinala, S. Kumar, A. Kruse, S. R. A. Kersten, W. P. M. van Swaaij and D. W. F. (Wim) Brilman, 'Supercritical water gasification of organic acids and alcohols: The effect of chain length', *The Journal of Supercritical Fluids*, vol. 74, pp. 8–21, 2013. DOI: 10.1016/j.supflu.2012.11.013.
- [57] M. J. Antal, W. S. L. Mok, J. C. Roy, A. T-Raissi and D. G. M. Anderson, 'Pyrolytic sources of hydrocarbons from biomass', *Journal of Analytical and Applied Pyrolysis*, vol. 8, pp. 291–303, 1985. DOI: 10.1016/0165-2370(85)80032-2.
- [58] M. Watanabe, T. Iida, Y. Aizawa, T. M. Aida and H. Inomata, 'Acrolein synthesis from glycerol in hot-compressed water', *Bioresource Technology*, vol. 98, no. 6, pp. 1285–1290, 2007. DOI: 10.1016/j.biortech.2006.05.007.
- [59] S. Ramayya, A. Brittain, C. DeAlmeida, W. Mok and M. J. Antal, 'Acid-catalysed dehydration of alcohols in supercritical water', *Fuel*, vol. 66, no. 10, pp. 1364–1371, 1987. DOI: 10.1016/0016-2361(87)90183-9.
- [60] J. B. Müller and F. Vogel, 'Tar and coke formation during hydrothermal processing of glycerol and glucose. Influence of temperature, residence time and feed concentration', *The Journal of Supercritical Fluids*, vol. 70, pp. 126–136, 2012. DOI: 10.1016/j.supflu.2012.06.016.
- [61] W. Bühler, E. Dinjus, H. J. Ederer, A. Kruse and C. Mas, 'Tonic reactions and pyrolysis of glycerol as competing reaction pathways in near- and supercritical water', *The Journal of Supercritical Fluids*, vol. 22, no. 1, pp. 37–53, 2002. DOI: 10.1016/S0896-8446(01)00105-X.
- [62] M. Modell, 'Gasification and liquefaction of forest products in supercritical water', *Fundamentals of Thermochemical Biomass Conversion*, pp. 95–119, 1985. DOI: 10.1007/978-94-009-4932-4_6.
- [63] D. C. Elliott and L. J. Sealock, 'Low temperature gasification of biomass under pressure', *Fundamentals of Thermochemical Biomass Conversion*, pp. 937–950, 1985. DOI: 10.1007/978-94-009-4932-4_52.

- [64] D. C. Elliott, L. J. Sealock and E. G. Baker, 'Chemical processing in high-pressure aqueous environments. 2. development of catalysts for gasification', *Ind. Eng. Chem. Res.*, vol. 32, no. 8, pp. 1542–1548, 1993. DOI: 10.1021/ie00020a002.
- [65] D. C. Elliott, L. J. J. Sealock and E. G. Baker, 'Chemical processing in high-pressure aqueous environments. 3. batch reactor process development experiments for organics destruction', *Ind. Eng. Chem. Res.*, vol. 33, no. 3, pp. 558–565, 1994. DOI: 10.1021/ie00027a012.
- [66] M. H. Waldner and F. Vogel, 'Renewable production of methane from woody biomass by catalytic hydrothermal gasification', *Ind. Eng. Chem. Res.*, vol. 44, no. 13, pp. 4543–4551, 2005. DOI: 10.1021/ie050161h.
- [67] D. C. Elliott, T. R. Hart and G. G. Neuenschwander, 'Chemical processing in high-pressure aqueous environments. 8. improved catalysts for hydrothermal gasification', *Ind. Eng. Chem. Res.*, vol. 45, no. 11, pp. 3776–3781, 2006. DOI: 10.1021/ie060031o.
- [68] M. H. Waldner, 'Catalytic hydrothermal gasification of biomass for the production of synthetic natural gas', Doctoral Thesis, ETH Zurich, 2007. DOI: 10.3929/ethz-a-005379296.
- [69] H. Nakagawa, A. Namba, M. Böhlmann and K. Miura, 'Hydrothermal dewatering of brown coal and catalytic hydrothermal gasification of the organic compounds dissolving in the water using a novel Ni/carbon catalyst', *Fuel*, vol. 83, no. 6, pp. 719–725, 2004. DOI: 10.1016/j.fuel.2003.09.020.
- [70] A. Sharma, I. Saito, H. Nakagawa and K. Miura, 'Effect of carbonization temperature on the nickel crystallite size of a Ni/C catalyst for catalytic hydrothermal gasification of organic compounds', *Fuel*, vol. 86, no. 7, pp. 915–920, 2007. DOI: 10.1016/j.fuel.2006.11.001.
- [71] M. H. Waldner, F. Krumeich and F. Vogel, 'Synthetic natural gas by hydrothermal gasification of biomass: Selection procedure towards a stable catalyst and its sodium sulfate tolerance', *The Journal of Supercritical Fluids*, vol. 43, no. 1, pp. 91–105, 2007. DOI: 10.1016/j.supflu.2007.04.004.
- [72] T. Sato, M. Osada, M. Watanabe, M. Shirai and K. Arai, 'Gasification of alkylphenols with supported noble metal catalysts in supercritical water', *Ind. Eng. Chem. Res.*, vol. 42, no. 19, pp. 4277–4282, 2003. DOI: 10.1021/ie030261s.
- [73] M. Osada, O. Sato, K. Arai and M. Shirai, 'Stability of Supported Ruthenium Catalysts for Lignin Gasification in Supercritical Water', *Energy Fuels*, vol. 20, no. 6, pp. 2337–2343, 2006. DOI: 10.1021/ef060356h.
- [74] M. Osada, O. Sato, M. Watanabe, K. Arai and M. Shirai, 'Water density effect on lignin gasification over supported noble metal catalysts in supercritical water', *Energy Fuels*, vol. 20, no. 3, pp. 930–935, 2006. DOI: 10.1021/ef050398q.

- [75] G. Peng, C. Ludwig and F. Vogel, 'Ruthenium Dispersion: A Key Parameter for the Stability of Supported Ruthenium Catalysts during Catalytic Supercritical Water Gasification', *ChemCatChem*, vol. 8, no. 1, pp. 139–141, 2016. DOI: 10.1002/cctc.201500995.
- [76] G. Peng, M. Steib, F. Gramm, C. Ludwig and F. Vogel, 'Synthesis factors affecting the catalytic performance and stability of Ru/C catalysts for supercritical water gasification', *Catal. Sci. Technol.*, vol. 4, no. 9, pp. 3329–3339, 2014. DOI: 10.1039/C4CY00586D.
- [77] A. Yamaguchi, N. Hiyoshi, O. Sato, M. Osada and M. Shirai, 'EXAFS study on structural change of charcoal-supported ruthenium catalysts during lignin gasification in supercritical water', *Catal Lett*, vol. 122, no. 1, pp. 188–195, 2008. DOI: 10.1007/s10562-007-9368-2.
- [78] G. Peng, F. Gramm, C. Ludwig and F. Vogel, 'Effect of carbon surface functional groups on the synthesis of Ru/C catalysts for supercritical water gasification', *Catal. Sci. Technol.*, vol. 5, no. 7, pp. 3658–3666, 2015. DOI: 10.1039/C5CY00352K.
- [79] J. Yu, Q. Guan, Q. Chen, P. Ning, J. Gu, X. Huang, Y. Shi and R. Miao, 'Catalytic gasification of phenol in supercritical water with Ru/graphitized carbon black', *RSC Advances*, vol. 6, no. 79, pp. 75 512–75 521, 2016. DOI: 10.1039/C6RA15601K.
- [80] D. J. M. de Vlieger, D. B. Thakur, L. Lefferts and K. Seshan, 'Carbon Nanotubes: A Promising Catalyst Support Material for Supercritical Water Gasification of Biomass Waste', *ChemCatChem*, vol. 4, no. 12, pp. 2068–2074, 2012. DOI: 10.1002/cctc.201200318.
- [81] D. J. M. de Vlieger, L. Lefferts and K. Seshan, 'Ru decorated carbon nanotubes – a promising catalyst for reforming bio-based acetic acid in the aqueous phase', *Green Chem.*, vol. 16, no. 2, pp. 864–874, 2014. DOI: 10.1039/C3GC41922C.
- [82] K. C. Park and H. Tomiyasu, 'Gasification reaction of organic compounds catalyzed by RuO₂ in supercritical water', *Chem. Commun.*, no. 6, pp. 694–695, 2003. DOI: 10.1039/B211800A.
- [83] W. C. Ketchie, E. P. Maris and R. J. Davis, 'In-situ X-ray absorption spectroscopy of supported Ru catalysts in the aqueous phase', *Chem. Mater.*, vol. 19, no. 14, pp. 3406–3411, 2007. DOI: 10.1021/cm0702868.
- [84] S. Rabe, M. Nachtegaal, T. Ulrich and F. Vogel, 'Towards understanding the catalytic reforming of biomass in supercritical water', *Angewandte Chemie International Edition*, vol. 49, no. 36, pp. 6434–6437, 2010. DOI: 10.1002/anie.201001160.
- [85] A. A. Peterson, M. Dreher, J. Wambach, M. Nachtegaal, S. Dahl, J. K. Nørskov and F. Vogel, 'Evidence of scrambling over ruthenium-based catalysts in supercritical water gasification', *ChemCatChem*, vol. 4, no. 8, pp. 1185–1189, 2012. DOI: 10.1002/cctc.201100450.
- [86] M. Dreher, B. Johnson, A. A. Peterson, M. Nachtegaal, J. Wambach and F. Vogel, 'Catalysis in supercritical water: Pathway of the methanation reaction and sulfur poisoning over a Ru/C catalyst during the reforming of biomolecules', *Journal of Catalysis*, vol. 301, pp. 38–45, 2013. DOI: 10.1016/j.jcat.2013.01.018.

- [87] D. C. Elliott, 'Catalytic hydrothermal gasification of biomass', *Biofuels, Bioprod. Bioref.*, vol. 2, no. 3, pp. 254–265, 2008. DOI: 10.1002/bbb.74.
- [88] D. C. Elliott, M. R. Phelps, L. J. Sealock and E. G. Baker, 'Chemical processing in high-pressure aqueous environments. 4. continuous-flow reactor process development experiments for organics destruction', *Ind. Eng. Chem. Res.*, vol. 33, no. 3, pp. 566–574, 1994. DOI: 10.1021/ie00027a013.
- [89] D. C. Elliott, G. G. Neuenschwander, T. R. Hart, R. S. Butner, A. H. Zacher, M. H. Engelhard, J. S. Young and D. E. McCready, 'Chemical processing in high-pressure aqueous environments. 7. process development for catalytic gasification of wet biomass feedstocks', *Ind. Eng. Chem. Res.*, vol. 43, no. 9, pp. 1999–2004, 2004. DOI: 10.1021/ie034303o.
- [90] N. Boukis and I. K. Stoll, 'Gasification of biomass in supercritical water, challenges for the process design — lessons learned from the operation experience of the first dedicated pilot plant', *Processes*, vol. 9, no. 3, p. 455, 2021. DOI: 10.3390/pr9030455.
- [91] N. Boukis, E. Hauer, S. Herbig, J. Sauer and F. Vogel, 'Catalytic gasification of digestate sludge in supercritical water on the pilot plant scale', *Biomass Conv. Bioref.*, vol. 7, no. 4, pp. 415–424, 2017. DOI: 10.1007/s13399-017-0238-x.
- [92] G. Peng, F. Vogel, D. Refardt and C. Ludwig, 'Catalytic Supercritical Water Gasification: Continuous Methanization of *Chlorella vulgaris*', *Ind. Eng. Chem. Res.*, vol. 56, no. 21, pp. 6256–6265, 2017. DOI: 10.1021/acs.iecr.7b00042.
- [93] J. Reimer, G. Peng, S. Viereck, E. De Boni, J. Breinl and F. Vogel, 'A novel salt separator for the supercritical water gasification of biomass', *The Journal of Supercritical Fluids*, vol. 117, pp. 113–121, 2016. DOI: 10.1016/j.supflu.2016.06.009.
- [94] G. Peng, J. Reimer, F. Vogel, H. Zoehrer and E. D. Boni, 'A salt separator and a method for producing a methane-containing gas mixture from biomass using a salt separator', U.S. Patent 20170081229A1, 2017.
- [95] G. Peng, C. Ludwig and F. Vogel, 'Catalytic supercritical water gasification: Interaction of sulfur with ZnO and the ruthenium catalyst', *Applied Catalysis B: Environmental*, vol. 202, pp. 262–268, 2017. DOI: 10.1016/j.apcatb.2016.09.011.
- [96] Y. Matsumura, 'Chapter 9 - hydrothermal gasification of biomass', in *Recent Advances in Thermo-Chemical Conversion of Biomass*, A. Pandey, T. Bhaskar, M. Stöcker and R. K. Sukumaran, Eds., Boston: Elsevier, 2015, pp. 251–267. DOI: 10.1016/B978-0-444-63289-0.00009-0.
- [97] F. Vogel, 'Hydrothermal Production of SNG from Wet Biomass', in *Synthetic Natural Gas from Coal, Dry Biomass, and Power-to-Gas Applications*, T. J. Schildhauer and S. M. A. Biollaz, Eds., John Wiley & Sons, Inc., 2016, pp. 249–278. DOI: 10.1002/9781119191339.ch10.
- [98] D. C. Elliott, T. R. Hart, G. G. Neuenschwander, L. J. Rotness, M. V. Olarte and A. H. Zacher, 'Chemical processing in high-pressure aqueous environments. 9. process

- development for catalytic gasification of algae feedstocks', *Ind. Eng. Chem. Res.*, vol. 51, no. 33, pp. 10 768–10 777, 2012. DOI: 10.1021/ie300933w.
- [99] Z. Kowalczyk, S. Jodzis, W. Raróg, J. Zieliński and J. Pielaszek, 'Effect of potassium and barium on the stability of a carbon-supported ruthenium catalyst for the synthesis of ammonia', *Applied Catalysis A: General*, vol. 173, no. 2, pp. 153–160, 1998. DOI: 10.1016/S0926-860X(98)00175-6.
- [100] J. N. Jocz, P. E. Savage and L. T. Thompson, 'Thermodynamic analysis of catalyst stability in hydrothermal reaction media', *Ind. Eng. Chem. Res.*, vol. 57, no. 26, pp. 8655–8663, 2018. DOI: 10.1021/acs.iecr.8b01334.
- [101] Y. Wang, Y. Zhu, Z. Liu, L. Wang, D. Xu, C. Fang and S. Wang, 'Catalytic performances of Ni-based catalysts on supercritical water gasification of phenol solution and coal-gasification wastewater', *International Journal of Hydrogen Energy*, vol. 44, no. 7, pp. 3470–3480, 2019. DOI: 10.1016/j.ijhydene.2018.08.218.
- [102] S. Li, P. E. Savage and L. Guo, 'Stability and activity maintenance of Al_2O_3 - and carbon nanotube-supported Ni catalysts during continuous gasification of glycerol in supercritical water', *The Journal of Supercritical Fluids*, vol. 135, pp. 188–197, 2018. DOI: 10.1016/j.supflu.2017.12.006.
- [103] A. Cardoso, T. R. Reina, I. Suelves, J. L. Pinilla, M. Millan and K. Hellgardt, 'Effect of carbon-based materials and CeO_2 on Ni catalysts for Kraft lignin liquefaction in supercritical water', *Green Chem.*, vol. 20, no. 18, pp. 4308–4318, 2018. DOI: 10.1039/C8GC02210K.
- [104] C. Hunston, D. Baudouin, M. Tarik, O. Kröcher and F. Vogel, 'Investigating Active Phase Loss from Supported Ruthenium Catalysts during Supercritical Water Gasification', *Catalysis Science & Technology*, 2021. DOI: 10.1039/d1cy00379h.
- [105] J. H. Bitter and K. P. d. Jong, 'Preparation of carbon-supported metal catalysts', in *Carbon Materials for Catalysis*, Wiley-Blackwell, 2008, pp. 157–176. DOI: 10.1002/9780470403709.ch5.
- [106] C. Freire and A. R. Silva, 'Carbon-anchored metal complex catalysts', in *Carbon Materials for Catalysis*, Wiley-Blackwell, 2008, pp. 267–307. DOI: 10.1002/9780470403709.ch8.
- [107] P. Munnik, P. E. de Jongh and K. P. de Jong, 'Recent developments in the synthesis of supported catalysts', *Chem. Rev.*, vol. 115, no. 14, pp. 6687–6718, 2015. DOI: 10.1021/cr500486u.
- [108] A. Ochoa, J. Bilbao, A. G. Gayubo and P. Castaño, 'Coke formation and deactivation during catalytic reforming of biomass and waste pyrolysis products: A review', *Renewable and Sustainable Energy Reviews*, vol. 119, p. 109 600, 2020. DOI: 10.1016/j.rser.2019.109600.
- [109] H. Zöhrer, F. Mayr and F. Vogel, 'Stability and Performance of Ruthenium Catalysts Based on Refractory Oxide Supports in Supercritical Water Conditions', *Energy Fuels*, vol. 27, no. 8, pp. 4739–4747, 2013. DOI: 10.1021/ef400707f.

- [110] M. Bagnoud-Velásquez, M. Brandenberger, F. Vogel and C. Ludwig, 'Continuous catalytic hydrothermal gasification of algal biomass and case study on toxicity of aluminum as a step toward effluents recycling', *Catalysis Today*, vol. 223, pp. 35–43, 2014. DOI: 10.1016/j.cattod.2013.12.001.
- [111] Y. Matsumura, T. Minowa, B. Potic, S. R. A. Kersten, W. Prins, W. P. M. van Swaaij, B. van de Beld, D. C. Elliott, G. G. Neuenschwander, A. Kruse and M. Jerry Antal Jr., 'Biomass gasification in near- and super-critical water: Status and prospects', *Biomass and Bioenergy*, vol. 29, no. 4, pp. 269–292, 2005. DOI: 10.1016/j.biombioe.2005.04.006.
- [112] S. Bjelić, U. Gasser, I. Alxneit and F. Vogel, 'Deactivation of Methanation Catalyst (Ru/C) Under Supercritical Water by Deposition of Non-Volatile Organics: First Insights Into Deposition Patterns and Chemical Properties', *ChemCatChem*, vol. 11, no. 6, pp. 1747–1755, 2019. DOI: 10.1002/cctc.201801615.
- [113] M. Osada, N. Hiyoshi, O. Sato, K. Arai and M. Shirai, 'Effect of Sulfur on Catalytic Gasification of Lignin in Supercritical Water', *Energy Fuels*, vol. 21, no. 3, pp. 1400–1405, 2007. DOI: 10.1021/ef060636x.
- [114] M. Osada, N. Hiyoshi, O. Sato, K. Arai and M. Shirai, 'Reaction pathway for catalytic gasification of lignin in presence of sulfur in supercritical water', *Energy Fuels*, vol. 21, no. 4, pp. 1854–1858, 2007. DOI: 10.1021/ef0701642.
- [115] M. Dreher, M. Steib, M. Nachtegaal, J. Wambach and F. Vogel, 'On-stream regeneration of a sulfur-poisoned ruthenium–carbon catalyst under hydrothermal gasification conditions', *ChemCatChem*, vol. 6, no. 2, pp. 626–633, 2014. DOI: 10.1002/cctc.201300791.
- [116] R. A. Van Santen, 'Complementary structure sensitive and insensitive catalytic relationships', *Accounts of Chemical Research*, vol. 42, no. 1, pp. 57–66, 2009. DOI: 10.1021/ar800022m.
- [117] R. van Hardeveld and A. van Montfoort, 'The influence of crystallite size on the adsorption of molecular nitrogen on nickel, palladium and platinum: An infrared and electron-microscopic study', *Surface Science*, vol. 4, no. 4, pp. 396–430, 1966. DOI: 10.1016/0039-6028(66)90016-1.
- [118] R. Van Hardeveld and F. Hartog, 'The statistics of surface atoms and surface sites on metal crystals', *Surface Science*, vol. 15, no. 2, pp. 189–230, 1969. DOI: 10.1016/0039-6028(69)90148-4.
- [119] C. J. H. Jacobsen, S. Dahl, P. L. Hansen, E. Törnqvist, L. Jensen, H. Topsøe, D. V. Prip, P. B. Møenshaug and I. Chorkendorff, 'Structure sensitivity of supported ruthenium catalysts for ammonia synthesis', *Journal of Molecular Catalysis A: Chemical*, vol. 163, no. 1, pp. 19–26, 2000. DOI: 10.1016/S1381-1169(00)00396-4.
- [120] G. L. Bezemer, J. H. Bitter, H. P. C. E. Kuipers, H. Oosterbeek, J. E. Holewijn, X. Xu, F. Kapteijn, A. J. van Dillen and K. P. de Jong, 'Cobalt particle size effects in the Fischer-Tropsch reaction studied with carbon nanofiber supported catalysts', *J. Am. Chem. Soc.*, vol. 128, no. 12, pp. 3956–3964, 2006. DOI: 10.1021/ja058282w.

- [121] J. P. den Breejen, P. B. Radstake, G. L. Bezemer, J. H. Bitter, V. Frøseth, A. Holmen and K. P. de Jong, 'On the origin of the cobalt particle size effects in Fischer-Tropsch catalysis', *Journal of the American Chemical Society*, vol. 131, no. 20, pp. 7197–7203, 2009. DOI: 10.1021/ja901006x.
- [122] T. O. Eschemann, J. H. Bitter and K. P. de Jong, 'Effects of loading and synthesis method of titania-supported cobalt catalysts for Fischer-Tropsch synthesis', *Catalysis Today*, vol. 228, pp. 89–95, 2014. DOI: 10.1016/j.cattod.2013.10.041.
- [123] D. Baudouin, U. Rodemerck, F. Krumeich, A. d. Mallmann, K. C. Szeto, H. Ménard, L. Veyre, J.-P. Candy, P. B. Webb, C. Thieuleux and C. Copéret, 'Particle size effect in the low temperature reforming of methane by carbon dioxide on silica-supported Ni nanoparticles', *Journal of Catalysis*, vol. 297, pp. 27–34, 2013. DOI: 10.1016/j.jcat.2012.09.011.
- [124] R. van den Berg, G. Prieto, G. Korpershoek, L. I. van der Wal, A. J. van Bunningen, S. Lægsgaard-Jørgensen, P. E. de Jongh and K. P. de Jong, 'Structure sensitivity of Cu and CuZn catalysts relevant to industrial methanol synthesis', *Nature Communications*, vol. 7, p. 13057, 2016. DOI: 10.1038/ncomms13057.
- [125] J. M. G. Carballo, J. Yang, A. Holmen, S. García-Rodríguez, S. Rojas, M. Ojeda and J. L. G. Fierro, 'Catalytic effects of ruthenium particle size on the Fischer-Tropsch Synthesis', *Journal of Catalysis*, vol. 284, no. 1, pp. 102–108, 2011. DOI: 10.1016/j.jcat.2011.09.008.
- [126] S. Dahl, A. Logadottir, R. C. Egeberg, J. H. Larsen, I. Chorkendorff, E. Törnqvist and J. K. Nørskov, 'Role of Steps in N₂ Activation on Ru(0001)', *Phys. Rev. Lett.*, vol. 83, no. 9, pp. 1814–1817, 1999. DOI: 10.1103/PhysRevLett.83.1814.
- [127] F. R. García-García, A. Guerrero-Ruiz and I. Rodríguez-Ramos, 'Role of B5-Type Sites in Ru Catalysts used for the NH₃ Decomposition Reaction', *Top Catal*, vol. 52, no. 6-7, pp. 758–764, 2009. DOI: 10.1007/s11244-009-9203-7.
- [128] W. Raróg-Pilecka, D. Szmigiel, A. Komornicki, J. Zieliński and Z. Kowalczyk, 'Catalytic properties of small ruthenium particles deposited on carbon: Ammonia decomposition studies', *Carbon*, vol. 41, no. 3, pp. 589–591, 2003. DOI: 10.1016/S0008-6223(02)00393-7.
- [129] W. Zheng, J. Zhang, H. Xu and W. Li, 'NH₃ decomposition kinetics on supported Ru clusters: Morphology and particle size effect', *Catal Lett*, vol. 119, no. 3, pp. 311–318, 2007. DOI: 10.1007/s10562-007-9237-z.
- [130] P. Panagiotopoulou, D. I. Kondarides and X. E. Verykios, 'Selective methanation of CO over supported Ru catalysts', *Applied Catalysis B: Environmental*, vol. 88, no. 3, pp. 470–478, 2009. DOI: 10.1016/j.apcatb.2008.10.012.
- [131] T. Abe, M. Tanizawa, K. Watanabe and A. Taguchi, 'CO₂ methanation property of Ru nanoparticle-loaded TiO₂ prepared by a polygonal barrel-sputtering method', *Energy Environ. Sci.*, vol. 2, no. 3, pp. 315–321, 2009. DOI: 10.1039/B817740F.

Bibliography

- [132] E. Truszkiewicz, K. Zegadło, D. Wojda, B. Mierzwa and L. Kępiński, 'The Effect of the Ruthenium Crystallite Size on the Activity of Ru/Carbon Systems in CO Methanation', *Top Catal*, vol. 60, no. 17, pp. 1299–1305, 2017. DOI: 10.1007/s11244-017-0815-z.
- [133] S. B. Vendelbo, M. Johansson, J. H. Nielsen and I. Chorkendorff, 'Is the methanation reaction over Ru single crystals structure dependent?', *Phys. Chem. Chem. Phys.*, vol. 13, no. 10, pp. 4486–4493, 2011. DOI: 10.1039/C0CP02371J.
- [134] M. P. Andersson, F. Abild-Pedersen, I. N. Remediakis, T. Bligaard, G. Jones, J. Engbæk, O. Lytken, S. Horch, J. H. Nielsen, J. Sehested, J. R. Rostrup-Nielsen, J. K. Nørskov and I. Chorkendorff, 'Structure sensitivity of the methanation reaction: H₂-induced CO dissociation on nickel surfaces', *Journal of Catalysis*, vol. 255, no. 1, pp. 6–19, 2008. DOI: 10.1016/j.jcat.2007.12.016.
- [135] S. Shetty, A. P. J. Jansen and R. A. van Santen, 'CO Dissociation on the Ru(1121) Surface', *J. Phys. Chem. C*, vol. 112, no. 36, pp. 14 027–14 033, 2008. DOI: 10.1021/jp801754n.
- [136] I. Czekaj, S. Pin and J. Wambach, 'Ru/Active Carbon Catalyst: Improved Spectroscopic Data Analysis by Density Functional Theory', *J. Phys. Chem. C*, vol. 117, no. 50, pp. 26 588–26 597, 2013. DOI: 10.1021/jp406402a.
- [137] G. Peng, 'Methane production from microalgae via continuous catalytic supercritical water gasification: Development of catalysts and sulfur removal techniques', Doctoral Thesis, EPFL, 2015.
- [138] S. Brunauer, P. H. Emmett and E. Teller, 'Adsorption of gases in multimolecular layers', *J. Am. Chem. Soc.*, vol. 60, no. 2, pp. 309–319, 1938. DOI: 10.1021/ja01269a023.
- [139] B. C. Lippens and J. H. de Boer, 'Studies on pore systems in catalysts: V. the t method', *Journal of Catalysis*, vol. 4, no. 3, pp. 319–323, 1965. DOI: 10.1016/0021-9517(65)90307-6.
- [140] E. P. Barrett, L. G. Joyner and P. P. Halenda, 'The determination of pore volume and area distributions in porous substances. i. computations from nitrogen isotherms', *J. Am. Chem. Soc.*, vol. 73, no. 1, pp. 373–380, 1951. DOI: 10.1021/ja01145a126.
- [141] R. A. D. Betta, 'Measurement of ruthenium metal surface area by chemisorption', *Journal of Catalysis*, vol. 34, no. 1, pp. 57–60, 1974. DOI: 10.1016/0021-9517(74)90011-6.
- [142] C.-H. Yang and J. G. Goodwin, 'Particle size dependence for CO chemisorption on supported ru catalysts', *React Kinet Catal Lett*, vol. 20, no. 1, pp. 13–18, 1982. DOI: 10.1007/BF02063576.
- [143] A. Borodziński and M. Bonarowska, 'Relation between crystallite size and dispersion on supported metal catalysts', *Langmuir*, vol. 13, no. 21, pp. 5613–5620, 1997. DOI: 10.1021/la962103u.
- [144] A. Sadezky, H. Muckenhuber, H. Grothe, R. Niessner and U. Pöschl, 'Raman microspectroscopy of soot and related carbonaceous materials: Spectral analysis and structural information', *Carbon*, vol. 43, no. 8, pp. 1731–1742, 2005. DOI: 10.1016/j.carbon.2005.02.018.

- [145] D. Scholz, O. Kröcher and F. Vogel, 'Deactivation and regeneration of sulfonated carbon catalysts in hydrothermal reaction environments', *ChemSusChem*, vol. 11, no. 13, pp. 2189–2201, 2018. DOI: 10.1002/cssc.201800678.
- [146] I. Alxneit, 'Particle Size Distributions from Electron Microscopy Images: Avoiding Pitfalls', *J. Phys. Chem. A*, 2020. DOI: 10.1021/acs.jpca.0c07840.
- [147] R. Coloma Ribera, R. W. E. van de Kruijs, S. Kokke, E. Zoethout, A. E. Yakshin and F. Bijkerk, 'Surface and sub-surface thermal oxidation of thin ruthenium films', *Appl. Phys. Lett.*, vol. 105, no. 13, p. 131 601, 2014. DOI: 10.1063/1.4896993.
- [148] M. Osada, A. Yamaguchi, N. Hiyoshi, O. Sato and M. Shirai, 'Gasification of sugar-cane bagasse over supported ruthenium catalysts in supercritical water', *Energy Fuels*, vol. 26, no. 6, pp. 3179–3186, 2012. DOI: 10.1021/ef300460c.
- [149] E. Auer, A. Freund, J. Pietsch and T. Tacke, 'Carbons as supports for industrial precious metal catalysts', *Applied Catalysis A: General*, vol. 173, no. 2, pp. 259–271, 1998. DOI: 10.1016/S0926-860X(98)00184-7.
- [150] D. Bergna, T. Hu, H. Prokkola, H. Romar and U. Lassi, 'Effect of some process parameters on the main properties of activated carbon produced from peat in a lab-scale process', *Waste Biomass Valor*, vol. 11, no. 6, pp. 2837–2848, 2020. DOI: 10.1007/s12649-019-00584-2.
- [151] X. Xu, Y. Matsumura, J. Stenberg and M. J. Antal, 'Carbon-catalyzed gasification of organic feedstocks in supercritical water', *Ind. Eng. Chem. Res.*, vol. 35, no. 8, pp. 2522–2530, 1996. DOI: 10.1021/ie950672b.
- [152] F. L. P. Resende and P. E. Savage, 'Effect of metals on supercritical water gasification of cellulose and lignin', *Ind. Eng. Chem. Res.*, vol. 49, no. 6, pp. 2694–2700, 2010. DOI: 10.1021/ie901928f.
- [153] J.-Y. Chang, A. Ghule, J.-J. Chang, S.-H. Tzing and Y.-C. Ling, 'Opening and thinning of multiwall carbon nanotubes in supercritical water', *Chemical Physics Letters*, vol. 363, no. 5, pp. 583–590, 2002. DOI: 10.1016/S0009-2614(02)01283-6.
- [154] J. N. Jocz, L. T. Thompson and P. E. Savage, 'Catalyst Oxidation and Dissolution in Supercritical Water', *Chem. Mater.*, vol. 30, no. 4, pp. 1218–1229, 2018. DOI: 10.1021/acs.chemmater.7b03713.
- [155] S. Lee, X. Bi, R. B. Reed, J. F. Ranville, P. Herckes and P. Westerhoff, 'Nanoparticle size detection limits by single particle ICP-MS for 40 elements', *Environ. Sci. Technol.*, vol. 48, no. 17, pp. 10 291–10 300, 2014. DOI: 10.1021/es502422v.
- [156] M. Schubert, J. B. Müller and F. Vogel, 'Continuous hydrothermal gasification of glycerol mixtures: Effect of glycerol and its degradation products on the continuous salt separation and the enhancing effect of K_3PO_4 on the glycerol degradation', *The Journal of Supercritical Fluids*, vol. 95, pp. 364–372, 2014. DOI: 10.1016/j.supflu.2014.09.011.

- [157] A. Cabañas and M. Poliakoff, 'The continuous hydrothermal synthesis of nano-particulate ferrites in near critical and supercritical water', *Journal of Materials Chemistry*, vol. 11, no. 5, pp. 1408–1416, 2001. DOI: 10.1039/B009428P.
- [158] Y. Tian, X. Lan, Y. Song, C. Liu and J. Zhou, 'Preparation and characterization of formed activated carbon from fine blue-coke', *International Journal of Energy Research*, vol. 39, no. 13, pp. 1800–1806, 2015. DOI: <https://doi.org/10.1002/er.3327>.
- [159] P. Kritzer, 'Corrosion in high-temperature and supercritical water and aqueous solutions: A review', *The Journal of Supercritical Fluids*, vol. 29, no. 1, pp. 1–29, 2004. DOI: 10.1016/S0896-8446(03)00031-7.
- [160] Properties: Titania, [Online]. Available: <https://www.azom.com/properties.aspx?ArticleID=1179> (visited on 13/06/2021).
- [161] Properties: Alumina, [Online]. Available: <https://www.azom.com/properties.aspx?ArticleID=52> (visited on 13/06/2021).
- [162] Properties: Zirconia, [Online]. Available: <https://www.azom.com/properties.aspx?ArticleID=133> (visited on 13/06/2021).
- [163] M. L. Toebes, J. M. P. van Heeswijk, J. H. Bitter, A. Jos van Dillen and K. P. de Jong, 'The influence of oxidation on the texture and the number of oxygen-containing surface groups of carbon nanofibers', *Carbon*, vol. 42, no. 2, pp. 307–315, 2004. DOI: 10.1016/j.carbon.2003.10.036.
- [164] F. Winter, L. G. Bezemer, C. van der Spek, J. D. Meeldijk, A. Jos van Dillen, J. W. Geus and K. P. de Jong, 'TEM and XPS studies to reveal the presence of cobalt and palladium particles in the inner core of carbon nanofibers', *Carbon*, vol. 43, no. 2, pp. 327–332, 2005. DOI: 10.1016/j.carbon.2004.09.019.
- [165] P. Yin, S. Hu, K. Qian, Z. Wei, L.-L. Zhang, Y. Lin, W. Huang, H. Xiong, W.-X. Li and H.-W. Liang, 'Quantification of critical particle distance for mitigating catalyst sintering', *Nature Communications*, vol. 12, no. 1, p. 4865, 2021. DOI: 10.1038/s41467-021-25116-2.
- [166] Jiong Lu, Xiao Hai, Shibo Xi, Sharon Mitchell, Karim Harrath, Haomin Xu, Dario Akl, Debin Kong, Jing Li, Zejun Li, Tao Sun, Huimin Yang, Yige Cui, Chenliang Su, Xiaoxu Zhao, Jun Li and Javier Pérez-Ramírez, 'Scalable two-step annealing method for preparing ultra-high-density single-atom catalyst libraries', *Nature Portfolio*, 2021. DOI: 10.21203/rs.3.rs-394916/v1.
- [167] E. E. Finney and R. G. Finke, 'Catalyst sintering kinetics data: Is there a minimal chemical mechanism underlying kinetics previously fit by empirical power-law expressions — and if so, what are its implications?', *Ind. Eng. Chem. Res.*, vol. 56, no. 37, pp. 10 271–10 286, 2017. DOI: 10.1021/acs.iecr.7b02633.
- [168] C. T. Campbell, S. C. Parker and D. E. Starr, 'The Effect of Size-Dependent Nanoparticle Energetics on Catalyst Sintering', *Science*, vol. 298, no. 5594, pp. 811–814, 2002. DOI: 10.1126/science.1075094.

-
- [169] K. Wettergren, F. F. Schweinberger, D. Deiana, C. J. Ridge, A. S. Crampton, M. D. Rötzer, T. W. Hansen, V. P. Zhdanov, U. Heiz and C. Langhammer, 'High Sintering Resistance of Size-Selected Platinum Cluster Catalysts by Suppressed Ostwald Ripening', *Nano Lett.*, vol. 14, no. 10, pp. 5803–5809, 2014. DOI: 10.1021/nl502686u.
- [170] T. W. van Deelen, H. Yoshida, R. Oord, J. Zečević, B. M. Weckhuysen and K. P. de Jong, 'Cobalt nanocrystals on carbon nanotubes in the Fischer-Tropsch synthesis: Impact of support oxidation', *Applied Catalysis A: General*, vol. 593, p. 117 441, 2020. DOI: 10.1016/j.apcata.2020.117441.
- [171] N. A. Krans, N. Ahmad, D. Alloyeau, K. P. de Jong and J. Zečević, 'Attachment of iron oxide nanoparticles to carbon nanofibers studied by in-situ liquid phase transmission electron microscopy', *Micron*, vol. 117, pp. 40–46, 2019. DOI: 10.1016/j.micron.2018.10.009.
- [172] Z. Kowalczyk, J. Sentek, S. Jodzis, E. Mizera, J. Góralski, T. Paryjczak and R. Didusko, 'An alkali-promoted ruthenium catalyst for the synthesis of ammonia, supported on thermally modified active carbon', *Catalysis Letters*, vol. 45, no. 1, pp. 65–72, 1997. DOI: 10.1023/A:1018970318628.
- [173] C. Liang, Z. Wei, Q. Xin and C. Li, 'Ammonia synthesis over Ru/C catalysts with different carbon supports promoted by barium and potassium compounds', *Applied Catalysis A: General*, vol. 208, no. 1, pp. 193–201, 2001. DOI: 10.1016/S0926-860X(00)00713-4.
- [174] L. Li, Z. H. Zhu, Z. F. Yan, G. Q. Lu and L. Rintoul, 'Catalytic ammonia decomposition over Ru/carbon catalysts: The importance of the structure of carbon support', *Applied Catalysis A: General*, vol. 320, pp. 166–172, 2007. DOI: 10.1016/j.apcata.2007.01.029.

List of publications

Peer-reviewed publications

- C. Hunston, D. Baudouin, M. Tarik *et al.*, 'Investigating Active Phase Loss from Supported Ruthenium Catalysts during Supercritical Water Gasification', *Catalysis Science & Technology*, 2021. DOI: 10.1039/d1cy00379h

Conference posters

- C. Hunston, D. Baudouin, M. Tarik, O. Kröcher, F. Vogel, 'Hydrothermal Gasification of Wet Biomass to Methane: Investigating the Stability of the Active Phase in Ru/C SCWG Catalysts', *28th European Biomass Conference & Exhibition*, July 2020, Marseille, France (online).
- C. Hunston, D. Baudouin, O. Kröcher, F. Vogel, 'Performance and stability of commercial Ru/C catalysts for the supercritical water gasification of wet biomass to bio-SNG', *PSI ENE/NES Poster event*, December 2019, Villigen PSI, Switzerland.
- C. Hunston, D. Baudouin, O. Kröcher, F. Vogel, 'Performance and stability of commercial Ru/C catalysts for the supercritical water gasification of wet biomass to bio-SNG', *6th Biomass for Swiss Energy Future Conference*, September 2019, Horw, Switzerland.
- C. Hunston, D. Baudouin, O. Kröcher, F. Vogel, 'Hydrothermal gasification of wet biomass to methane: understanding the effect of activated carbon pore structure on Ru/C catalyst performance', *27th European Biomass Conference & Exhibition*, May 2019, Lisbon, Portugal.
- C. Hunston, O. Kröcher, F. Vogel, 'Optimisation of the Ru/C catalyst for the supercritical water gasification of wet biomass', *PSI Catalysis Seminar*, June 2018, Villigen PSI, Switzerland.

Curriculum Vitae

PERSONAL INFORMATION

Christopher Hunston
Swiss and British
Born on June 13, 1991 in Vevey, Switzerland

EDUCATION

Paul Scherrer Institute, Villigen, CH
PhD student in the Catalytic Process & Engineering
group, supervised by Prof. O. Kröcher (EPFL) and Prof.
F. Vogel (FHNW) Sep. 2017 - Aug. 2021

EPFL, Lausanne, CH
Research assistant in the group of Prof. J. Luterbacher Jan. 2017 - Apr. 2017
Master's thesis in the group of Prof. J. Luterbacher Sep. 2016 - Jan. 2017
MSc in Chemistry and Chemical Engineering Feb. 2015 - Jan. 2017
BSc in Chemistry and Chemical Engineering Sep. 2010 - Jul. 2014

Gymnase de Burier, La Tour-de-Peilz, CH
High school Aug. 2007 - Jul. 2010

EMPLOYMENT HISTORY

Saltigo GmbH, Leverkusen, DE
Chemical engineering internship Feb. 2016 - Jun. 2016